



The
University
Of
Sheffield.

Department
Of
Mechanical
Engineering

An experimental investigation of residual
stress and strain in rapidly cured fibre
reinforced composites

Benjamin Charles Seers

October 2022

A thesis submitted in partial fulfilment for the degree of
Doctor of Philosophy, Ph.D.

Department of Mechanical Engineering,
University of Sheffield

Dr Rachel Tomlinson
Prof. Patrick Fairclough

Abstract

Carbon fibre reinforced composites are becoming increasingly prevalent in the aerospace and automotive industries for use in structural, and safety critical, applications due to their high specific strength and stiffness. However, residual stress is present in all fibre reinforced composites to some degree, caused by their inherent anisotropy and differential material properties between fibres and reinforcing matrix. Residual stress can cause premature failure in structures and must therefore be understood and accounted for, particularly in safety critical applications. In recent years, rapidly curing resins have been developed to reduce the processing time required to cure parts. However, the effect of shorter processing times on residual stress formation is still not well understood. Therefore, this thesis aims to investigate how rapidly curing a composite alters the residual stress and strain state of that composite and how this affects its mechanical performance. Fibre Bragg gratings were embedded into laminates during cure to offer a novel insight into the mechanisms causing residual strain in rapidly cured composites.

To ensure that there was sufficient bonding, and therefore strain transfer, between the embedded optical fibres and resin matrix, an investigation of the interface between the two was conducted. Single fibre fragmentation was used to quantify the strength of the interface. A novel sample preparation methodology was developed to allow for rapidly cured samples to be manufactured. A novel fragmentation length measuring technique was also developed to allow for instantaneous measurements of fragmentation length to be made. While it was possible to use this fibre fragmentation analysis technique with a slow curing resin system it was found that it was not possible with the rapid curing system as residual stress was too high and samples failed before meaningful measurements could be made. However, scanning electron microscopy and micro x-ray computed tomography were used to qualitatively evaluate the interface and it was determined that there was sufficiently good bonding between the embedded fibre and resin matrix in rapidly cured laminates.

Fibre Bragg gratings were embedded in laminates of varying thickness and cure temperatures to determine the effect of these parameters on the formation of residual strain during cure. It was found that the final residual strain of all samples was similar, but the route taken varied

significantly. Samples cured at high (low) temperatures developed much of their strain at the end (beginning) of the cure which meant the final residual stress was thought to be higher (lower). A numerical analysis was then conducted to determine the residual stress state of the laminates cured with embedded sensors and the residual strain data captured with embedded FBGs was used to validate the model. A mechanical analysis of the transverse bending strength of variously cured laminates was conducted to further validate the numerical model and to experimentally link residual strain data to mechanical strength and by extension residual stress. It was found that it was not possible to accurately determine the effect of laminate thickness on bending strength due to their higher void content. Samples cured at a higher temperature had a higher bending strength which is indicative of a lower tensile residual stress. This was due to those samples only vitrifying upon cooling which allowed for a significant amount of residual stress to be relaxed during cure. Therefore, there is no clear trend between cure temperature and residual stress. However, it is hypothesised that higher curing temperatures will lead to higher levels of tensile residual stress if laminates are cured well below the T_g of the cured laminate and not allowed to relax excessively.

This work has shown the applicability of using fibre Bragg gratings in measuring residual strain during the rapid curing of fibre reinforced composites. They offer a novel insight into the formation of residual strain during cure of these resin systems and are also a powerful validation tool for numerical work. The innovative tools developed in this work show great potential for furthering the adoption of rapidly cured composites for structural applications.

Acknowledgements

First, thank you to my supervisors Rachel Tomlinson and Patrick Fairclough for their support and guidance over the last four years. A lot has happened, moving labs, a pandemic, but we made it. Thank you to all the technical staff who have helped me throughout my PhD: Richard Kay, all those in the workshop, AdAM, and Sorby centre for your help and expertise.

Thanks to the polymers, soft matter, and colloids CDT for partial funding of my PhD and to all its members for the fun activity days and free lunches. Thank you to my adopted research group, the Composite Systems Innovation Centre, for your support and advice.

Thank you to Solvay for proposing the project and partial funding of my PhD. Thanks Mark, Chris and Matt for your engagement, ideas and support over the last four years. It has kept me motivated and gotten the ideas flowing. Thanks to Steve for your support and help with materials and all my many questions.

Thanks to everyone that has helped me throughout my undergraduate degree and PhD over the last 9 years. Thanks to everyone from Formula student, for making engineering fun and being good mates. To the rowing club for being there with me for the character building early starts and training sessions. To everyone in the triathlon club for good vibes and chilled runs in the peaks. To everyone I have met through climbing, for the post work sessions and beta spraying. A massive thank you to all my friends who have supported me throughout my undergraduate degree and PhD, I can't list you all but I wouldn't have been able to get through it all without your support. A special thanks to Oli and Amy for being the best housemates I could've asked for, for always put up with my moaning and for all the good times.

Mum and Dad, thank you for inspiring me to do my PhD, for all the proofreads, your hard work and for your constant love and support. I honestly wouldn't have been able to do it without you. Thanks to Tim for keeping me grounded and making me overly competitive. Finally, a huge thanks to Emma, for being there for me through the ups and downs, for your amazing kindness and support, but most of all, for making me happy.

Contents

Abstract.....	ii
Acknowledgements.....	iv
Contents.....	v
Glossary.....	ix
Nomenclature.....	x
1. Introduction	1
2. Background and literature review.....	5
2.1. Carbon fibre reinforced composites.....	5
2.2. The viscoelastic nature of epoxy matrices	9
2.3. Mechanisms in the formation of residual stress in composite materials.....	14
2.3.1. Micromechanical residual stress mechanisms	14
2.3.2. Macromechanical residual stress mechanisms	16
2.3.3. Tool-part interactions mechanisms.....	19
2.3.4. Summary of causes of residual stress	21
2.4. Residual stress measurement techniques	22
2.4.1. Introduction	22
2.4.2. Destructive methods	23
2.4.3. Non-destructive methods.....	37
2.4.4. Experimental residual stress measurement techniques conclusions.....	48
2.5. The effect of residual stress	51
2.6. Conclusion.....	55
3. Material characterization	58
3.1. Introduction.....	58

3.2.	Materials.....	59
3.3.	Dynamic Scanning Calorimetry.....	61
3.3.1.	Cure Kinetics Theory.....	61
3.3.2.	DSC Methods.....	62
3.3.3.	DSC Results.....	62
3.4.	Through-thickness temperature variations.....	68
3.5.	Asymmetric bending.....	71
3.6.	Dynamic mechanical analysis.....	73
3.7.	Conclusion.....	76
4.	Interfacial Strain Transfer.....	78
4.1.	Introduction.....	78
4.2.	Interfacial shear strength testing theory.....	79
4.2.1.	Introduction.....	79
4.2.2.	Single fibre fragmentation.....	80
4.2.3.	Single fibre pull-out.....	82
4.3.	SFFT Methodology.....	83
4.3.1.	Slow curing SFFT materials/method.....	84
4.3.2.	Rapid curing SFFT materials and methods.....	88
4.3.3.	SFFT testing methodology.....	93
4.4.	SFFT results and discussion.....	97
4.4.1.	Strain validation.....	97
4.4.2.	Slow cure.....	100
4.4.3.	Rapid cure.....	107
4.5.	Scanning electron microscopy and micro x-ray computed tomography of the fibre optic sensor interface.....	112

4.5.1.	Scanning electron microscopy cross-sections.....	112
4.5.2.	Micro x-ray computed tomography analysis	115
4.6.	Conclusion.....	120
5.	Photoelastic analysis of residual stress in neat resin	122
5.1.	Photoelasticity theory.....	123
5.2.	Methodology.....	127
5.3.	Results and discussion.....	132
5.4.	Conclusions.....	136
6.	Measuring residual strain using embedded optical fibres.....	137
6.1.	Introduction	137
6.2.	FBG Theory	138
6.3.	Materials and Method.....	140
6.4.	Results and discussion.....	146
6.5.	Conclusion	159
7.	Modelling Residual Stress.....	160
7.1.	Introduction.....	160
7.2.	Numerical model theory.....	161
7.3.	Numerical model	166
7.4.	Results	174
7.4.1.	Thermal validation results	174
7.4.2.	Strain validation results.....	176
7.4.3.	Residual stress analysis.....	179
7.5.	Conclusions.....	187
8.	The effect of residual stress on mechanical performance	189
8.1.	Introduction	189

8.2.	Materials and method	190
8.3.	Results and discussion.....	194
8.4.	The effect of rapid curing on mechanical properties.....	201
8.5.	Conclusion.....	205
9.	Conclusions and future work.....	207
10.	References.....	213
11.	Appendices.....	234
	Appendix A	234
	Appendix B.....	235
	Appendix C.....	236
	Appendix D	241
	Appendix E.....	242

Glossary

Abbreviation	Meaning
CFRP	Carbon Fibre Reinforced Polymer
CHILE	Cure Hardening Instantaneous Linear Elastic
CT	Computed Tomography
CTE	Coefficient of Thermal Expansion
DHD	Deep Hole Drilling
DIC	Digital Image Correlation
DMA	Dynamic Mechanical Analysis
DOC	Degree Of Cure
DOS	Distributed Optical Sensors
DSC	Dynamic Scanning Calorimetry
DTG	Draw Tower Grating
DVSP	Digital Volumetric Speckle Photography
EDM	Electron Discharge Machine
EFPI	Extrinsic Fabry Perot Interferometric
FBG	Fibre Bragg Grating
FE	Finite Element
FSG	Femtosecond Grating
GFRP	Glass Fibre Reinforced Plastic
iDIC	Integrated Digital Image Correlation
IFSS	Interfacial Shear Strength
ILE	Instantaneous Linear Elastic
RSSD	Repeated Safe Slitting Distance
RT	Room Temperature
SEM	Scanning Electron Microscope
SFFT	Single Fibre Fragmentation Testing
T3PB	Transverse Three-Point Bending
TTS	Time Temperature Superposition
UD	Unidirectional

Nomenclature

Symbol	Variable	Unit
A	Pre-exponential factor	(1/s)
C_p	Specific heat capacity	(J/kgK)
d	Diameter	(mm)
$E/E', E''$	Elastic modulus, loss modulus (Tensile)	(MPa)
E_a	Activation energy	(kJ/mol)
E_r	Instantaneous resin modulus	(MPa)
f_σ	Material stress fringe value	(MPa/fringe/mm)
$G/G', G''$	Elastic modulus, loss modulus (Shear)	(MPa)
H_t	Heat of reaction	(J/g)
k	Thermal conductivity	(W/mK)
l_c, \bar{l}	Fragmentation length (critical, average)	(mm)
n	Refractive index	-
N	Fringe order	-
P	Force	(N)
R	Universal gas constant	(J/mol/K)
S_ε	Mechanical strain sensitivity	($\mu\varepsilon^{-1} \times 10^{-7}$)
S_T	Thermal strain sensitivity	($K^{-1} \times 10^{-6}$)
t	Time	(s)
T	Temperature	(°C)
T_g	Instantaneous glass transition temperature	(°C)
$T_g^{\text{hot}}, T_g^{\text{cool}}$	Glass transition temperature of (Hot, Cool) laminates	(°C)
T_{g^∞}	Maximum practical glass transition temperature	(°C)
T_{vit}	Vitrification temperature	(°C)
V_f	Fibre volume fraction	(%)
$\alpha, \alpha_{\text{gel}}$	Degree of cure (instantaneous, gelation)	-
α^{CTE}	Coefficient of thermal expansion	(1/°C)
β	Chemical shrinkage strain	(%)
δ	tan delta	-
ε	Strain	($\mu\varepsilon$)

η	Viscosity	(Pas)
λ, λ_B	Wavelength of light, Bragg wavelength	(nm)
ν	Poisson's ratio	-
ρ	Density	(kg/m ³)
σ	Stress	(MPa)

Subscripts

Symbol	Variable
11, 22, 33	Direction (x, y, z)
f	Fibre property
m	Matrix property

1. Introduction

A composite material has two or more constituent phases and combines the desirable attributes from each phase to produce a material with preferable properties over that of either of the constituent phases. They exist in many forms, from the natural composites like wood, leather and bone, to manmade construction materials like cob (straw and mud) and steel reinforced concrete. While these composites have been used ubiquitously throughout recent history, it was not until World War II that we saw the advent of the first “modern” composite material, Glass Fibre Reinforced Plastic (GFRP). This revolutionised the way composites were thought of, as engineers could now optimise the properties of the material for the required use case. GFRP’s use a two-phase system with a reinforcing fibre phase (glass) and a binding matrix phase (polymer). The fibre gives the high tensile strength and stiffness to the composite while the matrix facilitates force transfer to the fibres and offers a high level of toughness. A composite material made this way is therefore highly anisotropic with the properties along the fibre direction being very different to those perpendicular to the fibres. Thus, it is common to use multiple layers or “plies” of fibres and matrix to build a laminate to create a more well-rounded and robust structure.

Since the introduction of GFRP there has been a huge amount of development in composites with the introduction of various matrix materials like polyester, vinyl-ester, epoxy, polyamide, silicone and polyether ether ketone. New fibre reinforcement materials have also been introduced like carbon, boron, aramids, quartz and even carbon nanotubes. Advances in both matrix and fibre materials have widened the applicability of composites with new reinforcements offering even higher strength and stiffnesses while new matrix materials can offer high temperature performance, for example. Currently the highest performing matrix materials are thermoset based, and this is therefore the area on which this research will focus.

The global composites industry is growing rapidly and is expected to be worth over \$130bn by 2024 [1]. Composites are especially growing in popularity in the aerospace and automotive industries with the Airbus A350 XWB boasting a construction consisting of 53% composite [2]. This mass scale adoption of composite technology is primarily driven by composites’ high specific strength and stiffness which, in the aerospace sector offers increased efficiency and

reduced fuel usage/costs. This reduction in fuel usage is of particular importance at present, with climate change being felt more acutely around the world year on year. It has been estimated [3] that for every 1 kg reduction in mass of an aircraft there is a 200 GJ energy savings over the aircrafts entire life or around 8.5 tonnes of CO₂ per kg saved. Even with the reduction in aircraft numbers due to COVID-19 there are around 25,000 aircraft currently operational around the world with this number set to rise to around 38,000 in the next 10 years [4]. Therefore, it is clear that even a small increase in the use of composite materials in the aerospace industry can have a huge impact on global CO₂ emissions and ultimately the climate crisis.

More commercial aircraft are being produced than ever before with Boeing producing a record 806 commercial aircraft in 2018 [5] and Airbus delivering 800 [6] in the same year. Therefore, there is an ever-growing demand for lower production times and higher production quantities of composites for the aerospace industry. This has led to the development of rapid curing resin systems to meet the demand of the aerospace industry. However, reduced cure times requires there to be a change in the thermal and chemical developments within the resin system which can lead to higher residual stress. Residual stresses are stresses which are “locked” into a part and persist even when the initial cause of the stress has been removed. They can be compressive or tensile, beneficial or detrimental, and should always be considered during any rigorous design process. The effect of this residual stress on the structural performance of parts is not fully understood and it is critical for the advancement of the industry and for the safety of aircraft that this gap in knowledge is addressed. Without more research in this area, high factors of safety must be used to account for this gap in knowledge which will lead to reduced efficiency of parts or lower adoption in the aerospace industry. Thus, the effect of rapid curing resins on residual stress and mechanical performance is the focus of this work.

Recently, resin formulations have been developed for use in rapid curing thermosetting laminates which make use of a pre-heated hydraulic hot press to rapidly apply heat and compaction to pre-impregnated laminates. This allows for cure times to be reduced from 2-6 hours to 1-10 minutes. In the literature, little work has focused on rapidly cured thermoset hot-pressed pre-impregnated samples. However, there is some research using a combination of slower curing resin formulations with other composite manufacturing techniques (30-90 minutes) or neat resin samples as rapidly as 2 minutes [7][8][9][10][11][12][13]. None of

these studies investigated the effect of rapid curing on residual stress. There is no consensus in the literature on the definition of what is considered “rapid” curing (or in some work, “snap-curing”). For simplicity, this work will define laminates curing in the range of 1-10 minutes as “rapidly” cured.

The subject areas covered in this thesis are broad and varied. This is out of necessity as the formation of residual stress in rapidly cured fibre reinforced composites is a multi-physics and multi-disciplinary problem, ranging from polymer chemistry to structural mechanics. Very little is known about the formation of residual stress and strain in rapidly cured composites. Therefore, to best begin to quantify and evaluate the various physical and phenomenological mechanisms at play during this process a very broad and holistic approach is required.

Thus, the main aim of this research can be summarised as:

- To investigate how rapidly curing composites alters the residual stress and strain state of that composite and how this affects its mechanical performance.

To achieve this, the following objectives have been defined as:

- Carry out a literature review on the mechanisms causing residual stress in composites and the various techniques that can be used to experimentally determine residual stress/strain. (Chapter 2)
- Characterize laminate material parameters needed for the investigation of residual stress in novel, rapidly curing matrices. (Chapter 3)
- Investigate the feasibility of using embedded sensors in rapidly curing laminates for measuring residual strain during cure (Chapter 4)
- Perform a photoelastic analysis of rapidly cured neat resin samples, cured at various rates, to gain a full-field understanding of the through-thickness distribution of residual stress in those samples (Chapter 5)
- Monitor the development of residual strain with embedded sensors in laminates of various thicknesses and cure temperatures. Use these data to qualitatively analyse the development of residual stress in these laminates (Chapter 6)

- Use a simplified multi-physics model of rapidly curing composites to investigate the formation of residual stress and the influence of the previously experimentally determined residual strain (Chapter 7)
- Use transverse bending tests to quantify the effect of residual strain/stress on the mechanical performance of the variously cured composites (Chapter 8)

2. Background and literature review

2.1. Carbon fibre reinforced composites

The aim of this chapter is to outline the various mechanisms that contribute to the formation of residual stress/strain in fibre reinforced thermosetting composites and the numerous experimental methods for determining that stress/strain. First, some preliminary definitions are outlined with reference to inherent properties of fibre reinforced composites which cause residual stress/strain. Then, a brief introduction to the viscoelastic nature of epoxy matrices is given to show how both time and state play a role in the development of residual stress/strain. The mechanisms that cause residual stress/strain are then outlined on a micro, macro and global scale to identify which factors affect this build-up. Lastly, a comprehensive review into the various experimental techniques used to determine residual stress/strain in thermosetting fibre reinforced composites is then given which has been adapted from work already published [14].

Composites consist of two constituent phases. One reinforcement phase and one matrix phase which, when well designed and manufactured, work together cohesively to bring together complimentary attributes to form a whole which is stronger than the sum of its parts. In the case of Carbon Fibre Reinforced Polymers (CFRP), a carbon fibre is used as the reinforcing phase to bring high stiffness and strength to the composite while the polymer matrix phase adds toughness and allows load to be more effectively transmitted along the fibres. This makes composite materials highly anisotropic as each of the three orthogonal principal axes depend upon the principal reinforcement direction. This makes CFRPs highly customisable and efficient structures as reinforcements can be used in key, highly loaded areas, and omitted where they are not needed. However, this anisotropy is also a key driver in the development of residual stress in CFRPs, as will be discussed in detail in this thesis. Figure 1 provides a cross-section view of a fibre reinforced laminate. It can be seen that each layer called a laminae (or ply) is made up of thousands of fibres surrounded by a matrix. Multiple laminae are then stacked on top of each other in a given sequence to form a laminate. Here, intralaminar and interlaminar are terms that describe phenomena within a ply and between plies respectively.

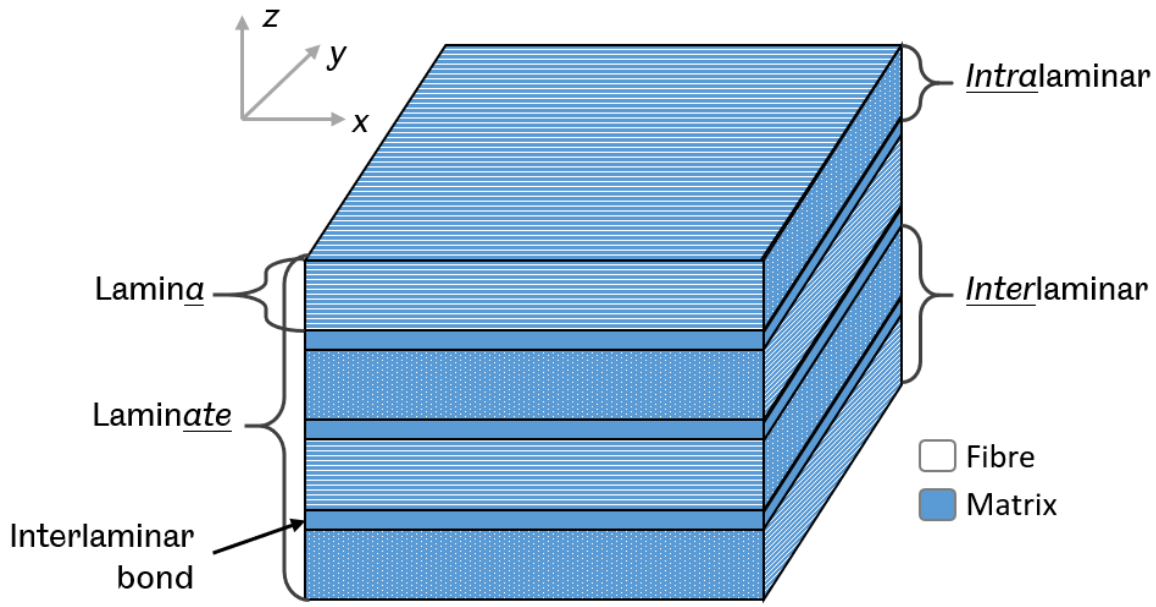


Figure 1: A fibre-reinforced laminate cross-section.

To categorise various stacking sequences, three main types of laminates are defined; balanced, symmetric, and quasi-isotropic. These have been summarised with examples in Table 1. Balanced laminates have pairs of plies with the same properties angled at $+\theta$ and $-\theta$ to each other where θ is the angle of the fibres relative to some defined axis. This means that the laminate has no bend-twist coupling. Symmetric layups are when there are the same number and angle of plies above and below the centre line of the laminate which causes there to be no bending moments within the laminate. Therefore, a balanced and symmetric laminate should have a zero-resultant force in the out-of-plane direction if the force is applied evenly. Finally, quasi-isotropic laminates are a special case where they can be assumed to act like isotropic materials as the material behaves the same regardless of loading direction. In this case the laminate is balanced, symmetrical and has an even distribution of fibre angles through the laminate.

For this thesis, all laminates will be represented using the following form: $[\pm A, \pm B, \dots]_s$, where A, B and the following letters will denote the angle of that ply to the normal direction in degrees and the \pm will denote if this angle is positive or negative. The subscript “s” can be used to show the laminate is symmetric around the mid-plane. For example, $[0, 90, +45, -45]_s$ is equivalent to $[0, 90, +45, -45, -45, +45, 90, 0]$.

Table 1: Laminate types and their properties

Laminate type	Example	Property
Symmetric & balanced	[+45, -45, 0, 0, -45, +45]	Constant mid-plane stress
Non-symmetric & balanced	[+45, 90, 0, 0, -45, 90]	Induced curvature
Symmetric & non-balanced	[-45, 0, 0, -45]	Induced twist
Non-symmetric & non-balanced	[-45, +45, 0, 0, -45, 90]	Induced twist & curvature
Quasi-isotropic	[0, 90, +45, -45] _s	Behaves isotropically

There is a variety of possibilities in the arrangement of the fibres in each ply. The simplest case is a Unidirectional (UD) arrangement of the fibres where all the fibres run along the same axis. This arrangement is popular as it has the highest potential for stiffness, strength and customizability. With all the fibres running along the same axis the highest possible stiffness and strength is achieved when loading along the same axis as the fibres as they carry the majority of the load. However, when loading transversely to the fibre direction the laminate is very weak as the matrix carries a large proportion of the applied load as the fibres contribute little in this direction. Thus, the fibres are often woven together so that the fibres run along the 0° and 90° directions. This offers a lower strength and stiffness as only half of the fibres are carrying the force if the load is along one of the fibre directions. However, the benefit of this is less anisotropy in the laminate making it more robust if the loading case is less well known. In this work, pre-impregnated (prepreg) plies consisting of carbon reinforcing fibres impregnated with β -staged (semi-cured) resin at a specific ratio for optimal material parameters will be used. This is commonly used in the aerospace and automotive industries as this offers a fast and efficient manufacturing route with superior laminate properties over other composite manufacturing methods.

Due to the orthotropic nature of composites the constitutive stress/strain relationship must be described in matrix form for ease and computational efficiency [15]. If we assume linear elasticity, the three-dimensional constitutive relationship can be described as shown in Equation (1).

$$\begin{bmatrix} \sigma_{11} \\ \sigma_{22} \\ \sigma_{33} \\ \sigma_{23} \\ \sigma_{31} \\ \sigma_{12} \end{bmatrix} = \begin{bmatrix} C_{11} & C_{12} & C_{13} & 0 & 0 & 0 \\ C_{12} & C_{22} & C_{23} & 0 & 0 & 0 \\ C_{13} & C_{23} & C_{33} & 0 & 0 & 0 \\ 0 & 0 & 0 & C_{44} & 0 & 0 \\ 0 & 0 & 0 & 0 & C_{55} & 0 \\ 0 & 0 & 0 & 0 & 0 & C_{66} \end{bmatrix} \begin{bmatrix} \varepsilon_{11} \\ \varepsilon_{22} \\ \varepsilon_{33} \\ 2\varepsilon_{23} \\ 2\varepsilon_{31} \\ 2\varepsilon_{12} \end{bmatrix} \quad (1)$$

where subscripts 1, 2 and 3 represent the three principal directions of the laminate with their associated stress, σ , and strains, ε . The stiffness matrix of the laminate, C , is described by Equation (2).

$$C = \begin{bmatrix} \frac{1 - \nu_{23}\nu_{32}}{E_{22}E_{33}\Delta} & \frac{\nu_{21} + \nu_{31}\nu_{23}}{E_{22}E_{33}\Delta} & \frac{\nu_{31} + \nu_{21}\nu_{32}}{E_{22}E_{33}\Delta} & 0 & 0 & 0 \\ \frac{\nu_{12} + \nu_{13}\nu_{32}}{E_{11}E_{33}\Delta} & \frac{1 - \nu_{13}\nu_{31}}{E_{11}E_{33}\Delta} & \frac{\nu_{32} + \nu_{31}\nu_{12}}{E_{11}E_{33}\Delta} & 0 & 0 & 0 \\ \frac{\nu_{13} + \nu_{12}\nu_{23}}{E_{11}E_{22}\Delta} & \frac{\nu_{23} + \nu_{13}\nu_{21}}{E_{21}E_{22}\Delta} & \frac{1 - \nu_{21}\nu_{12}}{E_{11}E_{22}\Delta} & 0 & 0 & 0 \\ 0 & 0 & 0 & 2G_{23} & 0 & 0 \\ 0 & 0 & 0 & 0 & 2G_{31} & 0 \\ 0 & 0 & 0 & 0 & 0 & 2G_{12} \end{bmatrix} \quad (2)$$

$$\text{where } \Delta = \frac{1 - \nu_{12}\nu_{21} - \nu_{23}\nu_{32} - \nu_{13}\nu_{31} - 2\nu_{12}\nu_{23}\nu_{31}}{E_{11}E_{22}E_{33}} \quad (3)$$

where the Young's modulus, E , Poisson's ratio, ν , and shear modulus, G are used to define the stiffness matrix. For the case of unidirectional composites, which can be assumed to be transversely isotropic, we can simplify these relations further as; $E_{22} = E_{33}$, $\nu_{12} = \nu_{13}$, $\nu_{21} = \nu_{31}$, $\nu_{23} = \nu_{32}$, $G_{12} = G_{13}$. Additionally G_{23} , ν_{21} and ν_{23} can be described in Equations (4), (5) and (6) respectively.

$$G_{23} = \frac{E_{22}}{2(1 + \nu_{23})} \quad (4)$$

$$\nu_{21} = \frac{E_{22}}{E_{11}} \nu_{12} \quad (5)$$

$$\nu_{23} = \nu_{12} \frac{1 - \nu_{21}}{1 - \nu_{12}} \quad (6)$$

Laminate properties can be calculated from the reinforcing fibres and resin matrix properties by applying a self-consistent field model which is shown in full in Appendix A. Here, the subscripts f and m refer to fibre and matrix properties respectively. Almost all of these laminate properties are dependent upon the fibre volume fraction, V_f , of the lamina which is defined as the volumetric proportion of reinforcing fibres to matrix material. Laminates with

a higher V_f will have properties that are more fibre dominant while laminates with a low V_f will be mostly matrix dominant. Thus, understanding and controlling V_f is critical in determining the final laminate properties.

Due to the anisotropic, complex nature of composite laminates and irregularities during the manufacturing process, residual stress forms in many different ways and on a number of scales. To ease the discussion of these mechanisms, three categories have been used in this thesis to group them into commonly used subsets [7][8]: micro scale, macro scale and tool-part interactions and these will be described in more detail in the following sections.

2.2. The viscoelastic nature of epoxy matrices

Throughout the cure, or polymerisation, of a thermosetting resin the physical state evolves from a low molecular weight liquid to a high molecular weight solid with a densely packed network of cross-linked polymer chains. In the case of commonly used thermosetting resins in composites, this irreversible reaction is initiated by temperature which adds energy to the system, thereby causing the reaction rate to increase. Additionally, this reaction is exothermic so heat is released during the cross-linking process which further increases the reaction rate of the cure. During the initial stages of the curing process the increase in temperature reduces the viscosity of the resin while cross-links begin to form. At the gelation point of the resin, α_{gel} , a critical number of cross-links have formed and one polymer chain spans the sample size. This causes the molecular weight of the resin to increase, the viscosity of the resin to increase sharply and for the resin solid properties to become more dominant than the liquid properties. While the viscosity of the resin increases throughout the entire polymerization process, the net change is a decrease in viscosity before gelation due to the increase in temperature. The Degree Of Cure (DOC), α , or degree of polymerisation of the resin, continues to increase and the glass transition temperature, T_g , of the resin also increases with DOC. The T_g is the temperature at which the resin transitions from a glassy elastic-like solid to a rubbery solid. The T_g continues to increase until the T_g is equal to the curing temperature T_{cure} at which point vitrification, T_{vit} is said to have been reached, and long range diffusion stops. After this, T_g increases to the practical maximum T_g of the resin system, $T_{g\infty}$, but more slowly as the molecular mobility of the resin is significantly reduced. The DOC of the resin also increases more slowly after T_g due to the lower molecular mobility of the resin.

In this way, thermosetting resins transition from a viscous, to rubbery and then finally, glassy state during cure if the $T_{g\infty}$ of the resin system is not exceeded. The evolution of DOC, T_g and viscosity (η) during a typical cure cycle where $T_{g\infty}$ is not exceeded by cure temperature is shown in Figure 2.

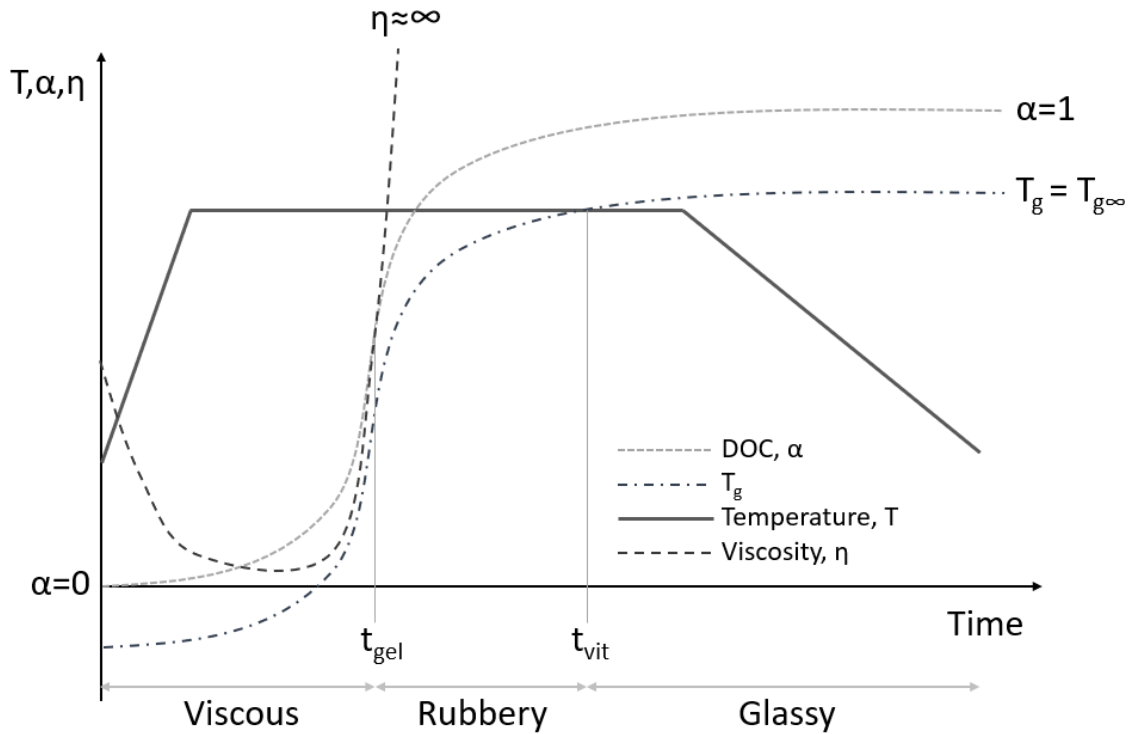


Figure 2: A typical cure cycle of a thermosetting resin with temperature, T_g , α and η profiles marked. Adapted from [18]

Viscoelastic materials like amorphous thermosetting polymers display both viscous and elastic behaviour during deformation and over time. When a force is applied to a long chained amorphous polymer, parts of the chain changes position, unravelling and stretching in the direction of the deformation. These polymer chains can be simply modelled as springs and, as such, store energy and rebound when the force is removed, thus giving the elastic part of the response. The viscous component of viscoelasticity comes from the loss of energy as heat during this deformation due to the diffusion of molecules in the amorphous solid. This lost energy cannot be recovered and is thus often modelled as a dashpot. The ability of the material to do this in any given cure state can be described in terms of the viscous loss modulus, E'' , of the material with E' defining the elastic storage modulus. The viscous component of a viscoelastic material causes a time and strain rate dependent response to be seen in

amorphous polymers. Therefore, there is not a linear relationship between stress and strain in the development of residual stress in curing composites. In this work, “stress” and “strain” terms cannot be used interchangeably as is sometimes done in the literature. It is only possible to experimentally measure strain and then infer stress with some knowledge of the instantaneous properties of the material. Thus, special care is taken to specify when talking about stress or strain. Additionally, materials can display viscoplastic behaviour where the elastic component of viscoelastic materials is replaced with permanent plastic deformation behaviour.

Stress relaxation is the process of the dissipation of stress with a fixed strain over time. However, it is not an intrinsic property of a material and is affected by a variety of factors including the magnitude of initial loading, speed of loading, temperature, DOC, loading medium, friction and wear and long-term storage [19]. Therefore, it is not an easy effect to measure or predict which leads most manufacturers to rely on extensive experimental testing and higher factor of safety to meet safety demands. Conventionally, laminates are cured for extended periods of time at elevated temperatures which can cause large amount of residual stress relaxation. However, in the case of rapidly cured composites, little time is spent at elevated temperature and as such stress relaxation is a less significant mechanism when below T_g .

If $T_{g\infty}$ is exceeded by the cure temperature the molecular mobility of the amorphous network increases dramatically allowing for further crosslinking (cure) and for stress to be relaxed much more readily. Phenomenologically, this expresses itself as a sudden drop of E' and an increase in E'' in the resin system. Thus, the resin transitions from a glassy-like state to a rubbery state while the cross-linked amorphous network is preserved. A Dynamic Mechanical Analysis (DMA) can be conducted to determine this relationship which often uses a $\tan(\delta)$ term to describe this behaviour which is simply the ratio of E'' to E' . A typical DMA of a thermosetting amorphous polymer going through its maximum glass transition temperature is shown graphically in Figure 3. Here, the sudden drop in E' and increase in E'' at $T_{g\infty}$ can be seen as temperature is increased.

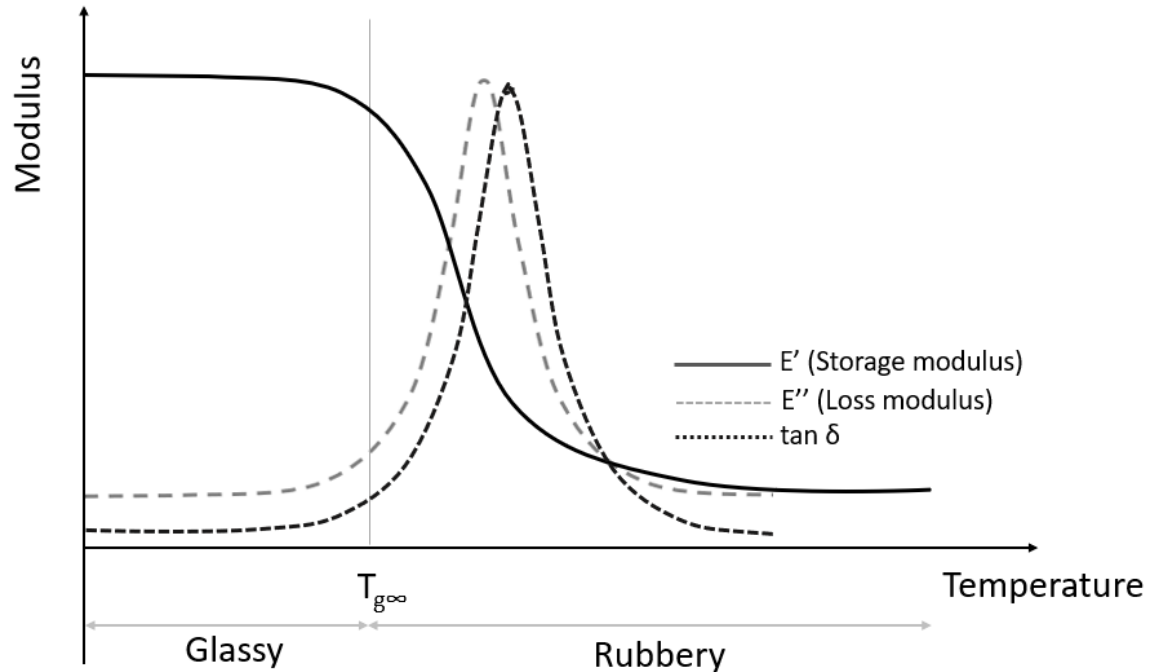


Figure 3: A typical DMA plot for a thermosetting amorphous polymer resin going through glass transition.

Viscoelasticity and residual stress

Bogetti and Gillespie [20] were the first to identify the presence of process-induced strain gradients in composite laminates caused by thermal and DOC gradients formed during cure. The modulus of the epoxy matrix was analysed experimentally with respect to its DOC and the deflection of an asymmetric laminate was measured with cure time. The rest of the study was limited to simulation and was not validated by experimental work. However, they were able to show successfully the potential for residual stress build up in curing polymers.

Kim and White [21] went on to conduct a systematic analysis of the effect of DOC on the T_g , relaxation modulus and the relaxation spectrum. Specimens were tested at various cure states using DMA to develop a master curve of the stress relaxation modulus of neat 3501-6 epoxy resin. A Prony series was then used in conjunction with the Time Temperature Superposition (TTS) theory to describe this relationship and a good match with experimental data was found. It was successfully shown that as the DOC of a resin increases so does the relaxation time. This was due to the increase in chemical cross-linking with DOC, thus reducing the molecular mobility of the molecules making it harder for the cured resin to flow viscously

(relax). A model was then constructed using the chemical hardening function which relates the T_g of a resin to the DOC. This was then modified to relate the stress relaxation time to the DOC by assuming that the same mechanism was responsible for both phenomena. Next, it was compared against the experimental data and an excellent correlation was found. Thus, validating the hypothesis that the T_g of a material and the stress relaxation time are governed by the same micro-mechanical mechanisms. While this work was limited to the relaxation behaviour of neat resins in the gelled state and not composite systems, this relationship is fundamental to much of today's research.

Kim and White [22] continued their investigation by analysing the cure-dependent stress relaxation properties of 3501-6 epoxy resin. A model proposed by Scherer [23] for thermorheologically complex behaviour was modified to include the cure-dependent stress relaxation modulus. These results were then used to construct a constitutive finite element model of an AS4/3501-6 composite system to describe the relaxation modulus/DOC relationship. As with their previous work [21], an excellent correlation between experimental and simulated data was found, thus, further validating the relationship between DOC and stress relaxation. However, the actual reduction in stress was not tested for experimentally and the study was limited to the development of residual stress during cool down. Thus, in the present work defining DOC and T_g will be critical because of their large effect on residual stress.

In this work, time and strain rate dependency of viscoelastic materials is initially assumed to have a small contribution to the final residual stress state of a laminate as the rapid cure cycles under investigation leave little time for this to have a significant effect. However, the transition between an elastic and a viscoelastic dominant state is critical and will be well defined.

2.3. Mechanisms in the formation of residual stress in composite materials

2.3.1. Micromechanical residual stress mechanisms

Micromechanical, or intralaminar, stresses are caused by the interaction between the fibre and the matrix. One of the main causes of this is a difference between the Coefficient of Thermal Expansion (CTE) of the fibre and matrix. Carbon fibres have a very small and sometimes negative CTE while the resin matrix has a significantly positive CTE which causes a disparity in volumetric change on heating and cooling. For example, during the cooling phase of the curing process (where the stiffness of the matrix is fully developed) a disparity in the longitudinal and transverse contractions of the fibres and matrix is formed. This causes the matrix, with a high CTE, to be constrained by the fibres, with a low and sometimes negative CTE. Therefore, in a simple UD lamina a longitudinal tensile stress develops in the matrix which must then be balanced by an equal and opposite compressive force in the reinforcing fibres [24]. These forces can be high enough to cause matrix cracking and debonding after the manufacturing process [25][26]. On heating the development of residual stress is additionally complicated by the simultaneous development of resin modulus as the cure progresses and is highly dependent on the mechanical boundary conditions imposed on the laminate during cure. Micromechanical residual stresses tend to be on an order of magnitude less than macromechanical but they can often lead to voids and other crack initiators so can still dramatically affect the fatigue performance of the laminate [27].

Similarly, chemical shrinkage of the matrix causes residual stress to form. In thermosetting resin matrices chemical shrinkage is caused by the rapid cross-linking of polymer chains causing an increase in density and thus a volumetric contraction. The magnitude of this effect is dependent upon a number of factors including matrix cure chemistry, volume fraction, cure rate and ply orientation. The fibre reinforcing phase does not undergo a volumetric change during cure while epoxy resins typically shrink by 3-7% upon cure [12][13]. The fibres of the lamina resist this volumetric shrinkage and a stress gradient is formed between the interacting matrix and the fibres. Chemical shrinkage occurs throughout the entire chemical reaction. However, it is only when the polymer reaches its gelation point that residual stresses

start to form. Prior to this the polymer is a viscous liquid ($E'' \gg E'$) and can pass between the fibres with much less resistance and any residual stress is dissipated into the resin matrix viscously. However, after gelation the polymer's elasticity increases ($E'' \ll E'$) causing energy to be stored elastically in the system in the form of residual stress. Using Digital Image Correlation (DIC), as explained in section 2.4.2.7, Kravchenko et al [30] found that the chemical shrinkage is linearly dependent upon the DOC after the gelation point. Therefore, polymers with a higher gelation point experience less residual strain due to chemical shrinkage [31]. For both thermal expansion and chemical shrinkage, it is important to remember that these processes do not generate residual stress in and of themselves. Residual stress is formed from these stress-free volumetric changes being constrained by either reinforcing fibres or the mould. Thus, having well defined boundary conditions is key in residual stress analysis.

A study by Morgan and O'Neal [32] has shown that an amine-cured bisphenol-A-diglycidyl ether epoxy, a common base in many commercial epoxy systems, will produce an inhomogeneous microstructure upon cure. This consists of variously interacting microgel particles of differing densities which are characterised to be either "hard", highly crosslinked and high density, or "soft", low crosslinking and low density. These have since been referred to as the "third phase" of a composite. Subsequently Patel et al [27] have found that if cure regimes are used that do not allow for a sufficient amount of time to be spent in a "pre-cure" stage (around the gelation point) then the fatigue life of the final part was significantly reduced. Using techniques like atomic force microscopy it was deduced that the reduction in the fatigue life of samples was caused by a larger region of a softer (lower crosslink density) phase. These microgel particles acted as crack initiation points thereby causing premature failure. However, it was found that static flexural tests, storage modulus and thermal decomposition remained unchanged as these properties are governed by the homogenized mechanical response of the entire composite and not the inhomogeneous microstructure. Therefore, this "third phase" of CFRPs operates in only the micromechanical level and not at larger scales. So, while this phenomenon is not a direct result of residual stress it is caused by similar mechanisms and will result in similar mechanical responses.

A number of different mechanisms cause voids to form in composite laminates such as volatiles being released during cure, entrapped air within laminate and dissolved moisture in

the resin forming bubbles upon cure of the laminate. Work by Liu et al [33] has shown an exponentially decreasing relationship between void content and cure pressure of a laminate. It was also shown that increases in void content reduce the strength and modulus of the laminate. Therefore, to accurately determine the influence of residual stress on the material properties of a laminate an understanding of the void content of a laminate is needed.

2.3.2. Macromechanical residual stress mechanisms

Macromechanical residual stresses is defined here as stress that occurs at the interlaminar (between/among plies) scale and can often lead to excessive warping, delamination and transverse layer cracking. These stresses can sometimes be of an order of magnitude larger than micromechanical stresses and are often the main contributing factor towards failure and poor dimensional stability. Therefore, it is critical to characterize the way they form in composite laminates.

Bogetti and Gillespie [20] were the first to include temperature and DOC gradients within their analyses of process-induced residual stress in laminated composites. Classical methods of residual stress determination would conclude that UD laminates have a zero-stress state due to their stacking sequence. However, Bogetti and Gillespie found large residual stress gradients in UD laminates due to DOC gradients causing laminates to self-constrain. They found residual stresses generally increase with laminate thickness, autoclave temperature and resin shrinkage. It was shown that a tensile stress develops in the centre of the thick specimen while a compressive force is present at the edges after cool-down. This residual stress mechanism is at play when the full stiffness development of the matrix after cure occurs. Then, during the cooling phase the low CTE of the fibres constrict the movement of the high CTE matrix causing residual stress to develop. Therefore, the faster curing outer layer of the laminate retains a compressive residual stress. This was later corroborated with work by Teplinsky and Gutman [34]. These two studies were largely simulation based but work by Dharia et al [35] has shown experimentally that thicker laminates have a greater tendency to microcrack during thermal cycling. Residual stress in composites is known to be a leading cause of microcracking [36]. Additionally, uneven heating/curing is caused by the non-linear cure kinetics and exothermic chemical reaction of the thermosetting resin matrix. As heat is applied to the system the chemical reaction rate increases. This then causes more heat to be

added to the system as the reaction is an exothermic one. Heat is released at a faster rate than the rate at which heat can be conducted away from a given region. This then increases the rate of reaction further which can lead to large temperature gradients throughout the part.

The design of the curing cycle is another critical factor in controlling the build-up and dissipation of residual stress within composite components. Work by Kim and Hahn [37] has shown that through the use of long cure times at elevated temperatures it is possible to reduce residual stress. This was attributed to the ability of the resin to relax stress when it's in a viscous state at an elevated temperature, before vitrification, as it is allowed to flow for longer and matrix movement is not constrained. It is also common to use dwell periods in the cycle at around the gelation point of the resin. This allows for the temperature to fully equilibrate throughout the thickness of the part before CTE differences and chemical shrinkage effects induce residual stress. However, the trade-off with these approaches is that they can massively increase the curing time and therefore process time of the composite component.

An example of a typical cure cycle and the thermal and chemical volumetric changes can be seen with progression of DOC in Figure 4. Chemical shrinkage can be seen to start to occur after a critical DOC (gelation) is reached during the initial hold stage. This then stops when the temperature is reduced and only starts again during the second ramp stage as the DOC increases again. Chemical shrinkage continues until vitrification at which point it stops and the progression of cure slows significantly. Thermal strain only increases after the initial ramp as before this the matrix is not gelled and therefore flows instead of strains. However, during the second ramp, thermal strain increases due to the thermal expansion of the matrix which is semi-constrained by the gelled matrix.

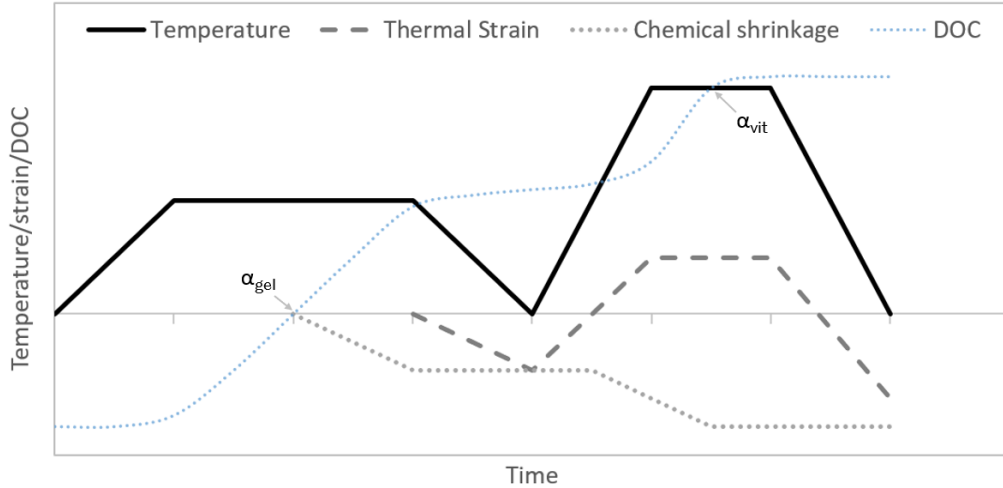


Figure 4: A typical cure cycle with the development of DOC and the resulting thermal and chemical volumetric changes

Further work by Kim and White [38] expanded their research by introducing a 2D model to consider thicker laminates which they define to be 7.5 cm or larger and to consider both unidirectional and cross-ply laminates. For thicker laminates, the models suggested that the development of residual stress was much more complicated than that of thin laminates. It was found that “The transverse stress distribution in unidirectional laminates is tensile at the centre and compressive on the edge at the end of cool-down. The profile is inverted twice during the cure cycle as competing mechanisms of thermal expansion, chemical shrinkage, and chemical hardening interact” [38] (pg. 361). This finding is fundamental to all future research in the area as these interactions are key in defining the effect of process parameter on residual stress. This finding has been corroborated in work by Wenani [18] and similar effects, although by different processes, have been observed in thermoplastics in work by Tsukada et al [39]. Kim and White’s models were also able to show that the effects of nonuniformities in temperature and degree of cure are small for the 2.54 cm thick samples simulated and significant for the 7.5 cm samples. However, it should be noted that this model was only said to be valid for the specific cases analysed. This is because in thicker laminates or in cases with differing cure kinetics, the rate of reaction and gradient of cure throughout the part differs. However, these analyses neglect the effect of the tool-boundary interface which will further constrain the laminates and alter the residual stress distribution seen in these studies. The mechanical boundary conditions used in each model drastically change the final residual stress state of the laminate and must be well defined to gain a realistic understanding of the true residual stress state of a laminate.

2.3.3. Tool-part interactions mechanisms

When studying the formation of residual stress, it is critical to examine the tool-part interface as this is an area of high differential strains between tool and part. This strain differential is driven by two main factors, global thermal gradients and a difference in expansion between tool and part [40]. When this strain is “locked” into the composite after cool-down it manifests itself as a residual stress.

In the aerospace and automotive sectors, it is common to use steel or aluminium open or closed moulds in the production of composite parts. The CTEs of composite laminates vary with layup and DOC, but a common value has been suggested as $3.5 \cdot 10^{-6}/K$ for a quasi-isotropic laminate [41]; while aluminium and steel have CTEs of 21 and 11 $10^{-6}/K$, respectively [42]. Therefore, during cure, uneven thermal expansion of the mould and part occur. The tool expands more than the laminate which causes a shear force to act upon the part due to the friction/bonding between tool and part. Inter-ply slippage through the thickness of the part causes there to be a stress gradient through the part with the highest stress being at the tool/part interface. This shear force is then “frozen” into the part upon solidification of the composite matrix leaving the areas of the part that have been in contact with the tool with a residual tensile stress. In unconstrained cases such as single sided moulds this leads to an unbalanced stress which causes warpage of parts after demoulding [43]. This is shown diagrammatically in Figure 5.

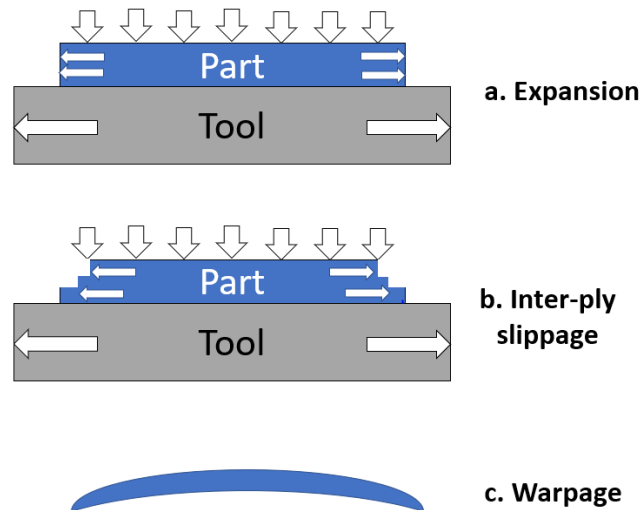


Figure 5: Tool-part interaction leading to warpage. Adapted from [43]

A study by Twigg et al [43] investigated the effect of various processing conditions and part aspect ratio on tool-part interaction induced warpage. Single sided tools were used to cure flat symmetric and balanced laminates of UD prepreg. The cure cycle was kept constant, and an aluminium mould was used for all testing. It was found that there was a strong correlation between the aspect ratio of the part (thickness to length) and the amount of warpage seen. It was also seen that consolidation pressure was another key factor in induced warpage. Their results led to the derivation of the following empirically determined relationship seen in Equation (7) where w_{max} is the maximum warpage seen, P is the consolidation pressure, L is the length of the part and t is the thickness.

$$w_{max} \propto \frac{P^{0.2} \cdot L^3}{t^2} \quad (7)$$

As can be seen from this equation, the longer and thinner flat plates warped more than shorter thicker ones due to the tool-part interaction. It is suggested that longer parts have increased tool-part interaction due to greater contact area which leads to higher residual stress thus increasing warpage. Thicker parts tend to be stiffer, thus leading to less warpage. However, it was noted that there were quite high levels of variability within the experiment which led the authors to believe that there are likely other unknown effects at play which have not been adequately accounted and controlled for.

The variation of CTE between tool and part is generally accepted to be the major contributor to residual stress when considering tool-part interactions in traditionally cured composites. The other major tool-part interaction to consider is the differential thermal gradients during cooling through the thickness of the part [40]. These gradients are caused by the relatively high thermal conductivity of the moulds which leads to an increased cooling rate of the part at the tool-part interface. Therefore, a thermal gradient is formed during cool-down which as previously explained leads to the formation of residual stress.

However, in this work a pre-heated hot press is used to rapidly cure the laminate. The hot-press is then removed while the laminate is hot and allowed to cool outside of the mould. Therefore, there are no CTE differentials during heating or tool-part interaction effects during the cooling phase of the cure cycle for the laminates under investigation in this work. However, during cure all the faces of the laminate will be in contact with a moulding surface.

Therefore, upon gelation of the resin matrix, a stress gradient will form between the moulding surfaces and the resin. It is hypothesised that this will be a leading cause of residual stress in hot-pressed rapidly cured composites.

There has been controversy in the literature as to whether cooling-rate effects the residual stress in the part. A number of studies found no significant difference in residual stress or distortions [44][45][46] while others have found differences of up to 12% when measuring spring-in [47]. However, the literature is in agreement that cooling-rate is a key factor in thermoplastics as the formation of the crystalline structure of the polymer network causes residual stress to form [40][48][49][50]. It is evident this area needs to be explored further.

2.3.4. Summary of causes of residual stress

From the literature survey presented on the governing mechanisms in the formation of residual stress, it is clear that these mechanisms are varied and complex and operate on many different scales with varying impacts on residual stress. A summary of some of the causes of residual stress can be seen in Figure 6.

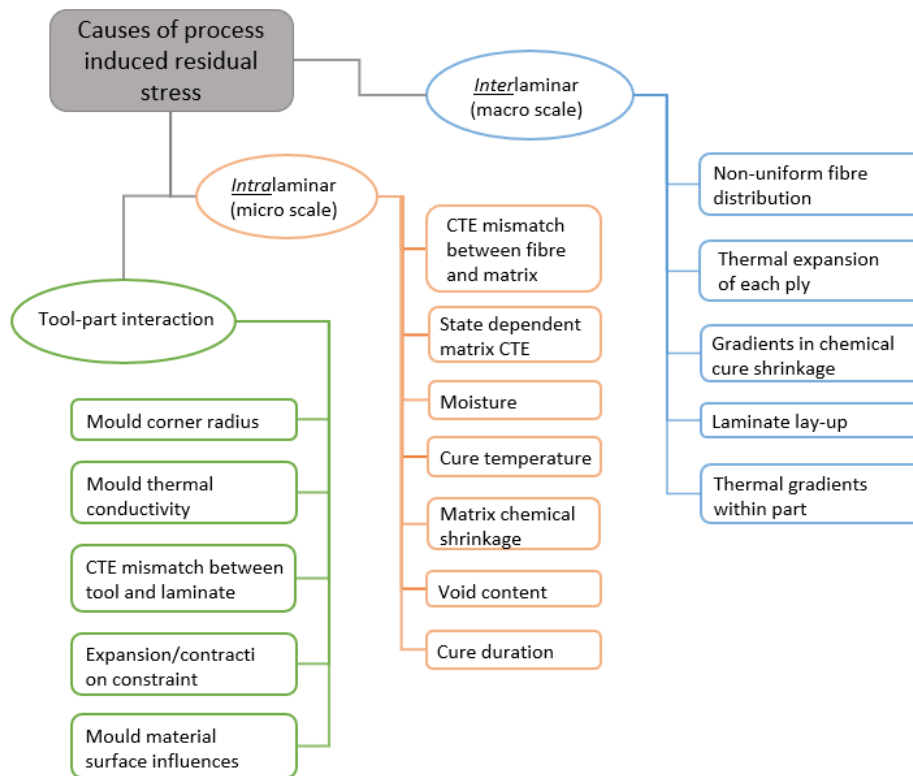


Figure 6: Summary of residual stress mechanisms. Adapted from [18]

2.4. Residual stress measurement techniques

The following review of residual stress measurement techniques in thermosetting fibre reinforced composites has been adapted from work published in the Journal of Polymer Composites [14].

2.4.1. Introduction

Process-induced residual stresses in thermosetting laminates have been modelled extensively in the literature from the initial characterization of thick laminates by Bogetti and Gillespie [20] to more recent methods reviewed by Baran et al [51]. While advances have clearly been made in this area in the past decades, it is still vital that these models are validated by experimental techniques to ensure corroboration between theoretical and experimental results. Therefore, the focus of this thesis and this section of the review will be on experimental techniques for the determination of residual stresses in fibre reinforced composites.

Two previous reviews of residual stress measuring techniques of note are works by Shokrieh [52], who presented a comprehensive review of all residual stress measurement techniques for all fibre reinforced composite systems and Parlevliet et al [53], who presented a review focused on thermoplastic matrices. This review aims to summarise and update these previous works, in the context of techniques that will be useful for the study of thermosetting matrices, noting that some techniques are generic to all composites. To better characterize the various experimental techniques, they have been divided into two categories, destructive and non-destructive techniques.

It should be noted that residual stress cannot be measured directly. However, residual strain or the displacement of the material due to the formation of residual stresses can be measured and the residual stress determined from these. Residual stress determination techniques are commonly referred to in the literature as measurement techniques and therefore this thesis will refer to both determining and measuring residual stresses. Residual stress can often be difficult to determine, especially in composites, as it can be in a self-equilibrated system where the compressive and tensile forces are equal and opposite. In this case there is no observable global strain and techniques must be used which rely on an intrinsic change in a material

property due to the applied stress, or a strain must be induced. Strains are typically induced by removing material and observing the resulting strain which is necessary to restore equilibrium in the system. This is the basis for many of the destructive techniques outlined in this review.

2.4.2. Destructive methods

2.4.2.1. Layer Removal

The layer removal method was first developed in the 1950's by Treuting and Read [54] for the analysis of through-thickness residual stress in metallic plates. Layers are incrementally removed from the surface of a fully equilibrated stressed part. Thus, residual stress is removed from the part and a force imbalance is created in the system. The plate then deforms to restore equilibrium and the resulting strain is measured and used to calculate the residual stress that has been removed. By doing this incrementally through the thickness of the sample, a picture of the through-thickness variation in residual stress starts to emerge.

Attempts have been made to apply the same technique to composite materials with Eijpe and Powell [55] being the first to validate its applicability to composites. However, the method used in this study required machining of the composites surface which imparted additional stresses. More recently, Gower *et al.* [56] incrementally milled individual plies of a laminate to release residual stress and found through observation that there were often visual traces of either incomplete milling of a ply or milling into the subsequent ply. It was suggested that with current technology it would not be possible to mill laminates accurately enough for this technique to be viable. It was also found that this led to quite substantial error when compared to the slitting method, which will be discussed later.

Attempts to overcome the shortcomings of milling have been made with knife splitting techniques [57], hand sanding methods and placing films at intervals throughout the thickness of the laminate which could be later removed [58]. However, these suffered from inaccuracies and this latter technique was not able to capture accurately the interply residual stress which forms in the boundary between plies as the film used to separate the layers has a sufficiently different induced stress to that of a laminate without an inserted film. The main disadvantage of using embedded films, as cited by Reid [59], is that only information about

the macro-scale residual stress distribution can be observed. As the layers removed are thicker than that of the individual lamina it is not possible to gain an understanding of the intralaminar stress distribution. Therefore, it is not possible to discriminate between fibre and matrix stresses as these stresses are in a state of equilibrium with each other and if fibre and matrix are removed together no elastic response will be seen. This technique is limited to macro-scale residual stress measurements and even with this caveat it is still limited by the introduction of additional residual stress during the material removal process. Thus, one of the other techniques outlined in this review is generally preferred when investigating composite systems.

2.4.2.2. Hole-drilling method

The hole-drilling technique operates on the same principle as many of the following destructive techniques used for measuring residual stress. A self-equilibrated stressed body has material removed and then the resulting biaxial surface strain caused by the equilibrium being restored is measured. This strain change can be measured using a variety of different techniques and then correlated to the relaxed stress. This correlation is typically done by applying a model which assumes that each ply is homogenous. This approach works reasonably well for a macro-scale view of the residual stress but struggles to give a full idea of the micro-mechanical mechanisms at play in the process. As the name suggests, the hole-drilling technique removes material by using a drill bit to incrementally drill a hole through the thickness of the material. Thus, relaxing the residual stress and causing a change in the surrounding strain field which is then measured. This technique is generally preferred to the layer removal method as it is easier to achieve more accurate measurements by virtue of the smaller area being machined and it also has the advantage of being less destructive which makes it more useful in an industrial setting. Additionally, it captures the biaxial surface strain response which allows for the identification of the biaxial residual stress distribution, unlike the slitting method which will be discussed later. However, it only offers a view of the residual stress being released from the drilled area while the layer removal method averages over the entire area being milled which might be beneficial in some cases.

Hole-drilling can be separated into two types: Centre-hole drilling (or Incremental-hole drilling) and Deep-Hole Drilling (DHD). For clarity, this thesis will talk about centre-hole

drilling unless otherwise explicitly stated. Centre-hole drilling measures the induced surface strains caused by the drilling of a hole through a material and can either be done in one step or incrementally to measure the residual stress variation through-thickness. This is commonly done with strain gauges in a rosette formation to allow for biaxial strain measurements, a typical arrangement can be seen in Figure 7. DHD first drills a reference hole through a material which has its diameter accurately measured. Residual stress is then released by trepanning another hole coaxially around the first. The diameter is then re-measured and the difference is used to calculate residual stress. Both variations of the hole-drilling method can be performed in one step through the entire thickness of the part or incrementally. If the hole is drilled through the entire thickness that is under investigation in one step then only an average stress over the entire depth of cut can be obtained. However, if the process is performed incrementally, a shallow cut is taken, a measurement is made and then the process is repeated. Then, measurements can be made at the same resolution as that of the depth of cut. Therefore, this latter technique is slower but offers a degree of insight into the through-thickness residual stress in a component.

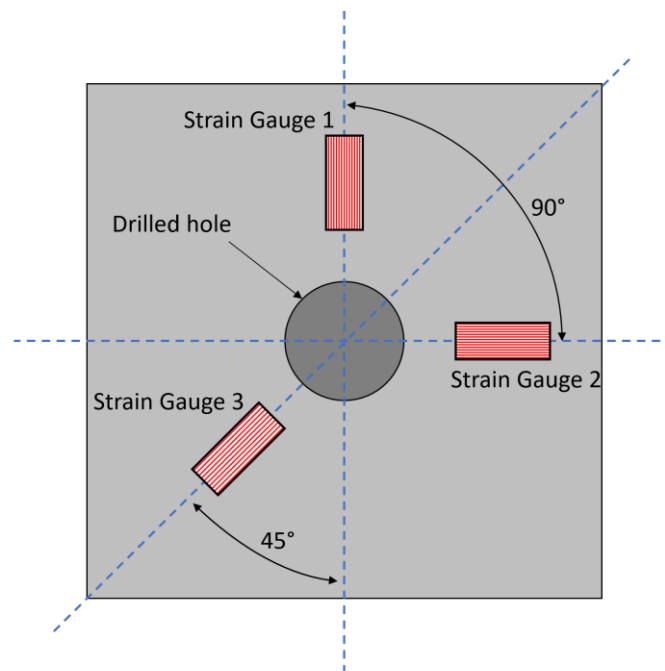


Figure 7: Centre-hole drilling strain gauge arrangement

The hole drilling technique was originally developed for homogeneous isotropic materials, commonly metallics, and is a very common method for determining residual stress in these

materials [60]. However, with some adaptations this method can also be used for composite, inhomogeneous, anisotropic materials [61][62]. In these cases there are often large variations in residual stress through the thickness of a part. Therefore, to understand the true nature of the residual stress within a composite part it is crucial to build up an idea of the residual stress at various depths through the component. Thus, this review will only consider incremental variations of hole-drilling.

Work by Sicot *et al.* [63] used an approach which assumed each depth increment released a unit pulse of uniform stress. Coupling this with taking many small depths of cut this allowed for an approximation of the residual stress through the thickness of a single ply. However, this method requires many regulated depth increments to be used in order to have the required depth resolution to determine variations within a single ply, thus increasing measurement time and complexity. Therefore, it is often impracticable to apply this method to thicker laminates where there are significant variations in stress within each ply. Pagliaro and Zuccarello [64] were the first to apply this method to analyse uniform through-thickness residual stress in a generic orthotropic laminate. This technique gave good correlation between experimental and modelled results for this case. However, high levels of errors were found when using laminates with too few plies (less than 16) and rosette strain gauges were too far away from the hole. This method also assumed that there was constant stress in each ply which gave a low through-thickness resolution of the residual stress. However, they were able to show that this method is generically applicable to composites.

Works done by Baldi [65][66] aimed to combine both hole drilling and Digital Image Correlation (DIC) as a replacement for the traditional strain gauges. An optical measurement technique was preferred here over the use of strain gauges as it offers high sensitivity, full-field and non-contact advantages. Previous to this research other authors have proposed using interferometric techniques such as holographic interferometry [67], moiré interferometry [68] and speckle interferometry [69] in conjunction with deep-hole drilling to measure residual stress in a variety of materials. However, these techniques have been found to be highly sensitive to vibrations [65] making their use more difficult in a lab and inappropriate for an industrial setting. In Baldi's study it was found that the classical DIC method was inherently unsuitable to this application as it is not possible to accurately follow the displacements and have a small standard deviation of results which are both required for

meaningful residual stress measurements. However, work from Hagara *et al.* [70] has suggested that standard DIC hole-drilling techniques are still suitable in some circumstances, citing an approximately 3-19% difference between DIC and strain gauge rosette results. Baldi [65][66] went on to suggest that these problems could be overcome by implementing an Integrated Digital Image Correlation (iDIC) approach. It was shown that this approach gave results that were as accurate as previously proposed methods but also had the ability to measure a wider range of stress values and has a smaller standard deviation of results. However, it should be noted that the standard deviation of the results increased as the depth of the hole increased which could be caused by the weaker response seen when the residual stress is relieved further away from the point of measurement.

One of the shortcomings of the hole-drilling technique is that it struggles to have a high enough resolution to determine the intra-ply and the inter-ply interface stress variations. To overcome this, Smit and Reid [71] successfully implemented a power series evaluation approach and showed it can be used to determine eigenstrains through the thickness of the laminate. These can then be used to determine the stress distribution through the thickness of the ply and ply interface. It was found that this approach was less sensitive to error compared to the standard Legendre function evaluation approach. This makes it possible to take measurements of shallower depths of cut and consequently have a high enough measurement resolution to capture the intra-ply effects.

Meanwhile, Garza *et al.* [72] have shown that DHD is not able to accurately capture cure induced residual stress unless the thickness of stacks of similarly orientated plies is larger than the hole size being used. Therefore, for most cross-ply laminates it is not possible to use the DHD technique to measure cure induced residual stress. However, it was still possible to measure assembly stresses but some significant calculation errors were found. A study from Hu *et al.* [73] went on to modify the approach taken by Garza *et al.* by implementing an integrating stress calculation method, finding this reduced calculation errors and gave results for assembly stress which matched well with simulations. Additionally, work by Liu *et al.* [74] added an additional strain gauge on the bottom of the laminate surface to improve the accuracy of measurements taken further away from the drilling surface.

The machining of composites is an area of research that has had much attention as it poses a unique set of challenges such as delaminations, fibre pull-out and crack propagation [75] and is therefore not trivial. These challenges have the potential to induce large amounts of error into any residual stress measurement techniques that require composite machining, such as hole-drilling. This is because the formation of a delamination or a fibre being pulled out during machining, could potentially relieve residual stresses that were not from the area under investigation which would give a false reading. However, as already shown, it is possible to mitigate these issues if the correct machining parameters are used and to achieve accurate results for residual stress analysis. Typically, high spindle speeds and low feed rates are used in conjunction with composite specific tooling to mitigate machining damage in composites [76]. Liu *et al.* [77] has presented a comprehensive review of various mechanical drilling techniques and the best practices for achieving accurate and undamaged holes. A study by Yuksel *et al.* [78] found that when using a 3 mm diameter drill, there was a drilling affected region of approximately 2 mm around the edge of the hole and that measurements needed to be taken away from this area to avoid machining induced errors in the results.

The hole-drilling technique offers an unmatched insight into the multi-axis through-thickness variation in residual stress in composite laminates. Traditionally, the large amounts of computation required and extensive time-consuming testing limited this techniques popularity. However, more recently this is much less of an obstacle to overcome and the technique has become more popular. The primary shortcoming of hole-drilling is that it relies on surface measurements of strains that propagates through the thickness of a laminate from the point of relieved stress. Thus, there is an inherent reduction in the accuracy of the results as the distance between the cutting and measurement surfaces increases, making it particularly unsuitable for very thick composites. However, one new technology that might be able to overcome this shortcoming is Digital Volumetric Speckle Photography (DVSP). DVSP uses x-ray Computed Tomographic (CT) images to reconstruct a 3D volume image of a composite. Various internal markers in the CT image such as fibres and fibre interfaces can then be tracked (without the need for additional contrasting particles) using DIC and a 3D quantitative strain map can then be developed. The use of this technique for quantitatively measuring strain in woven laminated fibre reinforced composites was first applied by Mao and Chiang [79] where they investigated internal strains in a beam in bending. Presently, this

technique has not been used to quantify residual stress in fibre reinforced laminates. However, it is the view of the author that this technique could be used in conjunction with a variety of the techniques outlined in this review, and particularly with hole-drilling, to overcome surface measurement errors.

2.4.2.3. Ring-core method

The ring-core method operates on a similar principle to the hole-drilling technique. However, instead of a hole being drilled, an annular groove is cut and the elastic response is measured by the strain gauge rosette placed in the centre of the groove, as can be seen in Figure 8. This technique was first developed by Gunnert [80] to investigate the residual welding stress in metallic plates and has since been widely adopted in the determination of residual stress in metallic structures. This method has not seen widespread adoption in the measurement of residual stress in fibre reinforced composites despite a number of benefits that the ring-core method has over the more common hole-drilling technique. The ring-core method allows for a greater strain response to be measured as more stress is relaxed during the trepanning process which should reduce measurement errors. This technique also reduces the stress concentration around the machined area which means, compared to the hole-drilling technique, larger residual stresses can be measured without exceeding the yield stress of the material [59].

The ring-core method has been combined with interferometric strain/slope rosettes [81][82] and 3D digital image correlation [83] with both techniques finding good corroboration with theoretical predictions. These non-contact global measurement techniques offer a more robust measurement solution as they do not rely on the accurate placement of strain gauges or suffer from the difficulties of cable management that traditional strain gauges do during trepanning. Baldi [84] suggested that it would be possible to use non-contact interferometry methods to restart the ring-core technique at multiple depths throughout a components thickness. This could be achieved by removing the core left by the ring-core method when an appropriate depth is reached and re-applying the virtual strain gauge to the new surface and then continuing to trepan at a greater depth. This could be very advantageous as with an increase in distance from the surface where strain is being measured to where the strain is being released causes an increase in error. If this distance could be reset at appropriate points

the depth of accurate measurement could be vastly improved. However, these techniques still seem to be confined to homogenous and isotropic materials and have not been used in anisotropic, inhomogeneous fibre reinforced laminates.

Korsunsky et al [85] investigated the use of focused ion beams to create a micro-scale ringed groove, citing this technique's ability to measure strains on a much smaller scale and being much less destructive to the sample being tested. Work by Lunt et al [86] reviews the applicability of using focused ion beams in conjunction with digital image correlation to determine the spatially resolved strains. Due to the high resolution and accuracy that ion beams afford it is possible to measure strains on the micron scale with nano-scale precision. With a few modifications it is possible to use focused ion beams on non-conductive materials like most common polymer matrices. Therefore, in theory it is possible for this technique to be applied to fibre reinforced composites and even has the potential for examining micro-scale residual stress interactions between fibre and matrix. However, current efforts in this area have been limited in depth of cut to around $0.3\ \mu\text{m}$ [87] making it difficult to apply this technique effectively to composites where fibre diameters are on the order of $5\text{-}7\ \mu\text{m}$.

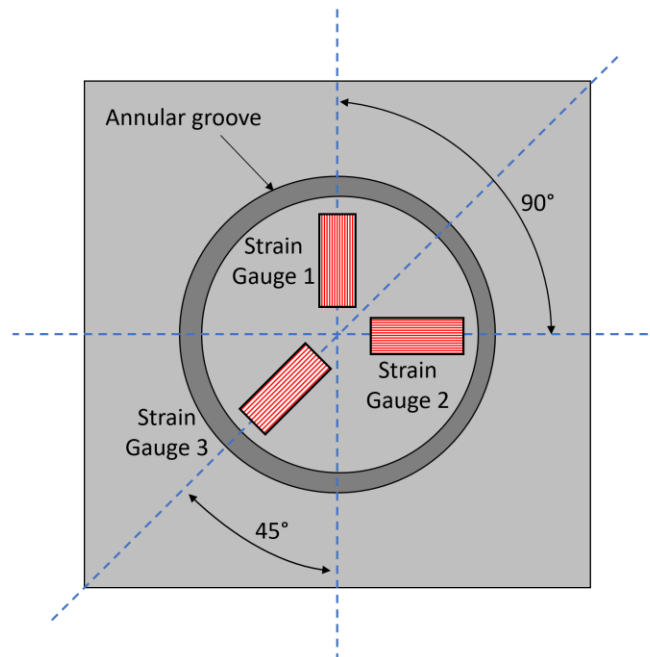


Figure 8: The ring-core method

Recent studies, comparing the ring-core, hole-drilling and slitting methods (see below), was conducted by Ghaedamini et al [88][89] where glass fibre fabrics were used to create

symmetrical and balanced cross-ply laminates through the use of hand layup. It was found that the slitting method had the largest strain response followed by the ring-core method and then the hole-drilling method. Nevertheless, it was concluded that the ring-core method was preferred as it released the most residual stress out of any of the processes which was said to increase the methods accuracy. However, few repeats were conducted in this study meaning the experimental error was not determined for all cases, therefore it was not possible to validate this claim rigorously through experimental analysis. Currently, the hole-drilling technique seems to be preferred over the ring-core method in academia due to its generally easier implementation, without the need for special strain gauge wiring or annular drill bits. But it is clear that the ring-core method still offers some unique benefits, particularly at the micro-scale, and more research needs to be done in this area to explore its full potential.

2.4.2.4. The slitting method

The slitting method can be found in literature under a number of different names such as “crack compliance”, “compliance” and “incremental slitting”. However, they are all fundamentally the same and, in this review, the “slitting method” will be used. A small slit or slot is made in a pre-stressed sample and the resulting deformation normal to the direction of the slot caused by force equilibrium being restored is measured. This process is repeated at increasing depths, thus residual stress through the thickness of the part can be determined. This method is similar in application to that of the hole-drilling method. However, only the average stress along the width (y-direction in Figure 9) can be determined as all of this material is removed per increment.

This method was developed for measuring hoop stresses in homogeneous metallic cylinders by Cheng and Finnie [90] and good agreement with hole-drilling and x-ray results was found. The major advantage of this method found in the study was cited as its “simple experimental and computational procedures” making it ideal for rapid testing. These experiments implemented strain gauges perpendicular to the slot to measure the induced deformation after each cut is made. Today, strain gauges remain common when conducting slitting method testing due to their ease of implementation. The positioning of the strain gauge can be adjusted to best capture specific stresses. Placing a strain gauge on the back face, opposite the slot of the sample allows for detection of residual stress through the full thickness of the

sample while placing a strain gauge on the front face of the sample will give higher resolution close to the surface but is unable to resolve cuts of high depth. Therefore, it is common to use multiple strain gauges to get a more detailed picture of the residual stress distributions within a sample. One such arrangement is shown in Figure 9.

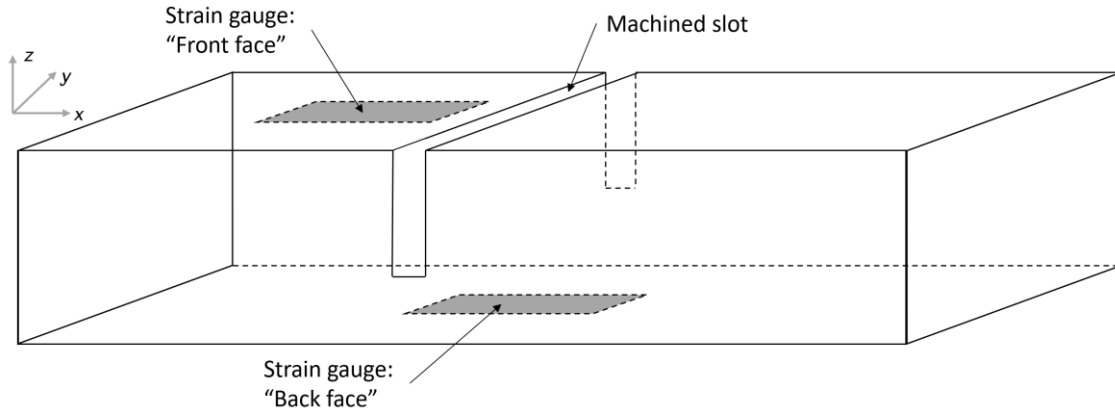


Figure 9: The slitting method experimental setup

Ersoy and Vardar [57] went on to extend this technique to layered orthotropic composites and compared their findings to the layer removal method (as discussed) and finite element modelling. They found high levels of scatter in the data when using layer removal and found the experimental procedure to be impractical. However, the slitting method offered lower result scatter, easier implementation and good agreement with the model used.

Various other methods for measuring the resulting displacements have been explored such as moiré interferometry [91] and micrograph DIC [87][92]. The latter of which has been used to investigate residual stress on a nanoscale in thin films. Recently, Salehi *et al.* [93] applied 2D DIC with incremental slitting to investigate the macro scale residual stress in a cross-ply sample. It was found that shear effects and rigid body motion was high for some of the slitting increments. However, these were able to be removed mathematically due to the large amount of data captured with DIC. It was found that there was acceptable agreement between results obtained via a traditional strain gauge and those found with DIC and it was suggested that this full-field technique can be extended to smaller scales.

Various methods for creating the slit have been used from the basic approach of using a thin saw blade [57][94][95][96][97][98] to using focused ion beams [87][92][99][100] and an Electron Discharge Machine (EDM) [91][101]. One obvious problem of using a saw, a mill or any other

abrasive method is that it will invariably introduce additional stresses into the specimen being tested. This can be mitigated through the use of lubrication and careful control of cutting parameters, but the introduction of some stress is intrinsic to the process. This is particularly true when measuring strains on the “front face” of the specimen when surface residual stresses are under investigation. When using a “back face” strain gauge it was found that this measurement is reasonably insensitive to cutting stresses [102]. Ion beams have been shown to be effective as they can be used on a very small scale and thus used to measure stress at high through-thickness resolutions. However, their application is currently limited to less than a thickness of a single ply. Thus, they cannot easily be used for gaining an understanding of the macro-scale interlaminar residual stress within a laminate but could lend an unmatched level of resolution for the intralaminar stresses. EDM has the advantage of imparting very low stresses into the sample during the slitting process due to the inherent nature of the material cutting process and the thin wire used. The laminate is also usually placed in a bath of deionized water which has the side-effect of acting as a mechanism for removing heat away from the part, again reducing unwanted stress. However, EDM only works on conducting materials such as metals and carbon, it will therefore not work on composite systems based on glass for example. There is also the potential influence of moisture on the laminate during the submersion in water and it has been shown that an increase in moisture content increases the relaxation of residual stress [103].

In a recent study, Salehi and Shokrieh [104] defined a repeated slitting safe distance (RSSD) as the minimum distance between the slitting experiments to exclude the effect of the previous one. In theory this allows for multiple slits to be made in a specimen along its length without subsequent slits affecting the previous ones. Thus, extending the capability of the slitting method to not only determine the residual stress perpendicular to the slit face but to also determine this along the length of a specimen. Using a numerical and empirical approach it was concluded that a RSSD of 2.5 times that of the thickness of the part is sufficient to diminish the experimental error to 1% for laminated composites. Future work proposed by Salehi and Shokrieh is to extend this analysis to hole-drilling, ring-core and other destructive methods.

2.4.2.5. The Contour Method

The contour method was first developed in 2001 by Prime [105] as a new method of mapping the two-dimensional residual stress distribution through a cross-section of a pre-stressed homogeneous specimen. First, the object under inspection is cut in half at the area of interest. This process releases the residual stress from within the object and causes the cut surface to deform a small amount. A detailed topographical map of the cut surface is then created using a coordinate measuring machine. Imposing boundary conditions upon a finite element model of the object under investigation to restore the residual stress induced deformations back to zero then allows for the determination of the original residual stress within the object.

This technique continues to be popular in the nuclear and oil and gas industry [106] for determining residual stress in pressure vessels and welds as it is able to provide high resolution stress maps of stresses normal to the cut surface and has been shown to have a high degree of accuracy [107]. However, this method has a few limitations which has led to it not being applied successfully to fibre reinforced polymer composites. Firstly, it is not possible to use standard mechanical machining for the slot as this process inherently imparts machining stress into the surface of the cut, thereby making the measurement invalid. Therefore, the standard practice for metallic materials is to use EDM to cut the specimen. This induces very little additional residual stress as the process only interacts with the material that is being removed and it is conducted in a bath of dielectric liquid which acts as a large heat sink rendering thermal affects insignificant. However, the EDM process requires that the material being cut is electrically conductive which is not the case for standard polymer matrices and glass/aramid fibre reinforcements. Therefore, this process is limited to carbon, or other electrically conductive fibres, and a metal matrix or a polymer matrix with additives causing it to be conductive. These limitations have resulted in little to no research in this area but it still possible in theory and would offer a unique insight into the distribution of residual stress through a cross-section.

2.4.2.6. The first-ply failure method

The first-ply failure method can be used to obtain the transverse residual stress found in a cross-ply laminate. The basis of this technique is to compare the transverse tensile strength of an unloaded UD reference specimen to that of an embedded stressed ply within a cross-ply

laminate. It is assumed that failure occurs upon initial crack growth within the matrix and this happens at the same stress throughout testing. The difference in failure strengths is then determined and then used to determine the residual stress that caused the disparity in strengths. This approach assumes that it is possible to achieve a perfectly stress-free UD sample which can be used as the reference. While it is possible to have a global residual stress of zero across the laminate this cannot be said to be true on a micromechanical level as there is a series of complex fibre matrix interactions at play at this scale as previously discussed. Therefore, this technique is limited to a macro-scale residual stress measurement.

Kim and Hahn [108] were the first to take significant steps in the development of the first ply failure technique. The approach was based around using strain gauges and acoustic emission to monitor initial cracking within the matrix of the laminate. While strain gauges were found to be effective when the crack occurred underneath the gauge, they were unreliable at detecting cracks in other regions. However, acoustic emissions were found to be very effective at detecting first ply failure. Later, Cowley and Beaumont [109] used this technique to investigate the effect of temperature on residual stress, finding a linearly increasing trend which is consistent with current theory and other experimental techniques. They found the first ply failure technique underpredicted residual stress compared to lamination theory by 5-25%. Reasons for the discrepancy were: the transverse strength not remaining constant as assumed; stress relaxation effects; and fibres in other plies of the laminate constraining the transverse ply. This latter point is corroborated by Flagg and Kural [110] who demonstrated that the transverse tensile strength is not an intrinsic property of the ply and is affected by neighbouring plies. Strengths of up to 2.5 times that of a UD ply were found in laminates with transverse shear strength being found to be strongly dependent upon laminate thickness and neighbouring ply orientations. Thus, the assumption that neighbouring plies have no effect on the strength of the ply under investigation is false.

There have been suggestions [59] that this method could be used in the longitudinal direction to measure the micro-scale residual stress aligned with the fibres. However, the problems previously stated also hold true in the longitudinal direction and it is therefore not possible to determine micromechanical residual stress using this method.

2.4.2.7. Digital Image Correlation

DIC is a full-field, non-contact, surface displacement measurement technique for 2D and 3D applications. It was originally developed in the 1990's by Sutton et al [111] and has since been shown to be widely applicable to a variety of applications, from the micro-scale [112] for ion beam slotting to a much larger 9 m composite wind turbine blade [113]. DIC can be used in conjunction with many of the previously mentioned techniques to measure the resultant strain. The main advantage of DIC is that it offers a full-field view of a given displacement instead of the one-dimensional information that would be able to be gathered by a strain gauge for example. Therefore, the user has much more flexibility in post processing and can apply “virtual strain gauges” to the surface of a component at will. This allows for checking of results and the ability to make multiple measurements without having to connect a large number of individual sensors.

DIC uses one or more optical cameras to take pictures of a sample before, during and after loading of a specimen. A point upon the surface of the specimen is identified and then tracked frame by frame by the software as the surface displacement develops. Various aspects of the specimen can be used as targets to track, in composites it has been shown that the fibres within the part can be used as tracking points [114]. However, it is common to apply a pattern to the surface of the specimen to make tracking easier and to reduce the chance of errors [115]. It is critical to use an irregular, random pattern so as to make it easier for the software to distinguish between points and thus track them more effectively. It is common practice to use an airbrush to apply dark (black) speckles to a light (grey/white) background to achieve this randomness. This technique yields a high contrast and highly random surface pattern which has been found to be the effective technique for producing accurate results [116].

2D DIC is used when the sample being tested is assumed to only displace in-plane and out of plane displacements are assumed negligible. Here only one camera is needed to locate and track a given position through its plane of motion. The obvious advantages of this method are that it is a cheaper and less complex method in comparison to 3D as only one camera is needed. 3D DIC works in much the same way as 2D but uses stereo cameras to triangulate a given point on a surface in the 3D space. This allows for the tracking of out of plane

displacements, thus expanding the possible use cases for DIC. A diagram of a typical 3D DIC setup can be seen in Figure 10.

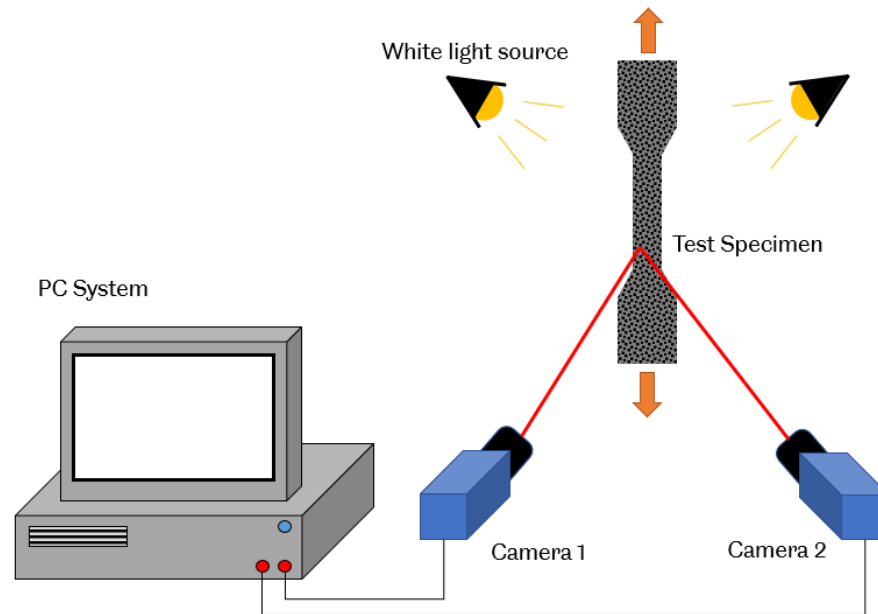


Figure 10: A typical 3D DIC setup

2.4.3. Non-destructive methods

2.4.3.1. Raman spectroscopy

Micro-Raman Spectroscopy is a commonly used method in the micro-electronics industry for determining areas of local mechanical stress in silicon circuit board parts [117]. Raman spectroscopy uses the scattering of light to investigate the vibrational energy of the chemical bonds of a crystalline structure. The scattered light is detected and characteristic Raman peaks can be observed. The position of these peaks is altered by any externally applied strains [118]. Therefore, it is possible to quantify the applied surface strain by measuring the differences in the Raman peak position between a stressed and unstressed sample.

Bannister et al [119] successfully applied micro-Raman spectroscopy in the analysis of fibre stress during pull-out in an aramid/epoxy composite. Fibre strains were able to be measured along the length of the fibre during pull-out and thus allowed for determination of the interfacial strength of the fibre/matrix bond. Thomsen and Pyrz [120] were also able to use this technique to measure creep in fibres in a carbon/polypropylene composite.

Measurements along the length of the fibre at 20 μm increments were used to develop a stress map along the axis of the fibre.

It is also possible to measure the strain in the amorphous polymer matrix by determining the distribution of molecular orientations in the polymer. This is achieved through measuring the angular variation in Raman peaks which relates to the applied strain [121][122]. However, Raman peaks for amorphous materials like thermosetting polymers or glass are quite wide and irregular in nature. Whereas the Raman peaks for crystalline polymer structures like thermoplastics are much more well defined [123]. Therefore, this technique is most suitable for examining micro-scale strain within crystalline fibres, such as carbon, or for use on a macro-scale with crystalline matrices such as thermoplastics but offers poorer resolution for amorphous materials like thermosetting polymers.

2.4.3.2. Warpage of asymmetric laminates

Arguably one of the simplest methods for determining residual stress is the evaluation of the warpage of asymmetric laminates. First imagine two perpendicular plies, a $[0/90]$ UD laminate, which are allowed to slide over each other and do not interact. Each ply will experience less shrinkage along the direction of the fibres than in the transverse direction as the fibres will constrain the matrix's movement. Therefore, if the coordinate system in Figure 11 is used, it can be seen that the 90° plies will shrink much more than the 0° plies along the x-axis as demonstrated in Figure 11(a). Now imagine the real case where the plies are bonded together, as shown in Figure 11(b), the difference in contraction between the upper and lower (90° and 0°) plies will cause the laminate to warp out of plane in the positive z-direction and a tension-bending couple has been formed. Thus, it is the chemical shrinkage of the matrix that causes warpage in an asymmetric laminate during cure. During cool-down the thermal effects due to the variation in CTE between matrix and fibre then come into play as previously discussed. This warpage can then be measured and compared to a theoretical model to determine the residual stress.

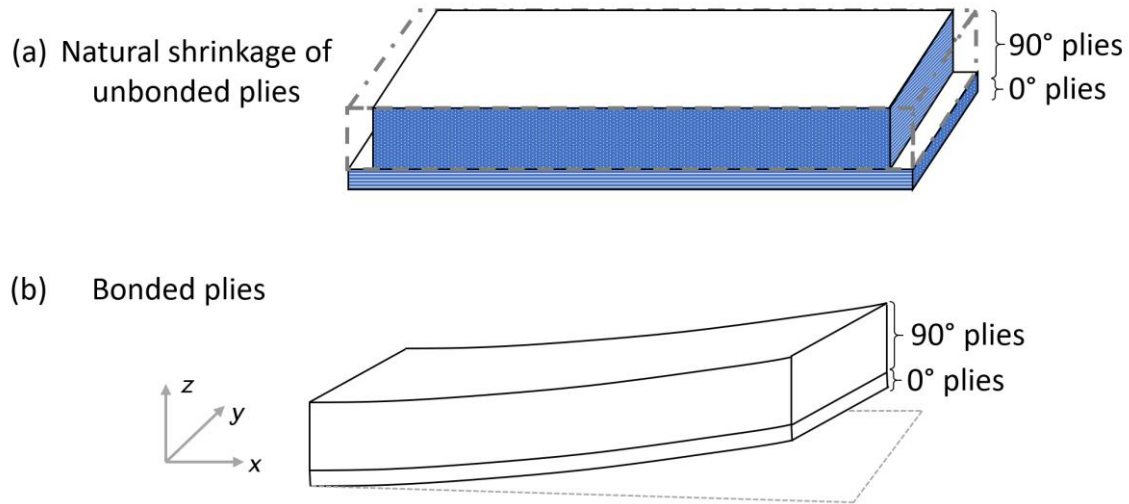


Figure 11: (a) Unconstrained shrinkage, (b) Constrained shrinkage and warpage of asymmetric laminates

This analysis works on the assumption that the residual stress induced during the curing process can be relieved through the out-of-plane bending of the laminate [109]. By using an asymmetric laminate of $[0_4/90_4]$ Kim and Hahn [37] were some of the first to apply this technique successfully to composites. A simple elastic analysis was utilised to relate measured deformation to residual stress; however it should be noted that constrained residual stress at the micro-scale was not accounted for in this analysis. Nairn and Zoller [124] later showed this technique's applicability to both thermoplastics and thermosets. Additionally, thermoplastics experience an increase in matrix density upon cooldown due to the crystallisation of the polymer structure, thereby increasing residual stress.

Gigliottia et al [125] used fringe projection on thin $[0/90]$ plates to measure the stress induced by hydrothermal loads. This allowed for a full-field view of the displacement, thereby allowing the authors to more robustly capture the non-linear behaviour seen during their experiments. The use of fringe projection also allowed for the detection of anticlastic deformations (saddling) in the composites which is indicative of an additional bending moment being present in the laminate. This would not have been possible using a non-full-field approach.

These previous studies were not able to monitor the in-situ build-up of residual deformation during the cure cycle as they were conducted in closed ovens. The samples were also cured on flat plates which introduced anticlastic deformations in the samples which were caused by bending and torsion moments combining, thus resulting in transverse curvature of the plate.

A pair of studies by Kravchenko et al [126][127] expand on previous studies by implementing both an asymmetric and unbalanced laminate with the latter being used to exaggerate the deformations seen. The setup also utilised a cantilever-beam mounted sample to avoid any tool/part effects and to also measure deformation due to self-weight. Finally, image tracking was carried out on the sample during cure by observing the curvature development of the sample through a window in the curing oven. These data were then combined with knowledge of the cure kinetics of the resin, coefficient of thermal expansion and chemical shrinkage with respect to degree of cure and the resins storage modulus to predict residual deformations. While these experiments did not predict residual stress, they were able to predict end-deflection with reasonable accuracy. It is thought that residual stress could be modelled using similar techniques.

Crasto and Kim [128] suggest that it is possible to determine the ratio of residual stress caused by chemical shrinkage to that caused by thermal expansion through the analysis of the stress-free temperature. A warped asymmetric laminate that has been fully cured can be reheated until it flattens again, at which point the stress-free temperature is said to have been reached. This temperature will be above the cure temperature as additional thermal expansion is required to overcome the permanent chemical shrinkage in the fully cured laminate. Later studies [129][130][131][132] have found a similar phenomena but are still cautious about heavily relying on this relationship. In general, it seems that there are many different mechanisms at play and as such it is difficult to be certain of the accuracy of this approximation. However, at the very least, it does allow for a qualitative comparison of the contribution of thermal expansion and chemical shrinkage to the build-up of residual stress.

In conclusion, it is possible to model the deformations due to cure of asymmetric laminates with reasonable accuracy if the properties of the matrix are well understood. It is also possible to model the total global-scale residual stress that forms due to chemical shrinkage and thermal expansion which is subsequently relieved due to deformation. However, it is not possible to measure or detect any residual stress which is self-equilibrated between the fibres and the matrix on the micromechanical level as this would not contribute to the curvature of the asymmetric laminate. This technique should be thought of as a way to validate thermomechanical models and not for directly measuring residual stress.

2.4.3.3. Photoelasticity

Photoelasticity relies on the relation between the stress or strain field in a material and the resulting changes in its optical properties. Birefringent materials have two refractive indices and these are dependent upon the stress state of the material. Therefore, through the use of optical measuring devices utilising polarised light, it is possible to determine the full field stress state of a loaded component that is made of a birefringent material. For a more thorough introduction to photoelasticity refer to section 5.1 and Dally and Riley [115]. Photoelasticity has been a preferred technique in academia for a number of decades as it allows the user to get a visual representation of the stress field in a component.

Within composite applications the use of photoelasticity has been for the most part limited to single embedded fibres samples. Experiments performed by Kim and Nairn [74] have shown this technique to be particularly helpful in evaluating fibre debonding in carbon fibre epoxy matrices. This technique has also been shown to work well at a micro-scale by measuring the micro-stress fields around a single fibre. It is also possible to investigate changes in maximum principle stresses at fibre/matrix interfaces whilst under load and to track these changes over time which allows for the investigation of phenomena like de-bond propagation [134]. Thus, it can be seen that if used correctly photoelasticity allows for a visual representation of the stress field in composites which is not possible using most techniques.

However, one of the main limitations of photoelasticity is that it requires light to be able to pass through the material that is being measured. Thus, this technique is limited to composites with very low fibre volume fractions (30-40% [135]) and unidirectional fibres so as to allow enough light to pass through the sample. If a cross-ply fabric, woven fabric or a fabric with a high fibre density is used, light will not be able to pass through and no measurements can be taken. A lack of transparency is the main reason that photoelasticity is not widely used in composite laminates. To overcome this, Andersson et al [136] investigated the residual stress present in a cross-section of unidirectional fibres. This thin cross-section had sufficient light penetrability through the fibre direction to allow the photoelastic effect to be observed. Good agreement was found between the stress distribution in the modelled and experimental results and they were able to demonstrate the formation of residual stress after cure. It was also found that fibre matrix debonding which occurred during cure caused a reduced light

band forming in the matrix making it difficult to analyse the stress distribution in the matrix effectively. They noted that upon the application of 0.5% strain on cured samples, there was hardly any change in the optical pattern. This was in sharp contrast to the modelled results. This led Andersson et al to conclude that “The optical pattern is therefore not an image of existing stresses but rather reflects the stress history.” [136]. However, this paper did not provide sufficient information about the experimental setup of the photoelastic equipment being used for the current author to be confident about this conclusion. Therefore, it is the opinion of the author that there is room for further exploration of this technique for the evaluation of residual stress in composites. If this technique can indeed be used, then it could offer a unique view of the formation of residual stress through the thickness of a composite system.

2.4.3.4. Cure Reference Method

The cure reference method was developed by Ifju et al [137] as a novel non-contact method for determining the build-up of residual stress on the surface of a fibre reinforced polymer laminate. A moiré grating is applied to the surface of an uncured uni-directional laminate in its stress-free state, i.e. before the gelation of thermosetting polymers. The part is then cured and the resultant surface displacement is determined using moiré interferometry. This gives a full field strain map of the surface of the laminate from which it is then possible to calculate the theoretical macro/micro-scale residual stress by applying laminate theory. It was also shown that it is possible to apply the same technique to a cross-ply laminate by curing it in parallel to the unidirectional one and calculating the free thermal expansion of the unidirectional laminate.

A similar technique using digital image correlation (DIC) has been used effectively by Kravchenko et al [30] to determine the chemical shrinkage and thermal expansion of a neat thermosetting resin. Here, an adherent pliable film containing a random speckle pattern was bonded onto the top of gelled resin sample before final curing. The surface deformation during cure was then captured by a camera and a standard DIC post-processing procedure was carried out of the images. This tracked the strain on the surface of the resin by determining the movement of each speckle between each frame of the video. From these data it was possible to calculate the chemical shrinkage after gelation and the thermal expansion of the resin. This

method has not been widely adopted with the exception of a few simple use cases [138][139]. This is primarily due to the inability of this method to measure the sub-surface strains during cure. Therefore, this technique relies on the assumption that the through-thickness strain is constant which is often not the case, especially when tool-part interactions occur. However, sensors embedded within a laminate can monitor the cure state and build-up of residual strain through the thickness of a laminate.

2.4.3.5. Embedded Sensors

Residual stress within a composite laminate is primarily caused by the thermal and chemical volumetric changes that occur during cure. Therefore, if these volumetric changes, or strains, could be measured during the curing process it would be possible to calculate the residual strains within the laminate. If a sensor such as a strain gauge or fibre optic sensor is embedded inside the laminate this allows for the calculation of the interlaminar laminar stresses in angle-ply laminates, intralaminar stresses in UD laminates [140][141] and residual stress in woven laminates [142]. It is also possible to use the fibre optic sensor as an embedded temperature sensor by encapsulating a section of grating in a sealed tube to make sure that any expansion or contraction of the fibre optic sensor in that area is purely down to thermal expansion and no other applied strain. This is particularly useful in an embedded composite application as it is often critical to have an accurate temperature reading within the laminate in order to have a good understanding of the cure and material state of the laminate.

The idea of embedding a sensor into a fibre reinforced polymer composite was first developed by Daniels et al [143] for measuring sub-surface strains in boron/epoxy laminates. Daniels et al were able to show this techniques usefulness in monitoring the development of sub-surface strain during cure. Kim and Daniel [140] later went on to expand on this work by analysing various cure cycles and the effect they had on cure-induced strain and comparing this against data gathered with fibre-optic sensors. Measured strain begins to occur after gelation as the matrix strains elastically instead of flowing around the sensor viscously. Past works [144][145][146] have used both Fibre Bragg Grating (FBG) and Extrinsic Fabry Perot Interferometric (EFPI) fibre optic sensors. However, the latter of the two sensors has since fallen out of common use [53] as they are significantly larger than FBG sensors which causes them to act in similar manor to voids and are therefore common crack initiation sites with

some studies finding the cure induced stress alone was enough to cause failures at the sensor interface [146]. More recently, investigations into the use of ferro-magnetic glass-coated microwire inclusions for the monitoring of polymerisation by Allue *et al.* [147] have begun. However, this technology is very much still in its infancy and more research is required in this area.

FBG sensors work by passing high-intensity ultraviolet light with wavelength λ , down the length of an optical fibre. This light then interacts with a series of gratings within the fibre that are at a known pitch, Λ and refractive index n . The reflected light has the relationship $\lambda_{ref}=2n\Lambda$ and is analysed by the interrogator unit connected to the end of the optical fibre and the changes in the reflected light spectra are analysed. If an external axial strain is applied to the fibre the distance between the gratings changes and the wavelength of the reflected light shifts and can be used to determine the applied strain [115] as shown in Figure 12. Caution must be taken when analysing the raw optical sensor data since factors such as the optical fibre coating, shear-lag effect and the mechanical properties of the optical fibre itself can cause a misinterpretation of the results. Work by Voet et al [148] investigated the strain transfer between an embedded optical sensor and resin matrix by experimentally determining the response of the sensor to a known transverse load and comparing this to a numerically derived case using finite element simulation. They showed that for their studied case there was good corroboration between experimental and numerical results meaning there was a high degree of strain transfer into the embedded sensor. However, the authors did caution, that similar tests for each individual case would be prudent to validate any experimental data gathered from embedded optical fibres. While this might not be practical for all cases it is evident that some form of validation to the efficacy of the ability of optical fibres to capture accurately the true internal strains must be a part of any rigorous study.

It is also possible for one optical fibre to contain many FBGs. This allows for multiplexing which is the ability of the sensor to measure strain at many discrete points along its length to create a quasi-distributed array of sensors [149]. However, it should be noted that a study by Shivakumar and Bhargava [150] found that if a fibre optic sensor is embedded perpendicular to the direction of the fibres then an eye-shaped resin pocket ("resin eye") defect forms with a length 16 times that of the fibre optic radius and a height of double the fibre optic

radius. This defect acts as stress concentrator and it was found that under tensile loading, initial failure occurred due to transverse matrix cracking at the defect.

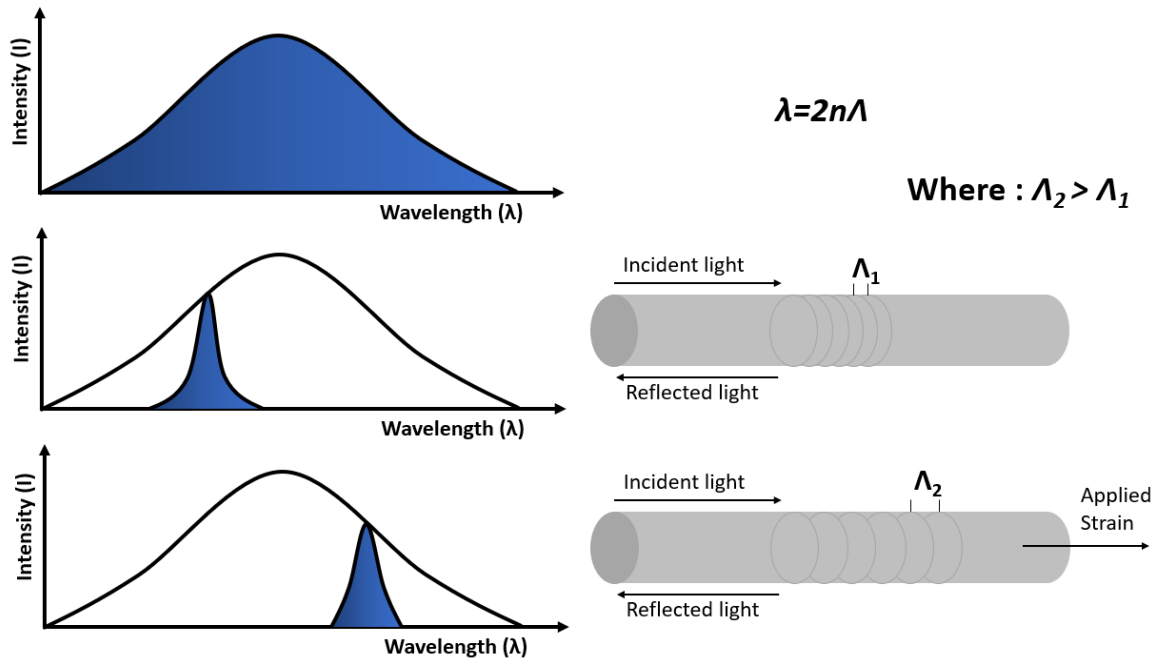


Figure 12: FBG response to an applied strain, adapted from [53]

Work by Okabe et al [151] investigated the effect of optical fibre diameter and coating variants on the, then thought, troublesome splitting of peaks in the reflection spectra, finding that decreasing fibre diameter and coating in polyamide would reduce this splitting. The splitting of peaks in the reflection spectra was attributed to transverse strains being applied to the optical fibres during cooling or in other words the chemical shrinkage of the resin matrix. Figure 13 shows the splitting of the reflection spectra due to unequal transverse strains. Later works by the likes of Sorensen et al [152] found that it was possible to use this peak splitting effect to monitor the build-up of transverse strain during cure and therefore investigate the chemical shrinkage of the resin matrix during cure. This is of particular use when investigating the build-up of residual stress in fibre reinforced composites as chemical shrinkage is a key contributing factor to residual stress.

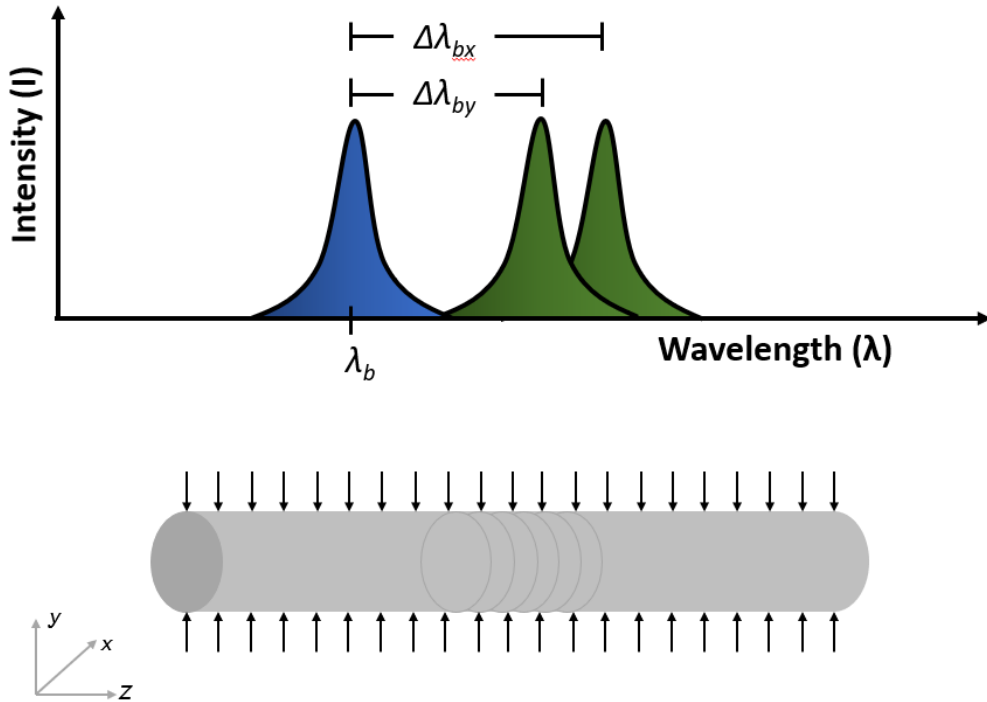


Figure 13: FBG response to transverse strain, adapted from [152]

The use of embedded fibre optic sensors in laminates is still very prevalent with many examples of this technique being successfully applied to the monitoring of internal strains during cure in thermosets [153][154][155][156][157] and thermoplastics [158][39][103] where a higher operating temperature is required. Another key benefit of fibre optic sensors is that they can often be repurposed after cure as condition monitoring devices. Arhant et al [103] demonstrated the ability of embedded fibre optic sensors to measure residual strain during cure and then using the same sensors to monitor the effect of an uptake of moisture within the part during the parts normal operating life without any apparent loss in measurement quality. The idea of having dual functionality of cure monitoring and structural health monitoring [74] is undoubtedly of great interest to those looking to implement this technology in industrial applications.

Recent work by Hu et al [159] has shown the viability of a novel implementation of FBG sensors in laminate by using a “tailed” FBG set. This consists of two parallel FBG sensors with one being shorter than the other. The shear lag effects between the two sensors causes more strain to develop on the long FBG sensor during cure and the difference between these two strains is a function of the modulus of the matrix. Therefore, the gelation point and effective

transverse chemical shrinkage can be determined. It is also possible to use the calculated matrix modulus to monitor the degree of cure of the matrix as these two quantities are proportional.

Work by Minakuchi [160] showed the possibility of using fibre optic sensor to characterise the direction-dependent cure shrinkage of thermosetting fibre reinforced composites in-situ during cure. This method relies on a combination of FBG placed in the out-of-plane direction through the thickness of the laminate and sets of short tailed paired sensors embedded in-plane through the thickness of the laminate. This technique gives a deep insight into the internal build-up of residual strain in three-dimensions during the curing of a composite laminate. It is also able to characterise the through-thickness shear strain of the resin matrix.

Distributed Optical Sensing (DOS) technology has gained much popularity in recent years for its ability to have continuous real time measurement capabilities along a fibre's entire length, unlike multiplexing which relies on many discrete sensing zones. It works on the principal of coherent Rayleigh optical time domain reflectometry, sending short laser pulses through the fibre and analysing the reflected laser spectra. It seems that it is currently not possible to measure strains transverse to the optical fibres in DOS as is done with peak splitting in FBG based sensors which means DOS fibres must be placed parallel to the direction of strain measurement. This comes with its own problems with voids and stress concentrations as previously explained. Work by Tsai et al [161] has recently shown the full capability of this technology by combing DOS with cure kinetic, viscosity and glass transition models in thermosetting fibre reinforced laminates to monitor cure strain in both UD laminates and structural cross-ply laminates. It was concluded that "cure shrinkage cannot accurately be measured by the DOS in a laminate where the ply 0° direction is aligned with the sensor" due to the small strain sensitivity parallel to the optical fibre caused restraining reinforcing fibres. This means that for the case of a cross-ply laminate and parallel to the fibres in a UD laminate it was not possible to accurately measure residual strain. However, with all other cases, good agreement was found between the recorded results and the results calculated with composite laminate plate theory. This technology shows good potential assuming its limitations are understood as it allows for an unmatched insight into the strain profile along the DOS fibre length.

2.4.4. Experimental residual stress measurement techniques conclusions

There has been a huge breadth of research that has been undertaken in the numerical modelling of the manufacturing process of fibre reinforced laminates, as Baran et al [51] showed. It is clear that much progress has been made over the past few decades and it is now possible to predict many physical phenomena accurately by choosing and correctly implementing one of the many models and techniques available. However, it is crucial that numerical simulations are validated through experimental rigour to have sufficient confidence in a given result. Early works from Daniel et al [143], Hahn and Pagano [162] and Nairn and Zoller [135] paved the way for the current state of the art research in the experimental determination of residual stress. In this work, a variety of the currently most-used experimental techniques have been presented and categorized into two groups, destructive and non-destructive techniques. A summary has been given in Table 2 for clarity. Destructive techniques work from the principle of bulk material removal to induce a relaxation of stress to induce a relaxation of strain which in turn can be measured and analysed to determine the relaxed stress. Traditionally, these methods have been limited to global or laminate scale stress as their resolution is generally too low to capture the variation of stress through the thickness of a single ply due to inaccuracies in the experimental method; machining, strain measurement, numerical approach. However, recent work like that of Smit and Reid [71] have shown the possibility of using these techniques for the measurement of intraply stresses with confidence in associated errors. This opens up destructive techniques for even wider adoption by those measuring all scales of residual stress. However, non-destructive techniques are still the preferred choice in academia for the analysis of micro-scale intralaminar residual stresses as they do not suffer from the same limits inherent to destructive techniques. With the exception of embedded sensor technologies, non-destructive techniques do not appear to be widely used in industry as they are generally not feasible for end use parts due to limitations like material properties, being permeable to light or having asymmetric lay ups. Embedded sensor technologies have great potential in the analysis of intraply, interply and laminate residual stresses arising from cure and have the potential to provide condition monitoring data during the operational use of the part. Therefore, embedded sensors offer an unparalleled insight into the internal residual strain/stress state of a laminate throughout the entire cure cycle of a laminate while still being

non-destructive, thereby allowing for further mechanical analysis to be carried out. Thus, embedded sensors will be the primary technique of choice for the experimental analysis of residual stress in rapidly cured composites in this work. Additionally, a photoelastic analysis of neat resin samples is proposed as a way to gain an insight into the through-thickness variation of residual stress in UD laminates where matrix properties are dominant in this plane.

Table 2: A review of all discussed measurement techniques

Technique	Residual stress scale			Comments	References
	Micro	Macro	Global		
Layer Removal		[56]	[55]	Low accuracy	[54] [11] [56] [57] [58] [59]
Hole-drilling	[63] [71]	[64]	~	-Potentially global scale if laminate is thin. -Biaxial stress distribution -Accuracy decreases with depth of cut	[60] [61] [62] [72] [73] [74][64] [63] [65] [66] [67] [68] [69] [70] [71] [75] [76] [77] [78] [79]
Ring-core	[85] [86] [87]	[82]	[84]	-Most applicable to micro scale -Potentially relieves more residual stress than hole drilling	[80] [59] [81] [82] [83] [84] [85] [86] [87] [88] [89]
Slitting method	[99]	[57] [94]	[95]	-Limited to the average stress across a width	[90] [57] [94] [95] [91] [87] [92] [163] [96] [97] [98] [99] [100] [101] [102] [103] [104]
Contour method	?	?	?	-Has not been done, but has potential	[105] [106] [107]
First ply failure		[108]		-Assumes a perfectly stress-free sample is possible	[108] [109] [110] [59]
Raman spectroscopy	[119]	~		-Macro if matrix is crystalline and aramid fibres are used	[117] [118] [119] [120] [121][122] [123]
Asymmetric warpage			[126] [127]	-Only validates model	[109] [37] [124] [125] [126] [127] [128] [129] [130] [131] [132]
Photoelasticity	[74]	[136]	[136]	-Only macro and global using a cross-section -Matrix must be transparent	[115] [133] [134] [135] [136]
Cure referencing	[137]	[137]		-Surface based measurement -Low accuracy	[137] [30] [138][139]
Embedded sensors	[148]	[140] [160]	[140] [149] [160]	-Sub-surface strain measurements allow for no thickness limitations -Possible debonding issues	[140] [141] [143] [142] [144][145] [146] [53] [146] [115] [148] [147] [149] [150] [151] [152] [153] [154] [155] [156] [157][158] [39] [103] [159] [160]

?: There is potential but it has not been done to date.

~: It is possible with some caveats

2.5. The effect of residual stress

Residual stress and shear strength

Residual stress has been shown to impact the transverse tensile strength, compressive strength, flexural strength and interlaminar shear strength of fibre reinforced laminates [52][164]. The shear strength of a laminate is critical for its in-service performance and is often the fundamental design parameter for a given part especially during bending and torsion loading. Therefore, understanding the effect that residual stress has on the maximum shear strength of a laminate is required if components are to meet the design requirements.

A study by Agius et al [165] compared the predicted residual stress due to chemical and thermal volumetric changes to the short beam shear strength of various laminates found experimentally. A short beam shear strength test, as defined by ASTM 2344 [166], is a 3-point bending test performed on short beams to minimise the flexural component and maximise the induced shear stress. DIC was used during the short beam shear strength tests to detect changes in the shear strain field during testing to determine the point at which initial failure occurred. They concluded that increased residual stress reduces the maximum shear strength of the material. Unlike a later study performed by the same group investigating fatigue [27], the microstructure of the composites was not examined or related to the decrease in shear strength. Similarly, in this later study, residual stress was modelled and not found experimentally so there is some unknown inaccuracy here. It should also be noted that other authors such as Adams et al [167] have questioned the usefulness of the short beam shear test as a method for accurately determining the shear strength in composites. This was due to the inherent tensile and compression loading during testing. The effect of residual stress on shear strength of composites is an understudied area in academia and more work is required to fully understand its effect. However, the focus of this current work is on UD laminates which have inherently low levels of shear stress through their thickness during loading and as such an alternative mechanical performance metric will be investigated.

Residual stress and fatigue

Understanding the fatigue life of a material is of a paramount importance when designing any structure. In the aerospace sector in particular it is vital that the service life of any given part is well understood so mitigation strategies can be put in place where necessary to avoid

failure. Without this fundamental understanding it is not possible to accurately predict the potential for failure of parts during service. Currently the fatigue behaviour of common aerospace metallics are well understood and the composites used are manufactured using longer cure times to minimise residual stress which allows designers appropriate confidence in the selected materials. However, with the drive toward lower manufacturing times and therefore reduced curing times understanding the effect of rapid curing on these fundamental material properties is critical.

There is a large body of research investigating the fatigue characteristics of composites. As with most mechanical properties of composites the anisotropic nature of composites introduces complexity to the problem. Some authors like Talreja and Singh [168] propose that using a traditional S-N curve or Wöhler diagram as it is not possible to determine the fibre and matrix phases contribution to the fatigue failure of a given composite. It is argued that without understanding the role that each phase plays in resisting cyclic loading it is not possible to determine the “true” fatigue limit. Thus, more complex fatigue life failure diagrams are suggested which fully describe the failure mechanisms at play during fatigue loading. However, others have used pure mode S-N curves to successfully predict the initiation of matrix cracking due to fatigue [169][170][171]. This approach has the benefit of being easier to implement and analyse. However, assumptions must be made about the loading case which can reduce the accuracy of the results if more complex loading occurs.

A study by Joosten et al [171] assumed pure mode (tensile/shear) interlaminar S-N curves are considered as a material property in their analysis. While their experimental results were found to have good agreement with the modelled ones, in this case it is possible to imagine scenarios where these assumptions are not valid. However, in this case DIC was used during fatigue testing so matrix cracking could be identified. This was then later verified by analysing the failed samples using optical microscopy where cracks in the matrix could be seen clearly. The results of the study found that increased residual stress led to the formation of macro-scale matrix cracking at a lower number of cycles for a given load level. This is in line with the conventional ideas around the effect of residual stress. However, this study was limited as the residual stress values used to compare samples were calculated from a model which related the thermal cool-down after cure to the theoretically induced residual stress. This literature review has already shown the limitations that this approach may have due to

the large number of variables at play in the formation of residual stress. The interlaminar tensile response was determined by testing a UD sample to failure and identifying when initial cracking occurred. This then informed the stress required during the fatigue tests. However, this assumed that the residual stress in the UD sample was negligible. This current thesis will show that this assumption is not valid for all cases, especially rapidly curing laminates. Additionally, the test requires a right-angled test specimen which will cause there to be residual stress in the part due to the uneven volumetric changes between resin and fibre [172] and because the shape itself constrains any relaxation [173]. The sample was then post-cured as per the manufacturer's instructions which, in this case, reduces the rate at which stress is relaxed from the system as increasing DOC increases the relaxation modulus [21]; which, if the strain is constrained, reduces the rate at which stress is relaxed. Nonetheless, a clear correlation was found between increasing residual stress and reduced cycles to failure.

Patel et al [27] went on to investigate the effect that curing temperatures, therefore curing rates and residual stress, have on the microstructure of the matrix and how this in turn effects the mechanical performance of the composites. This recent study is the first to attempt to link the change in microstructure induced by faster curing rate and the mechanical properties of the composites. Previous studies [32] have found the existence of a so called "third-phase" of composites as previously mentioned in section 2.3.1. Atomic force microscopy was used in tapping mode to determine the percentage of third phase found in the samples. This was required as the microgel nodules of third-phase were only around 10 nm in diameter. In this study three different curing methods were compared. First, a sample was cured at room temperature for 12 hours and then hot pressed 70 °C for 6 hours then hot pressed at 140 °C for another 6 hours, this sample was called "RT sample". A second sample went through the same curing cycle but without the initial room temperature cure and was called "70 sample". The third sample went through the same cure cycle as "70 sample" but did not do the initial 70 °C cure and was called "140 sample". These cure cycles have been summarised in Figure 14.

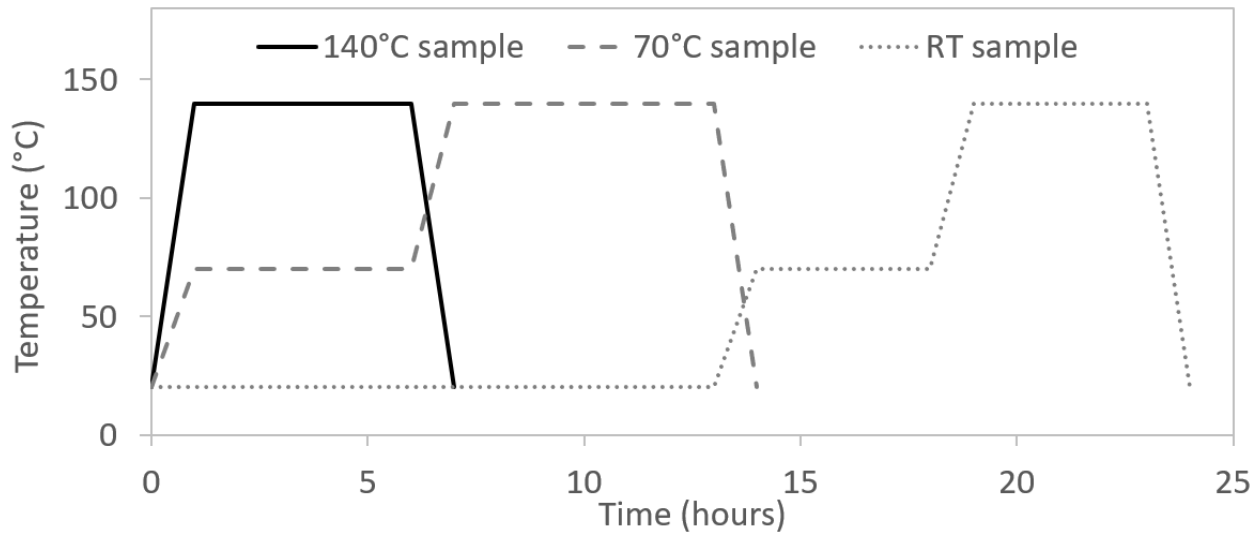


Figure 14: Cure cycles of experiments conducted by Patel et al [27]

As can be seen from these curing profiles none of these cycles would classify as rapid curing but they do differ in a critical way. The “RT sample” and “70 sample” were allowed to gel completely before post-curing at a higher temperature. Using AFM, it was found that the “RT sample” and “70 sample” that were allowed to gel before cure had around 15% of their microstructure made up of third-phase while the “140 sample” that was not allowed to gel had around 30%. The fatigue testing consequently showed that the “140 sample” with the higher proportion of the third-phase region failed at approximately 2.5 times as few cycles as the other two samples. This was postulated to be because the softer third-phase regions act as micro-crack initiation points and thus promote premature failure. Therefore, there is a clear link seen between the curing rate, microstructure and fatigue life of composites. To date this is the only study relating microstructure to fatigue life so it is clear more research is needed in this area to fully understand the micromechanical mechanisms at play. However, before being able to understand the relationship between rapid curing and fatigue properties, a more fundamental understanding of the effect on laminate matrix strength is required.

Residual stress and transverse matrix strength

One of the most common failure modes in fibre reinforced laminates with UD plies is matrix cracking [41]. Cracks occur perpendicular to the reinforcing fibre direction as this is the weakest plane within the UD ply. This is often the first failure mode to occur in a given cross-ply laminate as this is a low energy failure mode and is often called the first-ply failure [174]. Determining the onset of first-ply failure in cross-ply laminates can be difficult as

adjacent plies with an alternative ply orientation can have strong restraining effects on that ply. This can dramatically change the failure mode and load for that ply, making it difficult to make comparisons reliably between various laminates. However, UD laminates do not have this limitation and will reliably fail due to matrix cracking when loaded transverse to the fibre direction [175].

Multiple authors have found that residual stress plays an important role in transverse matrix failure in composites [176][177][178][179][180], either leading to an increase or decrease in transverse matrix strength by delaying or promoting failure initiation in the matrix. This is to be expected, as composite matrix failure is driven by crack growth which can be accelerated or retarded by tensile and compressive stress, respectively. In fact, residual stress generated during manufacture can be so large as to cause matrix cracks before mechanical loading has been applied [181]. Thus, similarly to the first-ply failure method, as discussed in section 2.4.2.6, transverse matrix testing can be used to investigate the presence of residual stress in fibre reinforced composites [182]. Relatively simple and well understood tests like transverse tensile tests and transverse three/four-point bending tests can be used to investigate the effect of residual stress on mechanical performance. Therefore, investigating the transverse matrix strength of composites is proposed as an effective and implementable way of differentiating the relative build-up of residual stress in UD laminates. This will be explored further in chapter 8.

2.6. Conclusion

In conclusion, not much is known about the effects that rapid curing (less than 10 minutes) resins have on the residual stress of composite parts. Additionally, little is known about the effect that residual stress has on the mechanical performance of composites. Therefore, it is clear that this will be an important gap to fill if the aerospace and automotive industries are to increase the adoption of rapid curing composites for structural applications. This thesis will be focused on gaining an understanding of the effect that various processing parameters, primarily laminate thickness and cure temperature, have on residual stress and strain and how this affects the mechanical performance of composite components.

There is a wide range of possible techniques for the determination of residual stress in composites. All the techniques discussed have got their own advantages and disadvantages and it is clear not one single technique will adequately satisfy the aim of the proposed research. Therefore, it has been concluded that a combined approach must be adopted. Initially, an analysis of some of the key material properties in the development of residual stress will be required so that the resin formulations under investigation can be better defined and thermal histories determined. Embedded optical fibres have been found to be a robust and insightful way of experimentally determining the build-up of residual strain during cure and as such will be the primary analysis technique used in this work. However, the ability of these sensors to effectively bond in rapid curing resins must be determined to quantify the usefulness of the residual strain data gathered from them. Additionally, photoelasticity has been identified as a useful full-field technique for the examination of residual stress with the limitation that samples must be optically transparent. Therefore, as an approximation of the build-up of residual stress due to uneven heating and DOC gradients, variably cured neat resin samples will be analysed using photoelasticity. A modelling step is required to relate residual strains, measured using embedded FBGs, to residual stress in composites due to the transient and anisotropic nature of the material properties of a laminate during cure. Lastly, a mechanical analysis of the transverse matrix strength with varying residual stress states will be made to quantify the effect of residual stress on the mechanical performance of a given laminate.

For a theoretical laminate that has no mechanical boundary constraints on its surfaces, it is proposed that in sufficiently thick rapidly cured UD laminate, a transverse compressive residual stress will form on the outside surfaces of the laminate stack with an opposing tensile stress in the through-thickness centre. This occurs because unlike a conventional curing resin system, the rapid curing causes the laminate to cure from the outside to the inside. Thus, the resin modulus develops from the outside to the inside and constrains the movement of the uncured resin in the centre of the laminate. However, it is unclear to what degree the tool-part interaction at the boundary of a real laminate would cause this distributed stress profile to change.

From the review of the mechanisms that contribute to the formation of residual stress in fibre reinforced composites, the initial hypothesis of this thesis is:

- Rapid curing of composites will lead to large thermal and DOC gradients through the thickness of laminates. This will in turn set up a differential stiffness, thermal expansion, and chemical shrinkage profile through the laminate. Therefore, a differential residual stress profile through the thickness of rapidly cured UD laminates is predicted.

The thesis objectives outlined in chapter 1 were constructed to best investigate the validity of this hypothesis.

3. Material characterization

3.1. Introduction

Two rapidly curing resin formulations, EF7017 and EF3718, have been provided by one of this work's sponsors, Solvay S.A. for analysis. Currently, little is known about the rapid curing resin formulations under investigation as they have been provided blind. Thus, this first chapter aims to characterize the resin formulations under investigation through: cure kinetics, thermal history, asymmetric bending, and dynamic response during cure. Additionally, the basic material properties used in the rest of this thesis will be quantified. As well as providing crucial material property data for use later in this thesis, this analysis also allows for an initial qualitative assessment of the potential key mechanisms in the formation of residual stress in these rapidly curing laminates. Cure kinetics parameters of the unknown resin matrices will be determined with Dynamic Scanning Calorimetry (DSC) to identify the most appropriate resin formulation to take forward and for future use in residual stress modelling (chapter 7). An investigation into the thermal profile through the thickness of the laminates during cure is conducted to determine the extent to which the predicted through-thickness thermal gradients are present. These data will also be used for model validation in chapter 7. DSC and thermal history data will then be used to give a first insight into how each resin formulation cured and develops residual stress. One resin formulation can then be chosen for further analysis in the rest of this thesis. Asymmetric bending tests should then be able to determine the contribution of thermal expansion and chemical shrinkage to residual stress in the laminate under investigation. Finally, the dynamic response of the laminate with varying temperature will be analysed with the use of a DMA so that the T_g of the cured laminate can be determined.

The aim of this chapter is:

- To develop an understanding of the resin formulations under investigation and the key mechanisms that contribute to residual stress development in fibre reinforced composites

The objectives of this chapter are to:

- Define basic constituent properties of reinforcing fibres and resin matrix

- Conduct non-isothermal DSC scans of the provided resin formulations to gain an understanding of their respective curing profiles
- Conduct isothermal DSC scans of the provided resin formulations to define cure kinetics parameters for use later in this thesis
- Carry out through-thickness thermal testing using the provided resin systems to quantify the thermal variation through a laminate during rapid cure.
- Determine which resin formulation to conduct further analysis with
- Use asymmetric bending tests to characterize the contribution of thermal and chemical effects to residual stress in rapidly cured composites
- Use DMA to determine the T_g of the cured resin system under investigation.

3.2. Materials

Initially, two experimental prepreg formulations, EF7017 and EF3718, were provided by the project's industrial sponsor, Solvay, in 300x300 mm prepreg sheets. Both of these formulations were specifically designed for very rapid or "snap-curing" conditions. The details of the EF7017 resin were not disclosed by the supplier due to commercial sensitivity but it was stated that it was a free-radical based polymerisation with a 190 gsm at 38% fibre volume fraction and a CTE of 105.3×10^{-6} [183]. The EF3718 resin was a more conventional epoxy based formulation using addition polymerisation and had a density of 190 gsm at 38% fibre volume fraction [183]. Both prepregs used an undisclosed reinforcing fibre with a modulus of 240 GPa and ultimate tensile strength of 4.1 GPa. The manufacturer's initially proposed curing schedule for each formulation can be seen in Table 3. These formulations were designed for use in industrial hot-pressing curing processes and as such it was suggested that 35 bar of compaction pressure is used during cure to ensure an adequate heat flow rate into the part and good consolidation of the part. An additional prepreg system [184], 5320-1 was used as a more traditional comparative resin system, also manufactured by Solvay, which is commonly used in the primary and secondary structures in the aerospace industry. The manufacture recommended cure times for the 5320-1 resin system ranges between 8 hours to 1-2 days as stated by the technical data sheet. However, it should be noted that the 5320-1 prepreg was left over from previous project and its expiration date was unknown. Therefore, any conclusions derived from the analysis of this prepreg will be viewed with some caution.

Table 3: Curing cycles for EF7017 and EF3718 laminates

Temperature (°C)		140	145	150	155	160	170
Press-cure time (mins)	EF7017	8	5	3		2	1
	EF3718		10		6.5		3

Many of the material and laminate properties are still unknown for the EF7017 and EF3718 prepregs. One difficulty with working with rapidly curing resin systems is that these data can often be very difficult to obtain as most standard testing machines simply do not operate with high enough heating rates to give representative data. For example, it is not possible to accurately use DMA or a cone-plate rheometer to cure the samples and thereby determine the gelation point, α_{gel} , or the change in elastic modulus, E' , with DOC using a conventional setup due to thermal lag and practical constraints at representative heating rates [185][186]. Therefore, to contain the scope of this work, some representative property values have been found in the literature and are presented in Table 4 and will be used in the rest of this work. It is also assumed that all of the resins under investigation have similar mechanical properties and only differ in their cure kinetics. However, while this is clearly not ideal it will still be possible to make relative comparisons between formulations. An area of future work should certainly be to develop methodologies for determining material properties of rapidly curing resins to allow for the more accurate determination of residual stress, but this is beyond the scope of the current work.

Table 4: Resin and fibre mechanical properties used throughout this work.

	E_{11} (GPa)	E_{22} (GPa)	ν_{12}	ν_{23}	G_{12} (GPa)	G_{23} (GPa)	α ($\times 10^{-6}$)
Fibre	240 [183]	25.2 [154]	0.2 [154]	0.25 [154]	15 [154]	7 [154]	0.5 [187]
Resin	1.56*	-	0.31 [154]	-	-	-	105.3 [183]

*as determined by tensile tests using the Image J method, developed and discussed in chapter 4.

3.3. Dynamic Scanning Calorimetry

3.3.1. Cure Kinetics Theory

As discussed, the material state, and therefore laminate state, are dependent on the DOC of the resin matrix. Therefore, efforts must be made to determine the cure kinetics parameters of the resin formulations under investigation to define the relationship between cure conditions and laminate state. Phenomenological models have been shown to accurately predict the cure of thermosetting resins and will be used here [188]. Firstly, it can be assumed that the degree of conversion, or degree of cure, α , of the reactive epoxy constituents is proportional to the heat of reaction within time t , and the total heat of reaction. This relationship can be described by Equation (8) [189][190].

$$\alpha(t) = \frac{\Delta H_t}{\Delta H_{total}} \quad (8)$$

where ΔH_t and ΔH_{total} are the heat of reaction over time t and the heat of curing reaction obtained from the area between the exothermic curve and baseline respectively. Here, the rate of the curing reaction, $d\alpha/dt$, is described by Equation (9).

$$\frac{d\alpha}{dt} = \frac{dH(t)}{\Delta H_{total} dt} = k(T) \cdot f(\alpha) \quad (9)$$

where $f(\alpha)$ is a curing kinetics related function and $k(T)$ is the reaction rate constant which in this case can be described by the Arrhenius Law as is shown in Equation (10). It is assumed that the polymerisation reaction follows fixed order curing kinetics and as such is a function of temperature and not time.

$$k(T) = Ae^{\frac{-E_a}{RT}} \quad (10)$$

where R is the universal gas constant (8.314 J/mol/K), T is the absolute temperature, A is the pre-exponential factor and E_a is the apparent activation energy. Additionally, for epoxy based systems it is reasonable to assume cure reactions take an n^{th} order form [51], thus defining $f(\alpha)$. Equations (9) and (10) can then be combined to give Equation (11).

$$\frac{d\alpha}{dt} = Ae^{\frac{-E_a}{RT}} (1 - \alpha)^n \quad (11)$$

where n is the reaction order. Then, from Equation (10) it is possible to determine the pre-exponential factor and the apparent activation energy by plotting a $\ln(k)$ by $1/T$ graph and finding the slope intercept and gradient respectively. This is more easily seen in the rearranged form of the Arrhenius equation shown in Equation (12).

$$\ln k = \frac{-E_a}{RT} + \ln A \quad (12)$$

3.3.2. DSC Methods

The analysis of the cure kinetics and cure time for all prepregs was undertaken by using non-isothermal and isothermal heat flux DSC techniques respectively. For this testing the Perkin Elmer, DSC8500, with a nitrogen flow rate of 20 ml/min was used having been pre-calibrated by the laboratory technicians. Samples were prepared by cutting out 5-10 mg β -staged (partially cured resin for fibre impregnation) prepreg samples and inserting them into aluminium DSC pans and then sealing with an aluminium lid using another empty aluminium pan as reference for the DSC machine. Isothermal hold DSC tests were conducted between 100-140 °C, 105-135 °C and 160-250 °C for the EF7017, EF3718 and 5320-1 prepregs respectively to accommodate for their respective curing conditions. For the non-isothermal tests, ramp rates of 5, 10, 25 and 50 °C/min were used during the ramp up between a temperature range of 220-400 °C. A ramp down to 25 °C at 25 °C/min was used and then the second ramp at the same ramp rate used in the first ramp was performed to ensure that the samples were fully cured. Isothermal DSC tests were conducted by rapidly ramping (50 °C/min) up to a specified temperature, after which a five-minute isothermal hold was carried out, then rapidly cooling back to 25 °C. This cured the samples a specific amount as a function of time and temperature. A second (10 °C/min) ramp stage was then completed to determine how much residual curing took place after the initial isothermal hold. As curing of thermosetting resins is an exothermic reaction, heat is released during cure. The second ramp stage was allowed to continue until the exothermic peak could no longer be detected to ensure full cure of the sample. Thus, by measuring this heat release in the second ramp a relation between DOC, temperature and time can be made.

3.3.3. DSC Results

Non-isothermal DSC analysis

Dynamic Scanning Calorimetry (DSC) tests were performed on the two rapid curing prepregs under investigation, EF7017 and EF3718, and a more conventional curing aerospace resin formulation, 5320-1, for comparison. The heating cycle for the initial tests was to heat up to past the point of exotherm at a controlled rate, which was varied on repeat experiments. Then

to hold at that temperature for one minute, then cool down to room temperature at that same rate, hold for one more minute and then repeat the whole cycle again. This allowed for easy detection of whether the sample had been fully cured on the initial ramp. The results of the 25 °C/min ramp rate for the three different samples can be seen in Figure 15.

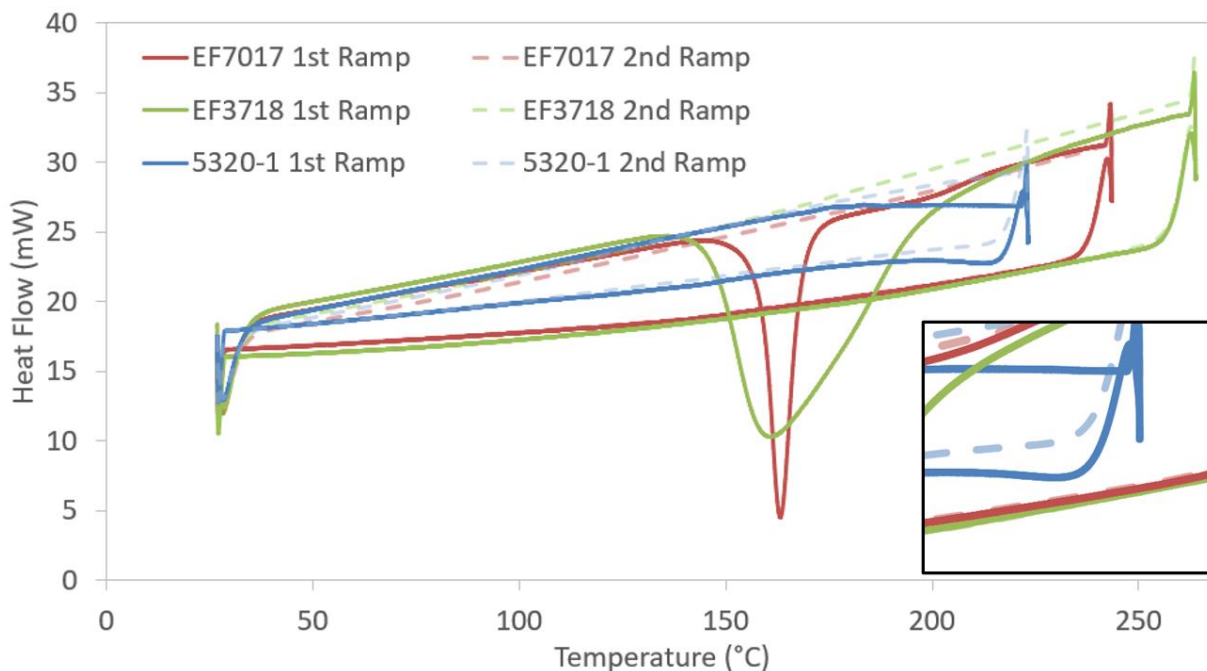


Figure 15: DSC results of the 25 °C/min ramp rate cycle.

From this figure the relative exothermic troughs of each material under analysis can be observed easily between approximately 140-200 °C. Clearly, the rate of reaction, as indicated by the gradient of the slope of the trough, of each of these materials is very different. EF7017 can be seen to react very quickly at its critical temperature and complete the majority of the reaction in a very short temperature/time window. This is indicative of a resin system with a high activation energy and low total heat of reaction. However, EF3718 reacts more slowly but over a longer period of time and does in fact release over three times as much energy as EF7017 during its exotherm. In contrast, EF5320-1, a non-rapid curing resin, can be seen to only just start to exotherm. Indeed, the difference between the ramp down stages of the first and second ramps is indicative of a partially reacted system; an enlarged view of this can be seen in the bottom right of Figure 15. This experiment was able to show how all three of these resins systems cure very differently, and as such it can be hypothesised that as EF7017 cures very rapidly in a small temperature window, it is likely that laminates with this resin matrix formulation cured in a hot press will experience much larger DOC gradients through their

thickness than similar laminates made with the EF3718 formulation. This is corroborated by the manufacturer's recommended curing times shown in Table 3. Thus, it is expected that larger residual stress gradients will occur in the EF7017 laminates.

Various ramp rates were used to determine the effect of the observed specific heat of reaction parameter. 5, 10 and 25 °C/min ramp rates were used, with three repeats of 10 and 25 °C/min and one 5 °C/min test for both EF7017 and EF3718. For each resin formulation the specific heat of reaction value was reported within one standard deviation of each other. Therefore, all heating rates were considered to provide accurate data. These results are shown in Appendix B. The remaining experiments were conducted at a ramp rate of 10 °C/min as this offers a good balance of resolution and time efficiency.

Looking at the EF7017 peak in Figure 15 it is possible to see two peaks, one large and sharp peak and one much smaller and longer peak after the first. This suggests that the EF7017 resin has multiple reactive groups and multiple chemical kinetic processes. This is likely better defined using a more complex model than the Arrhenius model used here. However, for this present work a first order assumption is thought to be sufficient to get a reasonable determination of the curing kinetics of the resin formulations under investigation. A useful area of future work would be to investigate the cure mechanisms in free-radical polymerizations in more detail to better define the cure kinetics of the system.

Isothermal DSC analysis

The following procedure was used to conduct the isothermal hold experiments: ramp up to the isothermal hold temperature as quickly as allowed by the machine (100 °C/min), hold at the given temperature for 5 minutes, ramp down to 25 °C, commence the second ramp stage at 10 °C/min and continue until there were no more signs of exotherm. By analysing the exothermic trough area during the second ramp stage and comparing that against a fully cured exotherm, the amount of conversion, or DOC that occurred during the isothermal hold could be determined. It was assumed that a linear relationship between conversion (DOC) and exothermic heat flow exists as it is also assumed that the energy of each bond made in the epoxy resin system has the same amount of energy. The results for EF7017 and EF3718 are shown in Figure 16. It is clear to see that EF7017 has a much more pronounced point at which

the exothermic reaction takes place compared to EF3718. This is shown by the small difference in isothermal hold temperatures causing dramatic changes in the DOC.

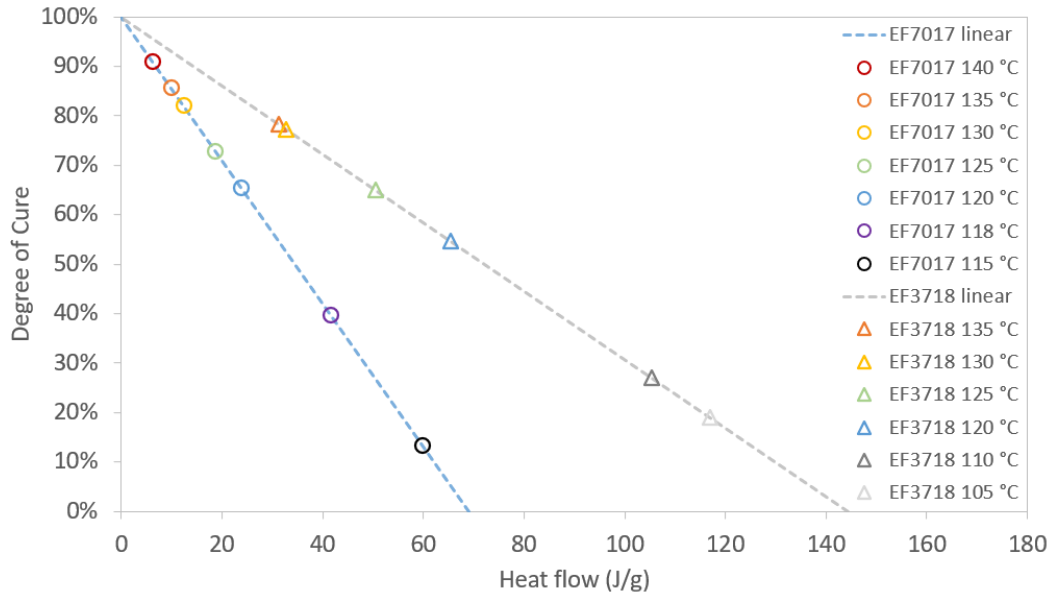


Figure 16: The development of degree of cure with isothermal holds at various temperatures for EF7017 and EF3718

From these data, it was possible to use the Arrhenius equation [191], Equation (12), to determine the activation energy of each of the resin systems under investigation. This is easily done by plotting a $\ln(k)$ by $1/T$ graph, as seen in Figure 17, and using the slope intercept and gradient to find pre-exponential factor and the apparent activation energy respectively. The cure kinetics parameters determined from this analysis are shown in Table 5.

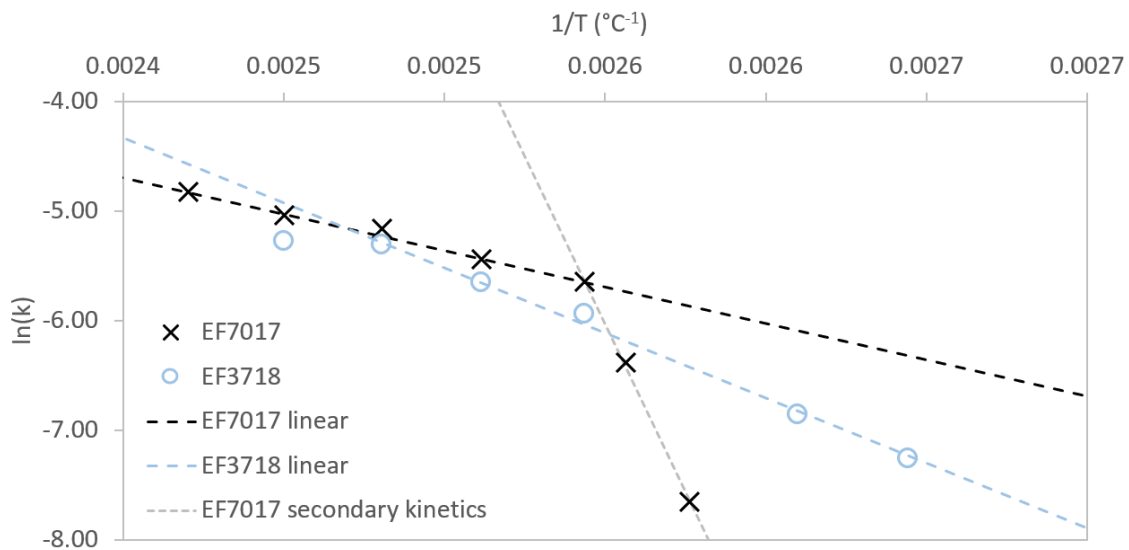


Figure 17: $\ln(k)$ by $1/T$ plot for EF7017 and EF3718 using isothermal DSC data

From Figure 17 it can be seen that two of the EF7017 data points do not follow the linear trend that is assumed by the first order assumption used in this work. These represent the 115°C (1/0.00258) and 118°C (1/0.00256) isothermal holds. This is thought to be due to the EF7017 resin formulation having at least two distinct chemical curing mechanisms, one being dominant at lower temperature (labelled “secondary kinetics”), as seen by the two outlier points, and the other being dominant at higher temperatures. The primary chemical curing mechanism is dominant from a temperature of 120°C (1/0.00254) and above. This is the much faster process, dominant in any realistic curing process and active for the majority of the curing cycle, being at a temperature that is exceeded in normal curing in around 20 seconds. This will be shown in section 0. Therefore, this second linear region is of the most interest in this work and the data points lying outside of this linear region will be ignored for this analysis. Additionally, the EF3718 135 °C (1/0.00245) point is seen to deviate from the linear trend. While it is difficult to determine any trends from a single data point, this does suggest that the curing rate slows at elevated temperatures. This could be contributed to higher molecular weight polymer chains being formed at elevated temperatures and impeding polymerization.

Table 5: Cure kinetics parameters as determined by DSC isothermal holds for EF7017 and EF3718

Parameter	Description	EF7017	EF3718	Unit
ΔH_{tot}	Total heat of reaction	182	380	J/g
A	Pre-exponential factor	8.05×10^4	3.28×10^{10}	1/s
E_a	Activation energy	54.7	98.9	kJ/mol
n	Order of reaction	1	1	N/A

This result agrees with Figure 16 which shows EF3718 starting to exotherm at a lower temperature, or lower energy than EF7017. It can also be seen that after the higher activation energy of EF7017 is surpassed, the rate of reaction is very high. This is ideal for the high temperature/pressure and rapid curing environment it is designed for.

If we assume that the epoxy polymerisation process is a first-order reaction then the first-order rate law, $n=1$, then Equation (13) can be applied. This assumption is valid if we also assume that only one reactant group is responsible for the polymerisation, which for a first approximation gives reasonable results, especially for the epoxy based EF3718. Using these

assumptions, it is possible to plot the development of DOC with time at a variety of different temperatures. This is shown for all temperatures tested in the isothermal analysis for EF7017 (solid-line) and EF3718 (dashed-line) in Figure 18. The findings from these figures are in agreement with the previous results seen in Figure 15 and Figure 16. The same rapid rate of reaction can be seen in the EF7017 at high temperatures and a sudden drop in reaction rate is evident when the temperature drops below a critical point.

$$1 - DOC = e^{-kt} \quad (13)$$

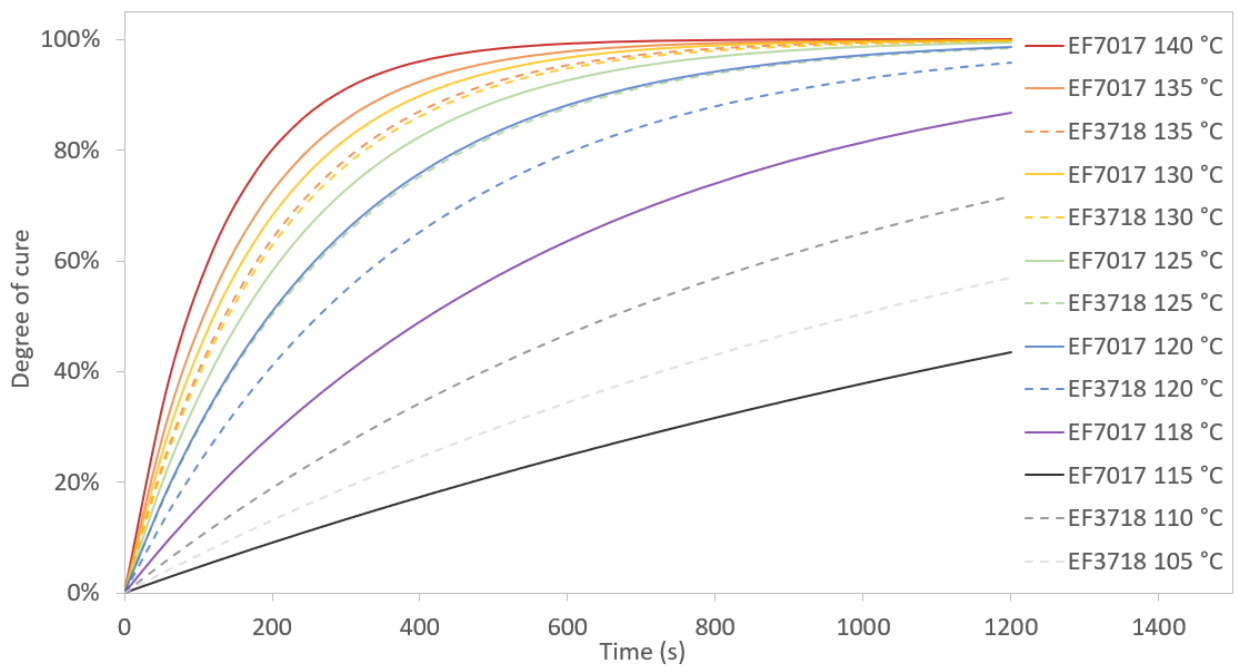


Figure 18: Progression of cure with time for EF7017 (solid-line) and EF3718 (dashed-line), as determined through isothermal DSC testing.

It was not possible to also plot the progression of cure as measured by DSC alongside the theoretical results presented here to validate the model. This was because the samples began to cure and exotherm during the ramp up to their isothermal temperatures which means there was no baseline from which to measure the heat released due to exotherm and thus to be able to quantify the progression of cure with time. This is compounded by the thermal lag experienced in the DSC due to the high heating rates used to try and reach isothermal temperature which causes large heat flow variations when the isothermal temperature is reached. It has been suggested that higher heating rates (around 200 °C/min) can be used to

mitigate this by reaching isothermal temperature before the curing exotherm begins [192]. However, it was not possible to reach these ramp rates due to the limitations of the equipment used in this study. However, the effectiveness of the model in predicting the thermal history of various laminates due to heating and curing will be explored further in chapter 7.

These initial experiments have given a useful first insight into the cure kinetics of both prepreg materials supplied by the project sponsor. The initial hypothesis that these faster curing prepreg materials would lead to higher residual stress seems to corroborate with these results.

3.4. Through-thickness temperature variations

To test the validity of this thesis' initial hypothesis that thick rapid curing laminates will have a large thermal and DOC gradient through their thickness, an initial through-thickness thermal test was conducted. K-type thermocouples were placed in the in-plane centre of, the 1st, 5th, 10th, 15th and 20th plies in a 75x75 mm [0]₄₀ UD laminate using EF3718 (Figure 19) and EF7017 (Figure 20) prepregs. This EF3718 laminate was then placed into a hot press that was preheated to 170 °C and the EF7017 laminate was placed in at 140, 150 and 160 °C. Various temperatures were used to more closely match the recommended cure cycles. For both laminates tested shims were used to ensure the laminate thickness did not go below 8.75 mm as this equates to a 0.22 mm cured ply thickness which is suitable for a 190gsm areal weight of the reinforcing fibres and a 38% resin fraction [193]. The results for the EF3718 and EF7017 cases can be seen in Figure 19 and Figure 20, respectively.

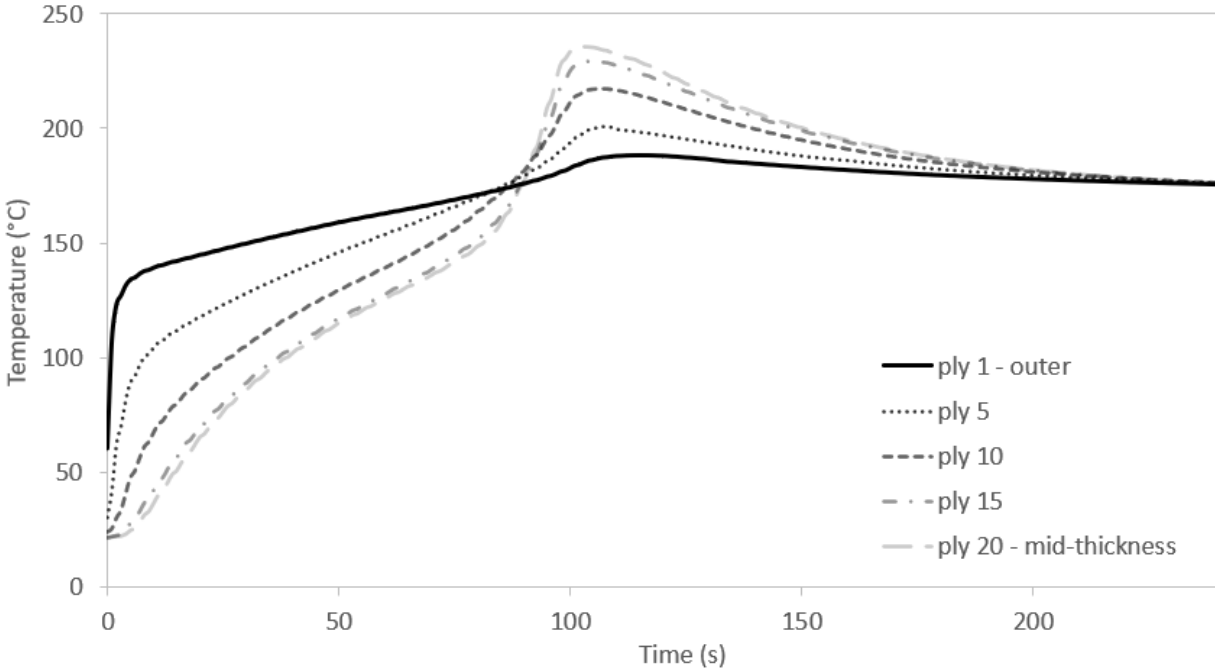


Figure 19: Through-thickness temperature distribution in EF3718 [0]₄₀ laminate

Pressure is applied to the laminate and full thermal contact is established causing a rapid increase of temperature in the outermost plies with a more modest temperature increase occurring in the middle of the laminate. This continues up until approximately 90 seconds when the centre of the laminate begins to exotherm causing there to be a rapid increase of temperature up to 240 °C, 60 °C above the temperature of the hot press. This large exothermic response is due to the large total heat of reaction of the EF3718, as determined through the DSC analysis. This excessive release of heat caused smoke to be emitted from the sample during cure. Therefore, due to safety concerns with making larger laminates and curing at higher temperatures causing even more heat to be released, the EF3718 formulation will not be investigated further. Additionally, this overshooting of the cure temperature will likely cause degradation of the embedded sensors used in chapter 6 which have a maximum operating temperature of 200 °C [194].

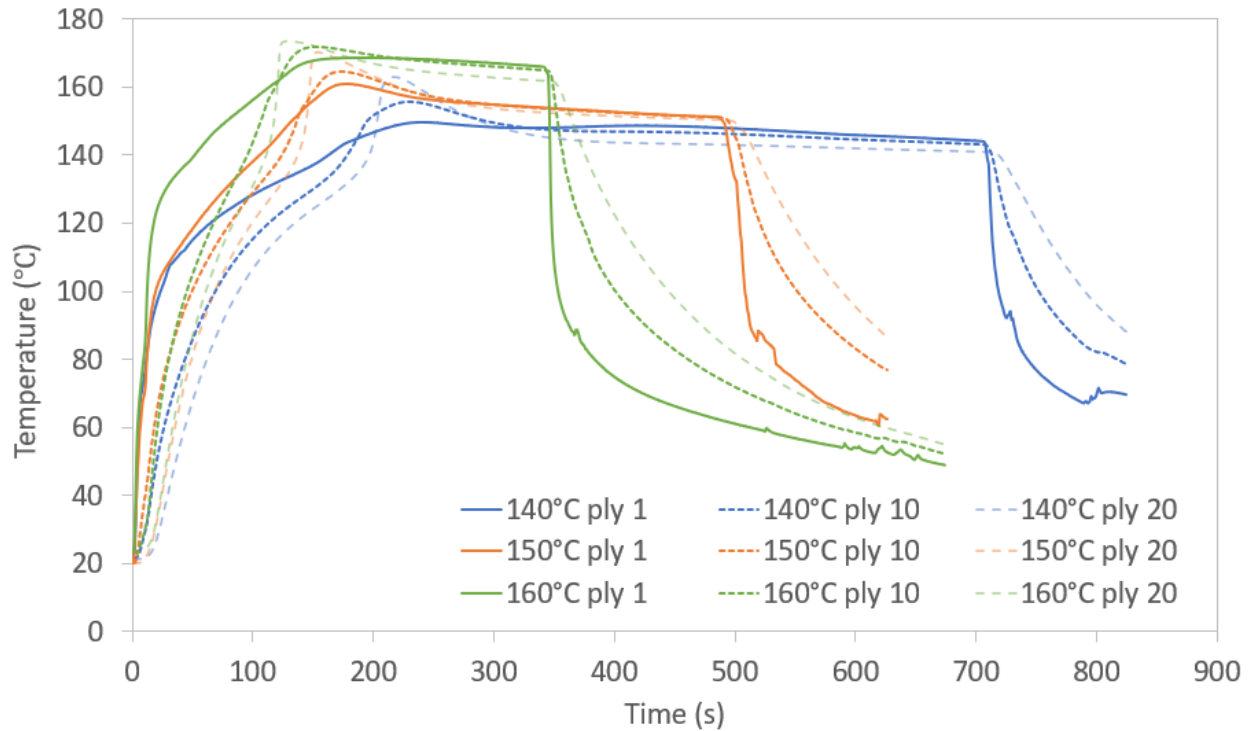


Figure 20: EF7017 through-thickness temperature distribution at various cure temperatures

From Figure 20 we can see that the outer plies of the EF7017 laminate experience very little exothermic effects with very small peaks present. This is because some of the exothermic heat generated on the outer plies of the laminate will be dissipated into the mould, reducing laminate temperature. Additionally, the outer plies of the laminate are already significantly cured by the time they reach their maximum temperature, thus most of the heat generated during cure has already been generated and not much of a peak is observed. However, this is not true of the internal plies where the cure state is much less than the outer plies due to thermal lag through the thickness of the laminate. This means that an exothermic peak from the internal plies does occur, with this being especially true of the laminates cured at a lower temperature. The 140°C laminate for example, has a much larger exothermic peak than the 160°C laminate as the internal plies of the 140°C laminate have cured much less when the cure temperature has been reached. These factors suggest that all EF7017 laminates, regardless of cure temperature are curing from the outside-in. Additionally, the exothermic peak is seen to be much lower than that of the EF3718 laminate which is due to the lower heat of reaction of the EF7017 resin system. This makes this resin ideal for rapid curing without excessive exothermic heat generation which has safety and residual stress implications.

From these results we can see that large temperature variations through the thickness of rapid curing laminates exist, with variations of around 100 °C being common. This is likely to cause high levels of residual stress as the DOC varies through the thickness of the laminates. This initial finding will be explored further by using embedded sensors in chapter 6. Additionally, this thermal data will be used to validate the thermal model employed in the numerical analysis in chapter 7.

3.5. Asymmetric bending

Asymmetric bending tests, as described in section 2.4.3.2, were carried out to investigate both the contribution of thermal expansion and chemical shrinkage to residual stress in rapidly cured composites and to validate thermochemical models which will be discussed in chapter 7. The methodology outlined by Kravchenko et al [126][127] was used to aid in the comparison of the results. Unsymmetrical unbalanced laminates or “bi-lamina strip” specimens of $[0,90_4]$ with dimensions of 158x25.4 mm were manufactured to induce large residual deformations which are simple to analyse. Initially, EF7017 bi-lamina specimens were placed in a cantilever jig to allow for free deflection without the influence of tool-part interactions. Thermocouples were placed at the cantilevered end (“edge”) of the specimen and in an oven to monitor the ambient oven temperature. This was to ensure that samples were cured in a way that was rapid enough to be representative of the true cure conditions and therefore residual stress experienced in an industrial setting. Thin CFRP cantilever mounts were manufactured to ensure that there was minimal heat flux from the specimen to the cantilever jig and to allow for curing to occur as rapidly as possible via convection in the oven. An example of a fully cured sample in the cantilever jig is shown in Figure 21 with thermocouple locations. The samples were placed into a pre-heated 170 °C oven with a glass window to monitor deflections during cure. The results of the thermal analysis can be seen in Figure 22 along with a sample cured in a 170 °C pre-heated hot press for comparison. The hot press manufacture method is described in more detail in chapter 6.

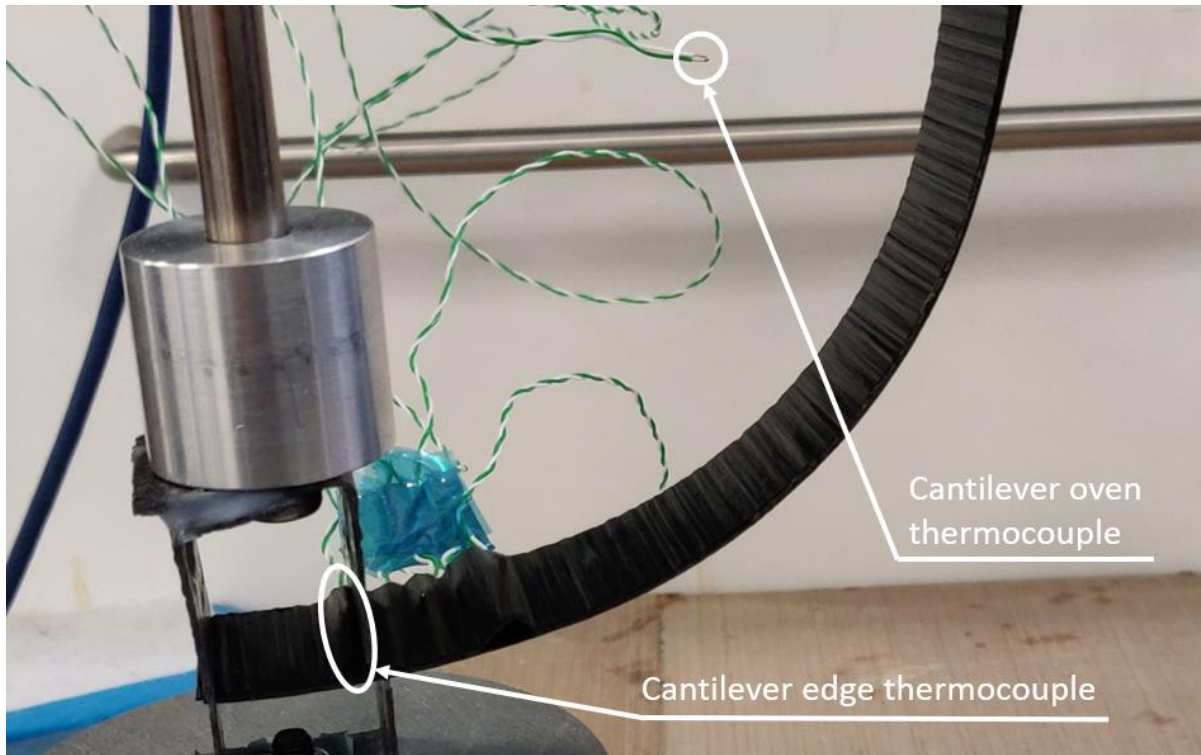


Figure 21: Asymmetric bending cantilever jig with edge and oven thermocouple

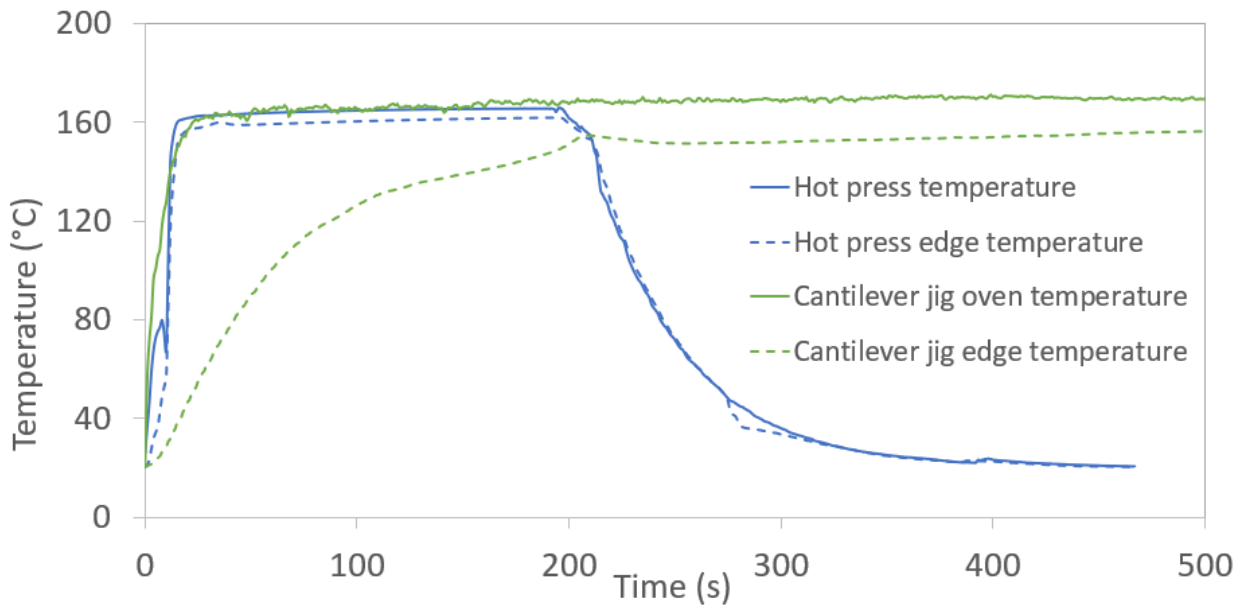


Figure 22: Thermal validation of EF7017 samples in asymmetric bending tests

As is evident from Figure 22 there is a significant lag in the temperature within the sample at the cantilever end when it is cured in a pre-heated oven. In fact, the hot-pressed control sample has been fully cured and removed from the press in the time it takes for the oven cured

sample to approach the ambient oven temperature and exotherm. Therefore, it is not possible to obtain a representatively cured sample of a rapidly cured composite using simple free convection heating and the methodology outlined by Kravchenko et al [126][127]. As the residual stress state and the end deflection in an asymmetric bending test is dependent on the thermal history that a laminate undergoes, it will not be possible to make any useful inferences from any deflection data gathered during this testing. Therefore, asymmetric testing will not be pursued further in this work

3.6. Dynamic mechanical analysis

With an understanding of the $T_{g\infty}$ of EF7017 an approximation of the relaxation behaviour of EF7017 during cure can be made. Laminates cured above $T_{g\infty}$ will experience much higher levels of relaxation during cure as the molecular mobility, and therefore ability to relax stress, greatly increase if the curing temperature exceeds $T_{g\infty}$. DMA applies a small cyclic load to a sample as it goes through a temperature ramp. The response can then be measured and $\tan(\delta)$ and G' can be determined. Either the peak of the $\tan(\delta)$ curve or the onset of the decline of the G' curve can be used to determine $T_{g\infty}$ with the definition varying depending on the application.

The $T_{g\infty}$ of EF7017 [0]_{II} samples cured at 180 °C and 140 °C in a hot press, as per the manufacturer's recommendations in Table 3, were determined using DMA testing. These temperatures were chosen as they will be used more later in this thesis and they incorporate the two most different curing conditions from those suggested by the manufacturer. Samples cured at 180 °C and 140 °C will be referred to as "Hot" and "Cool" curing respectively throughout the rest of this thesis. Cured samples were waterjet cut into dog-bones with gauge lengths of 25x4x2 mm. Samples were made with fibres orientated both longitudinally (long) and transverse (trans) to the gauge length direction to see if any difference in $T_{g\infty}$ measurements could be determined. Samples were then placed into an Anton Paar MCR502 rheometer with an Anton Paar CTD 450 heating chamber attachment and an oscillatory fixture was used. An oscillating frequency of 1 Hz with a strain amplitude of 0.01 % was used after a frequency scan at an isothermal temperature was conducted, confirming a linear G'/G'' response with strain rate. Additionally, the same settings have been used in the literature [195]. A temperature sweep ranging from 30 °C to 200 °C at a heating rate of 5 °C/min was then

performed for every sample configuration. A typical response (first repeat of a Hot transverse sample) of G' , G'' and $\tan(\delta)$ with thermal ramp is shown in Figure 23.

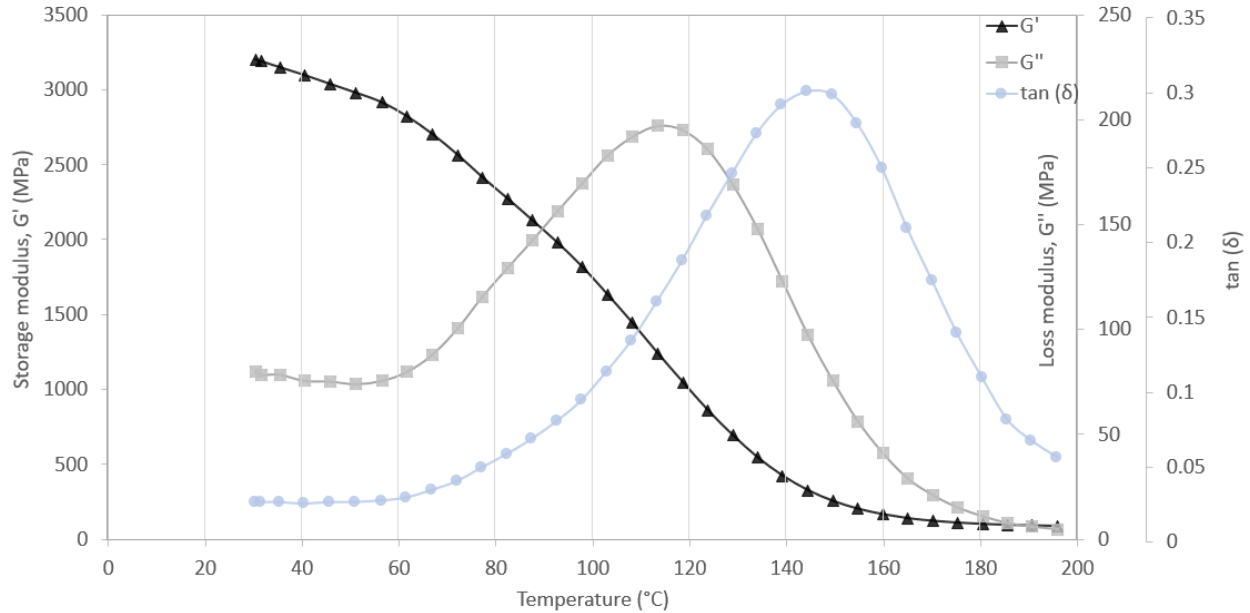


Figure 23: EF7017 DMA of a Hot transverse sample r1 (repeat one) with G' , G'' and $\tan(\delta)$.

A typical DMA response for a thermosetting resin going through glass transition is observed. The storage modulus begins to drop off sharply at around 60 °C and continues to decrease over the entire temperature ramp. The storage modulus begins to increase at around the same temperature until it reaches its maximum at around 115 °C. The $\tan(\delta)$, or the ratio between G'' and G' , is then seen to peak at around 150 °C in this case. The point at which glass transition occurs can be defined as any of these points [185] and indeed the glass transition point is more of a region rather than a singular point. However, in this work the T_g of the cured resin system will be defined as the peak of the $\tan(\delta)$ curve as this is commonly used in the literature [103][185] and is when the resin system will most readily relax residual stress and is therefore most relevant for this work.

To see more easily the effect of curing temperature and fibre orientation on the thermo-dynamic response in of EF7017 using DMA, $\tan(\delta)$ curves for all of configurations are shown in Figure 24. All tests were repeated three times (r1, r2 and r3) with the same sample without removing it from the testing rig. This was to determine the effect of further curing during DMA testing on the sample's thermo-dynamic response.

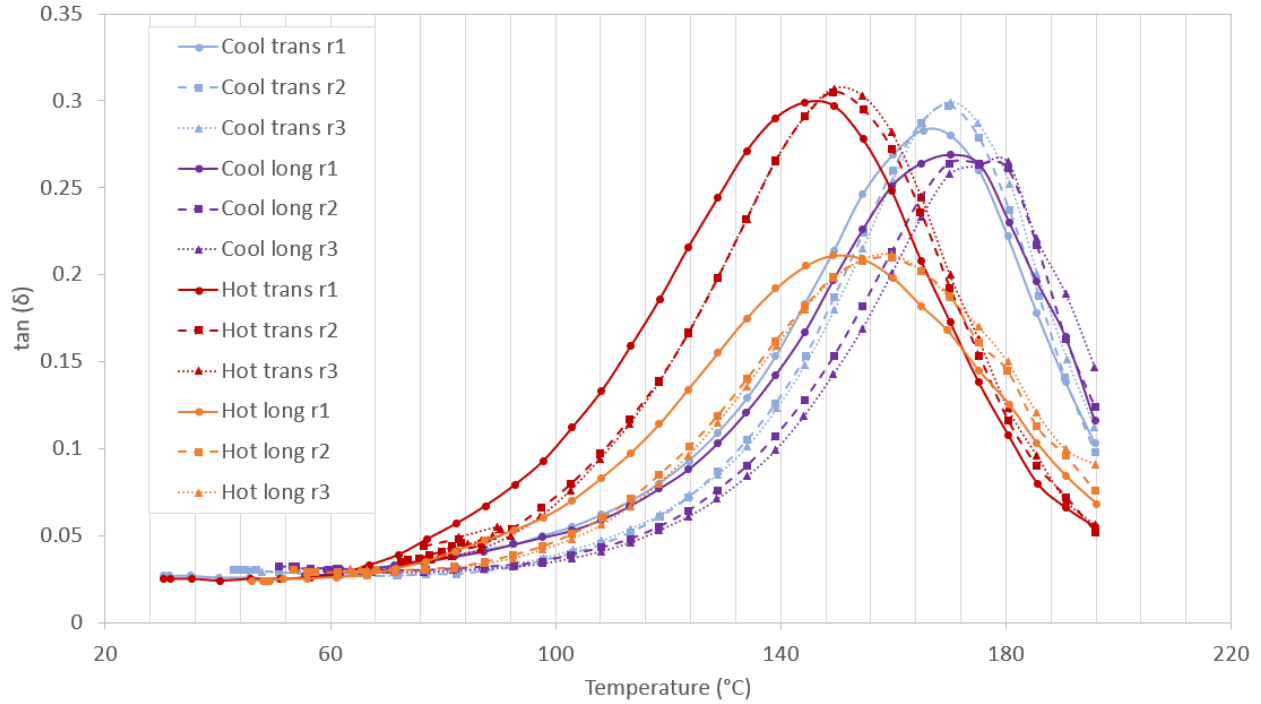


Figure 24: EF7017 DMA $\tan(\delta)$ response for all configurations and repeats tested.

Here, it can be seen that fibre orientation has little effect upon the measured $\tan(\delta)$ peak with samples having fibres aligned with the longitudinal axis (long) reporting only a slightly higher value on average. This is likely due to the increase in stiffness of the sample giving a slightly different mechanical response which is less dominated by the matrix properties. As this difference is small and this work is primarily interested in the matrix dominated response, values using the transverse samples will be used.

It can be seen that the curing temperature significantly changes the $\tan(\delta)$ peak (or T_g) with samples cured at a lower temperature having a higher T_g . This is thought to be due to the slower curing rate allowing for more, shorter, cross-links to be formed in the amorphous polymer chain network. Thus, increasing the amount of energy required for more polymer chain mobility and increasing the T_g of the “Cool” samples. This is also corroborated by the transverse three-point bending analysis conducted in chapter 8, where the “Cool” samples were found to be approximately 10% stiffer than the “Hot” samples. This is due to the more highly cross-linked polymer network of the “Cool” samples resulting in a stiffer resin matrix.

Additionally, running repeats slightly increases the T_g between repeat 1 and repeat 2, then remaining consistent between repeat 2 and repeat 3. This suggests that the first heating cycle

used in repeat 1 slightly increases the DOC of the samples and pushes the T_g higher. The samples can then be seen to be sufficiently cured for no further increase in T_g to occur in the subsequent heating cycles. As the T_g value for samples cured through a single heating cycle is the most relevant for this work, it is concluded that this T_g value will be determined from the first repeat. T_g values determined from the initial cure cycle will be defined as T_g^{cured} . However, this does show that these samples are largely cured. Therefore, the EF7017 T_g^{cured} values for the cured “Hot”, T_g^{hot} , and cured “Cool”, T_g^{cool} , case that will be used throughout the rest of this work have been found to be 145 °C and 170 °C respectively.

3.7. Conclusion

The sponsor of this research, Solvay, provided two “rapid-curing” prepreg UD laminates for this investigation, EF7017 and EF3718 which were specifically formulated for high pressure, rapid press curing applications. A resins system designed for use in the aerospace industry by Solvay, 5320-1, was also analysed with DSC to show a comparison between the rapid curing resin systems and a more traditional resin.

The aim of this chapter was to develop an understanding of the resin formulations under investigation and the key mechanisms that contribute to residual stress development in fibre reinforced composites. To that end the aim of this chapter has been met. The basic material parameters used throughout the rest of this work have been identified, a DSC analysis of the cure kinetics of each resin formulation has been undertaken and a thermal analysis of a curing laminate for both formulations has been made. From these data it was determined that the free-radical polymerising EF7017 resin formulation will be taken forward for further testing as it offers a high activation energy with low total heat of reaction which will likely cause large DOC gradients, and therefore residual stress, gradients in rapidly cured laminates. The DSC data determined here will be used throughout the rest of this thesis for further analysis and the thermal history data will later be used to validate the finite element model used in chapter 7. Additionally, it was found that the EF3718 formulation under investigation had safety concerns with excessive exotherm at large thicknesses and high curing temperatures and will not be used further in this work.

Asymmetric bending tests were attempted so that the contribution of thermal and chemical effects on residual stress could be analysed and used to validate the finite element analysis in chapter 7. However, it was found that it was not possible to achieve a representative curing scheme with free convection, thus this line of enquiry could not be continued. DMA tests were then conducted to determine the T_g^{hot} and T_g^{cool} of the EF7017 resin formulation as this will be critical in determining the build-up of residual stress at elevated cure temperatures later in this thesis.

Thus, a basic understanding of the EF7017 resin that will be used in the rest of this work has been established and key material properties determined. From this initial analysis it seems highly likely that the rapidly cured EF7017 laminate will generate large amounts of residual stress via the mechanisms previously outlined in section 2.3.

4. Interfacial Strain Transfer

4.1. Introduction

The aim of this chapter of the thesis is to investigate the validity of the assumption that there is always adequate strain transfer from the matrix to the embedded sensor for the case of rapid curing resin systems where there is predicted to be much higher levels of residual stress. In previous studies, [144][196][161][148][26] there is still some debate as to whether there is full strain transfer from the resin matrix to the embedded optical fibre sensor. It is not uncommon for the embedded sensors to de-bond from the matrix or for large voids to form at the fibre/matrix interface. Asperities like this will undoubtedly cause erroneous readings if the signal from the embedded optical fibre is assumed to be the true strain under all conditions. Several factors dictate the strain transfer at fibre/matrix interface: the bond strength between fibre and matrix, the modulus of the resin at the interface relative to the fibre modulus and any voids formed around the fibre. Therefore, multiple methods must be used to build up a full picture of the fibre/matrix interface of embedded optical sensors. Single Fibre Fragmentation Tests (SFFT) will be used to quantitatively investigate the interfacial bond strength of the fibre and matrix. Scanning Electron Microscope (SEM) images of fibre cross-sections and micro x-ray Computed Tomography (μ CT) volumes were examined to provide a qualitative view of the bonding around embedded fibres.

First, a SFFT protocol will be developed by using a more conventionally curing resin system and testing the applicability of using image processing software like Image J to aid in the analysis of strain and fibre fragment lengths. This addition to the traditional testing protocol will allow for contact-free strain and fragment length measurement which will aid in the analysis of highly stressed systems near to failure as will be found during rapidly cured SFFT. Secondly, SFFT was conducted in samples with varying levels of residual stress by changing the curing temperature, to investigate the effect of residual stress on the interfacial strength of both carbon/matrix and fibre optic/matrix bonds. Numerical work by Li *et al.* [197] has suggested that residual stress will negatively impact the strength of the carbon matrix interface. Therefore, validating that the fibre optic/matrix interface remains able to adequately transfer strain when high levels of residual stress are present will be vital for this

work. Lastly, SEM and μ CT will be used to qualitatively examine the fibre optic/matrix interface to look for voids or disparities around the interface which may cause erroneous strain readings from the embedded optical fibre. The aim and objectives of this chapter are summarised as follows:

Aim of the chapter:

- Determine the applicability of embedded fibre optic sensors for measuring strain in rapidly cured composite laminates.

Objectives of the chapter:

- Use SFFT to quantitatively compare and analyse the interfacial strength of carbon/resin and optical fibre/resin bonds in rapid curing resin systems with varying amounts of residual stress
 - Establish a useful and practical SFFT manufacture and testing procedure using a slow curing resin system which can then be applied to rapid curing systems
 - Investigate the effectiveness of using Image J software to measure strain and fragmentation length during SFFT, thereby allowing for contact free and instantaneous measurements.
 - Develop a methodology for manufacturing rapidly curing SFFT samples.
- Use SEM and μ CT to qualitatively evaluate the optical fibre/matrix interface in rapid curing resins with varying degrees of residual stress.

4.2. Interfacial shear strength testing theory

4.2.1. Introduction

When investigating the micromechanical interface of an embedded fibre in an epoxy matrix there are five techniques that are commonly used: Single Fibre Fragmentation Testing (SFFT) [198], fibre pull-out [199], microbond [200], three-fibre test [200] and fibre push-out [201]. In this study, only SFFT and fibre pull-out are considered as they are more common in the literature and allow for a varying cure profile of the matrix to be more easily implemented. Additionally, it is possible to use nano-indentation techniques to gain a high resolution understanding of the stiffness of the matrix, fibre and the interface [202].

4.2.2. Single fibre fragmentation

In Single Fibre Fragmentation Tests (SFFT) a single fibre is embedded in a matrix and is loaded in tension [41]. During loading, the fibre will fracture at a point randomly along its length as the strain to failure of the fibre, ϵ_f^{fail} is less than that of the strain to failure of the matrix, ϵ_m^{fail} . As the load continues to increase more fractures occur at other points along the length of the fibre by means of the shear lag effect transferring strain along the fibre. This process will continue, and more fibre breaks will occur until the fibre fragment lengths are too short for any more strain transfer to occur. At this point the number of fibre fragments will plateau and the saturation point is said to have been reached. This shown diagrammatically in Figure 25.

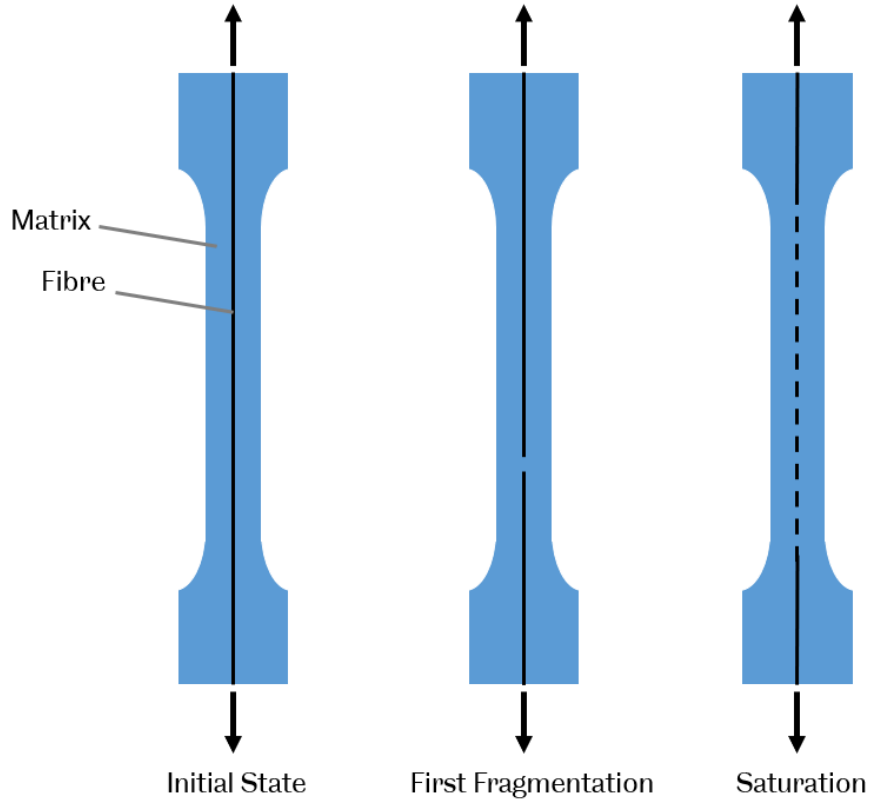


Figure 25: Single Fibre Fragmentation

The maximum length of the fibre fragments at the saturation point is known as the critical fragmentation length, l_c . In order to understand the forces acting on a single fibre, a free-body diagram of a representative embedded fibre segment can be drawn and is shown in Figure 26.

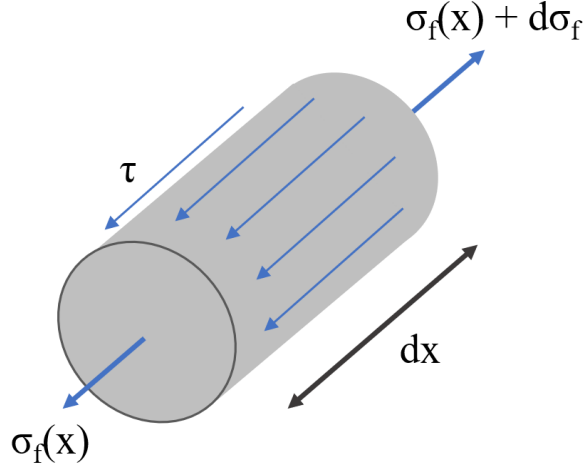


Figure 26: Free-body diagram of a representative embedded fibre segment.

Here, $\sigma_f(x)$ is the axial fibre stress which increases by $d\sigma_f$ over length dx with a shear force, τ acting at the interface. Applying an equilibrated force balance to the representative cell element gives Equation (14)

$$-\frac{\pi}{4}d_f^2\sigma_f(x) - \pi d_f \tau dx + \frac{\pi}{4}d_f^2(\sigma_f(x) + d\sigma_f) = 0 \quad (14)$$

where, d_f is the fibre diameter. Then, solving for $\sigma_f(x)$ gives Equation (15)

$$\sigma_f(x) = \frac{4}{d_f} \int_0^x \tau(x) dx \quad (15)$$

By assuming that there is a constant shear stress along the length of the fragment and that fibre stress is zero at the broken ends the maximum fibre stress, $\sigma_{f(max)}$ and consequently the maximum shear stress, $\tau_{(max)}$ is then given by Equation (16), the Kelly equation [203].

$$\tau_{(max)} = \frac{\sigma_{f(max)}}{2} \left(\frac{d_f}{l_c} \right) \quad (16)$$

If we assume that the applied shear stress is evenly distributed across all of the fibre fragments, then it must be true that any fibre length that is greater than the critical length will cause a fibre fracture. Therefore, the actual lengths of the fibre fragments must lie between l_c and $l_c/2$. If we then assume that there is a normal distribution of fibre length over this range then l_c can be determined from the average fibre length, \bar{l} , as is described by Equation (17).

$$l_c = \frac{4}{3} \bar{l} \quad (17)$$

Finally, by assuming that $\sigma_{f(max)}$ is equal to the ultimate tensile strength of the embedded fibre we can calculate the Interfacial Shear Strength (IFSS) of the fibre/matrix interface, $\tau_{interface}$ from the average fibre length, \bar{l} , as shown by Equation (18).

$$\tau_{(max)} = \frac{3\sigma_{f(UTS)}}{8} \left(\frac{d_f}{\bar{l}} \right) \quad (18)$$

Additionally, due to the viscoelastic time-dependent nature of epoxy, the sample must be allowed to relax after every step change in applied strain. For embedded carbon fibres the number of fibre breaks stabilizes after around 5 min [204]. Therefore, SFFT can be very time consuming as time needs to be allowed for the relaxation of the resin matrix after every small strain increment.

4.2.3. Single fibre pull-out

Single fibre pull-out was initially developed in the late 1960's [205] as a way of determining the bond strength between various reinforcing fibres and a concrete matrix. When investigating a resin/fibre interface, a fibre is embedded into a small drop of resin and a tensile load is applied to the fibre as can be seen in Figure 27.

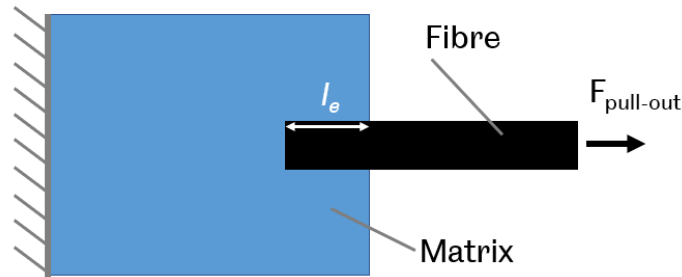


Figure 27: Fibre-pull out diagram

Several failure mechanisms have been suggested [206]. However, it is simplest to assume linear elastic failure, that the pull-out failure of the fibre is completely due to shear and that the force is evenly distributed over the length of the fibre. For these assumptions to be valid the embedded fibre length must be short enough to promote pure shear failure. With this assumption a standard force balance equation can be implemented to determine the interfacial shear stress, τ , and gives Equation (19)

$$\tau = \frac{P_{max}}{\pi d_f l_e} \quad (19)$$

where P_{max} is the debonding force, d_f is the fibre diameter and l_e is the embedded fibre length. This can then be rearranged to determine the minimum embedded fibre length needed so that failure is at the fibre/matrix interface and not failure of the fibre itself. This results in Equation (20)

$$l_e \leq \frac{\sigma_f d_f}{4\tau} \quad (20)$$

where σ_f is the yield strength of the embedded fibre. Using this relation, it becomes clear that this method is not well suited for fibres with small diameters. Assuming the use of a standard commercially available fibre, Toray T800H [207], with a tensile strength $\sigma_f = 5.49$ GPa, fibre diameter $d_f = 5 \mu\text{m}$ and an assumed typical interfacial strength of 50 MPa, then the minimum embedded length is only 137 μm . Clearly, there are practical challenges associated with this method and, as such, this method will not be used to investigate the interfacial strength of carbon fibres embedded in epoxy in this work. However, this technique may be viable for the testing of fibre optic sensors as they commonly have diameters of 195 μm , a tensile strength of 5 GPa [194] and a similar interfacial shear strength. This gives a calculated embedded fibre length of approximately 5 mm which is much less experimentally challenging.

It was concluded that due to the ability of SFFT to conduct both carbon/resin and optical fibre/matrix interface tests, SFFT would be the preferable technique for this work. This allows for a direct comparison of results rather than comparing IFSS values found from two different techniques with two sets of limitations and errors.

4.3. SFFT Methodology

Initially, all SFFT testing was conducted using carbon fibres as this would allow for saturation to be more easily reached as they have a lower ϵ_f^{fail} than optical fibres, approximately 2% [207][208] compared to 6% [194]. Additionally the quoted ϵ_m^{fail} of the slow curing resin being used is around 6-10% [209] and is initially unknown for the rapid curing resin. Thus, saturation of the optical fibre is not guaranteed before matrix failure.

Two resin systems were used during this testing. Firstly, a commercially available Easy Composites EL2 laminating resin [209], which is DGEBA based, with an AT30 slow hardener will be used for the “slow” or standard curing sample preparation. This has a manufacture’s

recommended cure cycle of 24 hours at room temperature and then 6 hours in an oven at 60 °C. Secondly, EF7017 was used for the “rapid” curing system which is a very fast curing unsaturated resin currently being developed by Solvay [183], with cure times between 1-8 minutes as discussed in section 3.2.

4.3.1. Slow curing SFFT materials/method

SFFT specimens are particularly difficult to prepare as they require the precise placement of a single tensioned fibre along the centre of a resin-filled dog bone sample. Feih *et al.* [198] outlined a testing methodology for SFFT which will be the initial basis for these experiments. Initially, the specimen dimensions suggested by Feih *et al.* were used but it was found that a gauge width and height of 2 mm left the samples very prone to breaking when releasing from the mould. Therefore, the gauge width was increased to 5 mm to make the specimens easier to handle. This will not impact the usefulness of the sample as the fibre will still fragment before the resin fails if the gauge width of the sample is increased. This male mould was machined from aluminium and sanded with 240 grit sandpaper to achieve a flat even moulding surface. After degreasing the mould, three coats of Easy Composites “Easy-Lease” release agent were applied to allow easy release. Then, Easy Composites AS40 addition cure silicone rubber was mixed with the included catalyst according to the manufacturer’s specifications and 2% w/w of Easy Composites red liquid silicone pigment was added to make it easier to see the fibres when placing them in the mould. The silicone was then degassed for 10 minutes and carefully poured on top of the male mould that had been surrounded in 3 mm thick polypropylene sheet to act as the rest of the mould. This was then placed back into the vacuum oven and degassed for a further 10 minutes before the vacuum was turned off and the mould was left to cure for 1 hour at 70 °C as per the manufacturer’s specifications. The female silicone mould was then released from the male mould and thoroughly cleaned with isopropanol and given three coats of Easy Composites “Easy-Lease”, following the manufacturer’s instructions. The finished male and female moulds can be seen in Figure 28.

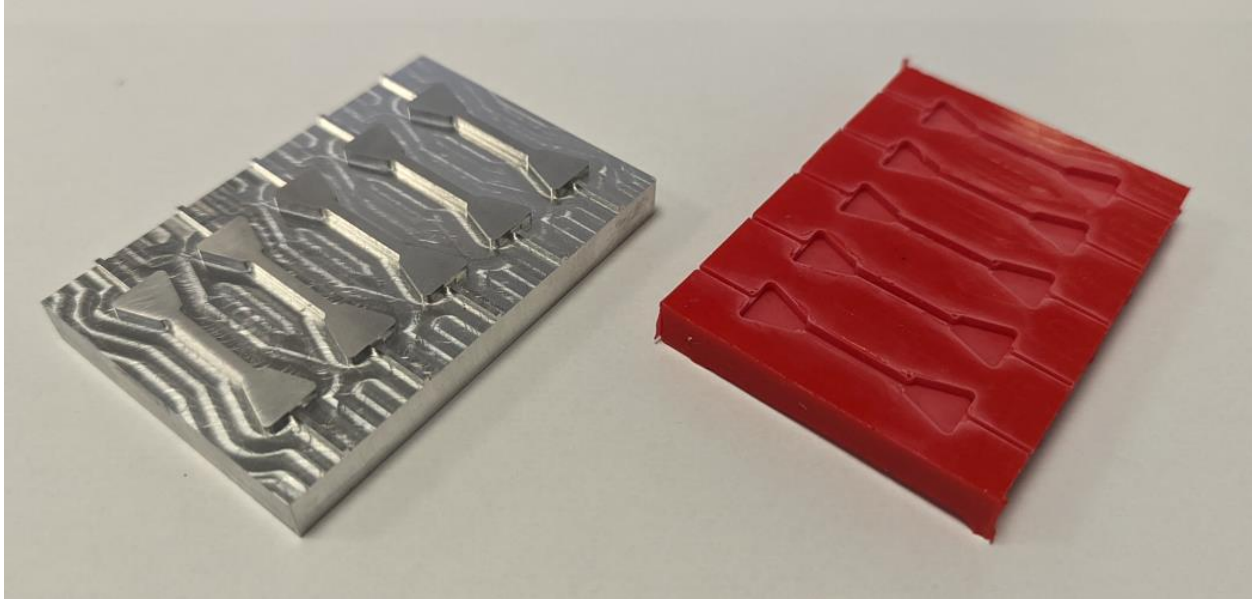


Figure 28: Finished male (left) and female (right) SFFT mould

Fibre extraction

Extracting single fibres for placement into the mould cavity was a significant challenge and little direction could be found in the literature. The following method was developed for the rapid and consistent extraction of a single fibre from a fibre tow. First, a length of 3k carbon tow was removed from the spool and fixed to a white table with masking tape to increase the contrast between the black fibres and table making it easier to single out fibres. An anti-static wrist strap was worn to reduce the static interaction between the fibres and the operator as this effect can be significant and makes it difficult to extract a single fibre. Using metal tweezers, the carbon tow was combed to separate out the tow into individual fibres which can then be carefully picked up by hand at one end and pulled in tension out of the tow. If the tweezers are used for this, they will shear the fibres, making it almost impossible to extract long fibres. Gloves are worn when handling the fibres for both health and safety considerations and to avoid contamination of the fibres with oils from skin. Next, it is critical to verify that each fibre extracted is a single fibre and not multiple fibres wrapped around each other. As each fibre has a diameter of approximately $5\ \mu\text{m}$ it is almost impossible to determine this with the human eye, so a USB microscope was used to aid with this. Figure 29 shows that even with the aid of a microscope it is difficult to determine if there are multiple fibres or a single fibre in a strand and therefore great care must be taken here.

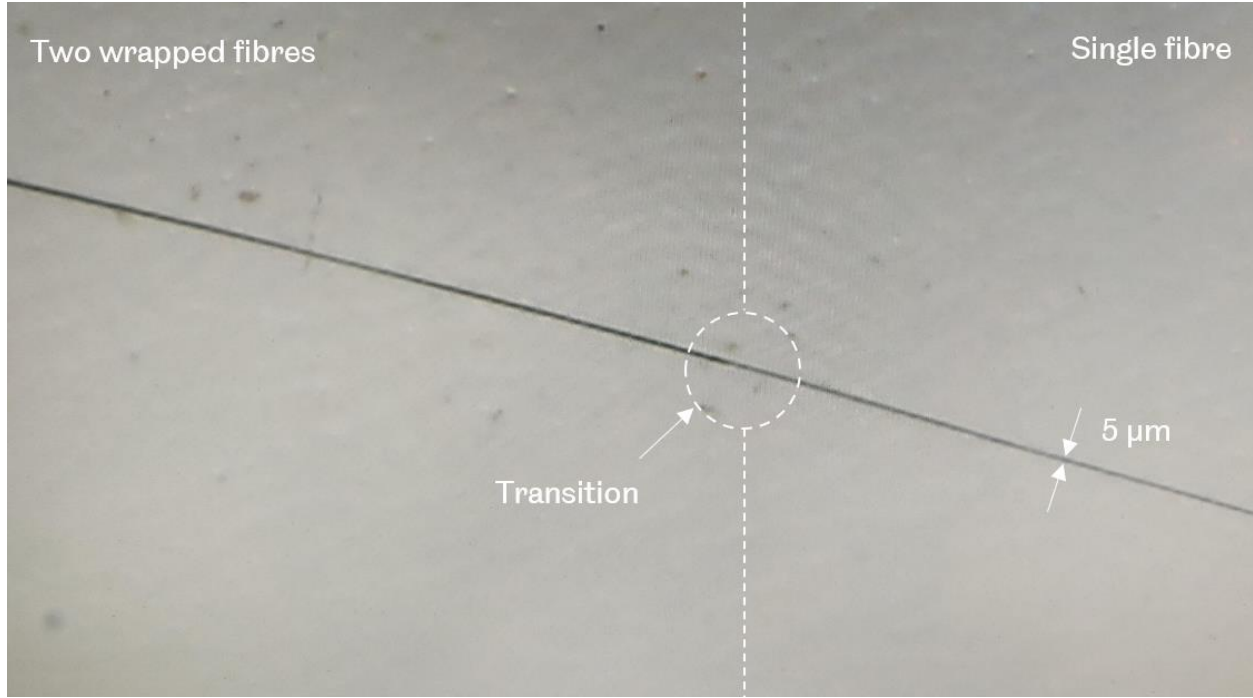


Figure 29: Single fibre separation under a microscope

After extraction, each fibre can be placed into a plastic container with double sided masking tape at each end to hold the fibres in place. This means the single fibres can be extracted ahead of time and then subsequently placed into the SFFT mould when required. This is especially useful as single fibre extraction can be done outside of a composites lab where air conditioning systems will cause the single fibres to move unpredictably.

Fibre tensioning

Using the same methodology outlined by Feih et al. [198] a pre-tension is applied to the fibres so that any thermally induced compressive stress, σ_f^{th} can be counteracted and alignment of the fibre can be maintained. Equation (21) shows a one-dimensional analysis of the field fibre stress, $\sigma_{f,\infty}$ in single fibre samples. This consists of the applied tensile stress, compressive thermal stress and the applied pre-tension stress, σ_{pre}

$$\sigma_{f,\infty} = \sigma_m \frac{E_f}{E_m} + \sigma_f^{th} + \sigma_{pre} \quad (21)$$

where:

$$\sigma_f^{th} = (\alpha_m - \alpha_f)(T - T_{ref}) \frac{E_f}{1 + \left(\frac{V_f}{V_m}\right)\left(\frac{E_f}{E_m}\right)} \quad (22)$$

and α_m and α_f are the CTE's of the matrix and fibre respectively, T is room temperature during testing, T_{ref} is the stress-free temperature (see section 2.4.3.2) and V_f/V_m is the volume fraction of the fibre and resin which in single fibre systems can be neglected and assumed to be zero. Therefore, using a CTE value of 72.5×10^{-6} (as used by Feih [198] et al in their work for a similar resin chemistry), for slow curing El2 samples there is a thermally induced compressive stress, σ_f^{th} of 848 MPa or 0.36% strain, ϵ_f^{th} assuming the fibre is behaving elastically. A 3 g mass is applied onto the ends of the fibre which results in a 0.32% pre strain to the fibre to largely counteract the compressive thermal strain on the fibre.

Thus, the 3 g washer was then carefully affixed at one end of fibre and then laid into the mould as shown in Figure 30. The 3 g washer was affixed to one end of the fibre by using cyanoacetate glue and masking tape. This combination is stable up to the maximum curing temperature of the specimens. The “slow” resin system was mixed with its hardener as per the manufacturer’s instructions [209] and degassed before being syringed into the mould cavity. This was then allowed to cure at room temperature for 24 hours and then post cured at 60 °C for 6 hours to achieve full cure. If the weights fell off during the initial 24-hour cure, the samples were discarded as it was assumed that the pretension had not been fully applied to the fibre. There was an approximately 30% success rate for samples to be produced with a properly pre-tensioned and aligned single embedded fibre.

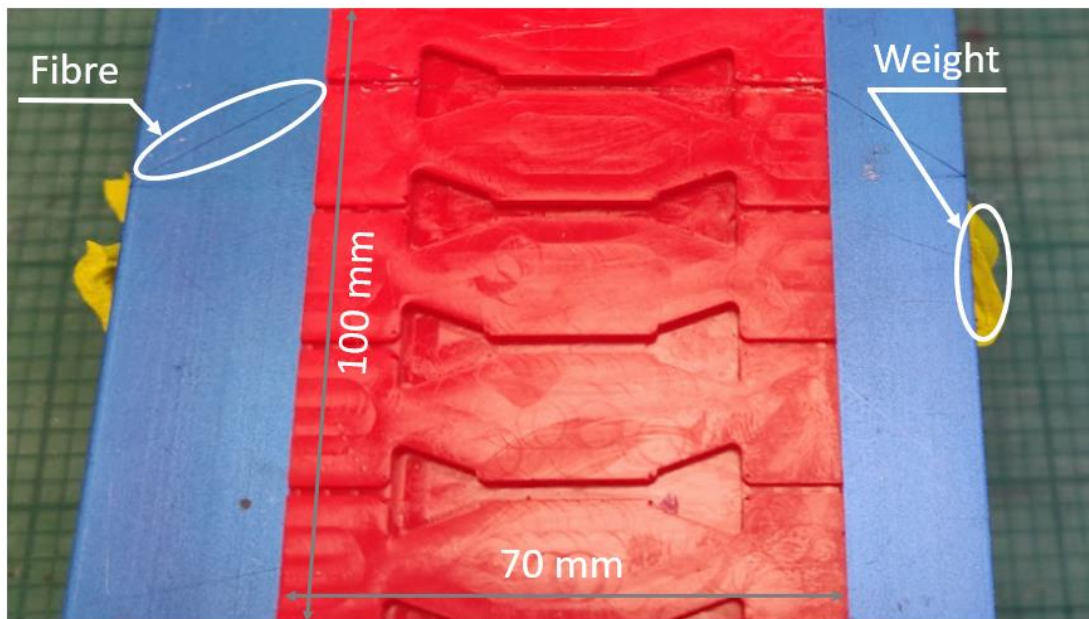


Figure 30: Placement of single fibres into the mould

After the samples have been removed from the mould and cleaned with isopropanol, they had any flashing removed with a scalpel and sandpaper. A scalpel was used to mark an approximately 10 mm long area on the gauge length. This both acts to mark the inspection area for fragmentation monitoring and as a reference point to take strain measurements off using Image J, as will be discussed in section 4.3.3. Just prior to testing the samples are coated in a thin layer of mineral oil to aid with the contrast of the image. A total of thirteen slow cured samples with pre-tensioned fibres were successfully manufactured. However, only six samples reached saturation, and these are the tests shown in the results.

4.3.2. Rapid curing SFFT materials and methods

The preparation of rapidly cured SFFT samples using the conventional silicone dog-bone approach proved to be challenging and had several limitations. The main challenge was to rapidly cure the SFFT specimens in a way that was representative of the manufacturer's recommended conditions. As these resin systems are usually cured using pre-heated hot plates which are then pressed into the part, it is critical to be able to have a high thermal conductance between the heat source and the laminate. Therefore, thermal contact and thus conductive heat transfer, are required to achieve a representative thermal ramp rate. Initially, a pre-heated block was placed on top of the filled silicone mould used in the standard curing resins. While this did result in a rapid temperature ramp within the sample it was found that this method caused air to be trapped within the sample, resulting in unusable specimens, as can be seen in Figure 31. Additionally, this method lacked control and any means of monitoring both the temperature of the mould and the sample itself making it impossible to make any inferences from the subsequent fibre fragmentation tests. Lastly, the rapid increase of temperature in the silicone moulds seems to have caused an off gassing of moisture from within the moulds resulting in micro-bubbles forming at the edges of the sample. While this could likely be mitigated by exposing the silicone moulds to a temperature of above 100 °C for an extended period and then leaving the moulds in a desiccator to remove as much moisture as possible, it was concluded the bubbles could be avoided with the use of an alternative mould.



Figure 31: Air bubbles in rapidly cured SFFT samples.

Rapid curing SFFT mould design

To address the above problems the mould seen in Figure 32 was designed and manufactured, full technical drawings can be seen in Appendix C. This steel mould design consists of four parts: the mould base, fibre collar, retaining collar and mould top. The design of the mould top incorporates cartridge heaters which were controlled by a Eurotherm 808 temperature controller using monitoring thermocouples embedded 1.5 mm from the mould surface at the in-plane centre of the mould and a safety thermocouple at the edge, thereby allowing for temperature control. Additionally, two thermocouples were located in the corresponding positions in the lower mould. This allows for the control and monitoring of the temperature input into the mould which can be used to help validate mould cavity temperature measurements. The fibre collar is seated on the mould base and has grooves which are used to allow for carbon fibres to be placed in tension through the mid-thickness of the mould cavity and to allow for k-type thermocouples to be placed inside the resin mould cavity. These thermocouples in the mould cavity provide an insightful direct measurement of mould cavity temperature during cure. The retaining collar is then placed on top of the fibre collar to act as a shim and create a corresponding 3 mm high mould cavity with fibres in the mid-thickness centre. At this point the mould can be filled with resin and the mould top placed on top of the whole assembly. An excess of resin is used when filling the mould cavity and slots in the mould top allow for excess resin to flow from the mould, thereby ensuring the mould is always fully filled. All parts of the assembly (excluding the mould top) are bolted together as they are mated to ensure resin does not leak out of the mould and the caps of the bolts are covered in

tape so as to ensure resin does not block them during disassembly. Additionally, threaded holes are incorporated into all of the mould components to allow for additional bolts to be threaded in during disassembly to act as a release mechanism. Using this mould, a 100x70x3 mm resin plaque is produced which has up to six tensioned fibres embedded into it. The individual dog bone specimens are then waterjet cut out, resulting in high quality samples with a single pre-tensioned fibre running along the longitudinal axis.

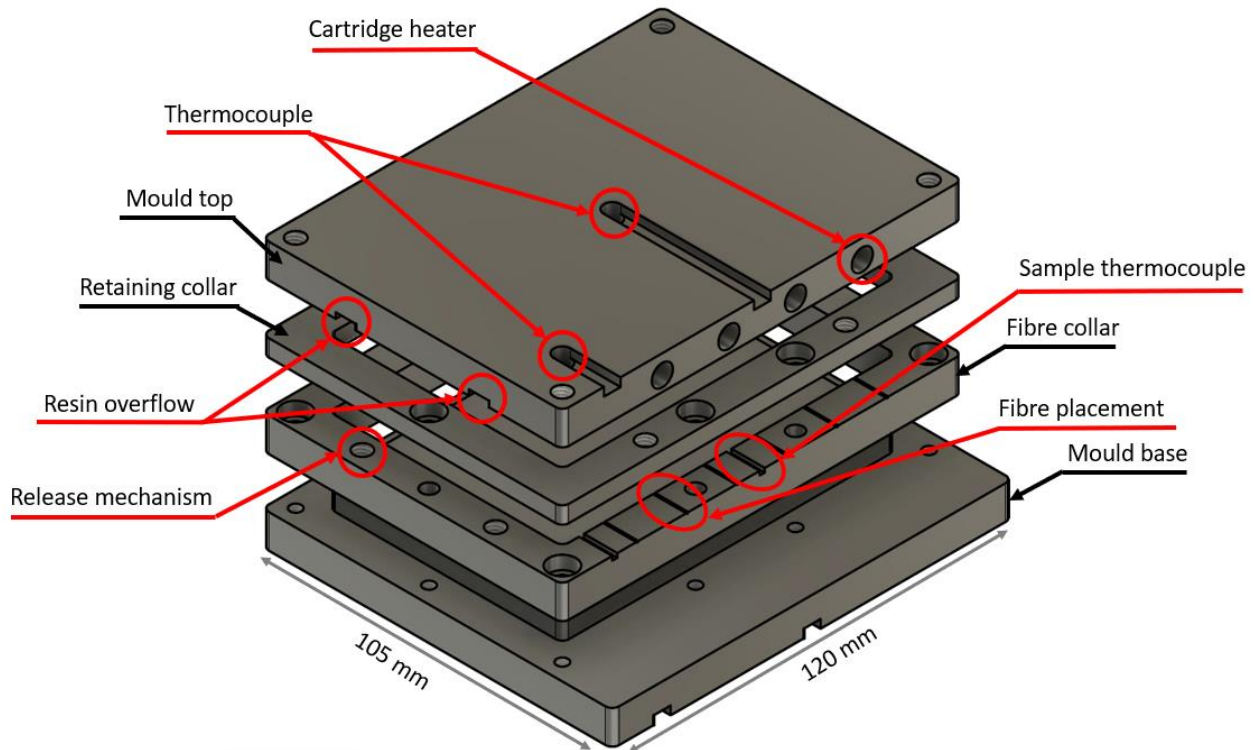


Figure 32: Rapid curing SFFT mould

Rapid SFFT sample preparation methodology

Solvay's EF7017 was used throughout for this testing regime to reduce the number of variables for a given cure condition. As this resin system is highly reactive it was shipped in the form of a pre-catalysed film and stored in a sealed bag at -18 °C when not being used. When needed, the bag was removed from the freezer and allowed to thaw completely before opening to reduce moisture absorption of the resin. The resin was then peeled off the film and placed into an 80 °C vacuum oven to degas for at least 30 minutes. An elevated temperature was required for the degassing stage as the EF7017 has a very high viscosity at low temperatures. Additionally, EF7017 is stable up to temperatures of around 110 °C and then begins to react

rapidly, as seen in section 3.3. Therefore, a degassing temperature of 80 °C was used to reduce the viscosity of the resin enough to allow it to degas without excessively curing it.

The Rapid SFFT mould was prepared and pre-heated and all moulding surfaces were treated with Easy Composites “Easy-Lease” release agent. Using 5 coats and allowing 10 minutes of drying between each coat for easy release of the resin plaque after cure. As shown in Figure 33, the fibre collar is then bolted down to the mould base and high temperature tape is placed along the outside edge of the fibre collar so that when the fibres are placed they do not instantly shear on the metal edges of the mould. K-type thermocouples are also added to the mould cavity to monitor the internal resin temperature during cure. Now, similarly to the standard curing sample preparation method, the fibres are very carefully placed along the length of the mould and held in tension with washers bonded onto the end of the individual fibres. 3 g washers are used which applies a 0.32% pre-strain to the fibres as discussed in section 4.3.1. It is often necessary to lay white paper onto the mould surface so the fibres can be seen while placing them into the mould. This can be carefully removed after the fibres have been placed. The retaining collar is then carefully bolted onto the fibre collar and mould base, heat proof tape is then placed over the bolt heads to avoid resin flowing into the bolt and making it difficult to release the mould. The lower mould assembly is then placed into the oven to preheat for approximately 1-2 hours or until the internal temperature of the lower mould (as determined by the lower mould thermocouples) reaches the desired temperature. This lower mould temperature is varied to induce various residual stress fields into the sample. The upper mould is pre-heated using the cartridge heaters array and the Eurotherm temperature controller. When the lower mould and upper mould have reached testing temperature and the resin has been fully degassed the lower mould is removed from the oven, the resin is poured into the mould cavity and the top mould is placed on top. The mould cavity, mould base and mould top temperatures are monitored using the embedded thermocouples and a Picolog TC-08 data logger. The samples are then allowed to cure as per the specifications outlined in Table 3 using the resin cavity temperature probe as reference. The cartridge heaters are then turned off and the mould is allowed to cool to room temperature and the plaque can be carefully removed from the mould. Upon vitrification of the resin the embedded fibres are thought to be fixed into position so if any washers fall off the fibres after this point the samples are still used.

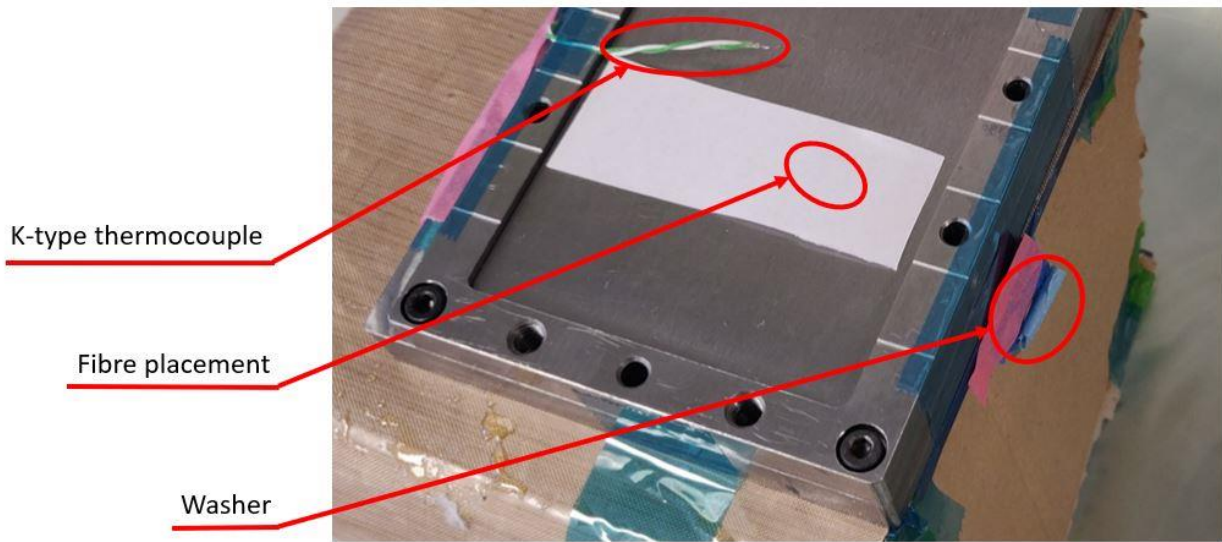


Figure 33: Fibre placement in rapid cure SFFT mould

If required, the plaques were sanded using the same procedure as outlined in the standard curing sample preparation methodology. The resin plaques with embedded fibres were then cut into dog bone samples with the fibres running along the centre of the gauge length using a Protomax waterjet cutter. Samples were waterjet cut instead of machined as it has been found that this can result in a superior surface quality and higher ultimate tensile strength, especially for CFRPs [210]. This resulted in samples that had well defined and clean edges reducing stress concentration sites and allowing for a representative ϵ_m^{fail} . An example of a rapidly cured resin sample can be seen in Figure 34 with the dimensions shown in Figure 35.



Figure 34: Rapid-cured SFFT sample

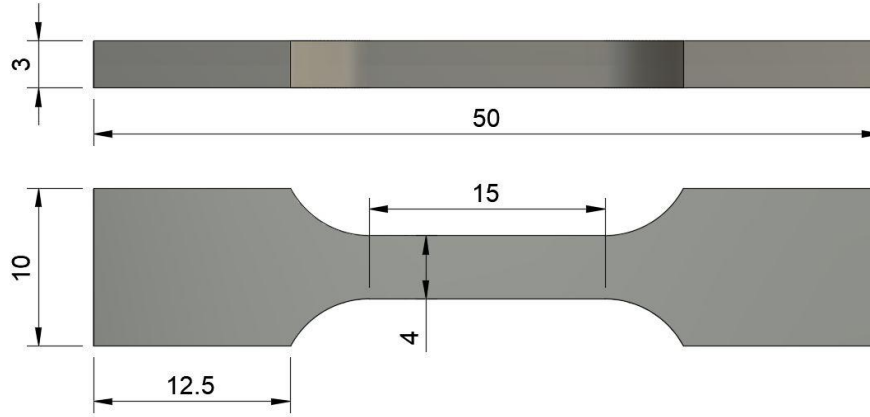


Figure 35: Rapid-cured SFFT sample dimensions in mm

Various upper and lower mould temperatures were used to vary the magnitude and distribution of the residual stress in the rapid SFFT samples. The aim was to provide as much variation as possible to be able to investigate any trends that emerged. The testing schedule shown in Table 6 was used to introduce a wide variety of curing conditions. As can be seen, the success rate of sample preparation for the rapidly cured samples is quite low. This is due to rapidly heating delicate, pre-tensioned carbon fibres, which fail during the curing process due to the introduced stresses.

Table 6: Rapid-cured SFFT samples testing schedule

Test	Samples with successfully embedded fibres	Upper mould temperature (°C)	Lower mould temperature (°C)
RC1	1	155	Room temperature (20°C)
RC2	1	160	Room temperature (20°C)
RC3	0	180	Room temperature (20°C)
RC4	3	140	85
RC5	2	160	85
RC6	2	170	90
RC7	2	180	100
RC8	0	200	100

4.3.3. SFFT testing methodology

Due to the small size of single fibre breaks it is necessary to use a linear cross-polarised photoelastic setup to determine the position of fibre breaks more easily and accurately. This allows for areas of high stress concentration around the fibre breaks to be illuminated making

fragments easy to detect [204]. Without this photoelastic setup it is almost impossible to detect fibre breaks along the 5 μm carbon fibres. Figure 36 shows the setup used in these experiments. A Tinius Olsen tensile testing machine with a 25 kN load cell was used to apply load to the sample. A light source was shone through a linear polariser which aligns the light along a single plane. This then travelled through a stressed birefringent sample which caused a retardation in the phase angle of the light passing through the stressed area of the sample. Another linear polariser perpendicular to the first then excludes all the light that has not had its phase angle retarded by the birefringent sample. Therefore, the image captured by the microscope and camera setup showed a completely black area where there was zero stress and light spots where there was stress, in this case at the fibre breaks. This photoelastic effect will be discussed further in section 5.1 when it is used to analyse the residual stress in cross-sections of rapidly cured resin. A Thor labs DCC154M 1.3 MP camera was used with an Infinity Photo Optical Company Infinivar microscope to capture images of the fragmentation for later processing.

A sample was securely clamped into the tensile stage and strain was applied in increments of 0.2%. After each strain increment was applied the sample was left for 5 mins to allow for any relaxation of the sample and additional fragmentation to occur [204]. After relaxation, an image was taken for later processing. This was done until no more fragmentation were seen for 4 consecutive strain increments or specimen failure.

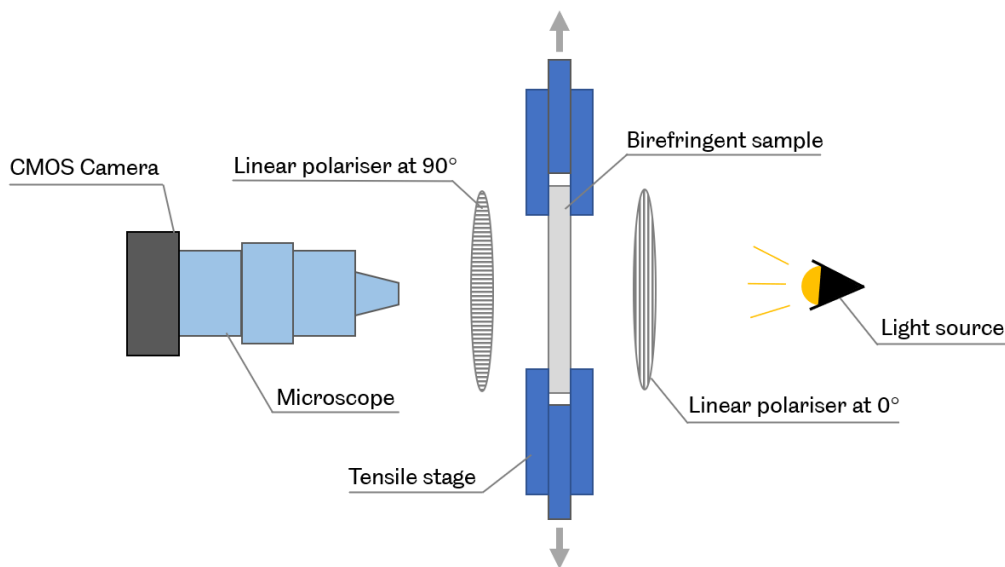


Figure 36: Single fibre fragmentation experimental setup.

Initial testing found difficulties with low extinction ratio polarisers, since it was found that these polarisers were unable to block out enough of the light that did not pass through the sample for there to be a high enough contrast in the final image. Therefore, it is suggested that polarisers with an extinction ratio in the order of 10,000:1 are used for the best results. An example image, using high extinction polarisers, of fragmentation at saturation seen along the sample length under polarised light is shown in Figure 37 and a close up image is shown in Figure 38.

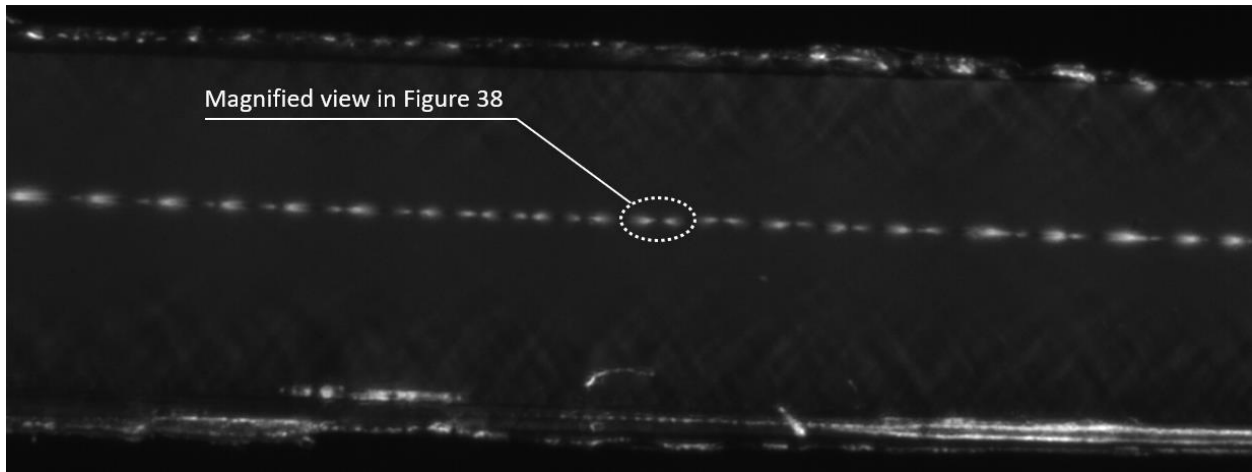


Figure 37: Example of fragmentation seen using polarised light

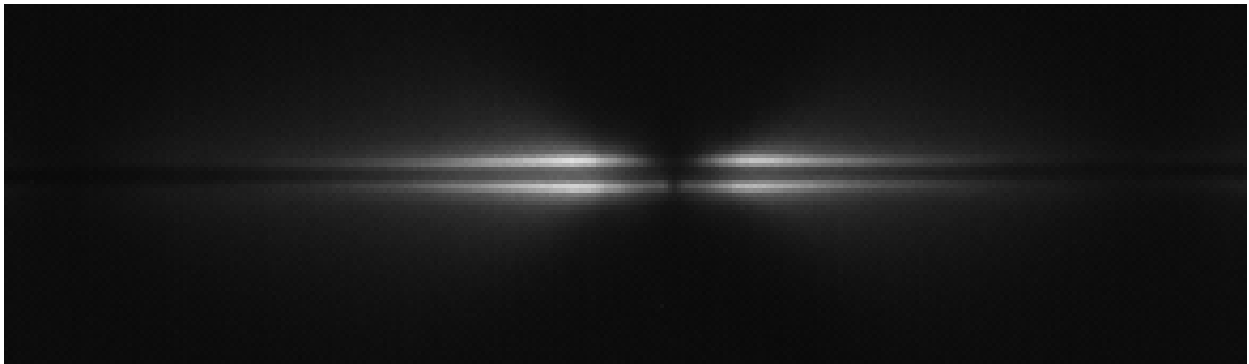


Figure 38: Close up of fragmentation seen using polarised light

Image J fragment length methodology

In this work, a novel method for measuring fibre fragmentation length is proposed. Traditionally, the camera viewing the breaks is set on a translational stage and the distance between the breaks can be measured by using the micrometer attached to the stage. However, one drawback with this approach is that the specimen must be held at saturation while taking

these measurements and this is often near specimen failure. This can mean that the specimen can break before all readings have been made. The alternative proposed method is to use an image processing software like Image J which allows for discrete measurements to be made in the post processing stage if a correctly calibrated image is used. First, a calibration image must be taken after the camera position has been fixed. Initially, for tests SC1-3 a 4 mm tall block was used as a reference length to calibrate the Image J images. However, for samples SC4-6 it was found that using a graticule slide worked well for this as it could be placed on the same plane as the sample and had sufficiently high resolution between line spacings. This was beneficial over the block as there were no parallax effects introducing error into the calibration. A graticule with 8 lines/mm was used when looking over a 10 mm gauge length. An example calibration image is shown in Figure 39. After this, pictures could be taken at any point during the experiment and post processed later, thus avoiding specimen failure before all desired measurements had been taken. In the post processing step, the global calibration was set using the calibration image and then lines can simply be drawn between the start and end points of the fragments and the distance between the points was returned. Images of the fragments along the gauge length of the sample were then taken at the end of each hold. The strain was then increased, and the process repeated. Using the Image J software package, the distance between fibre breaks was measured and recorded. The Image J method was done alongside the traditional micrometer on a translational stage method and the results are presented in section 4.4.

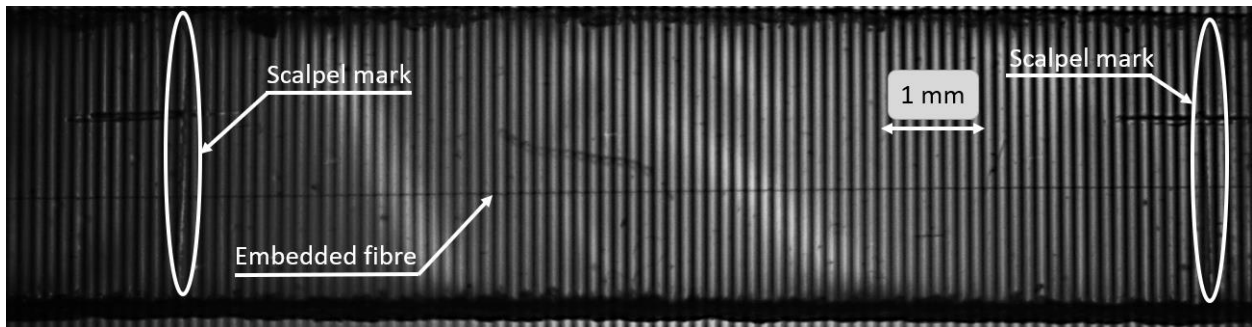


Figure 39: An example calibration image for Image J method using a graticule with 8 lines/mm

Additionally, Image J was proposed as a method for capturing strain data during SFFT. If proven effective this would allow for a contact free method of capturing accurate strain data without the need for additional equipment. The scalpel marks discussed in section 4.3.1, were used as reference points to track during the fragmentation testing. After each 5 min relaxation

period an image was taken which could later be manually analysed using Image J which was calibrated using the graticule as previously discussed. Therefore, a number of discrete strain data points were gathered and could be compared against the tensile testing bed position data and an Epsilon 3542 clip on extensometer placed on the gauge length of the SFFT specimen. This setup is shown in Figure 40.

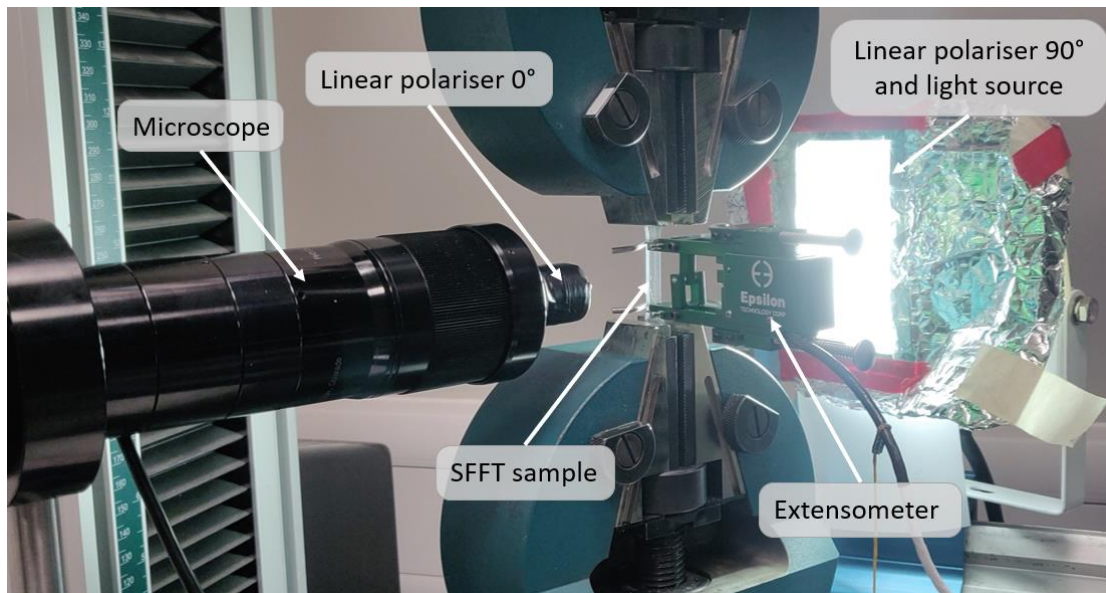


Figure 40: SFFT experimental setup with clip on extensometer, a slow cure example

4.4. SFFT results and discussion

Here, the results of SFFT of slow and rapid curing resins are presented and discussed along with the strain validation of the measuring techniques used. Additionally, SFFT fragmentation length data captured with a micrometer and Image J is analysed to test the applicability of Image J for measuring fragmentation length and strain during SFFT.

4.4.1. Strain validation

An example SFFT using the slow curing protocol is shown in Figure 41. Strain data captured using the bed displacement of the tensile tester, Image J and clip on extensometer is displayed to allow for easy comparison of results.

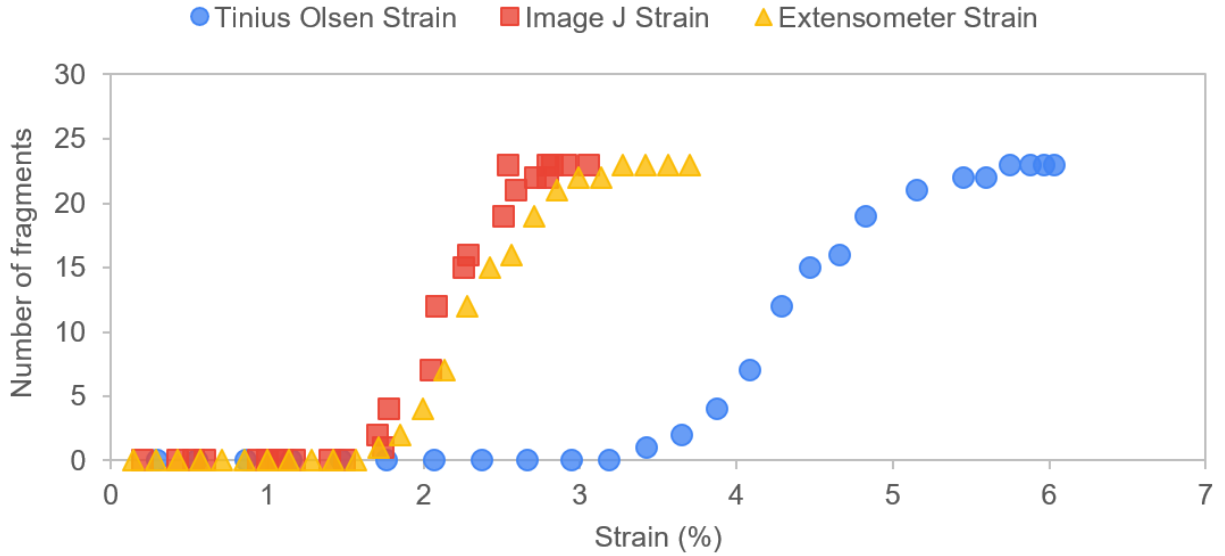


Figure 41: An example fragmentation vs strain plot for a slow cure (EL2) specimen. With strain measured using the tensile bed displacement, extensometer, and Image J method

It can be seen that strains reported by the tensile testing bed are around twice as high as those seen using the extensometer or image J. It is evident that values obtained from the tensile testing bed displacement would be misleading and could cause misinterpretation of the strain to failure and strain at onset of fragmentation of the embedded carbon fibre. This is due to the low stiffness of tensile testing machines and grips used which causes an overestimation of strain in the sample. This is also indicated by the under reporting of the stiffness values shown by the slope of the elastic region in Figure 42. When testing stiffer materials such as CFRP's or metals, the effect of the tensile testing rig's own deflection is proportionally much greater and so even more caution must be used when examining strain values derived from test bed displacements. From these data it can be seen that using machine displacement values is not a viable technique for monitoring the onset of fragmentation and failure in SFFT samples. Thus, external strain measuring solutions must be implemented.

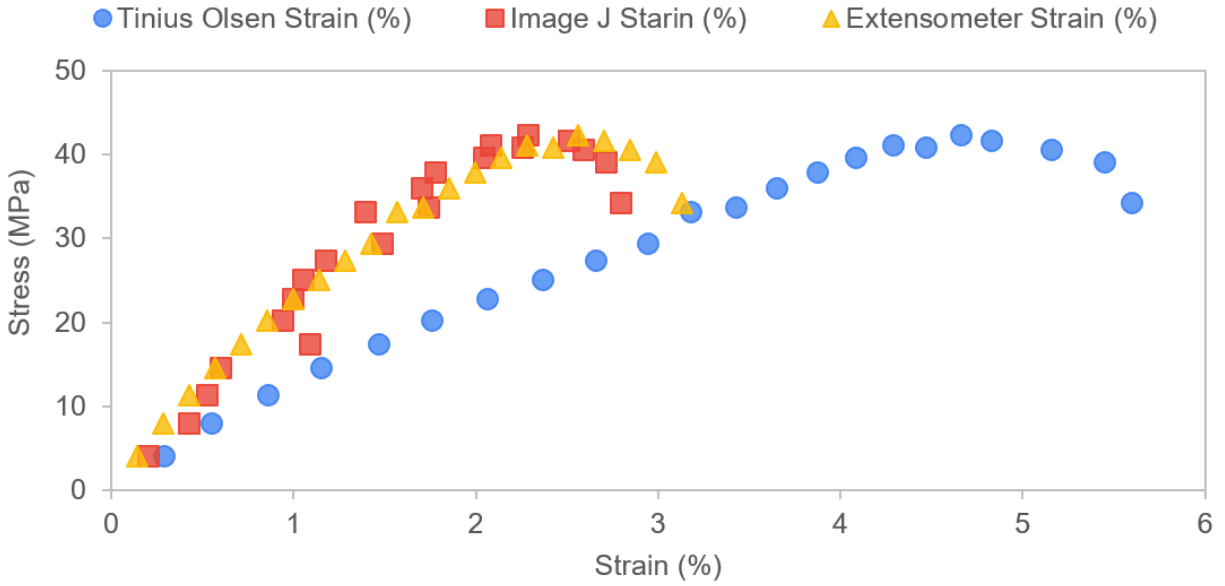


Figure 42: Stress strain graph validating Image J for measuring strain during SFFT of slow cure (EL2). With strain measured using the tensile bed displacement, extensometer, and Image J method

The stress strain graph from the same test shown in Figure 42 shows that there is mostly good corroboration between the extensometer strain value and that measured by Image J. There are a small number of Image J data points that deviate significantly from the extensometer reading and this thought to be due to user error when manually selecting the scalpel marks in the image processing step. Again, the strain derived from the tensile testing machines bed is shown to be an unsuitable method for measuring relatively soft materials like epoxy. It is widely agreed that clip on extensometers offer a high degree of accuracy [41]. Therefore, the good corroboration between extensometer and Image J shows the usefulness of Image J as a strain measuring technique in SFFT. Across all testing of the slow curing resin systems there was an average difference between the Image J and extensometer readings of 0.02% and 0.07% for fragmentation onset strain and failure strain respectively. This equates to a 1.8% and 3.0% percentage difference respectively in the Image J reading. This difference is small enough for Image J to be considered a viable alternative to an extensometer in terms of accuracy but offers a non-contact alternative. As will be discussed in section 4.4.2, clip on extensometers have the potential to cause premature failure. Thus, Image J strain data will be used for further experiments.

4.4.2. Slow cure

The results of the SFFT in slow curing resin systems are shown in Figure 43. The number of fragments per millimetre of fibre length vs the applied strain as recorded by Image J are plotted to aid in analysis. Here, the number of fragments has been normalised as some of the initial tests only observed fragments along a smaller length of fibre (4 mm instead of 10 mm). While this difference does not affect the value of interfacial strength calculated, as this is based on fragmentation length and not the number of fragments, this normalised data allows for easier visual comparison between tests.

From the asymptotic nature of the curves seen in Figure 43 it is evident that saturation has been reached. Therefore, measurement of fragmentation lengths can be made for IFSS calculations as described by Equation (18).

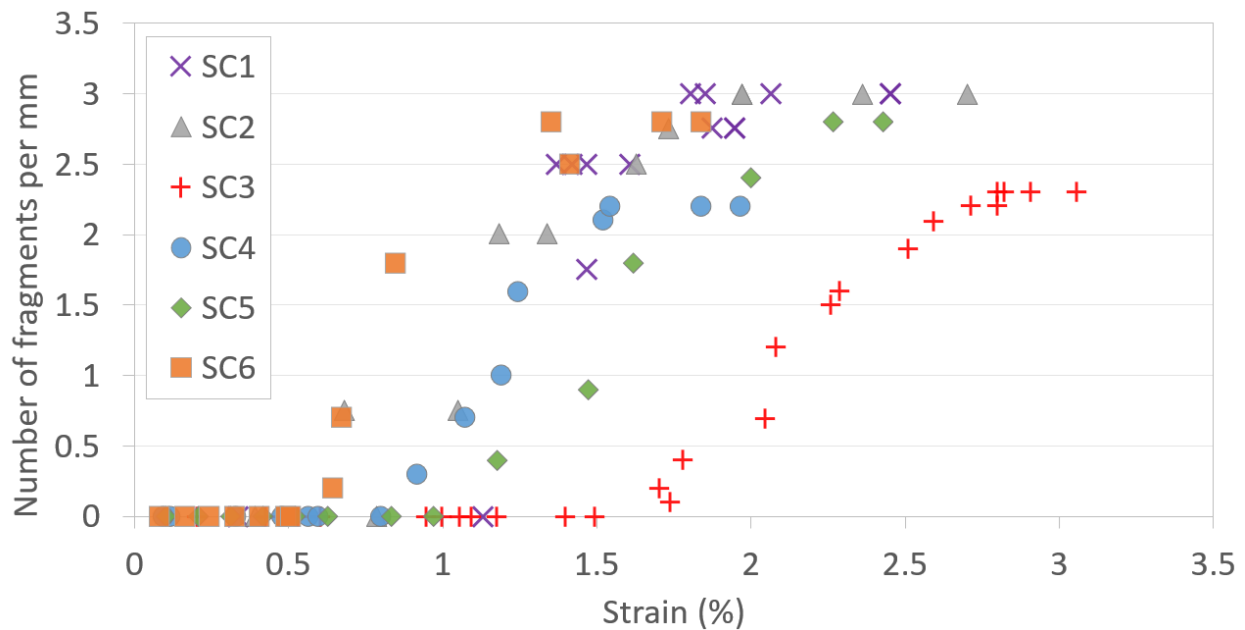


Figure 43: SFFT fragmentation with applied strain as captured by Image J for six repeats, SC1-6.

Figure 43 shows a wide range of fragmentation onset strains from around 0.6% to 1.7%. With the full results detailed in Table 7. While it is to be expected that there is some degree of variation in initial fibre failure as this is a flaw-driven failure mechanism, this variation is quite large. This suggests that either the manufacturer's quoted ϵ_f^{fail} value of 1.9% for the embedded fibre is over reported or that there is an additional tensile load that is produced either during manufacture or testing that is not being accounted for. This additional tensile

load in the fibre could be caused by an over pre-tensioning of the embedded fibre, which should account for a 0.32% pre-strain, as discussed in section 4.3.1. Or, from unaccounted for pre-loading of the tensile stage during SFFT which was zeroed after applying a clamping force on each specimen. However, for this current work the onset of fragmentation is not the primary phenomena under investigation and if saturation has been reached then it will be possible to make fragmentation length measurements and calculate interfacial strength.

Table 7: Onset of fragmentation and sample failure for slow cured SFFT specimens as measured by Image J

Test	Cure	Onset of fragmentation, ϵ_f^{fail} (%)	Failure, ϵ_m^{fail} (%)
SC1	24h RT/6h 60 °C	1.47	2.45
SC2	24h RT/6h 60 °C	0.68	2.70
SC3	24h RT/6h 60 °C	1.74	2.82
SC4	24h RT/6h 60 °C	0.91	1.97
SC5	24h RT/6h 60 °C	1.18	2.43
SC6	24h RT/6h 60 °C	0.65	1.84
Average		1.10	2.37
Standard deviation		0.40	0.36

Another key feature of note in Figure 43 and Table 7 is the failure strain, ϵ_m^{fail} of the various samples. This varies significantly from around 1.8% strain to 2.8% strain while the manufacturer’s quote 6.0-10.0% strain at failure [209]. To identify the cause of this discrepancy an analysis of the failure surface of the SFFT specimen was undertaken and is shown in Figure 44. It is evident from the rough edges and striations seen on the fracture surface that this sample has failed brittlely and suddenly. There are three potential initiators of this premature failure, first the samples could be misaligned in the grips causing non-uniform loading and stress concentrations. Secondly, the Epsilon extensometer grips the specimens with sharp blades, which again could have led to premature crack formation. In some specimens’ failure did occur around these blades. Correction fluid was applied to the contacting edges to mitigate this but did not have a noticeable effect. Lastly, the resin matrix may have been out of date or poorly cured, leading to a change in the predicted material response. However, manufacturer’s instructions regarding storage and cure were adhered to, so this latter reason is considered unlikely.

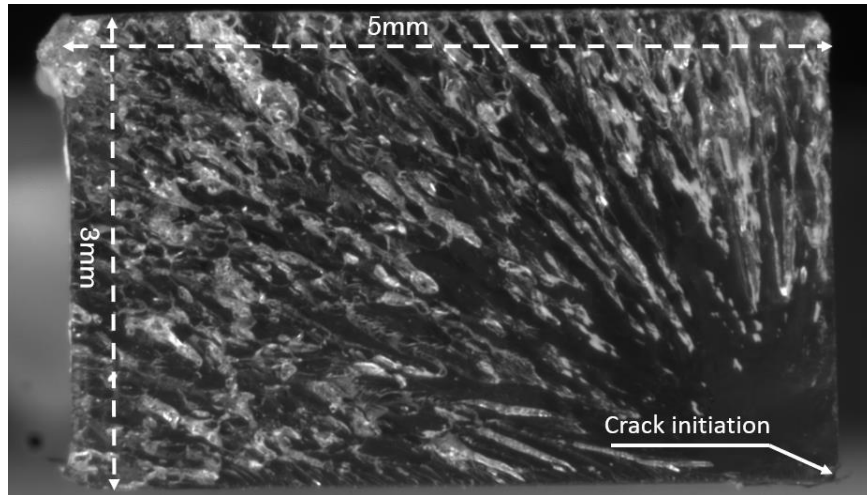


Figure 44: An example cross-section of the failure surface of EL2 SFFT test

Fragmentation length using Image J validation

In addition to the fibre matrix interface testing, an analysis into the applicability of using Image J image processing software to determine fragmentation length during SFFT was conducted. Figure 45 shows the fragmentation lengths of test SC5 as recorded with a more conventional micrometer translational stage and as recorded by Image J in the method outlined in section 4.3.1. Figure 46 shows the same data plotted on a histogram along with a Gaussian distribution curve for both micrometer and Image J readings.

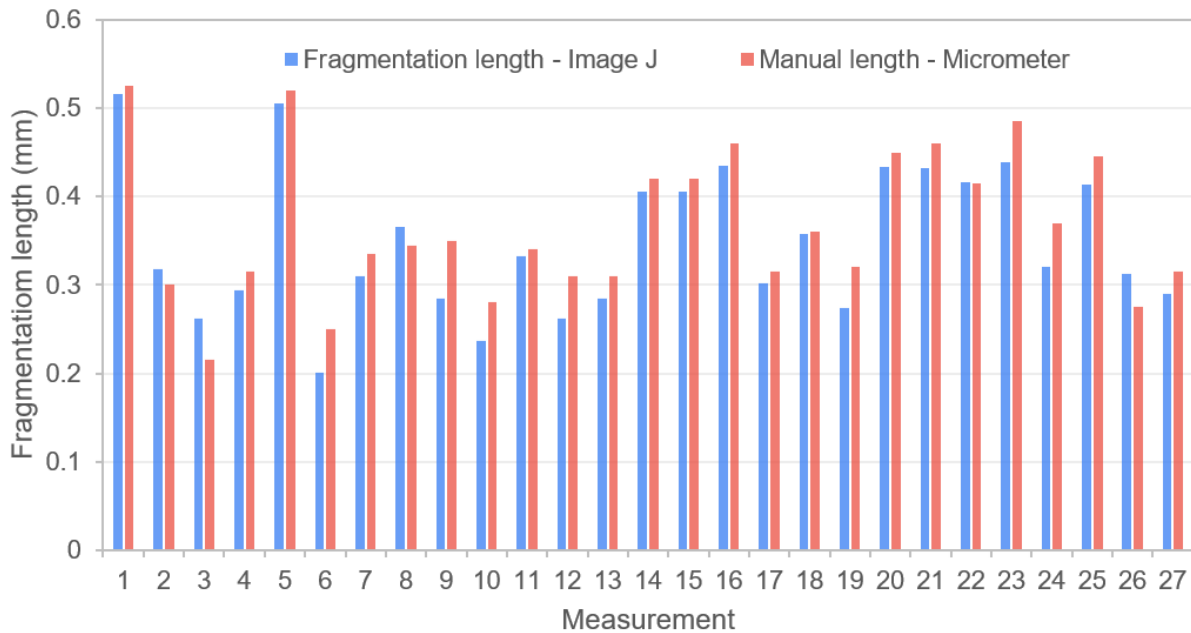


Figure 45: Fragmentation length of EL2 SFFT test SC5 as measured by micrometer and Image J

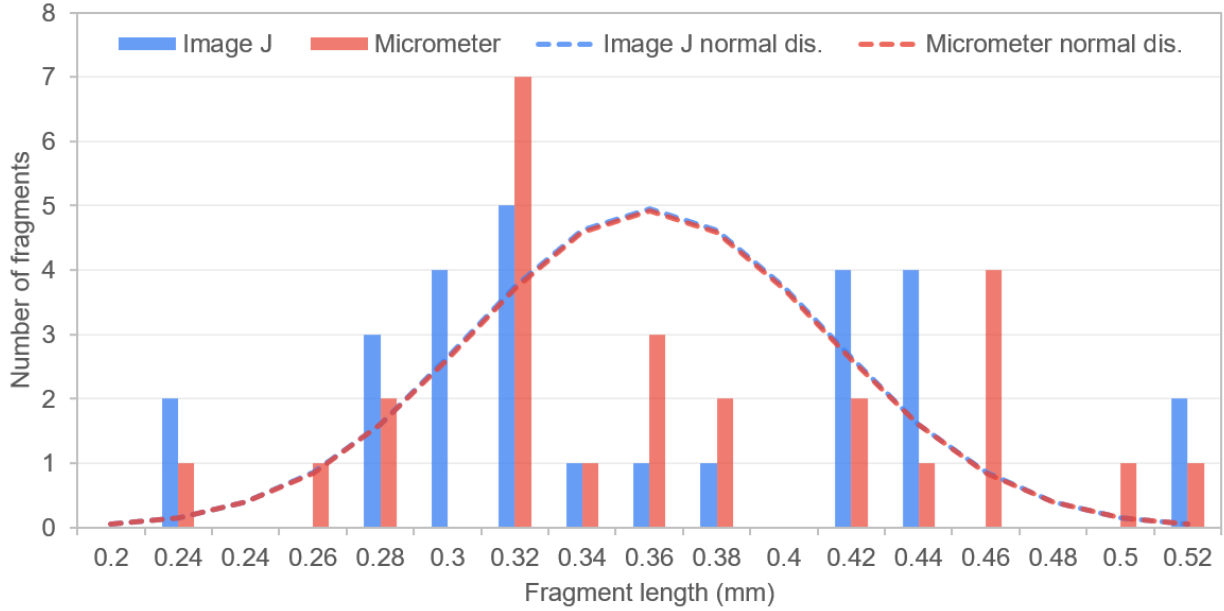


Figure 46: A histogram of fragmentation lengths seen in test SC5 with a Gaussian distribution

For SFFT tests, SC5 and SC6, Image J and a micrometer were used for the fragmentation length measurement. It was found that using Image J to calculate IFSS led to an underreporting of 5.0% and 1.8% for each test respectively compared to the micrometer. One reason for this discrepancy is the micrometer values were taken from the centre of the fibre break and not from the end of the fragment. This was due to the difficulty in finding the exact end of the fibre with the low-resolution camera setup. The camera used in this testing had a resolution of 1.3 MP which, when combined with the microscope optics and keeping the 10 mm gauge length in frame, resulted in the embedded carbon fibre appearing approximately 3 pixels wide when zoomed in. This is shown in Figure 47 with an approximation of the carbon fibre's morphology. However, when using the micrometer, measurements had to be made with a less zoomed image, as seen in Figure 37, which led to this discrepancy.

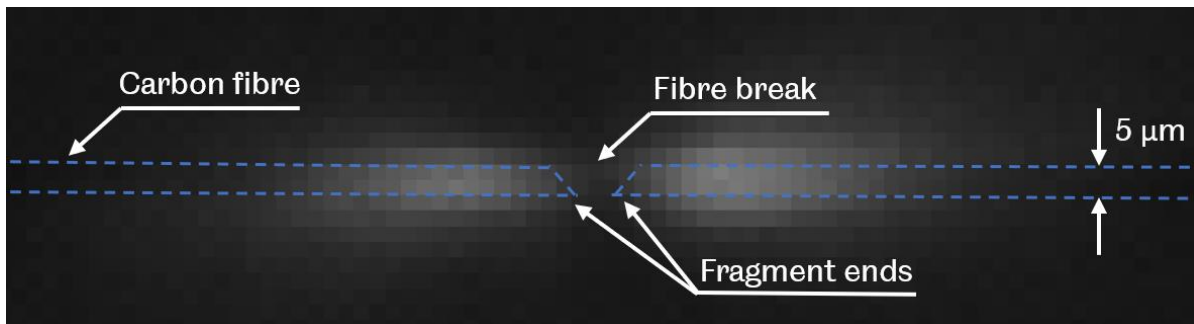


Figure 47: Zoomed image of single fragment captured during SFFT test

However, the Image J technique is preferred in this work as many samples failed very close to saturation of the sample. Often samples would fail while fragmentation measurements were being recorded using the micrometer, nulling the entire test. Image J allows for an instantaneous capture of the fibre fragments at saturation which can then be analysed later. As SFFT tests can take around 6 hours to complete due to the need to allow for relaxation time, not to mention sample preparation time, the use of Image J increasing the chance of a successful test is important for this work.

IFSS results for slow cure SFFT samples

Using the relationship described in Equation (18) and the material properties outlined in Table 4, the IFSS of the fibre matrix bond is calculated from the measured fibre fragmentation length and plotted in Figure 48.

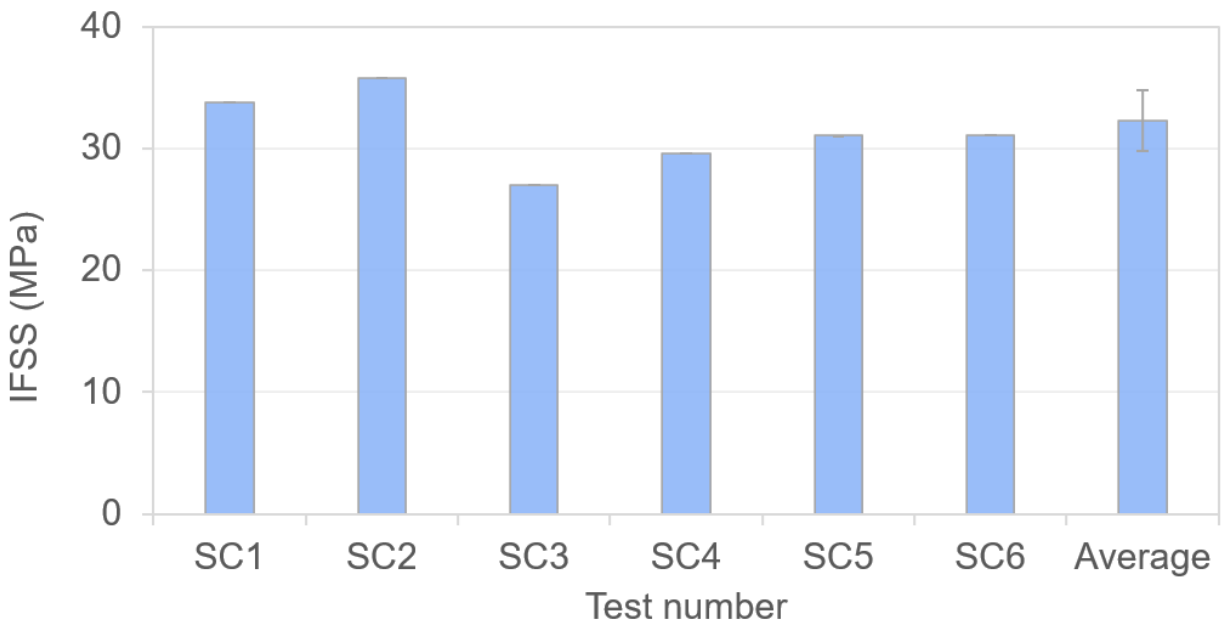


Figure 48: IFSS data of slow curing resin system using SFFT

Figure 48 shows the interfacial strength of the fibre matrix bond determined by SFFT of EL2 resin to carbon fibre. The results of six tests that reached saturation are shown and the average of the tests is also indicated with an error bar marking the 1σ standard deviation of all six tests. An average IFSS value of 32.3 ± 3.1 MPa was calculated which has a favourably low standard deviation when compared to other values in the literature. For example, work by Ramirez et al. [211], found IFSS values of 35.3 ± 12.9 MPa for the T700/epoxy SFFT tests

conducted. However, this scatter is to be expected in SFFT due to several factors. Firstly, as previously discussed fibre fragmentation is a fibre flaw driven process meaning that there will inevitably be some distribution in the way this occurs from sample to sample. Some studies [212] have implemented the Weibull weakest-link theory to establish a relation between the fibre length and the fibre strength. However, this is outside the scope of this work and the fibre strength will be assumed to be constant at all lengths investigated and to be as quoted by the manufacturer. Additionally, for all testing it was assumed that the embedded fibre diameter was constant and as reported by the manufacturer. While the carbon fibres used were sized and can be considered to have a reasonably constant diameter, measuring the diameter of every fibre using a microscope could be one way of increasing the accuracy of the results. Secondly, the length calibration technique was altered during the testing of the slow curing samples. Initially, a 4 mm reference block was used to calibrate the Image J dimensions for test SC1 to SC3. However, this was changed to a graticule, as outlined in the methodology, for specimens SC4 to SC6 as it was believed that this would decrease the percentage error which would occur from a poorly placed calibration line. Using reference blocks instead of a graticule meant there was the potential for parallax error to be introduced as the reference blocks had significantly more depth than the graticules. As IFSS values recorded in these experiments are entirely dependent on the measured average fibre length, any changes in the absolute fragmentation length values could have a large influence on the quoted values. However, all Image J analysis was repeated, and the secondary analysis agreed very well with the initial values. Additionally, as previously discussed, the calibration method was then changed to using graticules to eliminate this potential error for the rapid curing samples. Lastly, in test SC3 there was some off axis loading observed which was evidenced by the fragmentation stress fields not being parallel to the sample, as seen in Figure 49.

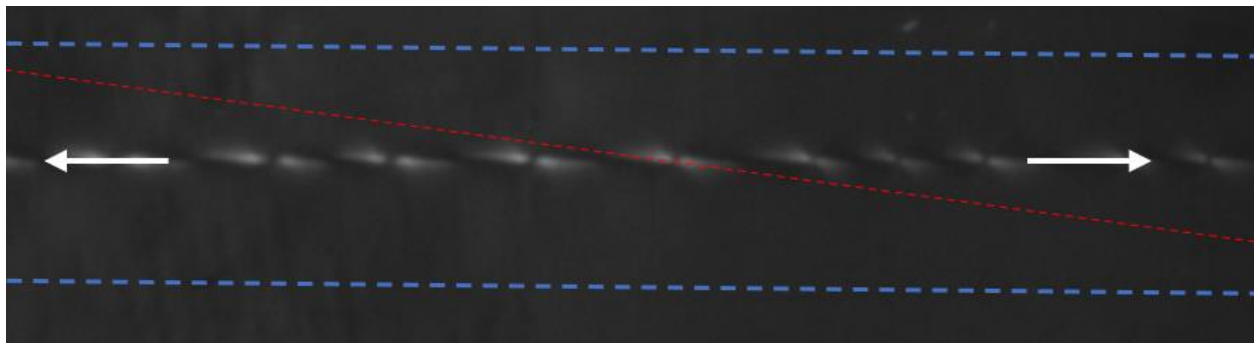


Figure 49: Off-axis fragmentation stress field in SFFT SC3

This off axis loading condition could be causing additional shear stresses to be applied to the fibre fragments which in turn could be causing strain to not be fully transferred along the fibre as the simple model used predicts. Thus, the average fragmentation length observed at saturation is lower than expected, resulting in an under-reporting of the IFSS value. Therefore, test SC3 has been removed from the average IFSS for overall slow cured tests. However, this test seems to be an anomaly and without further investigation this hypothesis cannot be verified.

The average IFSS value of 32.3 ± 3.1 MPa is lower than some of the other values found in the literature which range from around 35-60 MPa [211][213][214][215]. This is likely due to the higher fibre strength values used in the literature, ranging from 5-11 GPa. The fibres used in this work are assumed to have a constant fibre strength of 4.4 GPa. In fact, all the highest IFSS values seen in the literature come when the highest strength fibres are used. For example, work by Ramirez et al. found that fibre fragments with a l_c of 0.86 mm results in an IFSS value of 35.3 MPa. Whereas this relatively long fragmentation length would result in an IFSS value of 16.8 MPa if a fibre strength value of 4.4 GPa was assumed, as it has been in this work. This discrepancy is due to this current work using the manufacturer's quoted fibre strength values and works done in the literature have applied a Weibull distribution to the fibre strength values. This relation uses a Weibull factor to describe statistically how decreasing fibre lengths will increase the apparent fibre strength as less flaws are present in the smaller fibre length [216]. In the case of work by Ramirez et al. this increases the fibre strength value from 4.40 to 7.97 GPa. Therefore, when observing very small fibre lengths, like those seen in saturation in SFFT testing, <0.5 mm, very high values of fibre strength are seen due to the lower probability of flaws being present in that section of the fibre. This relation is shown in Equation (23), where σ_f is the fibre strength at the critical length, σ_{UTS} is the mean tensile strength of the fibre as measured by tensile tests, l_c is the critical fibre length in the fragmentation tests, l_0 is fibre length used in the tensile tests and ρ is the Weibull factor.

$$\sigma_f = \sigma_{UTS} \left(\frac{l_c}{l_0} \right)^{\frac{1}{\rho}} \quad (23)$$

The high values of fibre strength then lead to high IFSS values being reported with similar fragmentation lengths. However, the manufacturer's quoted values used in this work is simply the average fibre strength attained across a range of gauge lengths, thus under-reporting the

apparent fibre strength at the small fibre lengths seen in these tests. While it is clear from the literature that more accurate IFSS values can be obtained by conducting fibre tensile strength tests and developing a Weibull distribution from the results this was not done due to the time limitations of this work. Additionally, the focus of this work is on the change of IFSS values with cure and not on the IFSS values themselves. As has already been discussed, the methodology in this work performs well in the scatter of the data gathered compared to that of similar tests in the literature. Therefore, it can be concluded that the testing methodology used in this work for SFFT is suitable for the investigation of the effect of variable residual stress conditions on the IFSS in rapid curing resins and will be carried forward for subsequent testing.

4.4.3. Rapid cure

Using the testing methodology outlined in section 4.3.3 and validated by the results shown in section 4.4.1 and 4.4.2, rapid curing SFFT tests were conducted and the results are shown in Figure 50.

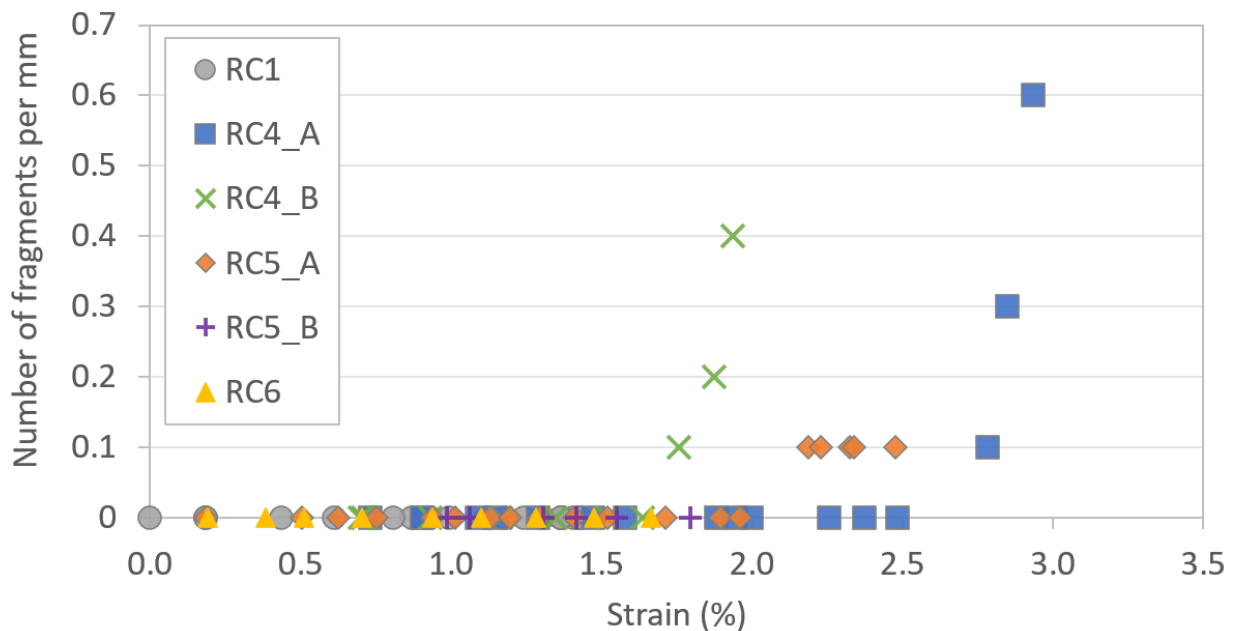


Figure 50: Rapid SFFT fragmentation/mm against Image J strain plot

As is evident from Figure 50 saturation was not reached with any of the rapidly cured SFFT samples tested. Indeed, only three samples fragmented at all, with the average fragmentation onset strain occurring at 2.24% while this was 1.10% for the slow curing resin system. Whilst

RC5_A shows a plateauing of fragments with increasing strain, this occurs at 0.1 fragments per millimetre or one fragment over the 10 mm gauge length at failure. Therefore, it is believed that saturation has not been reached here. Additionally comparing this against the standard curing resin results presented in Figure 43 we can see that the maximum number of fragments per millimetre (or fragmentation length) in the rapidly cured SFFT specimens was only 0.6 compared to 3 fragments per millimetre in the standard curing samples. Whilst we can expect these values to be different due to the different resin system being used, they will likely be more similar than this if saturation has been reached. Therefore, it is evident that saturation was not reached in any of these tests of the rapid curing resin system. Therefore, an analysis of the sample failure strains and onset of fragmentation strains was conducted to determine the cause of this result. The full set of fragmentation onset and failure strain results for both the rapid and slow curing conditions are presented in Table 8. Additionally, a representative example of increasing fragmentation with strain until failure for a slow cure sample, SC5, is shown in Figure 51 where the onset of fragmentation is marked in red. The same for a rapid curing sample, RC4_A is shown in Appendix D. RC2, 3, 7 & 8 are omitted as no usable data was captured during these tests due to poor sample alignment and fixturing.

Table 8: Onset of fragmentation and sample failure for slow cured and rapidly cured SFFT specimens as measured by Image J

	Test	Cure	Onset of frag, ϵ_f^{fail} (%)	Failure, ϵ_m^{fail} (%)
Slow				
	SC1	24h RT/6h 60 °C	1.47	2.45
	SC2	24h RT/6h 60 °C	0.68	2.70
	SC3	24h RT/6h 60 °C	1.74	2.82
	SC4	24h RT/6h 60 °C	0.91	1.97
	SC5	24h RT/6h 60 °C	1.18	2.43
	SC6	24h RT/6h 60 °C	0.65	1.84
	Average		1.10	2.37
	Standard deviation		0.40	0.36
Rapid				
	RC1	155 °C - RT	N/A	1.37
	RC4_A	140 °C - 85 °C	2.78	2.93
	RC4_B	140 °C - 85 °C	1.76	1.94
	RC5_A	160 °C - 85 °C	2.19	2.48
	RC5_B	160 °C - 85 °C	N/A	1.79
	RC6	170 °C - 90 °C	N/A	1.67
	Average		2.24	2.03
	Standard deviation		0.42	0.53

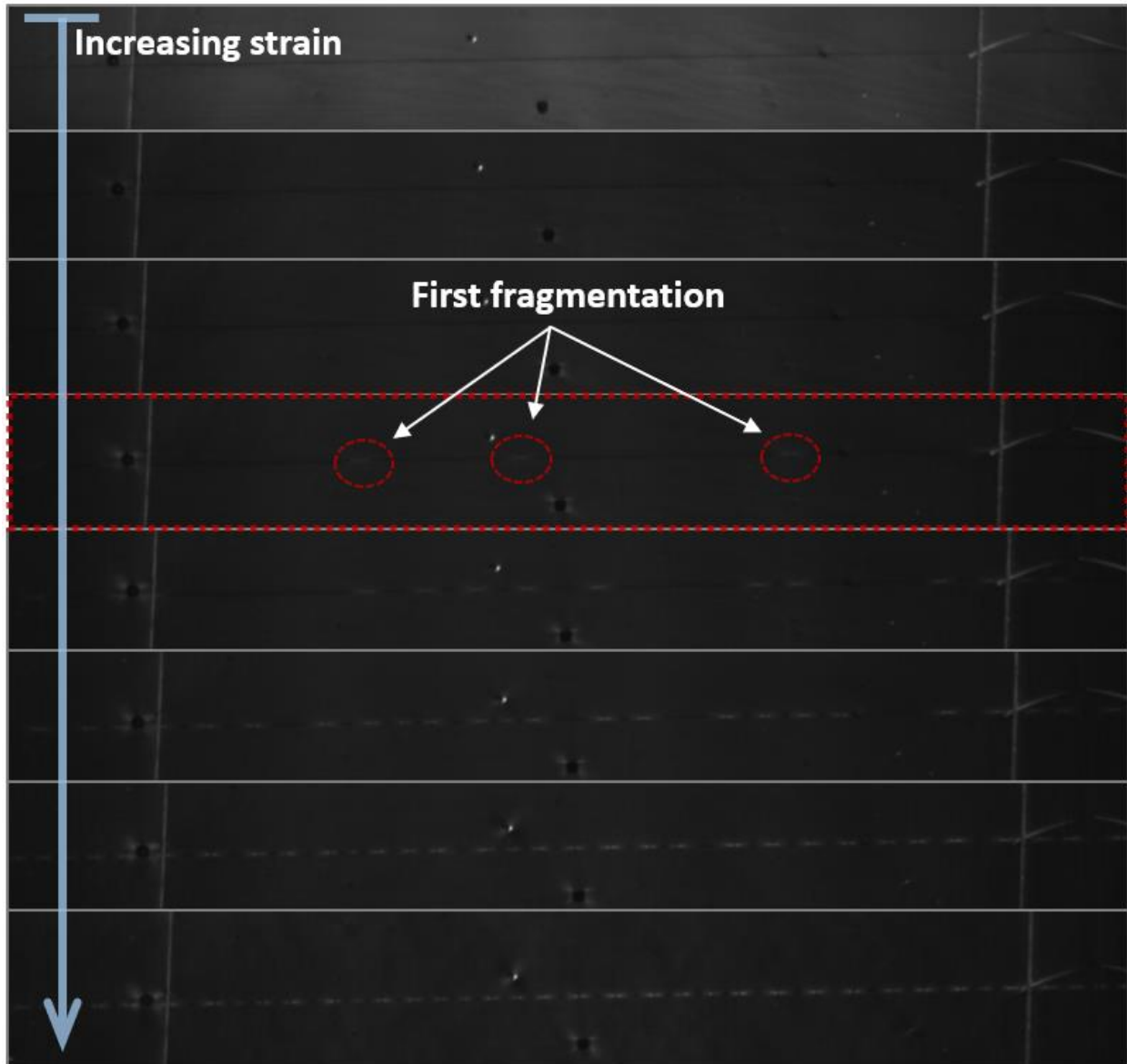


Figure 51: An example case of increasing fragmentation with strain for the SC5 sample with the onset of fragmentation marked in red.

Examining the average values for the onset of fragmentation of 1.10% and 2.24% for slow and rapid curing respectively, it is evident that the applied strain to the fibre is different between the slow and rapid curing system when the applied strain to the sample is the same. Therefore, either there is a micromechanical mechanism causing a disparity between resin strain and fibre strain or residual strains are present in either the fibre or resin. A micromechanical explanation for this behaviour has been suggested by Feih et al. [198] when they also observed the same phenomenon. It was postulated that there might be partial fibre de-bond before the

onset of fragmentation which leads to less strain being transferred to the fibre and therefore delaying the onset of fragmentation. However, without directly measuring the strain of the embedded fibre itself using a method like Raman spectroscopy (as discussed in section 2.4.3.1) it will not be possible to verify this. Another possible cause of this late onset of fragmentation was that it was not possible to apply an adequate pre-tension to the fibre to account for the high compressive thermal load experienced during cure. As discussed in section 4.3.1. a 3 g washer was suspended from the fibre to apply a 0.32% pre-tension to the fibre. Whilst this is adequate to account for the 0.36% compressive thermal load in the slow curing resin system this proved to be inadequate for the rapid curing resins system. Using Equation (22) and the material properties detailed in Table 4 it can be calculated that the rapid curing resin system applies a 1.31% compressive strain during cure. Therefore, we can assume that a 0.99% compressive strain, $\epsilon_{rapid}^{thermal}$, remains in the fibre in the rapid-curing samples at the beginning of testing. Unfortunately, it has not been possible to apply any further pre-load to the fibres before cure. If the entire 0.99% compressive thermal residual strain were to be counteracted with pre-tensioning, a 10 g mass hung off the end of the fibre would be required. During this testing this was found to not be possible and the use of only 3 g of pre-tensioning mass led to a very low success rate in the placement of fibres. When 10 g masses were used, all fibres failed before any resin could be added to the mould cavity and it was not possible to manufacture any samples with 10 g of pre-tensioning.

This additional compressive strain on the fibre in the rapid-curing resin system results in an effective fibre strain at failure of 1.25% ($\epsilon_f^{fail} - \epsilon_{rapid}^{thermal}$) which now agrees well with the fibre fragmentation onset strain of the slow curing system. However, both systems still show fragmentation occurring much earlier than expected with the fibre strain to failure quoted as being 1.9% by the manufacture. This can partially be explained by the omission of the chemical shrinkage effect of the resin on the fibre during cure.

Chemical shrinkage would apply an additional tensile load to the fibre, thereby causing early fibre fragmentation as calculated from specimen strain. For conventional curing resins this is often assumed to account for around 5% [217], but has been reported to be as high as 30% [218][219], of the total strain during cure. This wide range of residual stress contributions is due to the various points at which these resins gel. While most epoxy resins have a total volumetric shrinkage of around 3-7% [29][220][221] this shrinkage only contributes to residual

stress when they are not in their liquid or soft state. It is only shrinkage that occurs when the resin has a sufficiently large E' that results in residual stress being developed. When the resin has $E' \ll E''$ all volumetric shrinkage simply increases the density of the resin without adding additional residual stress. In the case of the slow curing resin system the epoxy chemistry is very typical and as such we can assume that it will have an $\alpha_{gel} \approx 0.55$ [222] which suggests that the contribution of chemical shrinkage to residual stress for the slow curing resin will be low, likely around 5%. Without further modelling work it will not be possible to verify this number exactly, but it does offer a reasonable approximation. If we assume viscoelastic behaviour this equates to an approximately 0.02% tensile strain being applied to the fibre from chemical shrinkage effects. Therefore, this contribution is often neglected in most work. However, in the case of the rapid curing resin system the effect of chemical shrinkage is less well understood and is likely to have a larger contribution to the total residual stress.

Additionally, the rapidly cured samples are seen to fail at a lower strain than the slow curing samples and there is more variation in when this occurs. This is despite the rapid curing samples being of higher quality and thereby reducing the chance of premature failure due to stress concentrations around cracks. This reduced strain to failure is believed to be caused by large amounts of residual stress in the rapidly cured samples caused by large thermal and cure gradients. This will be explored further in chapter 5. This has resulted in the average strain to failure of the rapidly curing resins being lower than that of the average fragmentation onset strain. Thus, it is not surprising that saturation has not reached on any of the tests carried out with any rapid curing condition. No correlation between the various rapidly curing conditions and the failure strains could be found. However, this premature failure is believed to be caused by residual stress but as will be discussed in chapter 5, the stress fields are not planar and areas of high stress concentrations do exist which will promote crack growth and failure.

Thus, it was not possible to reach saturation when using rapidly cured resin systems and it was not possible to calculate the IFSS of the resin fibre interface in rapidly cured samples. Additionally, the strain to failure of an optical fibre is approximately 6% [194] which is approximately three times that of the reported strain to failure of the rapid curing resins tested here. Therefore, it was not possible to test the IFSS between optical fibres and rapid curing resins with SFFT and no comparison can be made as saturation would not be reached.

However, while it was not possible to quantify the relative performance of the optical fibre/resin and carbon fibre/resin interfaces this was qualitatively investigated by examining the interface in section 4.5.

4.5. Scanning electron microscopy and micro x-ray computed tomography of the fibre optic sensor interface

To better understand the effect of rapid curing on the interface between the embedded optical fibre and resin matrix a qualitative analysis of the fibre interface was conducted. Various curing conditions were used to modify the magnitude of the residual stress around an embedded optical fibre in a UD laminate and cross-sectional images were taken and analysed using SEM and x-ray μ CT imaging. Using these approaches, it was possible to qualitatively determine the quality of the bond between optical fibre and resin matrix and thereby gain an understanding as to the extent of the strain transfer between the two.

EF7017 UD laminates with various levels of residual stress were prepared by altering cure temperature and laminate thickness. Here, “Cool” and “Hot” refer to hot press temperatures of 140 °C and 180 °C respectively. While, “thick” and “thin” refer to 6.35 mm (35 plies) and 2 mm (11 plies), respectively. The cure times stated in Table 3 and manufacturing method outlined in chapter 6 were adhered to. The optical fibres were embedded on the outer thickness (between the first and second ply) and in the mid-thickness (middle ply) of the laminates, transverse to the reinforcing fibre direction.

4.5.1. Scanning electron microscopy cross-sections

To prepare samples for SEM, cross-sections of the laminate were cut using a waterjet cutter and the samples were then mounted in resin for grinding and polishing. A Buehler Automet grinder and polisher was used to grind the samples to 2400 grit and then polished to 0.05 μ m with a force of 20 N as per the manufacture’s recommendations [223]. The samples were then gold coated using sputter coating to prepare them for SEM. Three samples from each curing condition were analysed, each with an embedded optical fibre at mid-thickness and outer thickness. Thus, six embedded optical fibre cross-sections were examined for each of the four

curing conditions, 24 optical fibre/matrix interfaces in total. Figure 52 shows representative images at 500x magnification for all four curing conditions, Cool_thin, Cool_thick, Hot_thin and Hot_thick.

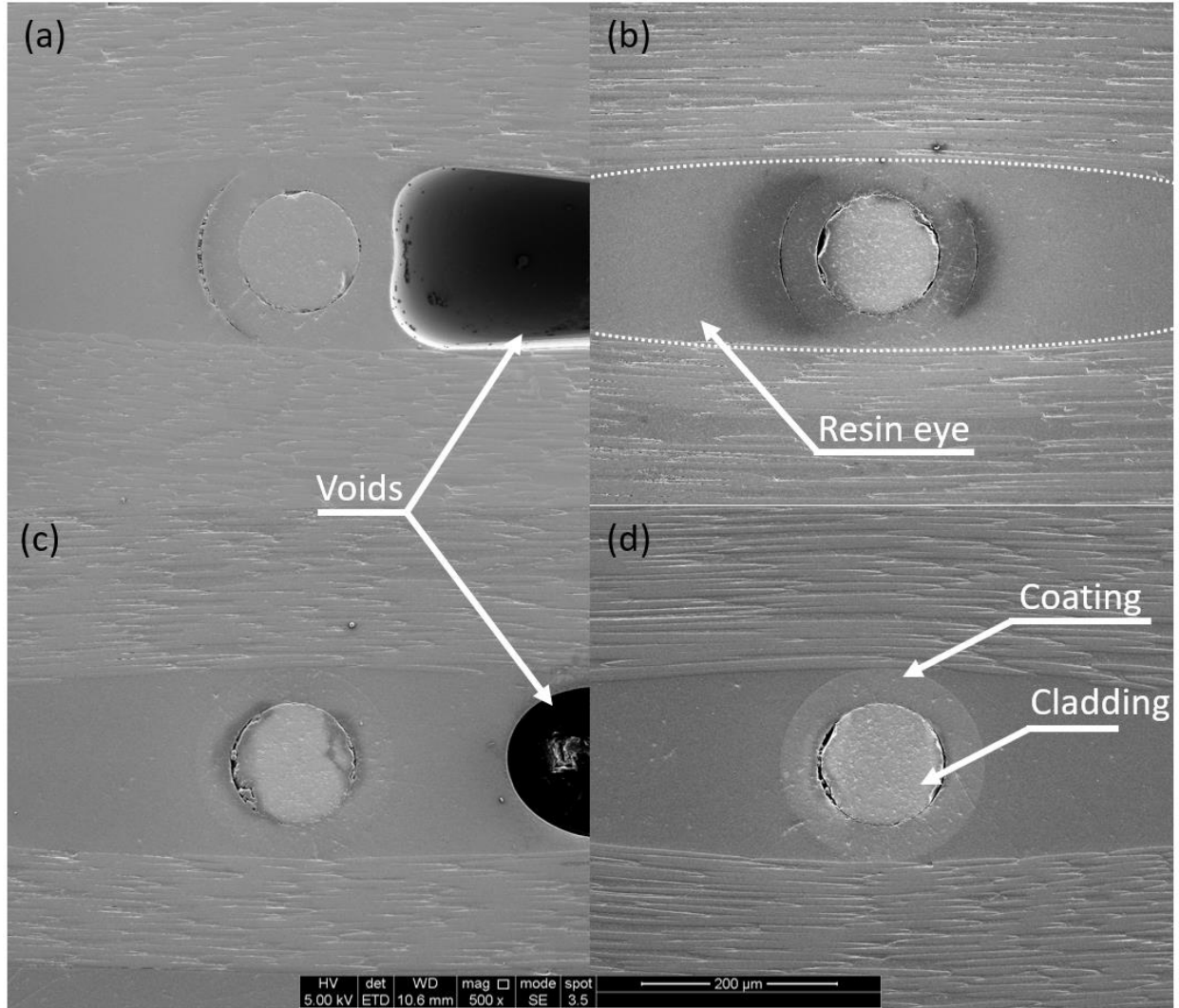


Figure 52: SEM of embedded optical fibres. (a) Cool_thin, (b) Cool_thick, (c) Hot_thin and (d) Hot_thick

Through analysis of Figure 52, three distinct trends can be observed. Firstly, large voids tend to form in the resin “eye” created by the embedded optical fibre in the “thin” samples. This is believed to be caused by the cure times being very short, especially in the case of the Hot_thin sample. The rapid cure meant that the resin matrix had insufficient time to flow around the embedded fibre while it was in its liquid state during cure. The lower compaction pressure reduced the ability of the liquid resin to fill in any voids which formed during the layup process. The extent to which these voids are formed along the length of the fibre will be

further examined using x-ray μ CT images in section 4.5.2 and chapter 8. The second trend seen is that the “cool” samples tended to have more debonding between the optical fibre coating and resin matrix on the left and right sides of the fibre (in the axial direction of the reinforcing fibres). Interestingly, debonding between the optical fibre coating and resin matrix was never seen on the top and bottom edges of the fibre (transverse to the fibre direction). This suggests that this debonding is actually caused by the grinding and polishing process as the fibres are able to effectively reinforce the coating/matrix bond when they are near the optical fibre. However, debonding of the coating/matrix interface occurs when it is surrounded by neat resin in the “eye” formed by the optical fibre. This is believed to only occur in the “cool” samples as there is less compressive residual stress around the optical fibre interface than in the “hot” samples. This compressive residual stress causes the threshold at which debonding occurs to increase and thereby ensures no debonding occurs in this case. The third trend that is evident in this analysis is that debonding always occurs at the cladding/coating interface. This is clearly seen in Figure 53, an SEM image of a Hot_thin sample. Here, the coating/matrix interface is clearly intact whilst the cladding/coating interface has debonded. The core of the optical fibre is barely visible due to its similar material composition to that of the cladding. The debonding is caused by the silica cladding breaking. This is thought to occur during the grinding and polishing process and is due to the relative brittleness of the silica cladding compared to the hybrid polymer ORMOCER® coating and resin matrix it is surrounded by. Therefore, this is not thought to impact the ability of the FBG to accurately measure strain during cure.

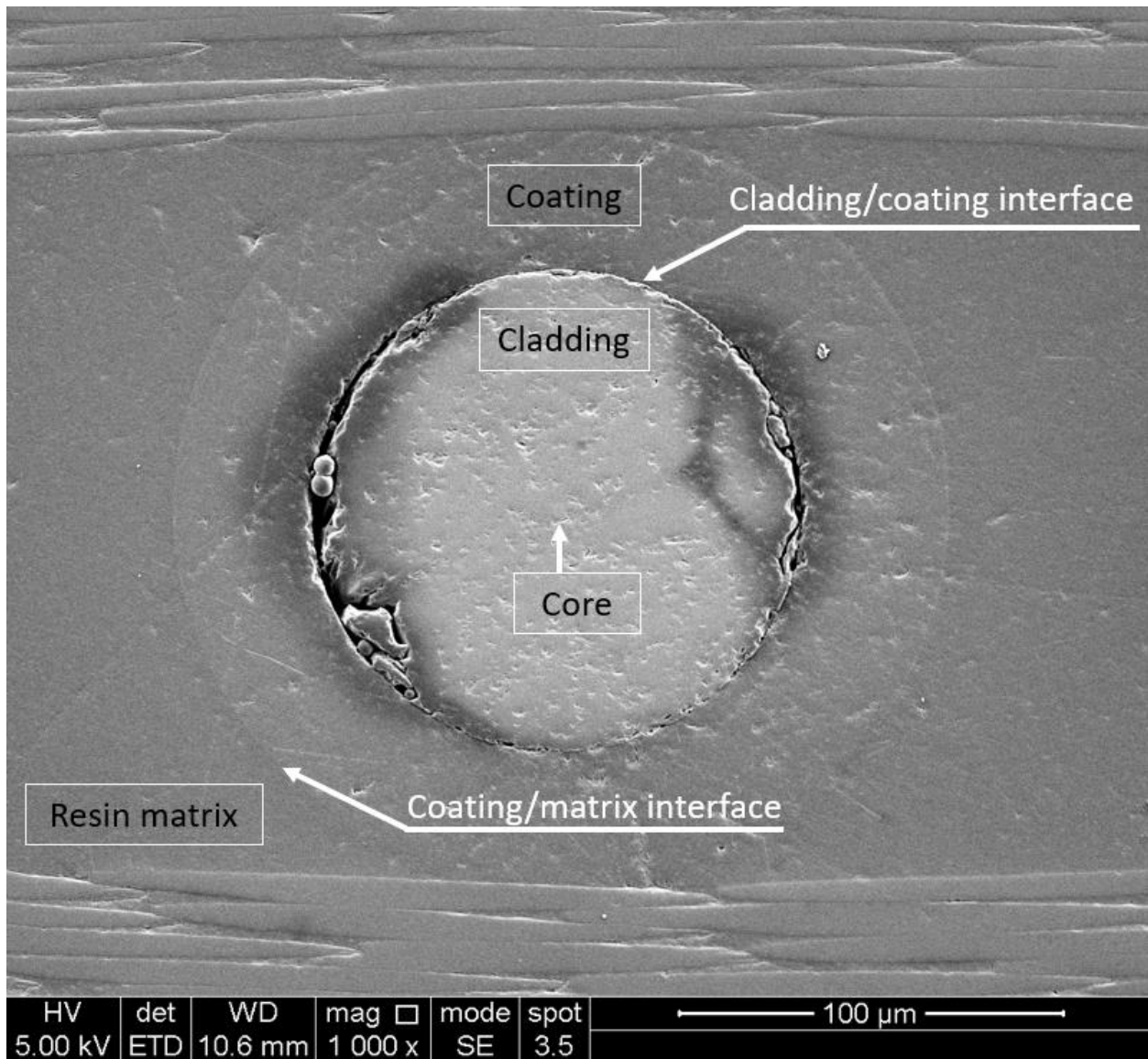


Figure 53: SEM image of Hot_thin embedded optical fibre at 1000x magnification

4.5.2. Micro x-ray computed tomography analysis

For the μ CT data acquisition, new sample sections were taken as the previously prepared SEM samples were not suitable for μ CT. The μ CT samples had dimensions of 5x10x40 mm. Therefore, the images cannot be compared directly but the processing parameters on bonding quality can be.

A Zeiss Xradia Versa 520 x-ray μ CT machine was used to carry out high-resolution non-destructive imaging of segments of embedded optical fibre from all the previously

described testing conditions. Scans used an x-ray tube voltage of 100 kV, a tube current of 140 μ A, and an exposure time of 2 seconds. A total of 1601 projections were collected. A filter (LE3) was used to filter out lower energy x-rays, and an objective lens giving an optical magnification of 4x was selected with binning set to 2, producing an isotropic voxel (three-dimensional (3D) pixel) size of 2.11 μ m. The tomograms were reconstructed from 2D projections using Zeiss Microscopy commercial software package (XMReconstructor) and an automatically generated cone-beam reconstruction algorithm based on filtered back-projection. Samples were scanned at Sheffield Tomography Centre at the University of Sheffield, UK. Images were then produced using the Dragonfly visualisation software and are presented for the “thin” samples in Figure 54 and for the “thick” samples in Figure 55. Red, blue and green axis lines are included for clarity

Comparing the SEM to the μ CT data, it is clear that SEM images are limited in this use case as they will only ever capture a small cross-section of what happens over the entire length of the embedded optical fibre. While the SEM images (Figure 52) indicate that voids form in the resin pockets of the thin laminates, this is not the case in the μ CT data (Figure 54, Figure 55). Here, there are no visible voids in the thin samples, but there are very significant voids present in the “thick” samples which were not present in the SEM cross-sectional images. These large voids in the “thick” samples are thought to occur from poor resin compaction and flow during the cure. However, while these voids are large it is thought that there is still sufficient bonding to the surrounding matrix as the matrix remains in contact with the optical fibre on at least three quarters of the fibre’s circumference over its entire length. Thus, there is sufficiently good bonding in the “thick” samples”

The Cool_thin sample (Figure 54) was the only sample that appears to have experienced debonding over the full length examined. While the void between the resin eye and the optical fibre is small, it does appear over the entire fibre length, as can be seen in the y-axis image of the Cool_thin sample in Figure 54. This debonding, which is in-line with the fibre direction, is consistent with what has been seen in the SEM images, although without the larger void. It is unclear what has caused this debonding as the Cool_thin sample has undergone a relatively slower and more controlled cure than the hotter and thicker samples. Thus, it is unlikely that debonding has occurred due to residual stress but could instead be from some contamination

of the fibre before it was embedded during the manufacturing process. Whilst this de-bond is over a significant length it is only occurs on the surfaces next to the resin eye and not on the surfaces close to the fibre. Specifically, it appears on 140° (approximately 40%) of the fibre circumference as measured by Dragonfly. There is still good contact on the surfaces close to the reinforcing fibres and it is thought that this is sufficient for the residual strain results to not be adversely affected. Looking at the results presented in chapter 6, no sudden drop-offs or anomalous behaviour is visible, which might be expected to occur if there was significant detachment between the embedded optical fibre and the laminate. Thus, there is sufficiently good bonding in the “thin” samples and the remaining samples. Future work should aim to do more repeat testing to add more certainty to these findings.

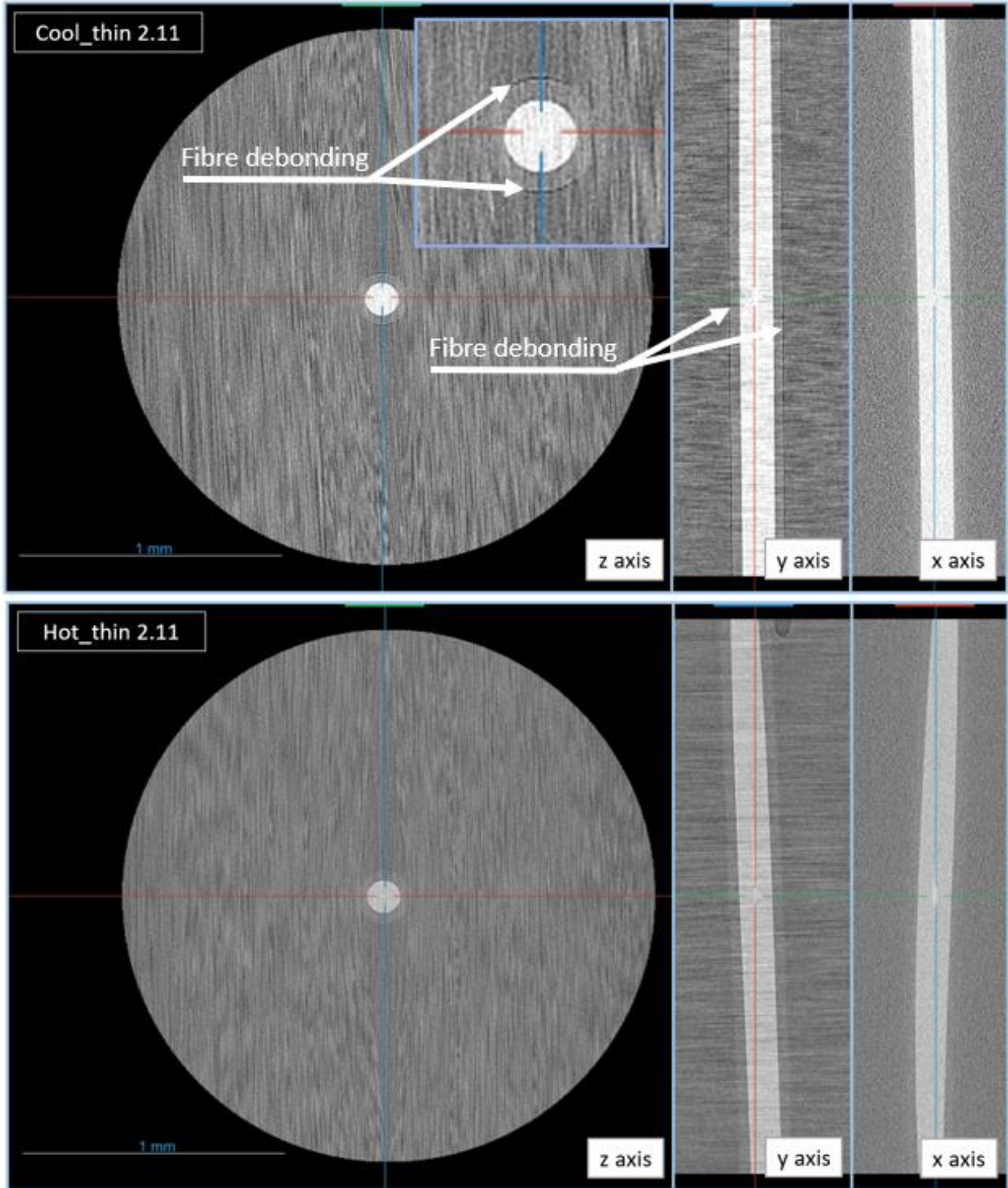


Figure 54: μ CT images of embedded optical fibres in the "thin" samples in the x , y and z planes with a 2.11 μ m voxel size.

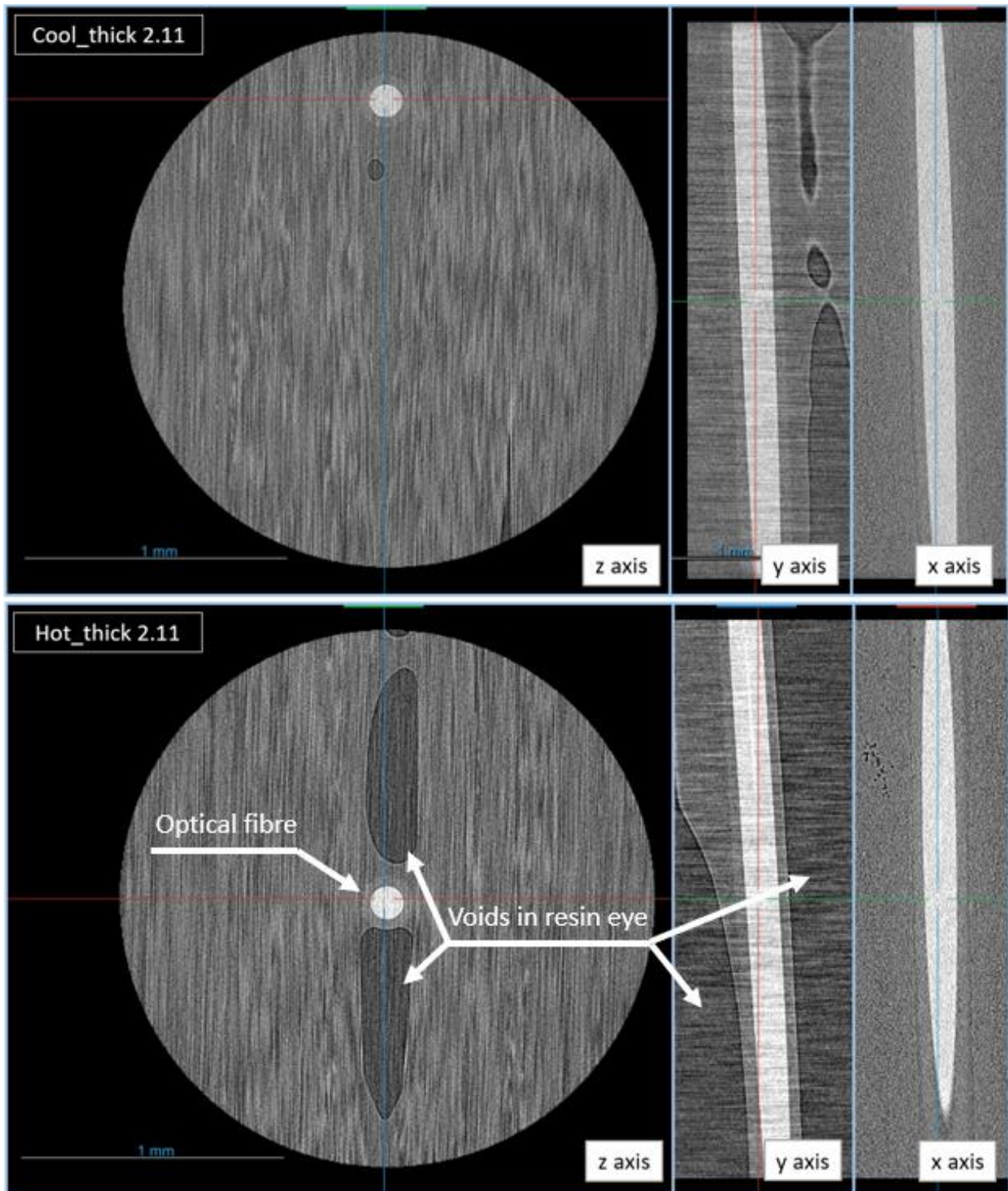


Figure 55: μ CT images of embedded optical fibres in the "thick" samples in the x , y and z planes with a $2.11 \mu\text{m}$ voxel size.

4.6. Conclusion

In this chapter it was found that optical fibres embedded into rapid curing resin matrices maintain a sufficiently high interface integrity for strain data captured by FBGs to be considered valid when determining residual strain during and after cure. Whilst it was not possible to quantify the IFSS of the fibre/matrix interface for rapidly cured resin systems using SFFT, this was validated qualitatively using SEM and μ CT.

A SFFT procedure using Image J software was developed to allow for contact free measurement of sample strain and fragmentation length which could be completed in a post processing step. This allowed for fragmentation measurements to be rapidly made when the sample was near failure and was shown to compare favourably with measurements taken using a more conventional micrometer method. Using this methodology, IFSS values for a slow curing resin system and carbon fibre were determined and values were found to match reasonably well to ones found in the literature for similar resin systems. However, in this work a Weibull distribution to describe how fibre strength increases with a decreasing fibre length was not used. This led to an underestimation of IFSS values as fibre strength values were underestimated. In future work, tensile tests to determine fibre strength at various fibre lengths should be conducted to allow for the determination of a Weibull distribution of fibre strength and a more accurate IFSS value.

A novel SFFT sample preparation method was developed for rapidly cured SFFT samples which allowed for accurate, measurable, and rapid heating and curing of SFFT samples. However, it was not possible to reach saturation during SFFT of rapid curing samples due to two factors. First, rapid curing led to high levels of compressive residual strain on the embedded fibres which delayed the onset of fragmentation as this had to be overcome before tensile strain could be developed. It was found that this could not be compensated for with additional fibre pre-strain due to the fragility of the fibres. Secondly, the rapid curing of the samples led to large amounts of tensile residual stress in the resin matrix which caused premature sample failure during SFFT. Therefore, it was not possible to quantify the IFSS of rapidly cured resin systems using SFFT. Additionally, due to the high strain to failure of the optical fibres, the IFSS between optical fibre and resin matrices was also not able to be

quantified. However, it was possible to use SEM and μ CT to qualitatively determine that there was good bonding between optical fibre and rapid curing resins from rapidly cured laminate cross-sections. Thus, it can be concluded that embedding optical fibres into rapidly cured laminates does offer a representative insight into the internal strain state of the laminate during and after cure.

5. Photoelastic analysis of residual stress in neat resin

In this chapter, an investigation into the through-thickness residual stress distribution in neat resin samples is undertaken. While focusing on purely neat resin and omitting the inclusion of reinforcing fibres does disregard the effect of the anisotropy between fibre and matrix, this does allow for a valuable full-field insight into the internal residual stress distribution in resin systems. Additionally, this investigation will still allow for an approximation of the transverse residual stress build up in a UD laminate as the resin matrix is the dominant driving force behind the apparent transverse material characteristics in these types of laminates. Therefore, this analysis will be a valuable tool when investigating the transverse matrix strength of UD laminates subjected to various residual stress fields, as will be discussed in chapter 8. For this analysis, residual stress fields within the samples are altered by applying various curing profiles to the different samples and photoelasticity is employed to gain a full-field insight into the residual stress distribution therein.

The aim of this chapter is:

- To gain a full field insight into the residual stress distribution in variably cured neat resin samples.

The objectives of this chapter are to:

- Use the rapid curing SFFT mould developed in chapter 4 to manufacture EF7017 neat resin samples at various cure temperatures to introduce varying residual stress fields
- Use circularly polarised light to examine and quantify the residual stress distribution through the thickness of the resin samples and to make inferences about the residual stress state of similarly cured UD laminates.
- Use a grey field polariscope to accurately quantify the residual stress distribution through the thickness of resin samples

5.1. Photoelasticity theory

In SFFT, the photoelastic effect is used to aid the detection of fragmentation as this is often impossible to see using standard optical techniques [134][133][224]. Photoelasticity is a valuable full-field stress/strain measuring technique which uses the photoelastic effect to analyse strain fields. It can be used to identify both stress/strain distributions and magnitudes, when calibrated. While this technique cannot be used on fibre reinforced laminates due to the need for light to be able to pass through the sample, it can be used on thin laminate cross-sections or neat resin. Photoelasticity is particularly valuable when investigating residual stress in neat resin samples as it is one of the few techniques that allows for a full-field view of the stresses that form and are stored during the curing process. Alternative full-field techniques can only investigate the effect of externally applied loads on samples with residual stress.

Photoelasticity works on the principal of the stress-optic law, Equation (24), which states that the changes in indices of refraction are linearly proportional to the change in the stress/strain state of a material [115][225]. In the case of isotropic birefringent materials, incident light is resolved into two components along the two principal stress directions. Each component of the light in a given principal stress direction has a given refractive index which is proportional to the magnitude of that principal stress. This means that each component of the light leaves the birefringent material at different times as the light travels at different speeds depending on that axis' refractive index. Therefore, there is a relative phase retardation between the two components of the light, Δ . When the two components of the light are recombined with a polariser, an interference pattern is formed which can be observed and analysed in the form of fringes which have a fringe order, N as shown by Equation (25)

$$\begin{aligned}\Delta_{12} &= \frac{2\pi t}{\lambda} C(\sigma_1 - \sigma_2) \\ \Delta_{23} &= \frac{2\pi t}{\lambda} C(\sigma_2 - \sigma_3) \\ \Delta_{31} &= \frac{2\pi t}{\lambda} C(\sigma_3 - \sigma_1)\end{aligned}\tag{24}$$

$$N = \frac{\Delta}{2\pi}\tag{25}$$

where σ are the principal stresses, λ is the wavelength of the light, t is the thickness of the material and C is the stress-optic coefficient. Hence, a birefringent sample placed between two polarisers shows the interference fringes caused by the differential of in-plane stress in the sample, as seen in Figure 56. Two types of fringes form, isoclinic and isochromatic. Isoclinic fringes show the direction of the principal stresses and the isochromatic fringes show the lines of constant stress difference. Therefore, the magnitude and direction of the principal stresses can be calculated [115].

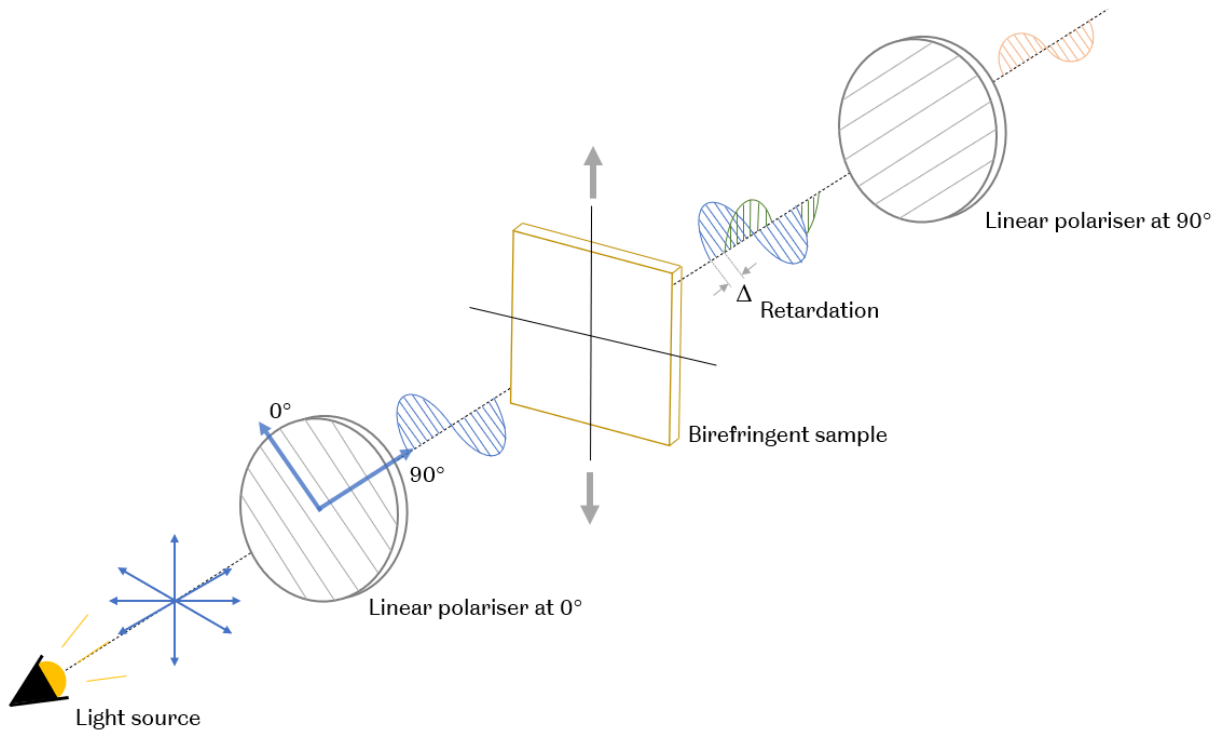


Figure 56: Plane polariscope setup in the dark field orientation

It is possible to remove the isoclinic fringes by applying circularly polarised light, thus offering the ability to see fringes that are obscured by isoclinics as seen in Figure 57. Circularly polarised light is achieved by adding quarter wave plates between the sample and polarisers, as shown in Figure 58. This resolves the plane polarised light into two components with a phase difference of $\pi/2$ between the two, creating elliptically polarised light. The two waves then travel through the birefringent sample and an additional phase difference, or retardation, is induced between the two components of light. When this light passes through the second quarter wave plate and polariser, the waves recombine with a residual phase difference between them. The interference between the two phases is observed as fringes and

can be examined to determine the amount of retardation that occurred as the light passed through the birefringent material, and therefore the amount of stress in the birefringent sample.

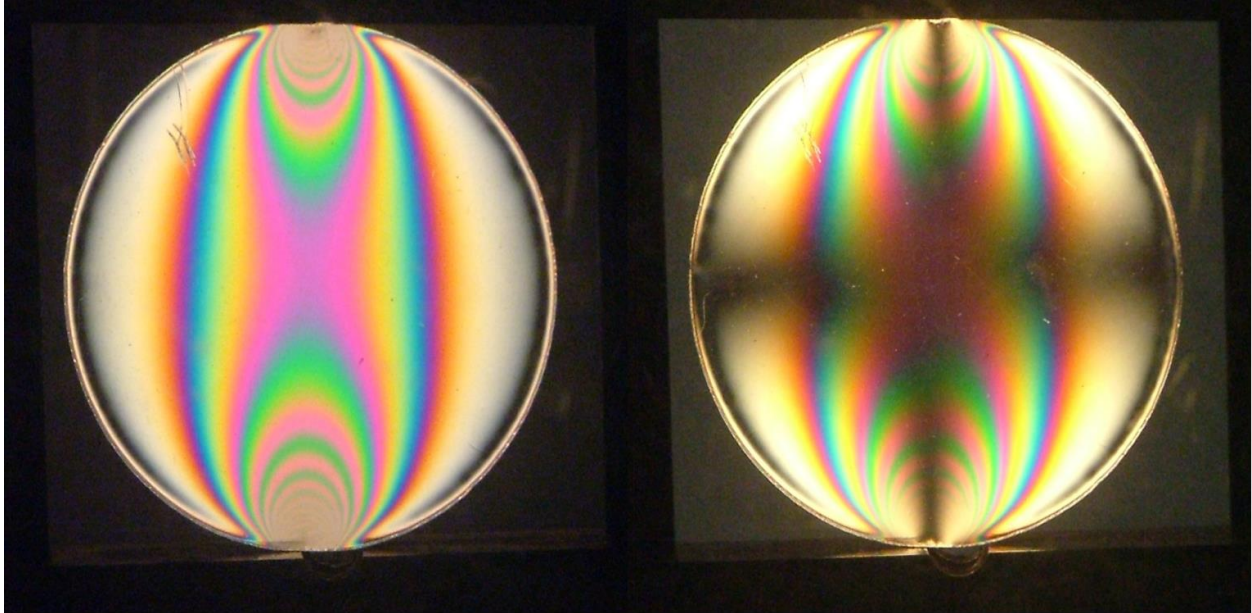


Figure 57: Isochromatic fringes (left) and Isoclinic fringes (right) in a stressed disc

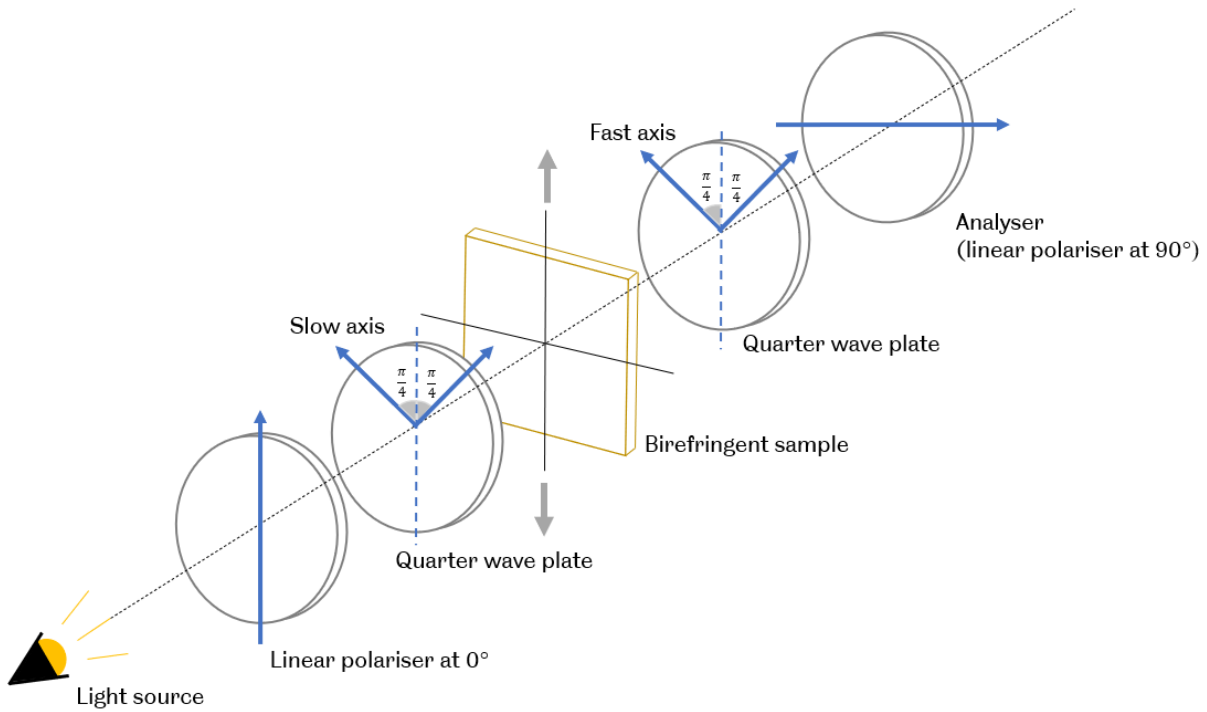


Figure 58: Circular polariscope setup in the dark field orientation

To relate the magnitude of the principal stress difference to the fringes observed during loading, a calibration must be performed. Using a dog bone specimen, an even in-plane and known stress state can be applied to a sample. Thus, assuming constant in-plane stress, we can combine Equations (24) and (25) to get Equation (26)

$$\sigma_1 - \sigma_2 = \frac{Nf_\sigma}{t} \quad (26)$$

$$f_\sigma = \frac{\lambda}{C} \quad (27)$$

where f_σ is the material stress fringe value property, described by Equation (27). Thus, by applying a pure tension to a dog bone sample and counting the resulting fringes we can reduce Equation (26) and calculate f_σ .

One problem with a conventional circularly polarised polariscope is that stress measurements can only be taken at discrete points at each fringe. Due to varying concentrations of stress, these fringes are not at regular intervals across a given part, thereby making it impossible to use simple linear interpolation to extrapolate the full-field stress profile. However, Tardy compensation can be used to analyse the stress state at any given point. This is done by rotating the analyser polariser until a fringe completely covers the area of interest and then using Equation (28) to determine fractional fringe order [115]

$$N = m \pm \frac{\gamma}{\pi} \quad (28)$$

where N is the fractional fringe order at the area under investigation, m is the original fringe order and γ is the amount of rotation in radians.

Phase stepping was introduced by Hecker and Morche [226] as a way supplementing the principal of Tardy compensation with the intensity of the output light to determine the full-field fractional fringe order. Phase stepping utilises four to eight images of the specimen through a circular polidroscope, each with the analyser polariser and output quarter wave plate set to a different and precise angle. By automating this process through the use of computational image processing and motorised optics, this method allows for a full-field analysis of the stress magnitude and direction for any in-plane stress in a birefringent material [227]. This is the basic principal of a Grey Field Polariscope (GFP).

5.2. Methodology

Sample preparation

During the manufacture of the rapidly cured SFFT samples additional specimens without fibres embedded in them were also produced in parallel so that a photoelastic analysis of the residual stress state of variously cured neat resin samples could be made (RC1-8). Additionally blank resin plaque were made specifically for the photoelastic analysis and were not presented during SFFT testing in chapter 4 (RC9-12). The blank dog bone specimens with varying levels of residual stress due to varying thermal histories are described by Table 9. A circularly polarised polidroscope setup, as detailed in Figure 58, was used to investigate the fringe order and therefore residual stress present in the samples. Additionally, “Slow cure” neat resin samples were made using EL2 resin in the same way as the EF7017 samples. The samples were cured for 24 hours at room temperature and then an additional post cure for 6 hours at 60 °C as per the manufacturer’s instructions [209].

Table 9: Photoelastic analysis specimen specifications

Test	Material	Upper mould temperature (°C)	Lower mould temperature (°C)
RC1	EF7017	155	Room temperature (20 °C)
RC2	EF7017	160	Room temperature (20 °C)
RC3	EF7017	180	Room temperature (20 °C)
RC4	EF7017	140	85
RC5	EF7017	160	85
RC6	EF7017	170	90
RC7	EF7017	180	100
RC8	EF7017	200	100
RC9	EF7017	160	110
RC10	EF7017	140	140
RC11	EF7017	160	160
RC12	EF7017	180	180
Slow cure	EL2	Room temperature (20 °C)	Room temperature (20 °C)

Figure 59 shows the coordinate system used throughout the circularly polarised light photoelastic testing. The “front-on” view being from the top of the mould surface to the

bottom, through the thickness of the sample. While the “side-on” view is perpendicular to this going through the waterjet cut surface of the gauge length.

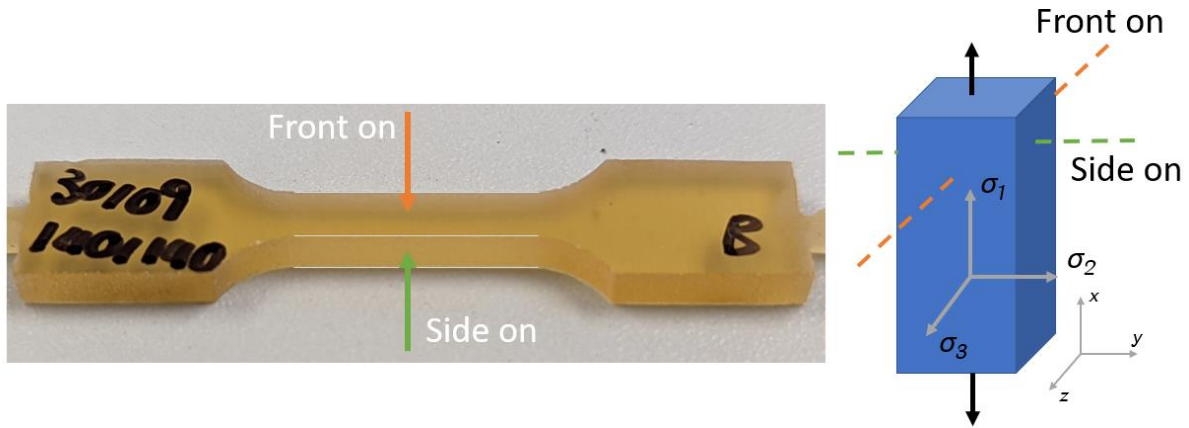


Figure 59: Coordinate system for photoelastic residual stress analysis

Material fringe value calibration

To determine the material fringe value, f_σ , and thereby convert fringe order to stress using Equation (26), a calibration was carried out. A sample was placed into a tensile testing rig front-on and was viewed with a circular polariser as described in Figure 58. Load was applied at 0.2 mm/min and the load when every yellow (half-fringe) and black fringe (whole-fringe – tint of passage) appeared was noted. Then, if it is assumed that the dog bone specimen is in pure tension and $\sigma_2 = 0$ then f_σ can be calculated over a range of stress values as the slope of the σ_1/f_σ graph. This calibration was performed over a wide range of stresses, and therefore fringe orders, five times for each resin formulation and the results are plotted for EF7017 and EL2 in Figure 60. Error bars indicating ± 1 standard deviation are included.

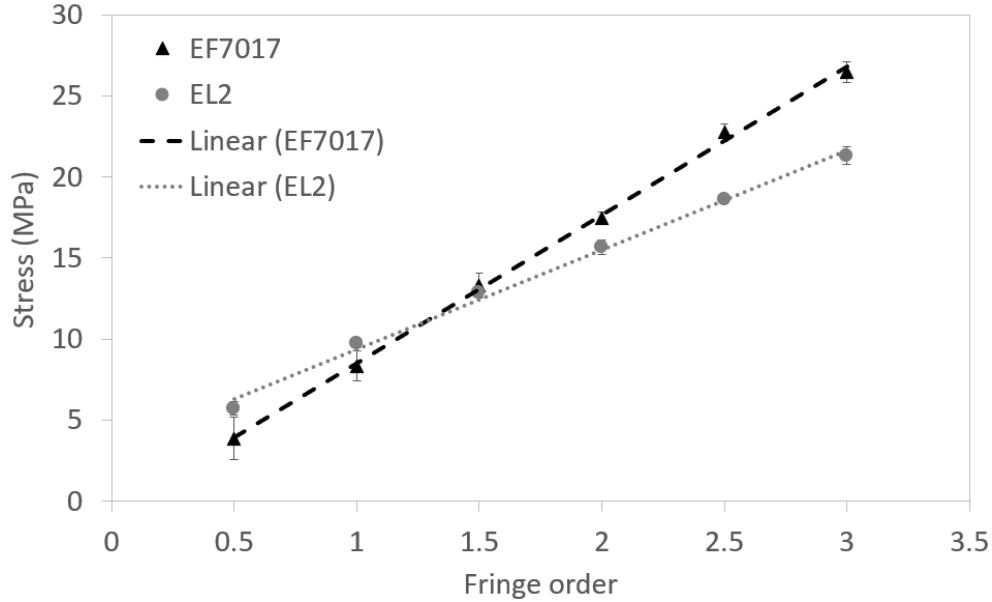


Figure 60: Material stress fringe constant calibration test over a range of fringe orders for EF7017 and EL2 resins. Error bars are ± 1 standard deviation and linear trend lines are included.

For both EF7017 and EL2 there are larger errors in the 0.5 fringe order reading due to grips “settling in” to the sample, causing non-uniform loading. Thus, the 0.5 fringe order readings are discarded for the determination of the average fringe order. The EF7017 and EL2 sample shows a good agreement with the linear assumption over the whole range of fringe orders, which is indicative of there being a uniform stress state. Thus, an average value taken from the fringe order of one and higher was used to determine the calibration coefficient for EF7017 and EL2. The material stress fringe constant, f_s , was found to be 28.0 and 26.6 MPa/fringe/mm for EF7017 and EL2 respectively.

Figure 61 shows the front-on view of the 170/90 °C specimen as an example. It is evident that a combination of a zero-order (black fringe) with some half-fringe (yellow fringe) is observed, indicating that the sum of the difference between σ_1 and σ_2 through the thickness of the sample is approximately zero.

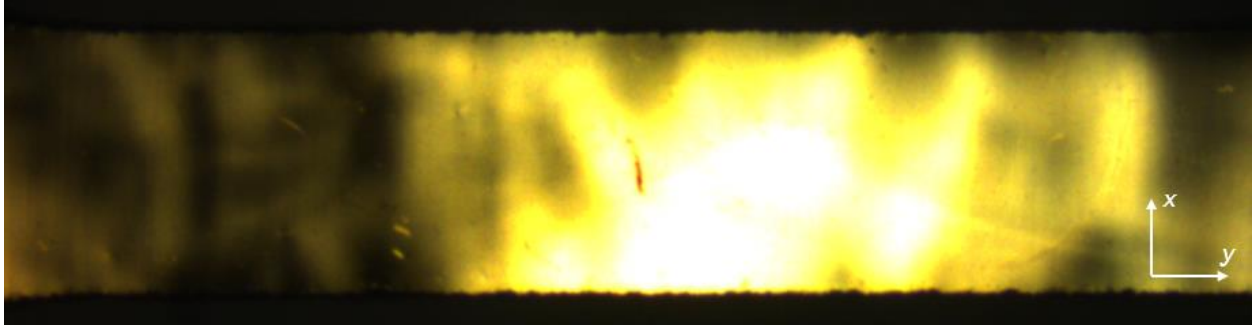


Figure 61: Front-on view in circularly polarised light – 170/90 °C sample

In contrast, in the side-on view shown in Figure 62 it is clear that there are multiple non-zero order fringes present. Thus, indicating that the sum of the differences between σ_1 and σ_3 through the thickness is not zero. Therefore, we can surmise that $\sigma_1 \approx \sigma_2$. Thus, residual stress does not vary in-plane and only varies through the thickness of the specimen, from the top of the mould surface to the bottom. Therefore, we can now relate the number of fringes seen from the side-on view to the sum of σ_1 through the y-direction thickness.

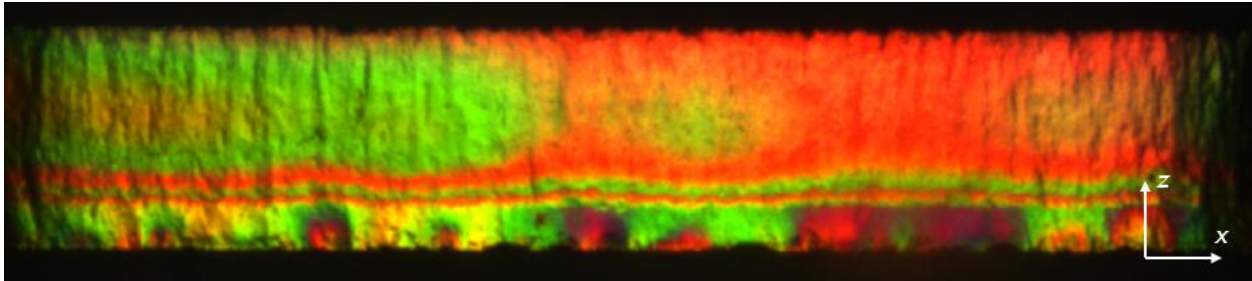


Figure 62: Side-on view in circularly polarised light – 170/90 °C sample (up is top of the mould)

Testing methodology

To determine the fringe order seen in Figure 62 the zero-order fringe must be found so that fringes can be counted back to the initial fringe order. By applying a bending load to the specimen, force in the positive and negative z-direction, a compressive load is induced in each side of the sample. For all samples the application of a compressive force yields a zero-order fringe which indicates that there is a tensile in-plane load on the top and bottom of the samples. Therefore, to determine the fringe order a load is gradually applied and pictures are taken periodically so that the fringe order of the unloaded sample can be tracked and counted. This progressive loading is shown in Figure 63 with the position of the original fringe being marked and tracked, and loading increasing from the top left to the bottom right. The bottom of Figure 63 shows an image of the maximum bending force being applied to both the left and

right sides of a sample and the zero-order fringe and the initial fringe order are indicated. From this image it is possible to count the number of fringes, thereby obtaining the fringe order, N and the principal stress difference as shown in Equation (26) for both the left (mould top) and right (mould bottom) sides of the samples.

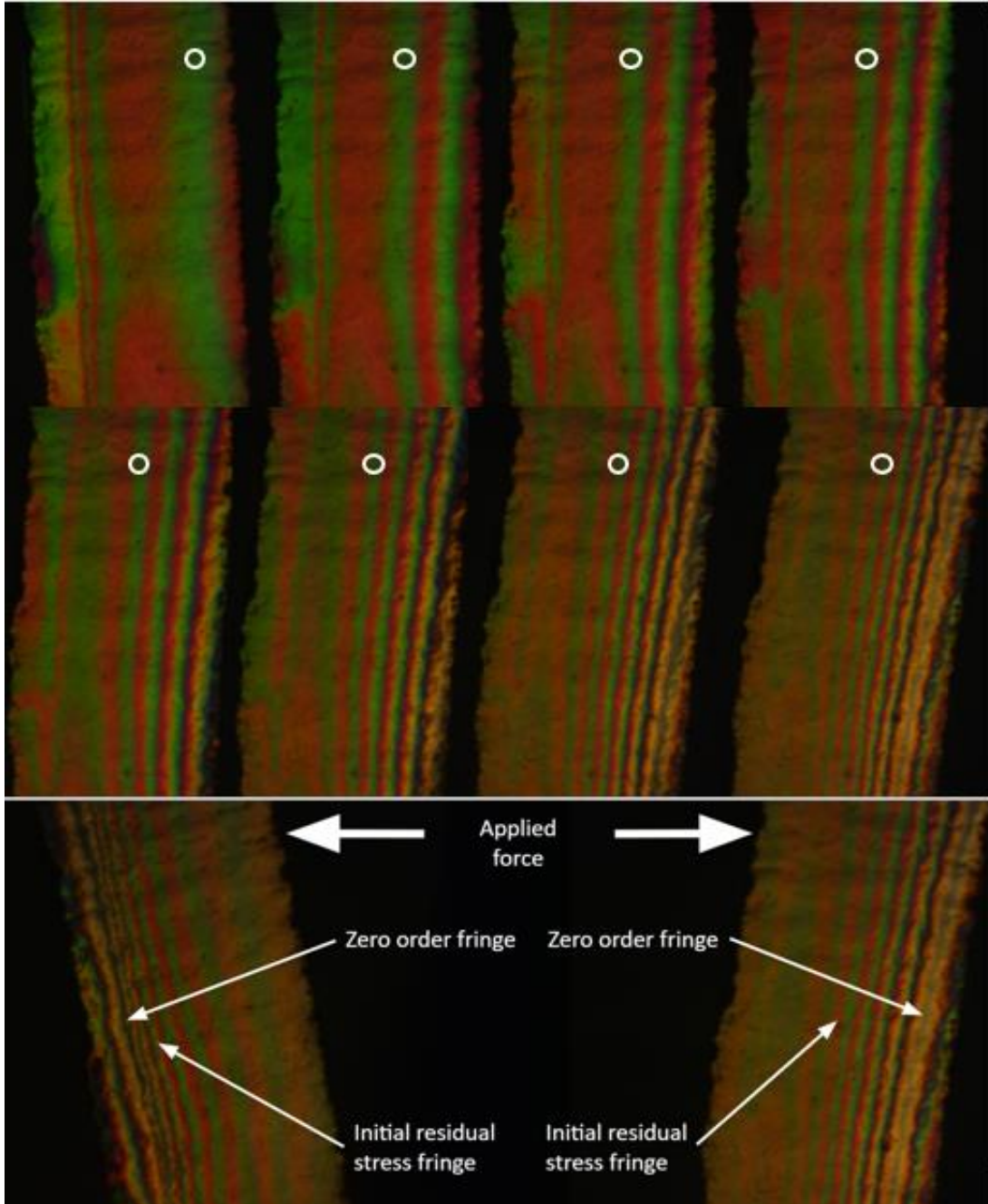


Figure 63: Side-on view in circularly polarised light with applied bending. Above, load increasing left to right and top to bottom. Below, final load in $\pm z$ -direction with initial fringe and zero-order fringes indicated. – 180/100 °C sample

Additionally, an attempt to measure residual stress distribution was made using a GFP [228][229]. This utilises the principles of phase stepping but removes the second quarter wave plate and automates the process of changing the orientation of the analyser polariser. The analyser polariser is rotated continuously, and eight images are taken at precise analyser orientations over one full rotation. This allows for a very accurate change in the angle of the analyser, mitigating errors caused by rotating the optical elements. Additional full rotations can be made, and an average taken between rotations to further increase accuracy. Through the analysis of the retardation of the incident light, a quantitative assessment of the through-thickness change in residual stress can be made. However, due to the high levels of residual stress the fringe orders seen were too high and the fringes too closely packed to be analysed by the GFP1600 which operates below fringe orders of around two [230].

5.3. Results and discussion

The results of the residual stress analysis through a circular polariscope for various cure temperatures for EF7017 and for the slow cure EL2 resin are shown in Figure 64.

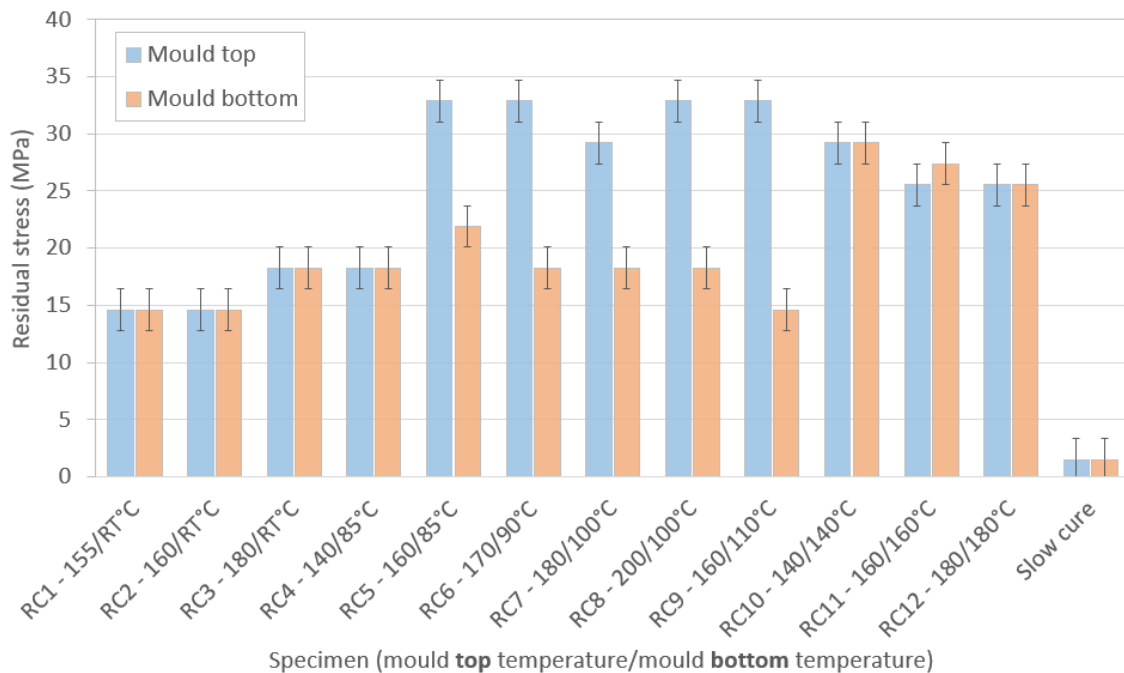


Figure 64: Residual stress distribution as calculated through photoelastic observations in circularly polarised light

In Figure 64, error bars are included to indicate the resolution of the technique (approximately $\pm \frac{1}{4} N$ or ± 1.8 MPa for EF7017). A number of trends are evident in these results. First, for all samples and all positions in the sample the residual stress is tensile. Similarly to the transverse strain in UD laminates investigated in chapter 6, this tensile stress is a result of the overall compressive strain generated during cure. This is formed from the constrained thermal and chemical contraction after α_{gel} when the elastic modulus begins to develop. Both the volumetric changes caused by chemical shrinkage and thermal contraction are stress free events if they are unconstrained. However, in the case of a closed mould they are fully constrained on all their boundaries, thus the resultant stress is tensile after the sample has reached room temperature and full cure.

Second, any samples manufactured without preheating the bottom mould and leaving it at Room Temperature (RT) saw relatively low levels of residual stress and had an even stress distribution through the thickness of the sample. This is caused by the RT bottom mould acting as a heat sink, drawing heat away from the liquid resin. This causes the heating/curing rate of the resin to decrease and to cure more uniformly through its thickness. Thus, by the time the resin begins to gel and elastically retain stress, there is only a small/zero temperature and DOC gradient through the thickness of the sample and a small/zero residual stress gradient is formed.

Third, when a differential heating regime is applied to the EF7017 resin there are high levels of resultant tensile residual stress which vary through the thickness of the sample. Higher levels of tensile residual stress occur on the hotter (top) mould surface side of the sample. This is because the samples are cured from the hot side (top) to the cooler side (bottom), thus the more cured (top) will constrain the expansion of the still curing cooler (bottom) half of the specimen. This induces a higher tensile residual stress in the hotter (top) section of the sample. This is indicated by Figure 65 which shows an approximated in-plane stress distribution in the 180/100 °C sample.

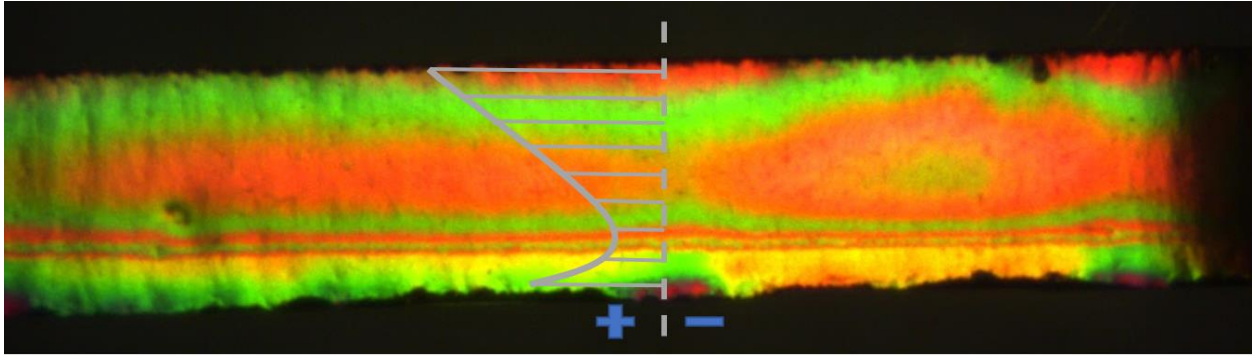


Figure 65: In-plane residual stress distribution as seen in circularly polarised light – 180/100 °C sample

Finally, when the temperature of the upper and lower moulds is the same there are high levels of residual stress which is distributed relatively evenly through the thickness of the sample. This is caused by the samples curing from the outside to the inside whilst all the boundaries are constrained, thus generating tensile residual stress. Here, RC10 (140/140 °C) and RC12 (180/180 °C) have tensile residual stresses of 29.2 MPa and 25.6 MPa, respectively. Thus, an increase in cure temperature results in a lower level of tensile residual stress. While this difference is small and the experimental error in this analysis is relatively high, this trend is still significant. Initially, this seems counterintuitive as higher curing temperatures should lead to higher levels of residual stress as there will be a larger thermal and DOC gradient through the thickness of the sample. However, one aspect to consider is the T_g^{cured} data gathered in section 3.6 from the DMA analysis. From this we can see that the 180 °C samples are curing above the T_g^{hot} temperature of the EF7017 resin, 145 °C. As the cure temperature is a lot higher than T_g , the resin remains in a rubbery phase for most of the cure cycle, molecular mobility is increased, viscoplastic behaviour is dominant and stresses can relax. This phenomenon is key to defining residual stress in rapidly cured laminates and will be discussed in more detail in chapters 6, 7 and 8.

Additionally, EL2 specimens cured at 60 °C for 6 hours were tested, and an EL2 material fringe value was found, to compare to a more traditionally cured resin system to the rapidly cured samples. As can be seen from Figure 64 and Figure 66, approximately half a fringe was visible through the thickness (side-on). This resulted in approximately 2 MPa of tensile residual stress in the slow cured samples, an order of magnitude lower than the lowest residual stress levels found in the rapidly cured samples. This corroborates with the findings in chapter 4.

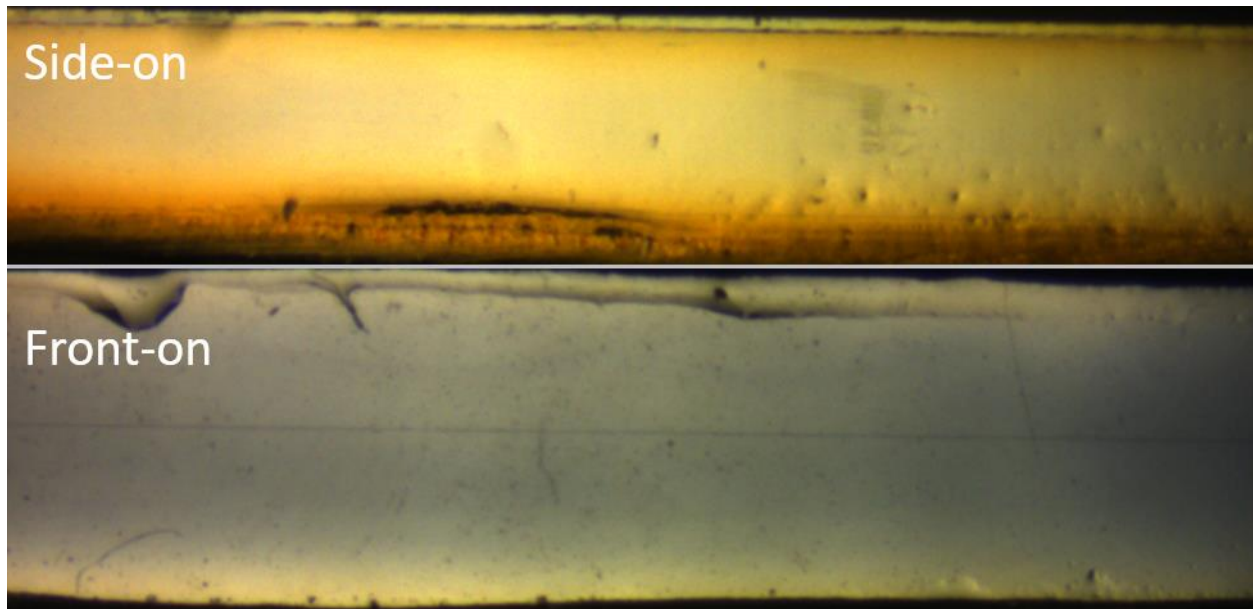


Figure 66: Above, side-on, and below, front-on, view in circularly polarised light - EL2 60 °C for 6 hours

While this technique has a limited resolution of approximately $\pm \frac{1}{4} N$ (or ± 1.8 MPa for EF7017) due to the difficulty in determining fringe orders lower than this with the human eye, this technique still offers a unique insight into the internal residual stress state of rapidly cured resin. With photoelasticity it was possible to differentiate between various residual stress states and successfully relate that to the curing condition. The effect of residual stress gradients through the thickness due to differential heating is clearly identified and a comparison to a slow curing resin system can be made. However, with residual stress being so high it was not possible to more accurately quantify this using a GFP. Future work will be to use manual phase stepping to more accurately decouple the closely packed fringes to better quantify the residual stress state in rapidly cured neat resin samples.

Again, this analysis of neat resin samples is limited in its application to fibre reinforced laminates as it clearly does not account for fibre restraining effects. However, while this might not reflect the true residual stress state of a fibre reinforced laminate, it does offer a unique insight into the effect of a temperature and DOC gradient has within a laminate. A traditional classical laminate analysis would conclude that a neat resin sample is completely stress free as it is not constrained by any fibres. From this experimental work it is evident that this is not the case and in fact there are very large amounts of residual stress present in rapidly cured

neat resin samples. This is also true for UD laminates in the transverse and out-of-plane directions. This will be shown in chapters 7 and 8.

5.4. Conclusions

In this chapter it has been shown that photoelasticity is an effective method for investigating full-field residual stress fields in rapidly cured neat resins. Regardless of the cure temperature, a tensile residual stress developed through the full thickness of the resin specimen with only small differences in residual stress found with varying cure temperature when symmetrical heating was applied. The assumption that the in-plane principal residual stresses were approximately equal, $\sigma_1 \approx \sigma_2$, was also confirmed through the lack of fringes when looking through the thickness of the sample. Differential heating resulted in higher levels of tensile residual stress being developed on the hotter side of the specimen due to an uneven DOC distribution across the thickness of the specimen. Additionally, the residual stress levels seen in a slow curing resin system (24 hours at room temperature and then 6 hours at 60 °C) was found to be an order of magnitude lower than that seen in the rapidly cured samples. Thus, the main aim of this chapter, to gain a full-field insight into the variation of residual stress in variably cured resins, has been met. However, one shortcoming of this technique is that it offers relatively low resolution and accuracy in the analysis of residual stress due to the subjective nature of the determination of fringe order. An attempt to use a GFP was made to quantify residual stress in rapidly cured samples. However, the fringe order of the samples was too high and the fringes too tightly packed for the signal to be decoupled and analysed. Future work would be to use phase stepping to quantify residual stress further and more accurately in neat resins [229].

6. Measuring residual strain using embedded optical fibres

6.1. Introduction

The purpose of this chapter is to gain a novel insight into the development of residual strain during the rapid cure of thermoset fibre reinforced composites. As discussed in chapter 2, embedding FBGs into laminates offers the unique ability to monitor the progression of cure while still being non-invasive and does not require the analysis to be destructive, allowing for future work to take advantage of the already embedded FBGs. Here, the transverse strain of UD composites will be measured using embedded FBGs at both the inner and outer thicknesses in a variety of laminates cured at different temperatures and of different thicknesses. FBGs have been shown to bond well in rapidly cured composites in chapter 4, and give a unrivalled insight into the of residual strain state of rapidly cured composites.

First, a methodology for measuring residual strain in composites with embedded FBGs will be outlined, taking into account the specific needs of rapidly cured composites. Next, the in-plane thermal history of rapidly cured composites will be investigated to determine how applicable a homogenous in-plane thermal assumption is. This is then used to determine the location of the embedded thermocouple to account for thermal effects on the FBG. A preliminary investigation as to the appropriateness of various FBG configurations in rapidly cured composites is then given and one configuration is chosen for further investigation. An example strain history of a rapidly curing composite is analysed to identify the various physical phenomena that occur during cure.

Finally, an analysis of the effect of laminate thickness and cure temperature can be made on the residual strain state of a rapidly cured laminate and a qualitative assessment of the residual stress state of those laminates can also be made. The experimentally determined strain histories will then be used to verify numerically determined residual stress simulations in chapter 7. Additionally, a preliminary investigation into the applicability of using tailed FBG sets to perform in-situ measurements of modulus/cure is given. This offers the potential for a more comprehensive data set to verify simulations in future work.

The aim of this chapter is:

- To determine the effect of varying laminate thickness and cure temperature in rapidly cured UD composites on the residual strain state of a laminate using embedded FBGs.

The objectives of this chapter can be summarised as:

- Establish an effective and reliable methodology for embedding FBGs in rapidly cured composites
- Perform a thermal validation of the in-plane variation in temperature during cure to verify the constant in-plane temperature assumption
- Use the residual strain history of various curing conditions to provide a qualitative assessment of the residual stress state of each laminate and the contributing mechanisms.

6.2. FBG Theory

An optical fibre consists of a glass core, a cladding layer with a lower refractive index than that of the core and a coating layer to aid adhesion and give strength. Light is passed through the core and is totally internally reflected by the cladding due to its lower refractive index. An FBG is fabricated by using a UV laser to periodically etch the surface of the core of an optical fibre resulting in a periodic variation in the refractive index of the core in the etched area. When light is passed through the etched area, or ‘grating’, a specific wavelength of light known as the Bragg wavelength, λ_B is reflected by the grating which is a function of the grating spacing, Λ and the effective refractive index of the core, η_{eff} as described by Equation (29). This is shown diagrammatically in Figure 67. The reflected light is then detected by an interrogator unit connected to the end of the fibre and the wavelength of the reflected spectra can be measured.

$$\lambda_B = 2\eta_{eff}\Lambda \quad (29)$$

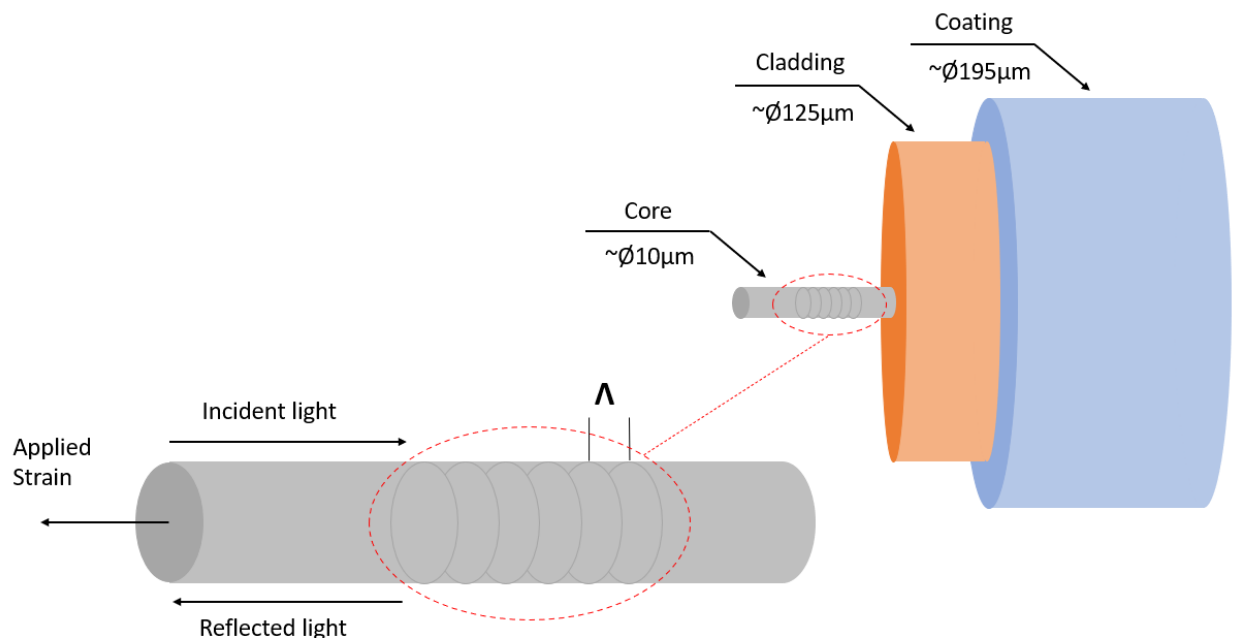


Figure 67: Working principal of FBGs

If a mechanical strain, ε is then applied to the FBG or it experiences a temperature change, T then the grating spacing changes and the reflected Bragg wavelength changes accordingly. This relation can be described with the partial differential equation shown in Equation (30)

$$\Delta\lambda_B = 2 \left[\frac{\partial n_{eff}}{\partial \varepsilon} \Lambda + n_{eff} \frac{\partial \Lambda}{\partial \varepsilon} \right] \Delta\varepsilon + 2 \left[\frac{\partial n_{eff}}{\partial T} \Lambda + n_{eff} \frac{\partial \Lambda}{\partial T} \right] \Delta T \quad (30)$$

then, Equation (29) and (30) can be combined to give Equation (31)

$$\Delta\lambda_B = \lambda_B \left[\frac{1}{n_{eff}} \frac{\partial n_{eff}}{\partial \varepsilon} + \frac{1}{\Lambda} \frac{\partial \Lambda}{\partial \varepsilon} \right] \Delta\varepsilon + \lambda_B \left[\frac{1}{n_{eff}} \frac{\partial n_{eff}}{\partial T} + \frac{1}{\Lambda} \frac{\partial \Lambda}{\partial T} \right] \Delta T \quad (31)$$

where the following constants are described in Equation (32)

$$\begin{aligned} \frac{\partial \Lambda}{\Lambda} &= \partial \varepsilon \\ P &= -\frac{1}{n_{eff}} \frac{\partial n_{eff}}{\partial \varepsilon} = \frac{n_{eff}^2}{2} [p_{12} - \nu(p_{11} + p_{12})] \\ \alpha_n &= \frac{1}{n_{eff}} \frac{\partial n_{eff}}{\partial T} \\ \alpha_f &= \frac{1}{\Lambda} \frac{\partial \Lambda}{\partial T} \end{aligned} \quad (32)$$

This results in Equation (33)

$$\Delta\lambda_B = \lambda_B(1 - P)\Delta\varepsilon + \lambda_B(\alpha_n + \alpha_f)\Delta T \quad (33)$$

where P is the strain optic coefficient of the glass, p_{11} and p_{12} are the elasto-optic coefficients of the strain optic tensor, ν is the Poisson ratio of the optical fibre, α_n and α_f are the thermo-optic constant and CTE of the fibre respectively. This can be further simplified to be expressed in terms of strain sensitivity, S_ε and thermal sensitivity, S_T as shown in Equation (34):

$$\begin{aligned} S_\varepsilon &= \lambda_B(1 - P) \\ S_T &= \lambda_B(\alpha_n + \alpha_f) \end{aligned} \quad (34)$$

which finally simplifies to Equation (35).

$$\Delta\lambda_B = S_\varepsilon\varepsilon_z + S_T\Delta T \quad (35)$$

The fibres used in these experiments were obtained from FBGS Technologies GmbH and have reported sensitivity values of $7.8 \mu\varepsilon^{-1} \times 10^{-7}$ and $6.5 \text{ K}^{-1} \times 10^{-6}$ for S_ε and S_T respectively [194]. From Equation (35), it can be seen that variations in both temperature and mechanical strain causes a shift in the Bragg wavelength. Therefore, when using FBGs to monitor cure in composite laminates it is critical to be able to separate these two components so that the actual mechanical strain due to resin thermal expansion and shrinkage is known and the contribution of the thermal expansion of the optical fibre is discretised. This can be done by measuring the temperature at the FBG and then removing this term from Equation (35). Measuring the temperature can be done with a simple thermocouple or an additional FBG can be embedded nearby with a sufficiently stiff tube surrounding the grating, thereby isolating the axial strain component and leaving just the thermal component. This latter way has the benefit of being less intrusive in the laminate, as optical fibres are an order of magnitude smaller than traditional k-type thermocouples. Additionally, if an optical fibre with multiple FBGs along its length is being used, one FBG can be used for temperature and another for strain. Due to the high expense of FBGs, k-type thermocouples were used to monitor temperature at the embedded FBG location in this work.

6.3. Materials and Method

In this work, FBGS low bend loss fibres with a cladding diameter of 125 μm and coated fibre diameter of 195 μm were used. Two manufacturing techniques for inscribing the gratings were

used. First, Drawn Tower Gratings (DTG) which inscribe the grating with UV light as the optical fibre is being drawn into a fibre were used which allows for superior mechanical properties of the fibre compared to more traditional techniques. Second, Femtosecond Gratings (FSG) were used for fibres with small grating lengths as this process has the advantage of enhanced reflectivity of the reflected spectra by utilising ultra-fast laser pulses during the manufacturing process. This is particularly useful when using small grating lengths as the intensity of the reflected peak is naturally lower than with larger gratings, and thus the stronger peak can be more easily detected by the interrogator. The specifications of the fibres used in this work are outlined in Table 10 with the nominal Bragg wavelength for the inscribed gratings being noted. In the case of DTG_1534/59, there were multiple DTG's along one fibre, a Bragg wavelength range has been given with each consecutive grating along the fibre having a Bragg wavelength of 2.5 nm more than the previous, starting at the lower end of the range.

Table 10: Specifications of the optical fibres used

Name	Manufacture method	Wavelength (nm)	Number of gratings	Grating length (mm)	Fibre length (m)
DTG_1534/59	DTG	1534 - 1559	11	8	7.8
FSG_1550	FSG	1550	1	1	1.5
FSG_1546	FSG	1546.5	1	1	1.5

All the fibres used have a proprietary ORMOCER® (Organic Modified Ceramic) polymer coating around the cladding of the fibre which provides high adhesion to the fibre (as shown in chapter 4), a high modulus, a large temperature operating range of -180 °C to +200 °C [231] and has been successfully used by many other authors [18][144][196]. All fibres were fitted with FC/APC connectors by the manufacture to minimise any errors caused by poorly fitted connectors. These are paired with a SmartFibres SmartScope interrogator unit which operates in a wavelength range of 1528 nm to 1568 nm, a scan frequency of 5 Hz and a wavelength resolution of 0.2 pm and a wavelength accuracy of +/- 2 pm (approximately +/-1.6 µε) [232]. SmartFibres SmartSoft software is used to capture the reflected wavelength data which was subsequently corrected for temperature using Equation (35).

All residual strain measurement experiments used 150x150 mm EF7017 [0]_n prepreg laminates, where n was varied to achieve various thicknesses. Fibres were embedded transverse to the fibre direction at the first ply in the laminate and at the mid-thickness ply to measure the transverse matrix residual strain during cure at the outer and inner thicknesses of the laminate. FBGs were embedded transverse to the fibre direction to better capture the matrix dominated response. The fibre gratings were placed in the in-plane centre of the laminate and the optical fibre continued to the edge of the laminate, thereby leaving a 75 mm “tail” of optical fibre after the grating. A Ø0.5 mm PTFE tube was placed around the fibre optic cable at the point where it enters the laminate to provide some mechanical support as initial tests had shown this to be an area prone to failure.

Preliminary testing methodology

For the preliminary tests, k-type thermocouples were placed approximately 25 mm away from the embedded grating on the same ply as the gratings to allow for a representative temperature reading and to not affect the strain measurement taken by the grating. However, for the final testing setup, a thermal validation procedure was carried out to determine the furthest distance from the embedded FBG that the thermocouple could be placed while retaining a representative thermal history. This is outlined in the following section. The embedded sensor layup for the preliminary test is shown in Figure 68.

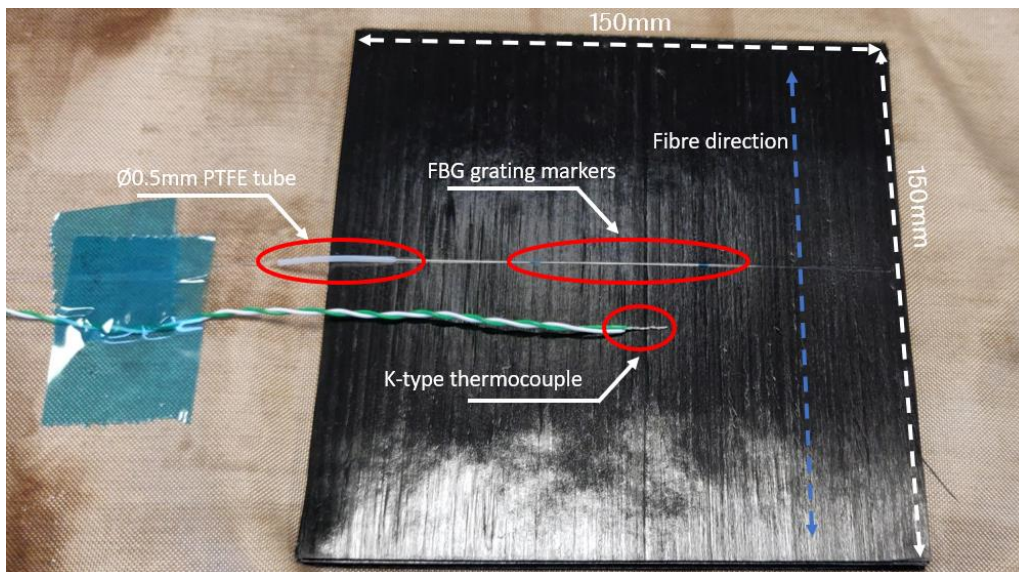


Figure 68: Embedded sensor for residual strain measurement setup at mid-thickness. An example from preliminary testing

For the preliminary tests, the DTG_1534/59 fibre was used. Initially, the end most FBG from the optical fibre was embedded into the laminate, the laminate was cured, the fibre was cut off and then the next FBG along the length of the fibre was embedded, and so on. This was done as one of the expenses involved in FBGs is the connector on the end, so this was thought to reduce cost. However, as will be discussed in the preliminary results section, this was not possible and optical fibres with one FBG were preferred for the final testing setup. Additionally, during preliminary testing, simple shims were used to set the thickness of the laminate in the hot press, ensuring it was not over compacted. However, as the samples being pressed were UD, resin was unconstrained in the transverse direction and would flow out of the laminate upon compaction and heating. A metal “collar” was developed to mitigate this as will be discussed in the final testing methodology. The cure schedule and laminate layup for the preliminary laminates is outline in Table II in the final testing methodology section.

Thermal validation

To ensure that the embedded thermocouples give a temperature measurement that is representative of the temperature at the embedded optical fibre, a temperature validation experiment was performed. An EF7017 [0]₂₀ 100x100 mm laminate with a width and length L , was made with three thermocouples, $T1$, $T2$ and $T3$ embedded at the mid-thickness. Thermocouples $T1$, $T2$, and $T3$ were placed at $L/2$, 50 mm from the edge, $L/4$, 25 mm from the edge and $L/8$, 12.5 mm from the edge respectively. The laminate was then placed in a pre-heated hot press at 180 °C and cured for 1 minute. The results of the thermal validation can be seen in Figure 69.

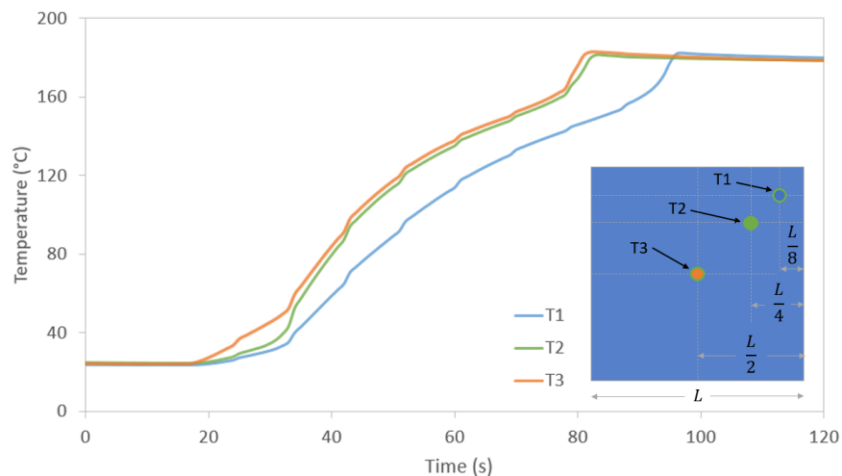


Figure 69: Thermal validation of thermocouple placement in EF7017 100x100 [0]₂₀ laminate

Here, it is evident that $T3$ and $T2$ give very similar values during cure with $T2$ reporting $2.3\text{ }^{\circ}\text{C}$ lower than $T3$ on average. When six thermocouples were placed in a heated water bath the average maximum difference between the thermocouples was $1.9\text{ }^{\circ}\text{C}$. Therefore, we can say that thermocouples 2 and 3 read results similar to that of the error between thermocouples. However, there was an average maximum difference of $12.6\text{ }^{\circ}\text{C}$ between $T3$ and $T1$. Thus, it can be concluded that for a thermocouple to representatively measure the thermal conditions at the centre of the laminate it must be placed at least 25 mm away from the edge of the laminate to avoid thermal leakage to the retaining mould.

Final testing methodology

A metal retaining “collar” with the same thickness as that of the final cured laminate is placed around the 150x150 mm laminate stack before being hot pressed. Grooves in the collar accommodate the optical fibre and thermocouples. The collar has two functions, firstly it allows the laminate to retain its shape as UD laminates will deform significantly in the transverse direction during cure as the material properties are resin dominated in this direction. Therefore, during liquid resin phase of cure, there is almost zero stiffness in the transverse direction which causes the laminate to completely lose its form. Secondly, it controls the thickness of the laminate. The hot press used in this work is completely analogue and lacks any displacement instrumentation. Additionally, pressure is controlled on an analogue gauge which has a resolution of approximately ± 3 bar. Therefore, the retaining collar is critical for controlling the final volume fraction of the laminate and for retaining its shape. The retaining collar which is placed over the final laminate stack is shown in Figure 70.

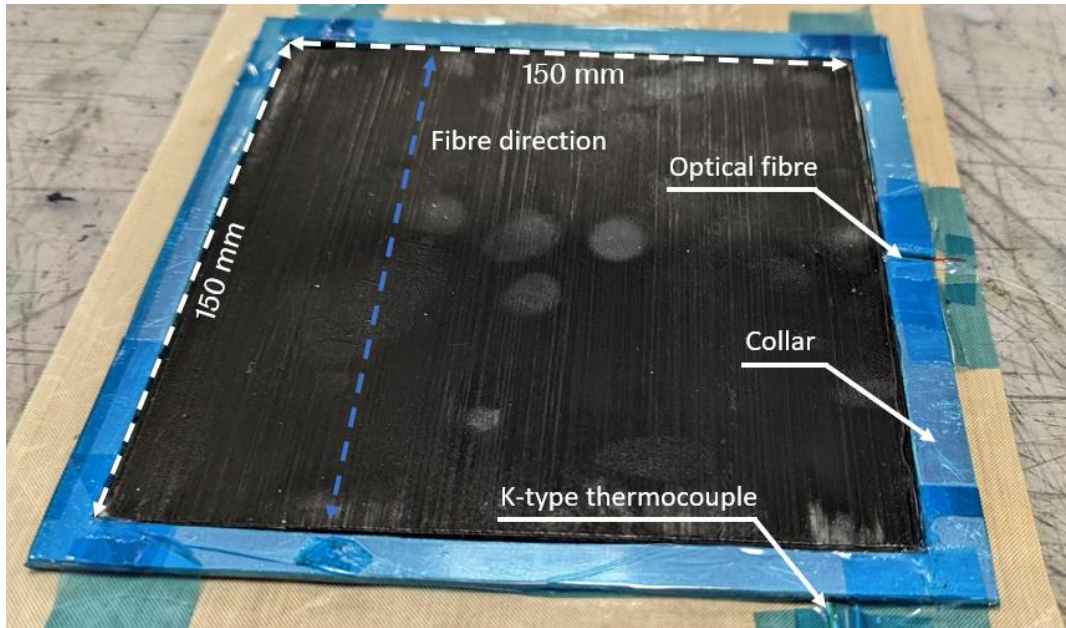


Figure 70: Embedded sensor with retaining collar

To investigate both the effect of thickness and curing temperature on residual strain, two extremes were chosen for thickness and temperature to better highlight these effects. For thickness, samples were designated as either “thick” or “thin” for 6.35 mm and 2 mm laminates respectively. For cure temperature, “Cool” and “Hot” conditions were used which were cure temperatures of 140 °C and 180 °C respectively with cure times altered accordingly. The full experimental specifications are outlined in Table 11.

Table 11: Residual strain experiment specifications

Test	Fibre used	No. plies	Thickness (mm)	Cure temperature (°C)	Cure time (min)
Preliminary	DTG_1534/59	40	8.75	140 & 170	8 & 2
Cool_thin	FSG_1550	11	2	140	8
Cool_thick	FSG_1550	35	6.35	140	8
Hot_thin	FSG_1550	11	2	180	1
Hot_thick	FSG_1546	35	6.35	180	1

Tailed FBG method

One of the key challenges of analysing residual stress in rapid curing composite systems is the difficulty of obtaining meaningful material property data that is representative of the actual cure of the resin system. For example, accurately determining the resin matrix modulus as it

changes with cure for a given cure cycle is almost impossible using conventional methods such as DMA or using rheometers as it is not possible to apply a representative heating rate of around 200 °C/min. Without a good understanding of the resin modulus throughout the curing process it is difficult to make any inferences into the residual stress state of the curing laminate. However, recent work by Minakuchi et al [233] outlines a technique for performing in-situ monitoring of the composite stiffness, and by extension the resin modulus, during cure using a pair of tailed FBGs whilst also capturing the shrinkage strain of the laminate. This technique works by utilising the shear-lag effect of the far field strain transferring along the edge of the optical fibre to the FBG. Upon gelation of the resin matrix, an interfacial bond is established between the optical fibre and the resin matrix and resin shrinkage strain is transferred to the optical fibre through interfacial shear stress at the edge of the optical fibre. At the beginning of the cure when the resin modulus and therefore interfacial shear stress is low, the length of fibre over which the resin shrinkage strain is transferred, d , is large. As the cure progresses and the resin modulus increases the stress transfer length decreases. Previous work by Minakuchi [160] found that the length of the “tail” of the optical fibre, the amount of optical fibre after the FBG, affects the measured strain value of the FBG with short tails leading to a reduced strain reading due to shear-lag. If the tail is longer than the stress transfer length, then the strain measured is the same as the far field strain. Therefore, by embedding a pair of FBGs with one having a short-tail and the other having a long tail which is greater than d , it is possible to calculate the laminate stiffness and therefore the resin modulus and DOC.

6.4. Results and discussion

Preliminary test results

During initial testing with the DTG_1534/59 fibre, which had multiple DTGs along its length, a sudden drop-off in strain readings was seen in every test conducted. This can be seen in Figure 71 where “FBG_1” is the FBG embedded into the laminate and “FBG_2” is the nominal Bragg wavelength of the subsequent FBG in the optical fibre that has not been embedded in the laminate.

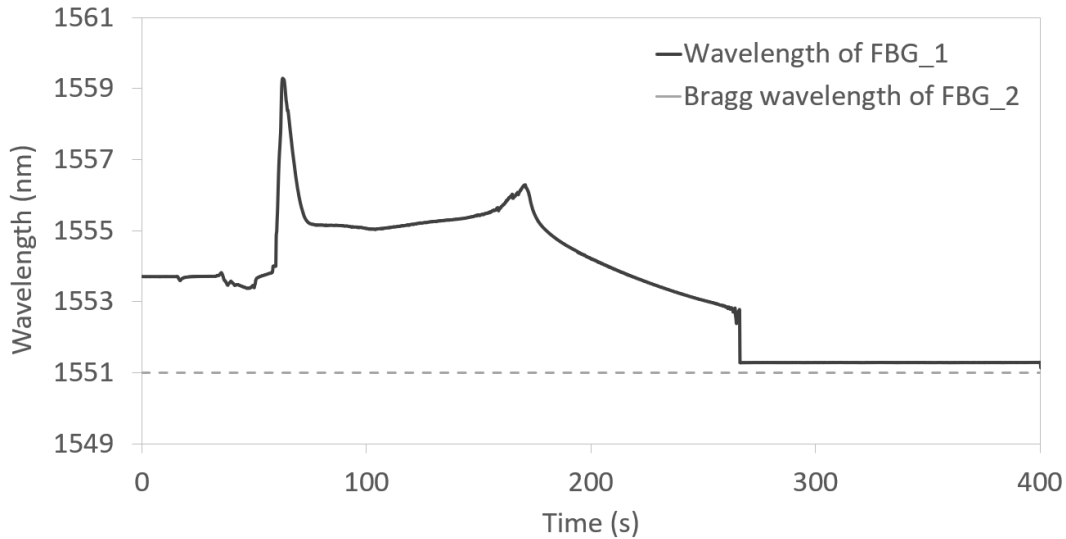


Figure 71: Preliminary embedded sensor wavelength results

Initially, it was thought that this was due to the optical fibres either de-bonding or failing completely due to high strains experienced during cure. However, as discussed in section 4.5, it has been established that there is good bonding between the embedded optical fibre and resin matrix in the samples tested. Additionally, the sensor drop off occurs after approximately 0.3% strain in the fibre which is well below the manufacturer's quoted strain to failure value of 5% [194]. Therefore, another explanation for this behaviour is required. A compressive strain is applied to the embedded sensor, FBG_1, the reflected Bragg wavelength then decreases causing the spectra peak to shift towards the peak of the next grating, FBG_2, in the optical fibre. When these two peaks begin to overlap the SmartSoft software is unable to discern one peak from the other and simply reports the wavelength value of the peak with the highest wavelength, FBG_2. Therefore, the strain reading after the sensor drop off is the strain reading on FBG_2 which is not embedded within the laminate and therefore returns a strain value of zero. As the nominal wavelength spacing between the gratings in these fibres is 2.5 nm (approximately 3000 $\mu\epsilon$) there can only ever be a maximum delta of 3000 $\mu\epsilon$ between gratings. Thus, for these experiments it was not possible to use fibres with multiple gratings on with only one grating embedded, as the strains being investigated are too high.

Figure 72 shows the progression of the reflected spectra during a typical cure. Extensive peak splitting of the reflected peak during cure can be seen. As the cure progresses and compressive strain develops, the reflected peak from the embedded grating widens and splits, forming multiple peaks. Peak splitting is caused by a growing differential in transverse to axial strain

acting on the fibre. This causes a birefringence effect in the core of the optical fibre, leading to two orthogonal polarization axes being developed in the grating. Thus the reflected peak splits and it becomes challenging to determine a true reflected wavelength, and therefore strain, value [148][151]. As previously mentioned in section 2.4.3.5, it is possible to use the reflected split peaks to determine transverse strain, relative to the axis of the grating. However, in this work the strain transverse to the reinforcing fibre direction (axially to the embedded optical fibre) is the primary strain of concern. Thus, the peak splitting seen here only serves to lower the accuracy of the reported reflected wavelength and therefore strain values. A smaller grating gauge length will lessen the peak splitting seen as there is a smaller area of optical fibre for the transverse strain to be applied to. Thus, a smaller grating gauge length of 1 mm, compared to 8 mm, will be used to minimise this effect. Indeed, in the subsequent testing of FBGs with a grating length of 1 mm, no significant peak splitting or reduction in reflectivity was observed.

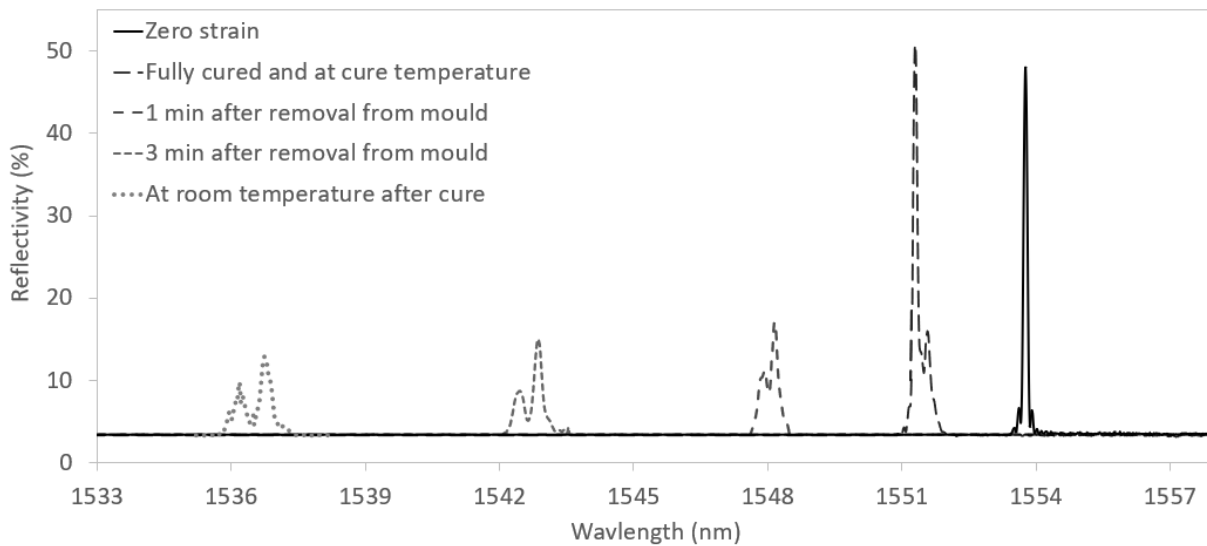


Figure 72: Entire reflected spectra for preliminary embedded sensor tests

Additionally, for the Hot_thick sample, there were such large strains, especially before gelation, that the Bragg wavelength exceeded that of the dynamic range of the interrogator with the 1550 nm gratings. Thus, to accommodate this, gratings with a Bragg wavelength of 1546 nm were used. With this change, the measured strain almost exceeded the entire dynamic range of the interrogator (high-end to low-end) and as such it is recommended that

for future work an interrogator with a larger dynamic range is used for rapidly curing composite investigations.

Throughout all the embedded FBG testing conducted in this work there were large amounts of noise in the reported Bragg wavelengths from the interrogator unit and therefore in the residual strain data. This is thought to be caused by a combination of several factors including fast strain development which the interrogator unit had difficulty determining, contamination of the interrogator unit and possible effects of elevated temperature. However, this resulted in single measurement points (with a 5 Hz sampling frequency) being an order of magnitude too large. Therefore, these errors could be easily determined, removed, and then interpolated between. Thus, the data presented here has had erroneous readings removed so that graphs can be more easily analysed. The original graphs can be seen in Appendix E.

Final test configuration – example strain history

The embedded strain measurements for the outer (ply 1) and inner plies (ply 5) along with the temperature measurements at those locations are presented for one experimental condition, Cool_thin. Figure 73 and Figure 74 show time periods of 0-120 seconds and 0-1100 seconds after being placed in the hot-press, respectively. By using this typical experiment as an example, various critical points in the curing process can be identified which will aid in future discussion in this work.

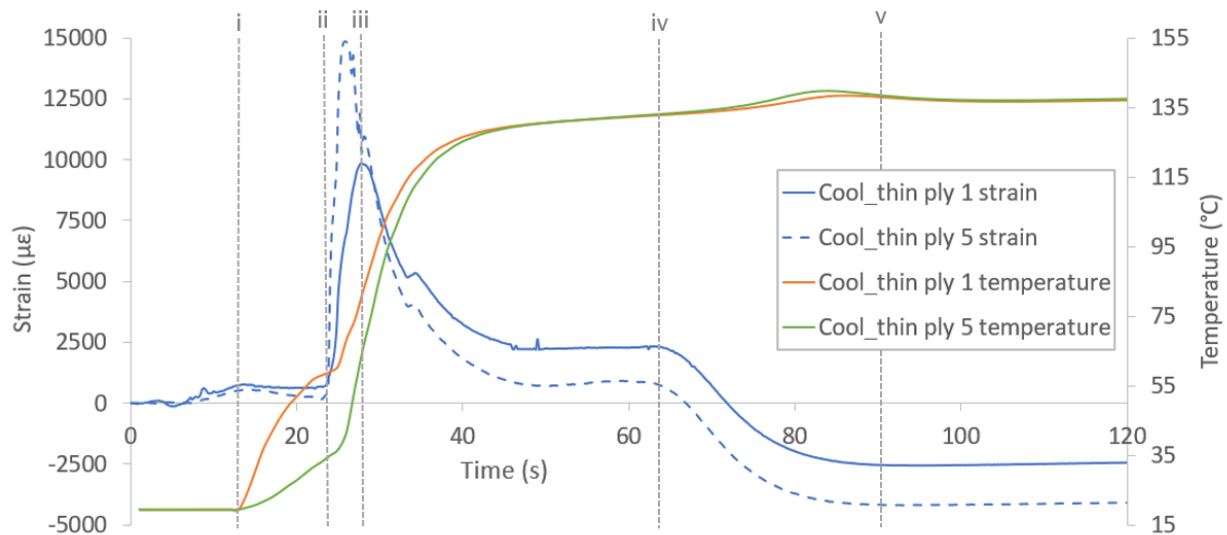


Figure 73: Cool_thin embedded strain and temperature data for 0-120 seconds

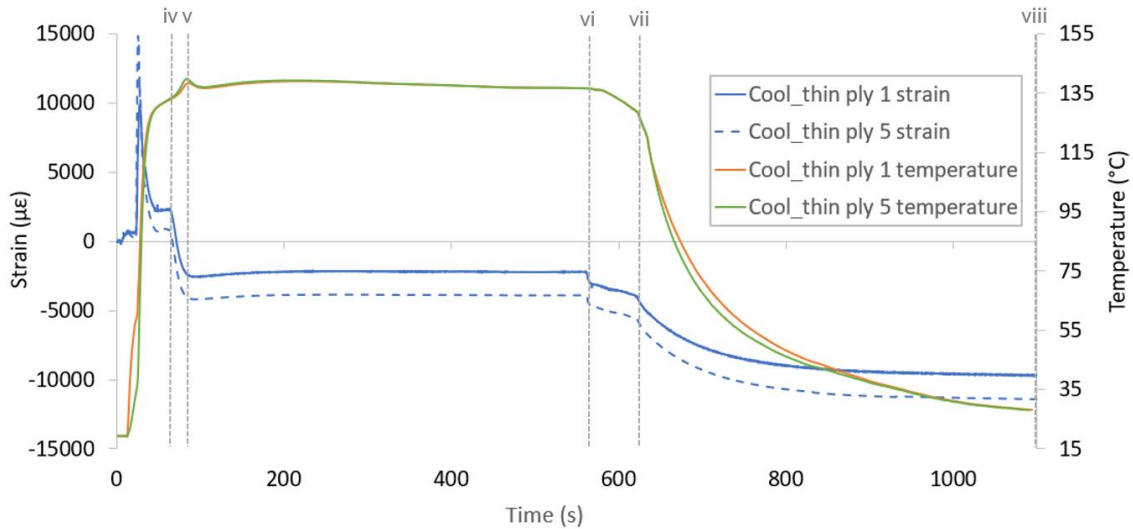


Figure 74: Cool_thin embedded strain and temperature data for 0-1100 seconds

From Figure 73 five key points can be identified. First, point i, is the moment the sample is placed in the pre-heated hot press and is identified by an increase in temperature within the outer ply of the laminate. Secondly, point ii, is the start of the hot press applying pressure to the laminate. The delay between point i and ii is due to the hot press hydraulics being manually pressurised with a hand pump. Next, point iii, is when the target applied pressure is reached and pumping of the hydraulic cylinder stops. A sharp decline in strain is then seen which is caused by the matrix becoming more liquid and the effective applied pressure of the cylinder dropping. This is because only the position of the head of the hot press is controlled and not the pressure being applied. Point iv occurs when strain begins to develop after the strain from the applied force of the hot press evens out. This is caused by the resin matrix gelling, α_{gel} , and E' increasing while E'' decreases, thereby allowing for strain to be stored elastically and residual strain to develop. In this work, the onset of α_{gel} will be defined as the point at which strain suddenly begins to develop after the pressing phase of the cure has been completed. This has been used by other authors in the literature [234][235][236] and is generally considered to be an accurate method for determining gelation. However, alternative methods for determining α_{gel} using FBGs will be discussed later in this chapter. This point in the cure cycle is critical as before this, all strain captured by the embedded sensor is dissipated viscously into the liquid matrix and does not contribute to residual stress [237][233][234][235].

It can be seen that in the Cool-thin example case, almost all of the thermal expansion of the resin matrix caused by the heating of the laminate happens before α_{gel} between point i-iv. This

is evident by the fact that the maximum temperature of the laminate is almost reached by iv. Therefore, all the tensile strain created due to this thermal expansion is dissipated viscously as the resin matrix is still liquid at this point. Thus, the majority of the thermal effect on residual strain is compressive and developed during the cooling of the laminate for the Cool_thin example. From point iv to v, chemical shrinkage is the dominant mechanism contributing to the strain being developed [159][238][239]. This is evidenced by the temperature remaining relatively constant during this time, indicating that the strain being developed is not being caused by thermal effects. Additionally, this strain occurs from α_{gel} to the exotherm of the sample as indicated by the sharp rise in temperature at 80 seconds. During this time a large part of the curing of the matrix takes place, and as such, a large part of the chemical shrinkage occurs during this time [126]. Now looking at a wider time range in Figure 74, point vi is when the pressure from the hot press is released after the given cure time, in this case 8 minutes after the laminate reached cure temperature (140 °C) and there is a sharp dip in strain. There is then a small delay until the laminate is removed from the mould at point vii and then a rapid development of compressive strain is observed as the temperature of the laminate drops to room temperature at point viii. As the resin matrix is liquid and $E'' \gg E'$ before α_{gel} then all strain that occurs before α_{gel} does not contribute to residual stress as it is dissipated viscously. Therefore, to gain a meaningful insight into the effect of residual strain on the residual stress state of the laminate and to allow for easy comparison between curing conditions, the measured strain is zeroed at α_{gel} . This is shown for Cool_thin in Figure 75 between 0-1000 seconds after α_{gel} .

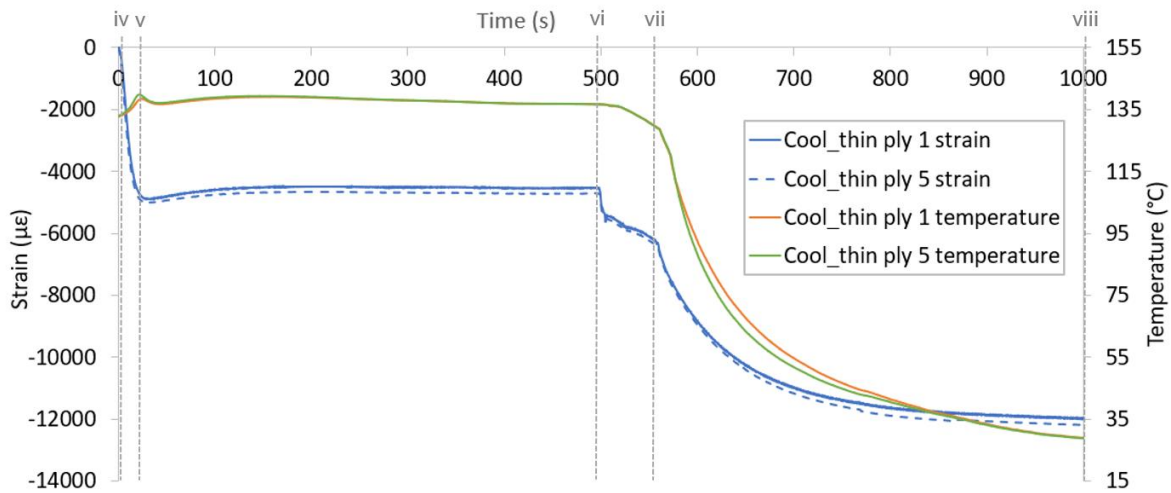


Figure 75: Cool_thin embedded strain and temperature data, strain zeroed at α_{gel} (iv)

Now, Figure 75 more clearly shows the development of transverse residual strain during cure, with both chemical shrinkage and thermal effects clearly visible. Chemical shrinkage occurs during the polymerisation of the resin matrix between iv-v. Then, the compressive thermal strain is applied when the temperature drops after removal from the hot press, vi-viii.

Final test configuration – all results

Results from all of the experiments outlined in Table 11 are presented in Figure 76 and Figure 77 between times of 0-3500 and 0-1000 seconds respectively.

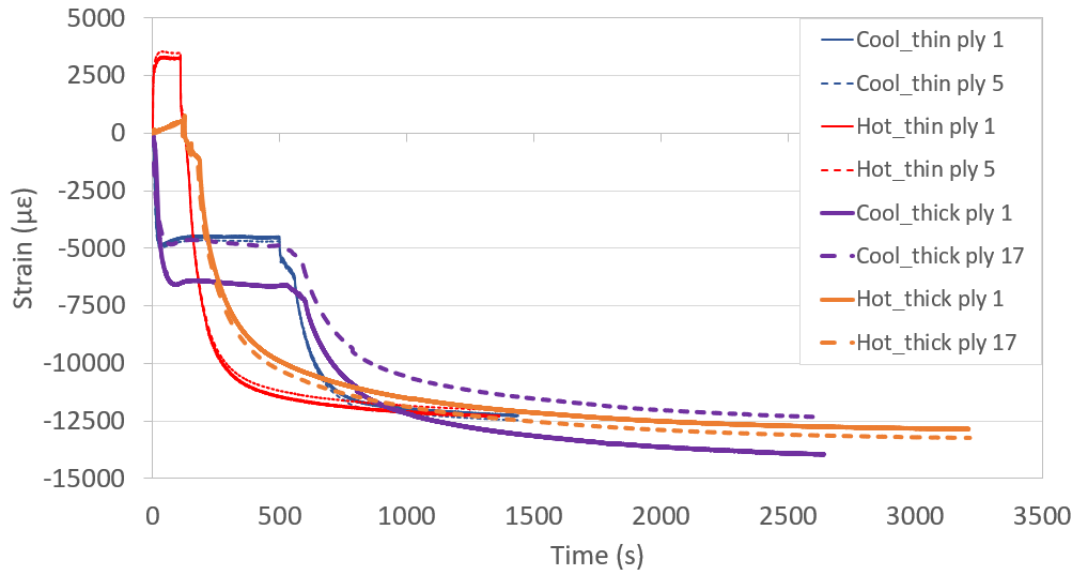


Figure 76: Embedded strain data, zeroed at α_{gel} for time 0-3500 seconds

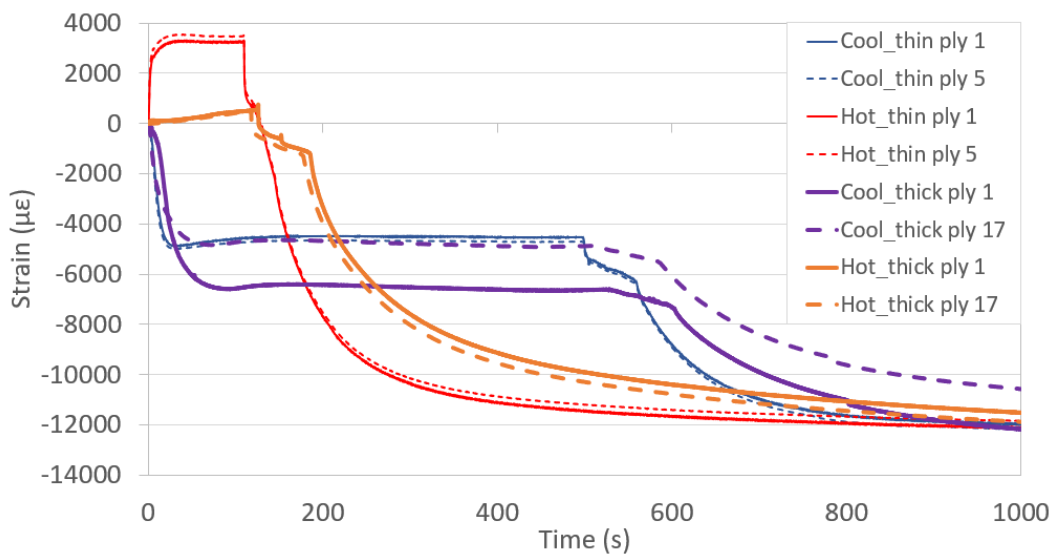


Figure 77: Embedded strain data, zeroed at α_{gel} for time 0-1000 seconds

Examining the full strain history for all the laminates tested in Figure 76, it can be seen that the final total residual strain for all thermal histories, laminate thicknesses and sensor locations are broadly similar across all cases. The largest deviation from the average being approximately a 9% difference in total strain in the Cool_thick ply 1 case. Additionally, the average total final residual strain is approximately $-12,800 \mu\epsilon$ (or -1.3%) which is significantly higher than the final strain seen for slower curing laminates found in the literature. For example, Minakuchi et al [233] measured a final mid-thickness in-plane strain of $-2850 \mu\epsilon$ with a $100 \times 100 \times 7.5$ mm UD laminate cured at 90°C for 5 hours; while Qi et al [240] found a final residual strain of $-5183 \mu\epsilon$ with a $200 \times 200 \times 2.5$ mm UD laminate cured at 80°C for 10 minutes and then 100°C for an additional 20 minutes. However, it should be noted that strain was not zeroed at gelation in the work by Qi et al [240], so the true value of residual strain is likely to be closer to $-3500 \mu\epsilon$. Again, Hu et al [154] found a total final residual strain of approximately $-7500 \mu\epsilon$ using a $110 \times 110 \times 10$ mm UD laminate with a cure schedule of 130°C for 60 minutes and then an additional 3.5 hours at 180°C . It is evident that the experiments seen in the literature have used a variety of experimental methodologies and as such cannot be directly compared. However, it is clear that the experiments conducted in the current work use cure times one or two orders of magnitude smaller than that seen in the literature. Thus, this current work gives us a unique insight into the residual strain history of rapidly curing laminates. These rapid curing conditions have resulted in very large levels of transverse residual strain to be developed within the laminate, both in the mid-thickness and outer edges for all cases tested.

However, the total final strain developed after cure tells us little about the residual stress state of each of the laminates tested other than it is likely to be higher than that seen in the literature. This is because the point at which the strain occurs during the curing process is critical as E' varies during cure which will consequently change the amount of residual stress developed with a given strain. Therefore, a closer examination of where strain developed during cure and the mechanisms that cause that strain must be undertaken to begin to analyse the residual stress state of the various laminates tested. As a first approximation, it is reasonable to suggest that strain developed from chemical shrinkage (iv-vi) occurs when $E' < E_{22}$, where E_{22} is the transverse modulus of the fully-cured laminate. This is because chemical shrinkage happens almost entirely during the curing process when E' is relatively

small, before α_{vit} . Then, it can also be approximated that $E' \sim E_{22}$ during the thermal contraction phase (vi-viii) as the resin is fully cured and near its final fully cured modulus. Thus, it is a reasonable approximation that strain developed from chemical shrinkage will result in less residual stress than that developed during thermal contraction. Hence, by analysing the proportion of residual strain developed during the chemical contraction and thermal shrinkage phases the relative total residual stress states of each laminate may be qualitatively analysed. The amount of strain developed in the outer and inner plies by chemical shrinkage (iv-vi) and thermal contraction (vi-viii) for each sample tested are presented in Figure 78 for further comparison.

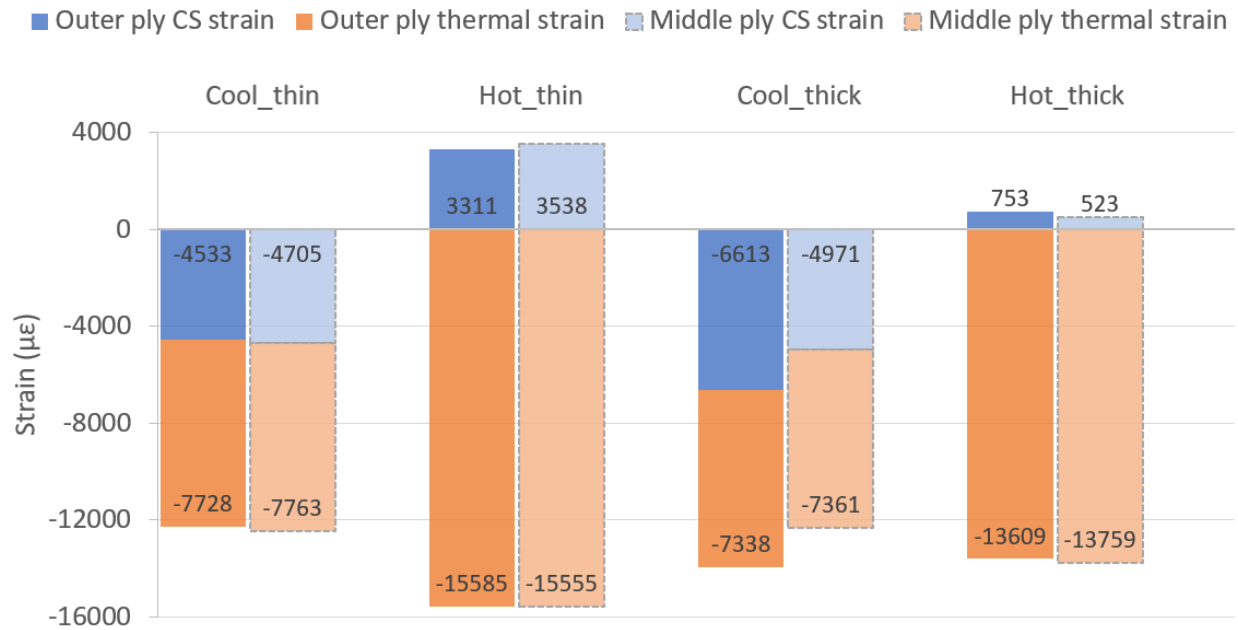


Figure 78: The proportion of residual strain developed from chemical shrinkage, CS, (iv-vi) and thermal contraction (vi-viii) during cure for all tested samples as measured by embedded FBGs at the outer and inner thicknesses.

Here, it is clear that the “Hot” samples have a larger proportion of their total residual strain developed during the thermal contraction phase than the “Cool” samples. As $E' \sim E_{22}$ during the thermal contraction phase, this suggests that the “Hot” samples have higher levels of residual stress than the “Cool” samples. Whilst the final residual strain is similar across all samples, the “Cool” samples have large proportions of their strain develop when the matrix is polymerizing and $E' < E_{22}$. Therefore, the final residual stress in the “Cool” samples will be lower. Of course, this is an oversimplification of the residual stress state of the various

laminates as E' is constantly evolving during cure and in the case of rapidly curing composites like EF7017, it evolves very quickly. However, this technique still offers a unique, if qualitative, insight into the residual stress state of a laminate.

To investigate the apparent positive chemical shrinkage strain developed in the “Hot” samples we turn to Figure 77. Here, we can see that the apparent compressive chemical shrinkage strain (points iv-vi in Figure 75) that occurs after gelation of the “hot” samples is less than that of the “cool” samples. Indeed, the apparent chemical shrinkage strain of the Hot_thin samples is positive. However, this is not the true chemical shrinkage strain of the resin matrix as this is caused by the polymerisation of the resin matrix and will be negative. This can be explained by examining Figure 79 where the temperature recorded by the embedded thermocouple for each cure condition is shown, and zeroed when the sample was placed in the hot press. The temperature at which gelation occurs, as measured by the embedded FBG, is marked with a triangle for every sample at the outer and inner thickness.

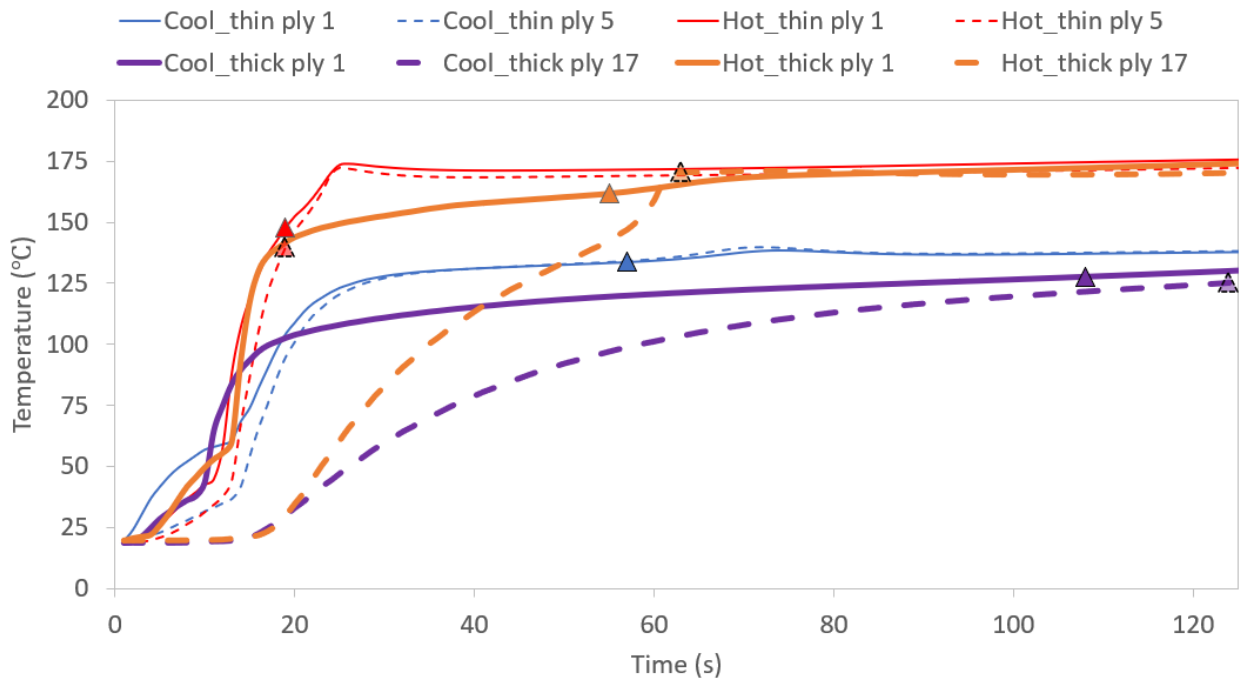


Figure 79: Temperature history of laminates cured with embedded FBGs. Gelation, as measured by embedded FBGs, is marked for each sample at the outer and inner thickness.

Here, the Cool_thin and Cool_thick samples gelation can be seen to occur after the laminate has reached its final cure temperature of 140 °C. This is in contrast with the Hot_thin sample where the temperature is still increasing after gelation. Therefore, in the Hot_thin sample, there is additional tensile thermal expansion counteracting the compressive chemical shrinkage strain, resulting in a net positive strain. Whereas, for the “Cool” laminates the temperature remains relatively constant after gelation so the compressive chemical shrinkage strain can be fully observed. The result of this is that the final total residual strain of “Hot” and “Cool” laminates is similar even though the thermal contribution of strain during the cooling phase is significantly higher for the “Hot” cure condition. However, it is vital to note that this does not mean the final residual stress state of the laminates is similar. In the case of the “Hot” laminates the majority of the strain developed during cure comes after the resin has fully developed its stiffness during the cooling phase of the cure cycle. However, a significant proportion of the strain developed in the “Cool” cure condition laminates is developed early in the cure cycle, right after gelation. Here, the storage modulus of the resin is much lower and as such the resultant residual stress will be much lower for the same given strain. This is because much of the energy imparted into the resin system from thermal expansion and chemical shrinkage is dissipated viscously as E'' and is not negligible at this stage of the cure. However, one factor that has not been considered in this analysis is the T_g and the role of the rubbery phase in dissipating residual stress via viscoplastic mechanisms. This will be discussed and explored further in the following chapters as it is key to determining the final residual stress state of the laminates tested.

Examining the Cool_thick strain response, it is seen to be the only laminate tested that shows a large residual strain gradient through its thickness at the end of cure. Whilst it might be expected that this is purely a function of the thickness of the laminate this does not seem to be the case as the Hot_thick sample shows a much more modest strain gradient through its thickness. The reason for this becomes more clear by examining Figure 79 where it can be seen that the difference between the onset of gelation in the outer and inner thicknesses of the laminate is larger in the Cool_thick sample (16 seconds) compared to the Hot_thick sample (8 seconds). It is thought that there may be some degree of error present in the determination of the onset of gelation in the “Hot” samples. This is due to the resin matrix remaining in its rubbery phase as it begins to gel due to the curing temperature being much higher than its

instantaneous T_g . Therefore, it is difficult to accurately capture the onset of strain at gelation as strain transfer to the FBG is impeded by the viscous resin. This is not the case for the “Cool” samples where a clear gelation point can be determined. Therefore, some care must be taken when interpreting the “Hot” FBG strain data. It is suggested that the Hot_thick gelation points may be earlier than suggested in Figure 79. It is likely that the onset of gelation on the outer plies of the laminate occurs in a similar time to that of the Hot_thin laminate as the thermal histories are similar near the edge of the laminate for both cases. In addition to this, it is thought that the “Hot” samples undergo an extended period of relaxation in their rubbery phase during cure, allowing strain to be equalised through-thickness. This will be discussed in more detail in the following chapters.

From Figure 78 an approximation of the total in-plane transverse chemical shrinkage strain, β_{22} , during cure of the rapidly cured laminates can be made. As will be discussed in the following chapters, it will not be possible to use any strain data from the “Hot” samples, as chemical shrinkage occurs from α_{gel} to α_{vit} which occurs above the T_g^{hot} in this case. Thus, any strain developed here is likely dissipated viscously and as such cannot be used to accurately determine the chemical shrinkage strain contribution. However, this is not the case in the “Cool” samples and the strain developed between iv-v (α_{gel} to α_{vit}) can be used to approximate the chemical shrinkage strain contribution during cure [159][154]. By taking an average between the outer and inner plies, the β_{22} values for the Cool_thin and Cool_thick experiments can be determined to be -4,619 $\mu\epsilon$ and -5,792 $\mu\epsilon$ respectively. This discrepancy is thought to be due to the “thin” sample being more restrained during cure as the surface area to volume ratio of the sample is lower than the “thick” case, thus chemical shrinkage strain is restrained more by the moulding surfaces. Unfortunately, it has not been possible to perform repeats for these experiments to validate this hypothesis. However, it is thought that the Cool_thick sample chemical shrinkage strain is likely to give a reasonable approximation of the in-plane transverse chemical shrinkage value. Therefore, for the numerical analysis conducted in chapter 7, β_{22} will be defined as the strain developed between α_{gel} to α_{vit} in the Cool_thick experiment, -5,792 $\mu\epsilon$ (-0.58%). It should be noted that this can also be used for the out-of-plane chemical shrinkage value, β_{33} as it is transversely isotropic [159] in UD laminates, $\beta_{22} = \beta_{33}$.

Preliminary tailed FBG tests

As previously discussed, it has not been possible to use conventional rheometric methods like DMA to determine the exact resin modulus during the entire cure cycle of the rapidly curing matrices used in this work. However, one potential method for overcoming this has been offered by Minakuchi et al [233] and expanded on by Hu et al [159]. Tailed FBGs are used to perform in-situ resin modulus development monitoring during cure. Tailed FBG modulus monitoring works on the principal of the shear-lag effect. During the cure of a thermosetting matrix, strain is transferred from the matrix to the FBG through an interfacial shear stress arising at the edge of the optical fibre after gelation of the matrix. The strain in the FBG reaches the far-field strain of the resin matrix over a given stress transfer length along the optical fibre. Beyond this stress transfer length, the FBG will measure the far-field strain. Thus, if two sensors are used, one with an FBG placed at a distance further than the stress transfer length and one placed at a distance less than the stress transfer length, then the ability of the resin matrix to transfer strain can be analysed. Therefore, the modulus and DOC of the resin can be determined if various numerical parameters are calculated or obtained through simulation. Due to the limited scope of this work tailed FBGs will not be used to directly determine DOC or modulus progression during cure. However, both gelation and vitrification points can be determined without the need to derive numerically obtained factors. Gelation can be simply defined to be the point at which the relative strain difference between the short and the long tailed FBG begins to increase [154][233][39]. Whilst vitrification can be defined as the point at which the relative strain difference between long and short does not change [159]. Thus, the effective start and end of the E' change can be determined.

An initial test with tailed FBG sets placed at the outer and inner thickness of a Hot_thick laminate was conducted as outlined in the methodology in section 6.3. However, gelation of the Hot_thick laminate does not occur until after the T_g of the fully cured laminate, T_g^{hot} , has been exceeded. This means the resin matrix likely remained in its viscous and rubbery phases during gelation, making capturing gelation and the development of the resin modulus with the shear lag effect challenging. This was due to the resins' rubbery phase having a low elastic modulus and a high loss modulus, causing shear stress to be dissipated viscously and not allowing for any meaningful measurements to be made. This will be discussed further in the

following chapters. Whilst tailed FBG sets offer a unique and exciting insight into the real-time DOC and E' development during cure, viscoelastic and viscoplastic complications were observed. It will not be possible to pursue this investigation further in this work due to material availability constraints. However, this is certainly an interesting area of future work.

6.5. Conclusion

In this chapter a novel insight into the development of residual strain in rapidly curing laminates has been given. Using this experimentally determined data a qualitative assessment of the residual stress state of various laminates has also been given with the effect of laminate thickness and cure temperature on the residual strain history of rapidly cured composites identified. It was found that for the four cases investigated, an increased laminate thickness increases the proportion of residual strain developed due to chemical shrinkage, in the early part of the cure cycle. However, it is unclear if this is indeed a function of only laminate thickness or because the thicker laminate is intrinsically less constrained than the thinner ones which allows for more strain to develop. The strain developed due to chemical shrinkage is complicated to analyse as there are various competing mechanisms at this stage of the cure. Then, it can be clearly shown that an increase in cure temperature leads to more thermal strain. This result is clearly to be expected due to larger thermal difference between cure temperature and ambient conditions. However, it is still not clear how this directly relates to residual stress as the instantaneous material properties are unknown.

While it is believed that the use of tailed FBG sets would enhance this work, allowing for gelation detection and in-situ modulus development for rapidly cured composites, it was not possible to utilise it here for the logistical reasons outlined. However, this methodology has great potential for use in rapidly cured composites and should be the subject of future works.

To experimentally relate the residual strain histories outlined in this chapter with the resultant mechanical properties, an analysis of the transverse matrix strength of each laminate will be explored further in chapter 8. Additionally, a numerical analysis of the development of residual stress in rapidly curing laminates will be conducted in chapter 7 where the experimentally measured strain data gathered in this chapter will be used to validate that work.

7. Modelling Residual Stress

7.1. Introduction

The aim of this chapter is to determine if a commercially available simulation package can be used to effectively determine the residual stress and strain state of a rapidly cured composite. Here, COMSOL MultiPhysics is used to develop a relatively simple and effective model of the curing process which couples a thermo-chemical and structural analyses together without writing dedicated user sub-routines needed in other commercial packages like ABAQUS. Using this approach, thermal data and experimentally determined strain data captured in chapter 6 will be used to validate the numerically determined strain values in this current chapter. Thus, inferences as to the residual stress state of the laminates tested with embedded FBGs can be made. Additionally, opting to not conduct this work in a package like ABAQUS avoids the need to implement HETVAL, UEXPAN and UMAT user sub-routines using FORTRAN which controls the scope of this work and allows focus to be kept on the experimental analysis of residual stress in rapidly cured composites.

As discussed in chapter 6, whilst useful insights into the curing process can be made by analysing the strain data captured by the embedded FBG sensors, it is not possible to determine the residual stress state of the final cured part. This is because the curing of a composite laminate is a multi-physics problem with a large number of transient variables which makes it impossible to apply a simple stress/strain relation to the problem. Therefore, a thermo-chemical and structural numerical model must be simultaneously implemented to determine the residual stress state of laminate after cure so that an analysis of the effect of residual stress on mechanical properties can be made.

In the literature, ABAQUS is commonly used [51][241][242][39][18] to model the cure of fibre reinforced composites. This is primarily because it allows for the implementation of user defined sub-routines which allow for a high degree of flexibility and for various physical processes to be coupled together for parallel computation. However, the primary objective of this work is to carry out an experimental investigation of the residual stress and strain state of laminates and the implementation of user sub-routines can be extremely time consuming. Thus, to avoid extending the scope of this work into a more numerically driven study,

COMSOL MultiPhysics is implemented as it allows for easy physics coupling and retains a reasonably high level of user control. Indeed, while COMSOL has been used less extensively in the literature than ABAQUS it has still been used effectively by a range of researchers to investigate fibre reinforced composite curing regimes [243][244][245].

Thus, the aim of this chapter is:

- To develop a simple model to investigate the effect of rapid curing on the development of residual stress in fibre reinforced composites

with the following objectives to meet this aim:

- Define laminate properties using experimentally determined values from work done in the previous chapter of this thesis and values determined numerically
- Validate the thermo-chemical model through a thermal analysis comparing experimental and numerical results
- Validate the structural model by using experimentally determined residual strain data captured using FBGs in chapter 6
- Use the model to predict the transverse residual stress of the laminates cured in chapter 6

7.2. Numerical model theory

The numerical model that is used in this work to simulate residual stress in laminates can be divided into two main sections. A thermo-chemical model is used to analyse the polymerisation process of the resin matrix and then a structural model is used to analyse the structural effect of polymerisation on a fibre reinforced laminate. The thermo-chemical model is in turn made up of two parts, the heat transfer model describing the uneven distribution of heat in the system and then the cure kinetics model which describes the progression of cure and associated heat release and rheological changes. The thermo-chemical model then outputs DOC and temperature data into the structural analysis module of the model so that cure dependent properties, cure shrinkage and thermal expansion can all be determined. These are then used to construct the mechanical analysis of the residual stress/strain in the laminate. This process is shown diagrammatically in Figure 80.

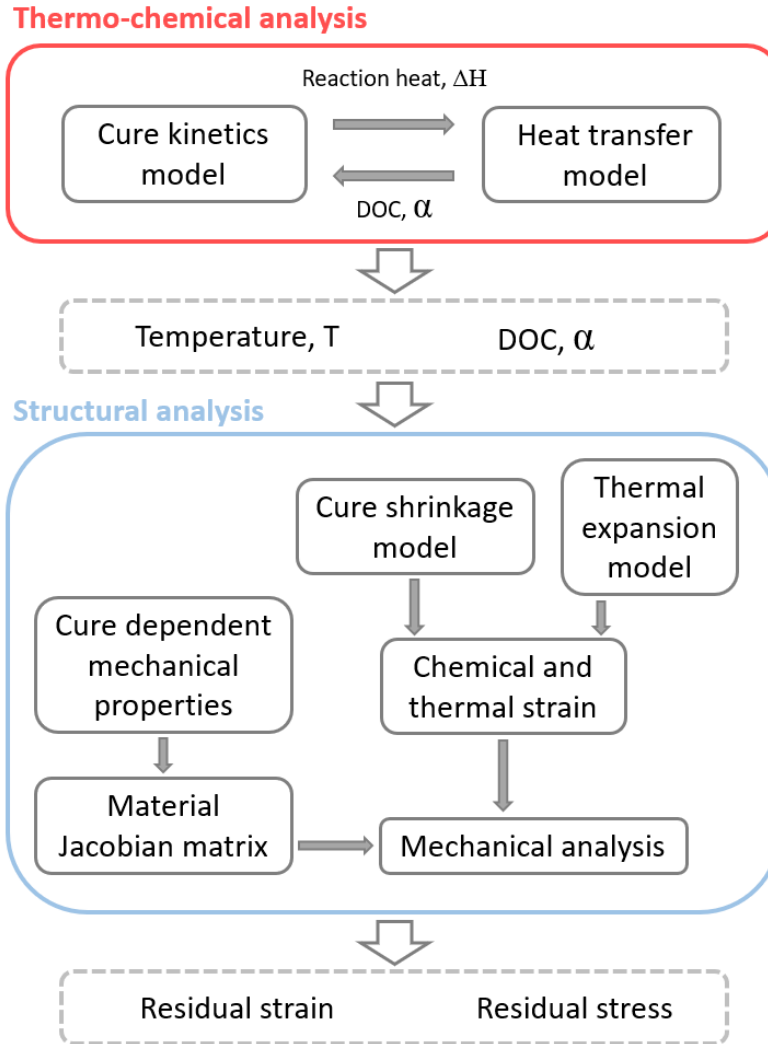


Figure 80: Residual stress simulation strategy

The heat transfer model in this analysis applies a Fourier heat conduction equation as its governing equation. Therefore, this assumes that there is no thermal convection or diffusion during cure which is a reasonable assumption as the cure times are very short and the thickness of the laminates are also quite small. The Fourier heat conduction equation for all three dimensions is described in Equation (36)

$$\rho_m C_p \frac{\partial^2 T}{\partial t} = k_x \left(\frac{\partial^2 T}{\partial x^2} \right) + k_y \left(\frac{\partial^2 T}{\partial y^2} \right) + k_z \left(\frac{\partial^2 T}{\partial z^2} \right) + \dot{Q} \quad (36)$$

where ρ_m is the density of the resin, C_p is the specific heat capacity of the resin, T is the temperature, t is the time and k is the effective anisotropic thermal conductivity in all three directions, x , y and z . Additionally, \dot{Q} is the internal heat generated in the system which, in

the case of curing thermosets, is the additional heat generated due to exotherm during cure. This can be described by Equation (37) [154]

$$\dot{Q} = \rho_m(1 - V_f)H_{total} \frac{d\alpha}{dt} \quad (37)$$

where V_f is the fibre volume fraction of the laminate, H_{total} is the total heat generated during polymerisation of the resin matrix, $d\alpha/dt$ is the cure rate and α is the DOC. The DOC is then governed by Equations (10) and (11) as described in section 3.3.1 with the Borchardt-Daniels model [246] defining $f(x)$ as $(1-\alpha)^n$. Thus, resulting in Equation (38).

$$\frac{d\alpha}{dt} = Ae^{\frac{-E_a}{RT}}(1 - \alpha)^n \quad (38)$$

Ideally, for the structural analysis, the effective chemical shrinkage in the laminate is determined from the results of the DOC numerical analysis. As UD laminates are transversely isotropic, it can be assumed that the transverse and out of plane chemical shrinkage are equal whilst the longitudinal shrinkage is assumed to be zero and is fully constrained by the fibre. Therefore, the effective transverse chemical shrinkage ε_{22}^{chem} can be related to the total measured chemical shrinkage strain during the tailed FBG experiments β_{tot}^{chem} (section 6.4) by assuming a linear relationship with DOC. Additionally, chemical shrinkage strain before gelation is assumed to be zero as all strain is dissipated viscously before this. This relation is described in Equation (39).

$$\begin{aligned} \varepsilon_{22}^{chem} = \varepsilon_{33}^{chem} = 0 & \quad 0 < \alpha \leq \alpha_{gel} \\ \varepsilon_{22}^{chem} = \varepsilon_{33}^{chem} = \beta_{tot}^{chem} \frac{(\alpha - \alpha_{gel})}{(\alpha_{vit} - \alpha_{gel})} & \quad \alpha_{gel} < \alpha \leq \alpha_{vit} \end{aligned} \quad (39)$$

However, it was found that it was not possible to implement a volumetric change as a function of DOC in COMSOL to model chemical shrinkage. This is one of the limitations of not using a software package like ABAQUS to carry out this investigation. It was possible to implement a single volumetric change to the whole laminate volume at the start of a study step to approximate the chemical shrinkage strain within the laminate. Thus, a volumetric contraction in the transverse, ε_{22}^{chem} and out of plane, ε_{33}^{chem} directions was applied at the midway point ($\alpha = 0.6$) between α_{gel} and α_{vit} to give an approximation of the residual stress that would normally be developed between these two limits. This is reasonable, as chemical shrinkage strain progresses linearly with DOC after gelation [247]. This is an oversimplification of the true development of residual stress from chemical shrinkage and it omits any through-thickness variation in residual stress from chemical shrinkage. However,

it is thought that it still offers a reasonable approximation of the total residual stress and relative inferences between curing conditions using the present model can still be made.

The thermal expansion model used in this analysis assumes that the laminate is transversely isotropic and the CTE in the fibre direction is only dependent on the fibres as expansion is constrained in this direction by the fibres. Work by Ifju et al [139] has shown that in UD laminates the CTE in the fibre direction can be approximated to be independent of temperature and increases linearly with DOC in the transverse direction. Additionally, before α_{gel} all residual stress is dissipated viscously and CTE of the resin is set to zero and only depends on material state [15][248]. After α_{vit} , the CTE of the resin is assumed to be constant. The thermal model used is outlined in Equation (40)

$$\begin{aligned} \alpha_{22}^{liquid} = \alpha_{33}^{liquid} &= 0 & 0 < \alpha \leq \alpha_{gel} \\ \alpha_{22}^{rubbery} = \alpha_{33}^{rubbery} &= \alpha_{resin} \frac{(\alpha - \alpha_{gel})}{(\alpha_{vit} - \alpha_{gel})} & \alpha_{gel} < \alpha \leq \alpha_{vit} \\ \alpha_{22}^{glass} = \alpha_{33}^{glass} &= \alpha_{resin} & \alpha > \alpha_{vit} \end{aligned} \quad (40)$$

where α^{liquid} , $\alpha^{rubbery}$ and α^{glass} are the CTEs of the laminate in the transverse direction in the liquid, rubbery and glassy phases, respectively. While it is possible to test the true variation of CTE with temperature using techniques like thermal dilatometry [154] or Moiré interferometry [139], this becomes very difficult due to the rapid curing resins used in this work. All existing testing apparatus for these experiments are unable to apply heat quickly enough to gain a representative understanding of cure and for the scope of this work to be contained the assumptions outlined above are assumed to be a reasonable approximation. To account for the viscous dissipation of residual stress before α_{gel} , a stress-free temperature was applied and assumed to be the temperature at which gelation occurred.

The mechanical properties of the carbon fibre reinforcing phase of the composites can generally be assumed to be relatively constant throughout the cure of the laminate [20]. Therefore, they will be assumed to remain constant in this analysis and focus will be given to the resin matrix phase of the laminate. Here, two main types of model can be employed to determine the resin properties during cure, elastic and viscoelastic constitutive models. For the analysis of residual stress, three models are commonly used, two elastic based models; Instantaneous Linear Elastic (ILE) and Cure Hardening Instantaneous Linear Elastic

(CHILE), and a Viscoelastic model. An ILE model, as first proposed by Bogetti and Gillespie [20], calculates the instantaneous elastic stiffness of the resin, E_r at every time step. The instantaneous cure dependent composite mechanical properties can then be calculated using a self-consistent field model using Equations (A1)-(A11) [20] found in Appendix A, where E_r varies up to the fully cured resin modulus, E_m , according to DOC with the relationship outline under the “Material parameters” heading in section 7.3. Thus, the instantaneous contribution to residual stress can then be summed over every time step, and the final residual stress/strain state is known. This model assumes there are no viscoelastic effects and that the material properties of the resin are constant after vitrification with no softening of the matrix beyond this point. This can lead to an overestimate of residual stress when compared to a CHILE model as the stiffer resin above its T_g can lead to higher residual stress values. However, ILE has been used extensively in the literature as an effective tool for determining residual stress in composites [20][249][250][233]. Additionally, as the simplest model presented it requires the least number of variables to be determined. For the current work this is a key advantage as reliably and accurately determining material properties for rapidly curing composites is a relatively new and unexplored area, requiring further research. Therefore, this work utilises an ILE model to examine the development of residual stress in rapidly curing composites. However, as will be discussed later, the ILE model used in this work underestimates residual stress in the case of the “Hot” laminates. Thus, a brief explanation of the CHILE and viscoelastic models available is also given to inform future work.

An ILE model can be expanded to consider resin matrix softening after vitrification of the resin by incorporating a temperature dependency to the model. The resultant model is known as a Cure Hardening Instantaneous Linear Elastic (CHILE) model and the instantaneous resin modulus between various temperature ranges can be described by Equation (41).

$$\begin{aligned}
 & E_r^0 & T^* \leq T_{C1} \\
 E_r^0 + \frac{T^* - T_{C1}}{T_{C2} - T_{C1}} (E_m - E_r^0) & T_{C1} < T^* < T_{C2} & (41) \\
 & E_m & T_{C2} \leq T^*
 \end{aligned}$$

where E_r^0 and E_m are the resin modulus when fully uncured and cured respectively. E_r^0 is often said to be $E_m/1000$ as it is very small and hard to define accurately. T_{c1} and T_{c2} are the critical

temperatures at the onset and completion of the glass transition respectively. $T^* = T_g - T$ with T_g being the instantaneous glass transition temperature and T the temperature of the resin. Thus, the CHILE model accounts for softening behaviour of the resin past vitrification. However, it is evident that multiple additional resin parameters must be well known and accounted for during modelling.

Lastly, a Viscoelastic model can be employed. As the name suggests, this model accounts for the viscoelastic stress-relaxation of resins during the curing process which has been discussed in section 2.2. A viscoelastic constitutive model is inherently more complex than an ILE or CHILE model as it has an additional time dependency and requires additional viscoelastic material parameters which can be difficult to determine [251]. However, in the case of cure cycles where viscoelastic effects are significant, where they maintain an elevated temperature for an extended period for example, it is important to account for these effects. In the case of rapidly curing composites, there is very little time for any viscoelastic behaviour to have a significant effect on the final residual stress state of the laminate as the relaxation time is short in the rubbery phase [233]. However, a laminate that has a curing temperature much higher than T_g^{cured} will experience significantly more viscoelastic stress relaxation due to the higher molecular mobility as described by an increase in E'' . Therefore, future work directed at investigating the effect of implementing a viscoelastic model for short cure times above T_g^{cured} would be beneficial.

7.3. Numerical model

A 3D model was implemented with the fitted material parameters to investigate residual stress/strain in a full laminate and for a comparison with experimental data to be made. To implement the heating and cooling phases of the cure cycle, two time-dependant study steps were required as different boundary conditions are present in the two cases. Additionally, to approximate chemical shrinkage in COMSOL, an additional time-dependant study step was required to apply an instantaneous chemical shrinkage strain to the entire laminate domain. Therefore, a total of three study steps were used in this analysis: “Step 1: Heating”, “Step 2: Chemical shrinkage” and “Step 3: Cooling”. “Step 1: Heating” occurred from when the laminate was placed into the hot press to when $\alpha = 0.6$, at which point it was assumed all chemical shrinkage strain occurred instantaneously. At this point the “Step 2: Chemical shrinkage”

step began and carried on until the hot press was opened. Then, the “Step 3: Cooling” study step modelled the development of residual strain as the laminate was released from the mould and cooled. All study steps used a backward differential formula solver for improved stability. An example strain history (Cool_thick) is shown in Figure 81 with the three study steps indicated. For the full residual strain results presented in section 7.4.2, strain is zeroed at α_{gel} ($\alpha = 0.4$) as strain before this is dissipated viscously and does not contribute to the build-up of residual stress as previously discussed.

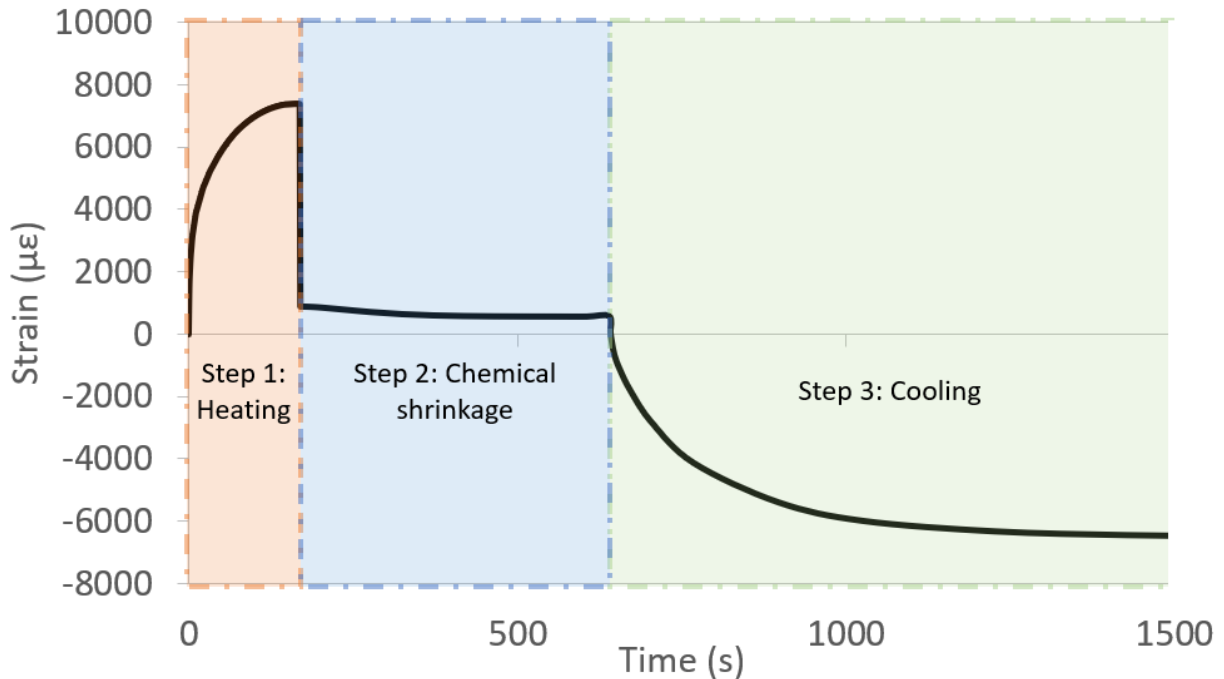


Figure 81: Cool_thick strain history as modelled from the FE analysis with the three study steps indicated.

Material parameters

The material parameters used in this model and where they were derived, is listed in Table 12. All values have been derived from either earlier work in this thesis or from the literature with the exception of thermal conductivity values, k . These values are determined in the thermal validation later in this chapter. Here, values are found by fitting the numerical results to experimental data. Results are still within a reasonable range as compared to those found in the literature [252][253][254][255].

Table 12: Material parameters used in numerical study

Property type	Property	Value	Unit	Source
Thermal/constitutive	k_{11}	0.86	W/mK	Section 7.4.1
	k_{33}	0.27	W/mK	Section 7.4.1
	C_p	862	J/kgK	[187]
	ρ_m	1530	kg/m ³	[154]
	E_m	1.56	GPa	Chapter 4
	V_f	0.6	-	[183]
	α_f^{CTE}	0.5 x10 ⁻⁶	1/°C	[187]
	α_m^{CTE}	105.3 x10 ⁻⁶	1/°C	[183]
	ν_{12}	0.20	-	[154]
	ν_{23}	0.25	-	[154]
	R	8.314	J/mol/K	Universal
	E_f	240	GPa	[183]
	α_{gel}	0.4	-	Chapter 6/FE
	α_{vit}	0.8	-	Chapter 6/FE
	β_{22}	0.58	%	Chapter 8
Cure kinetic	ΔH_{tot}	182	J/g	Chapter 3
	A	8.05x10 ⁴	1/s	Chapter 3
	E_a	54.7	kJ/mol	Chapter 3
	n	1	-	Chapter 3

The development of the resin modulus with DOC is unknown for the current resin formulation under investigation, EF7017. As discussed in section 3.1, this is due to the difficulty in accurately determining this value using conventional techniques such as DMA during cure. Therefore, to approximate this relationship a generalised curve is assumed between the two key points in the curing process, α_{gel} and α_{vit} . The DOC at which these points occur is determined from combining the experimentally measured points from the FBG analysis and the thermo-chemical model describing the DOC in that sample. As discussed in chapter 6, α_{gel} is determined from the onset of shrinkage strain and α_{vit} is defined at the point at which strain stops continuing to develop. These points have been marked on the Cool_thick laminate as an example in Figure 82. Now, α_{gel} and α_{vit} can be determined to occur at

approximately 40% and 80% DOC, respectively. Thus, a typical function describing modulus development during cure can now be fitted between the two key points in the cure cycle, α_{gel} and α_{vit} , and is shown in Figure 83.

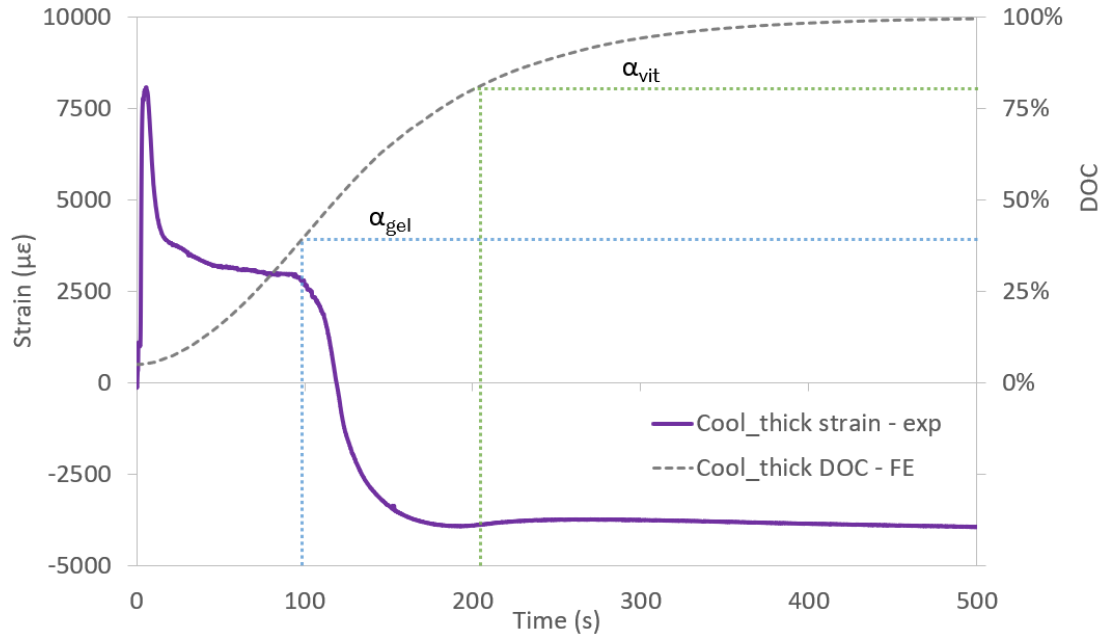


Figure 82: Experimental strain history of Cool_thick laminate with DOC as determined by the FE model. DOC at which α_{gel} (40%) and α_{vit} (80%) are determined to be

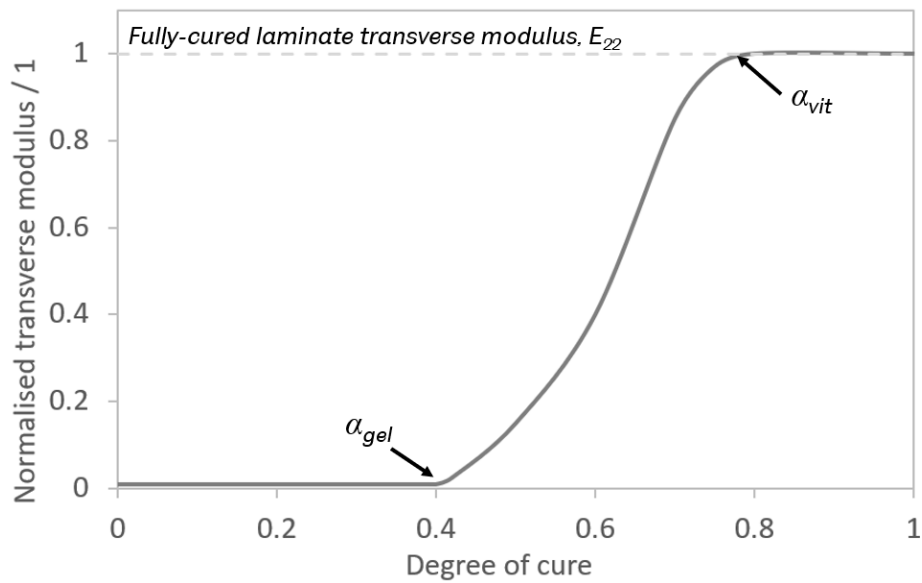


Figure 83: Development of transverse modulus (normalised) with DOC with α_{gel} and α_{vit} determined from embedded FBGs labelled

This assumed modulus development is going to be limited in its accuracy, however as the time between the onset of α_{gel} and α_{vit} is short, it is thought that this assumed function is a reasonable approximation and won't impact heavily on the final calculated residual stress value. In the future, more work is needed to develop a method to experimentally determine the development of modulus with DOC in rapidly curing laminates.

Geometry and mesh sensitivity analysis

To reduce the computational time required to compute the 3D laminate model, a quarter section of the laminate and mould/collar was modelled with symmetric boundary conditions applied on three faces of the quarter section as shown in Figure 84. Additionally, boundary conditions labelled i-viii are shown and are defined in Table 13 in the following section. Here, the x-direction is the fibre direction.

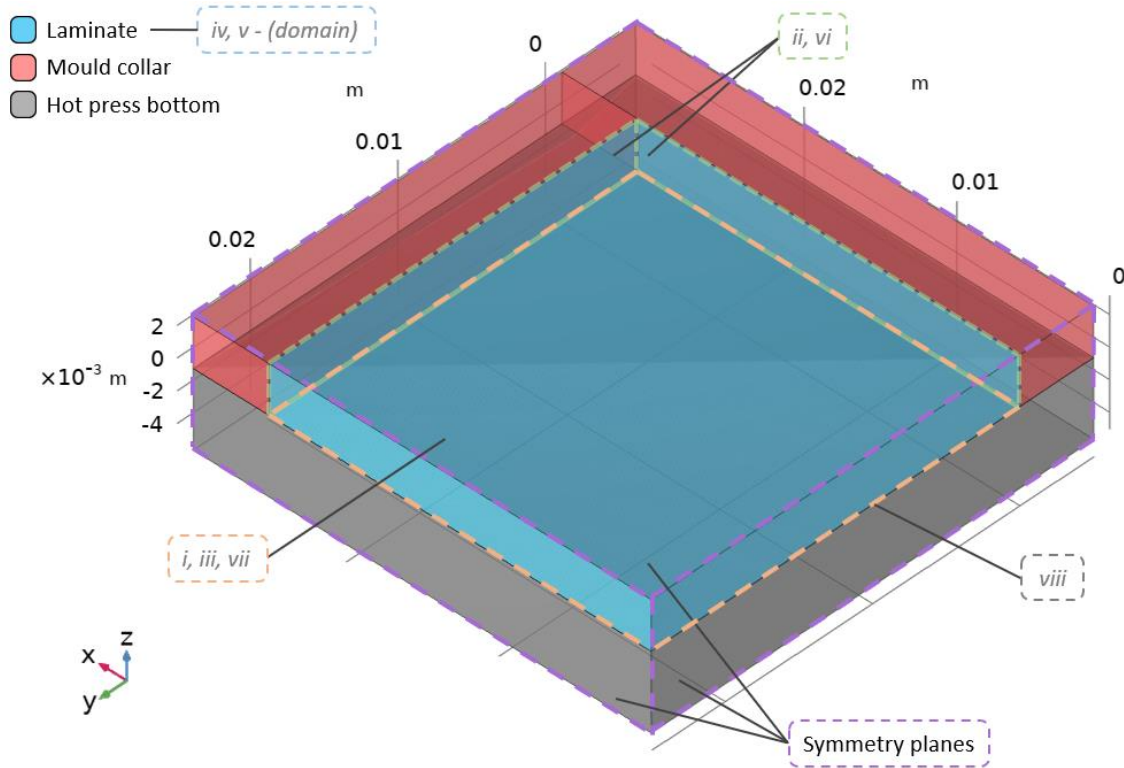


Figure 84: Geometry of FE model with symmetry planes labelled

To determine the mesh sensitivity of the model, a series of FE studies were carried out to determine the effect of the number of elements in the output strain value after a sample had been fully cured. A Hot_thick model was used and the strain at the mid-thickness of the laminate was monitored after 150 seconds as this would allow for the laminate to be fully

cured and for strain to be high as the temperature was still elevated. The number of mesh elements in the laminate domain was varied from 72-40,000 while keeping a constant element aspect ratio, and the strain output was normalised against the strain value obtained using the model with 40,000 elements. The results of the sensitivity analysis are shown in Figure 85.

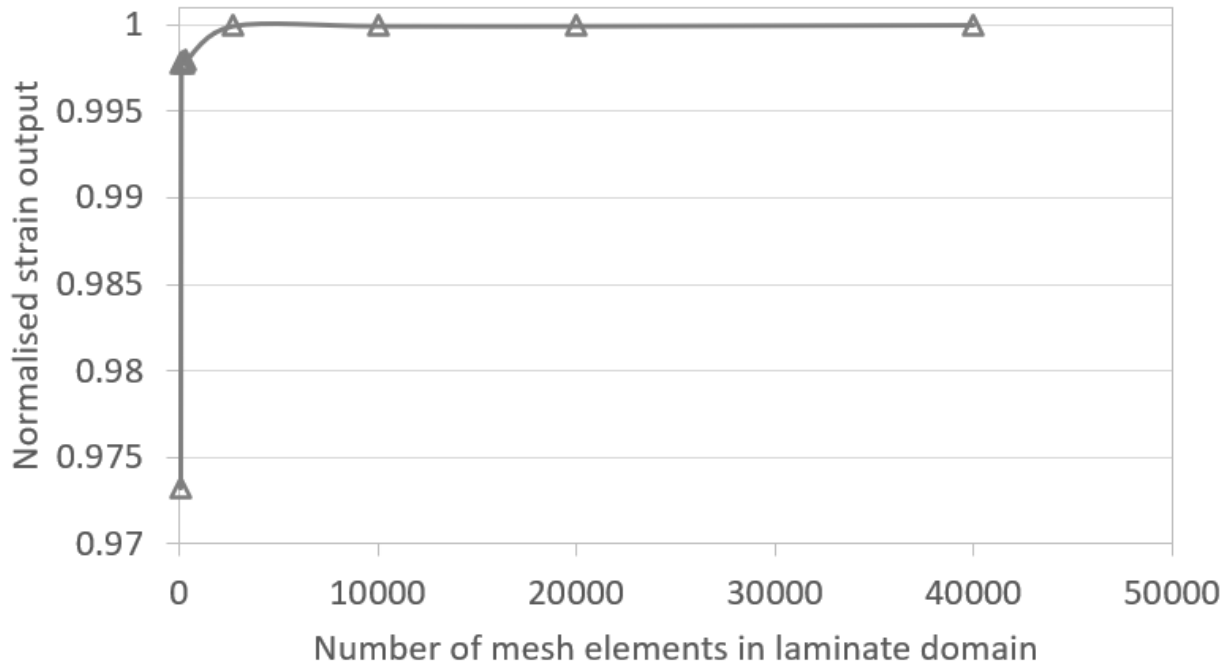


Figure 85: Mesh sensitivity analysis for Hot_thick FE model

Here, it can be seen that the number of elements has little effect on the final strain value reported by the model and convergence is exhibited around 2704 elements. Only a very small number of elements (72 elements) gives a solution that is more than 0.5% away from solution attained with a very large number of elements. The model being not very sensitive to mesh size is consistent with results reported in the literature [18]. Therefore, going forward, a model with 2704 elements will be used as the mesh sensitivity can be seen to converge here and the calculation time for a full cure is reasonable at around 4 minutes for the Hot_thick case.

Boundary conditions

The heat flux into the laminate from the hot press and out to the surroundings during cooling was unknown. Therefore, the thermal analysis outlined in section 7.4.1 was used to determine appropriate values which would match well with experimentally determined thermal histories. It was determined that a heat flux of 250 W/m²K between the lower mould and the

laminate during heating and $50 \text{ W/m}^2\text{K}$ during cooling was required. The lower mould temperature was set to the curing temperature on heating and the ambient temperature was assumed to be $22 \text{ }^\circ\text{C}$ upon cooling. Additionally, a $25 \text{ W/m}^2\text{K}$ heat flux between the laminate and mould collar was applied to account for thermal conductivity from the laminate to the collar during heating. These results were considered to be reasonable when compared to the literature [256][245][154]. Additionally, the differential Equation (38) is then solved for the entire laminate domain to determine the progression of cure. An exothermic heat source is applied over the entire laminate domain using the results of the cure progression and Equation (37). As will be shown in section 7.4.1, good corroboration was found between experimental and numerical results using these values to model the thermo-chemical process.

For the structural boundary conditions, it was assumed that the laminate was entirely constrained by the retaining collar and hot press. Fixed boundary constraints were added to all moulding surfaces during the heating and chemical shrinkage study steps as this was thought to more accurately model the fully enclosed laminate during the hot-pressing process. Other authors [257][239][241] have used a frictionless assumption at the boundaries for residual stress during cure analysis. However, this assumption completely negates the effect of tool-part interactions which will cause an uneven development of residual stress during cure from the fixed mould boundary. The completely fixed case might be overly constrained, as the real boundary case is transient in nature and will be a function of the DOC of the resin matrix. Initially, when the matrix is soft, a frictionless boundary assumption may be appropriate. However, as cure progresses the boundary condition becomes more ridged as the modulus of the resin matrix increases. The resin systems used in this analysis cures so rapidly that the time in which the resin matrix near the outer edge of the laminate is not stiff, is quite low. Therefore, it is thought that the completely fixed boundary condition is more appropriate than a completely free case for the laminate cured in a hot press. However, efforts of future work should be directed to better defining this boundary, and how it develops during cure, as it can have a large impact on the final residual stress state of a laminate [18].

As discussed, it was not possible to apply a volumetric chemical shrinkage strain as a function of DOC to the laminate in COMSOL. Therefore, a single instantaneous strain was applied in the ϵ_{22} (transverse shrinkage) and ϵ_{33} (out-of-plane shrinkage) direction at the start of study

“Step 2: Chemical shrinkage”. This was equal to the total chemical shrinkage strain expected throughout the entire cure of the laminate. This modelled behaviour is thought to approximate and average residual stress resultant from chemical shrinkage strain as it occurs at $\alpha = 0.6$, halfway between α_{gel} and α_{vit} . However, this approach does omit any through thickness variation in chemical shrinkage during cure which can result in an underestimation of residual stress. This is especially likely to affect the development of residual stress in thick laminates where larger DOC gradients exist through the thickness of a laminate.

During the cooling study step, the lower mould is lowered 5 mm away from the laminate surface and boundary conditions are removed from the lower laminate surface. This is to model the laminate being removed from the hot press, while still at cure temperature. To the best of the author’s knowledge, this has not been modelled before in the literature as most models allow laminates to come back down to room temperature before demoulding.

The boundary conditions change at every study step to account for the varying loads and boundaries being modelled during cure. Table 13 details which boundary is active for each of the three study steps of this analysis and their locations are shown in Figure 84.

Table 13: Numerical model boundary condition status over every study step

Label	Boundary	Step 1: Heating	Step 2: Chemical shrinkage	Step 3: Cooling
i	Heat conduction: lower mould to laminate	Active	Active	Inactive
ii	Heat conduction: laminate to collar	Active	Active	Active
iii	Heat conduction: laminate to atmosphere	Inactive	Inactive	Active
iv	Curing exotherm	Active	Active	Active
v	Chemical shrinkage	Inactive	Active	Active
vi	Fixed boundary: laminate to collar	Active	Active	Active
vii	Fixed boundary: laminate to lower mould	Active	Active	Inactive
viii	Lower mould in contact	Active	Active	Inactive

7.4. Results

To first validate the thermo-chemical model used to model the curing process, a thermal analysis is carried out to compare the model to experimental measurements. Additionally, some unknown material parameter properties are determined by fitting the modelled data to the experimentally measured data. Embedded FBG data gathered in chapter 6 is then used to validate the numerically derived strain values outputted by the proposed model to ensure good agreement with the structural analysis. Finally, an analysis of the residual stress state of all the laminates under investigation is given with reference to similar results found in the literature.

7.4.1. Thermal validation results

To validate the results from the thermo-chemical model used in this work, a thermal history comparison is made as this allows for the heat transfer and cure kinetics models to be analysed. The methodology and results from the thermal history analysis conducted in section 0 have been used to validate this model. Thus, a number of $[0]_{40}$ EF7017 laminates were cured at 140, 150 and 160 °C with k-type thermocouples embedded at ply 1 (outer) and ply 20 (mid-thickness). The inward and outward heat flux parameters and the thermal conductivity, k in all three laminate directions was changed iteratively until good agreement with the experimental results was found. The experimental and FE results for the ply 1 temperature history are outlined in Figure 86. Heat flux and thermal conductivity values remained within acceptable bounds when compared to similar materials found in the literature.

From these data, it can be seen that there is reasonably good agreement during the heating stage in ply 1 and very good agreement during cooling which is indicative of the heat transfer model being accurate. However, it can be seen that the exotherm is not well captured, even on the outer edge of the laminate. This discrepancy in thermal histories during the exotherm is even more evident at the mid-thickness of the laminate as seen in Figure 87.

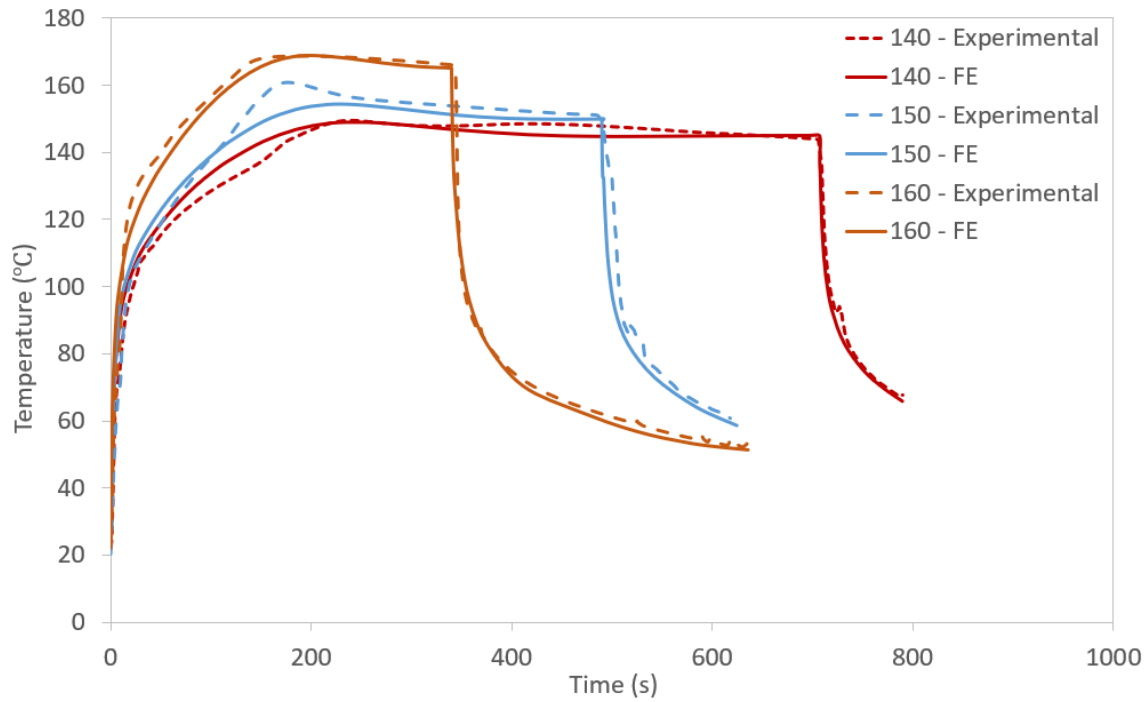


Figure 86: Finite element analysis validated with experimental thermal history data for ply 1 temperature curing at 140, 150 and 160 °C.

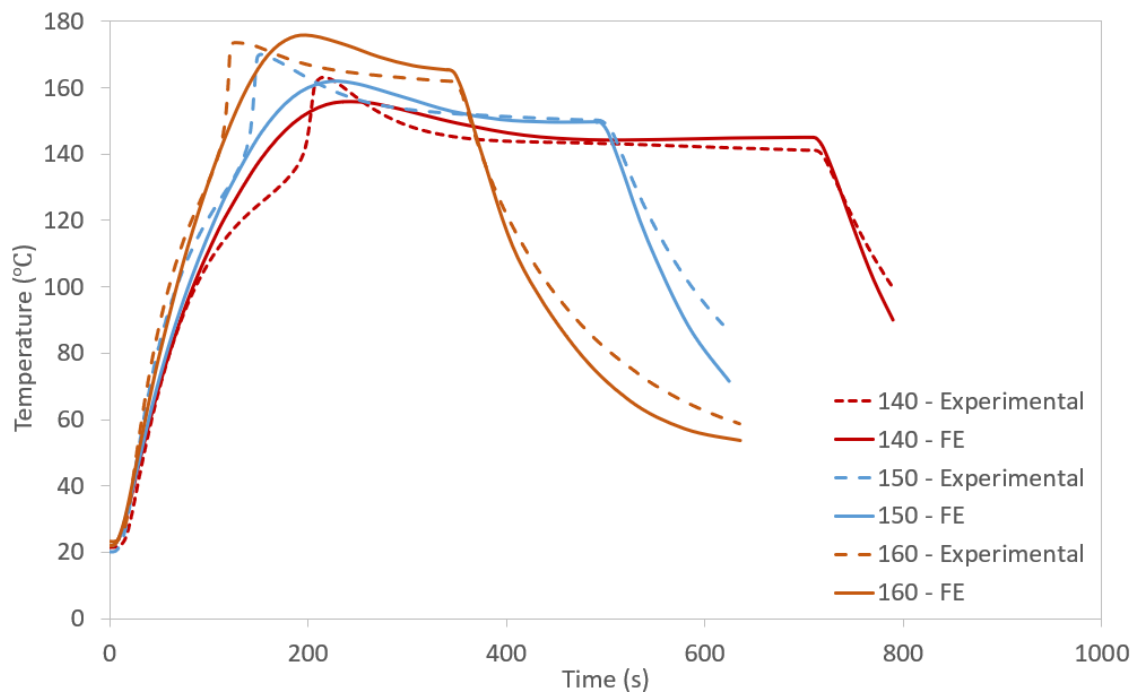


Figure 87: Finite element analysis validated with experimental thermal history data for ply 20 temperature curing at 140, 150 and 160 °C.

Here, the exceptionally rapid increase in temperature during the exotherm can be seen to not be captured well by the somewhat simplistic Arrhenius model being used in this work, as described in chapter 3. This is likely because the free-radical based chemistry of the EF7017 resin formulation being used is not accurately described by a first-order equation. This kind of chemistry can often have multiple reacting groups operating with different ΔH , E_a and other cure kinetics parameters for each constituent reaction. Thus, we can see that the first-order assumption used here does not accurately capture this as it effectively averages these separate reactions over the entire cure range. However, for this work it can be seen that the model that has been implemented captures the relative difference between the heating profiles well as all cure temperatures show a similar response. Thus, an analysis of the difference in residual stress between them can be made with some degree of confidence that the thermo-chemical model differentiates between curing conditions. Additionally, while the detail of the exothermic peak is not well captured, the general trend is captured well, and it is only the small timescale being analysed that makes this difference so evident. Therefore, it is thought that the current model is sufficiently accurate for further analysis to be made but it is suggested that future work develops a more complex cure kinetics model that can better describe the multiple chemistries occurring in this subset of resin formulations. It is thought that an auto-catalysed model such as a Kamal Sourour phenomenological model [258][259] which adds additional fitted parameters to the $f(x)$ term would be well suited for future investigation. Alternatively, a free-radical chain-growth model could be employed to better suit the resin system. However, this requires deeper knowledge of the resin chemistry which is currently unavailable.

7.4.2. Strain validation results

The rapid curing of composites is a complex multi-physics problem with many variables. It is therefore critical that any model be validated to ensure that the model output is reasonable. One powerful use of experimentally measuring strain using embedded FBGs is the ability to then use that strain to validate the strain output from a numerical model. Here, strain data captured using the outer ply (ply 1) embedded FBG is compared with the FE results of strain data captured from a probe point located at the ply 1 thickness in the centre of the laminate. The probe reports the ε_{22} tensor at this location during cure. The results for the experimental

and numerically determined strain for all cure conditions tested is plotted in Figure 88 from time 0-1500 seconds after gelation for comparison.

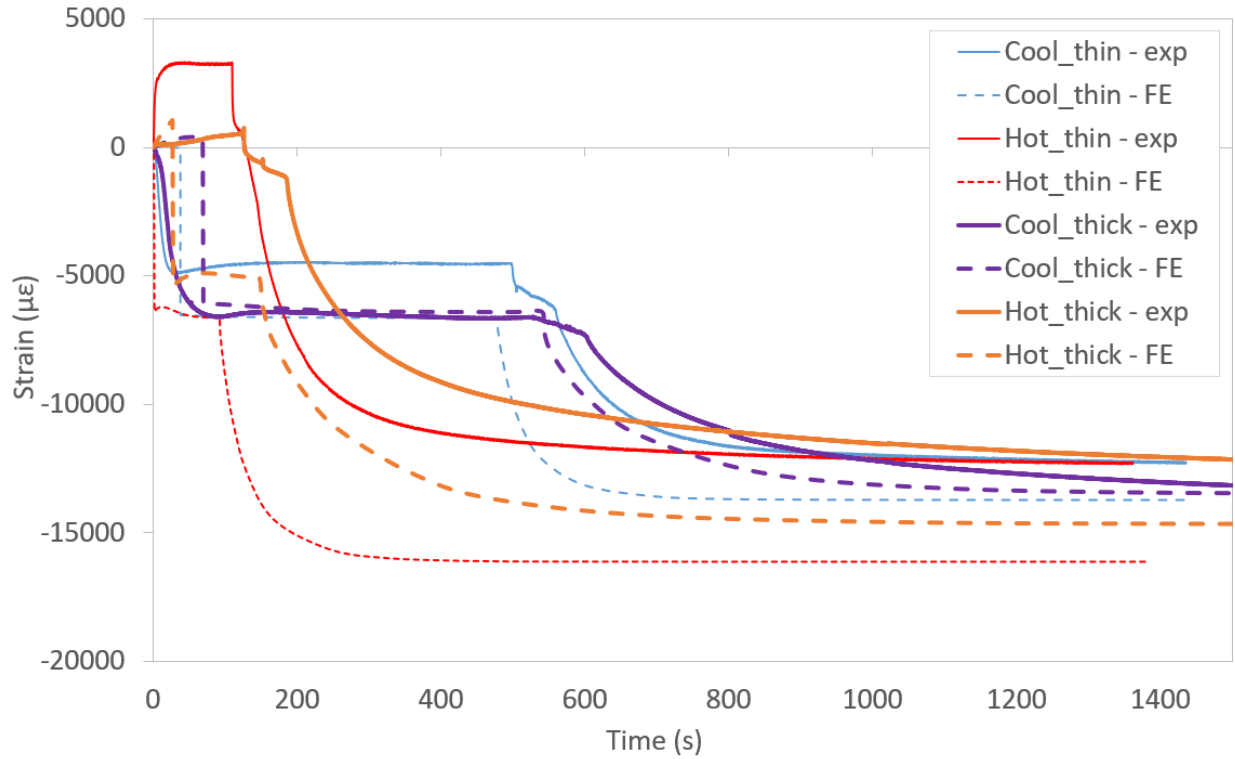


Figure 88: Strain validation of FE model using the ply 1 strains. Experimentally measured strain from embedded FBGs shown with a solid line and FE determined strain in a dashed line

The most evident trend from Figure 88 is the reasonable agreement between experimental and FE results for the “Cool” samples while there is a large over reporting of strain by the FE model for the “Hot” samples. As has been mentioned in chapter 6, and will be discussed in more detail in section 8.4, this drop in strain measured with embedded FBGs during the chemical shrinkage phase of cure is caused by the “Hot” samples exceeding T_g^{hot} during cure. The T_g^{hot} of the “Hot” samples is exceeded around the point at which the “Hot” samples begin to gel and store stress elastically. Therefore, the compressive chemical shrinkage strain which would be expected to occur in this early stage of cure is dissipated viscously as the resin matrix has transitioned into a rubbery phase. The exception to this is the Hot_thin sample that has an increase in strain but, as discussed in section 6.4, this is caused by more thermal expansion as laminate temperature is still increasing. The ILE model used in this work does not account for resin softening after vitrification or viscoelastic effects and as such is unable to capture this transition and overestimates the compressive residual strain for the “Hot”

samples. Future work is to implement a CHILE or a viscoelastic model [51] to better account for these effects as they clearly play an important role in laminates cured above T_g^{cured} . This also means that the corresponding residual stress values obtained for the “Hot” samples will overestimate the amount of tensile residual stress as the relaxation around T_g is not accounted for in this model. This will be discussed further during the residual stress analysis later in this chapter.

In Figure 88, both the “thick” and “thin”, “Cool” samples corroborate well with the experimental data, suggesting that ILE model implemented works well for samples cured below T_g^{cured} . The “thick” sample matches particularly well with experimental results. It is thought that the “thin” sample overestimates strain when compared to the experimental results as the model does not fully capture the additional constraints imposed by the laminate being thinner and thereby reducing the apparent strain produced from chemical shrinkage. Boundary conditions and tool-part interactions are known to have a large influence on the outputted strain result when modelling residual stress/strain during cure [18][51][260][261][262]. Therefore, this result suggests that the simplified fixed constraint used in this model does not adequately describe the boundary and more attention should be focused in defining this boundary in future work, especially for “thin” laminates.

One feature that is not well captured by the model is the chemical shrinkage strain after gelation, during the initial part of the cure. Using COMSOL it was found that it was not possible to apply a volumetric shrinkage to the entire volume that was a function of DOC, as is the case for polymerization induced chemical shrinkage. Instead, an additional study step was implemented when the DOC reached 0.6 (halfway between α_{gel} , 0.4, and α_{vit} , 0.8) which instantaneously applied the entire chemical shrinkage contribution. This was done to achieve an approximate average result for the development of residual stress from chemical shrinkage. Thus, instead of the model outputting a smooth development of residual strain during chemical shrinkage, a large instantaneous increase in the amount of compressive strain is given. As this was applied to the entire laminate domain instantaneously, this approach does not allow for any through-thickness variation in chemical shrinkage to be applied. This is one of the key drivers in the development of a differential through-thickness

residual stress profile in thick composites and as such the residual stress output of the “thick” samples is likely under-reported.

Lastly, the model does not capture the time between the opening of the hot press and the removal of the laminate from the mould (vi-vii). As can be seen in the experimental data, there is a gradual decrease in strain when the hot press is opened and then a larger drop-off when the laminate is removed from the hot press entirely. This is due to the rapid cooling and reduction in thermal expansion when the laminate is removed from the still hot, hot press. However, the model assumes that the hot press pressure and temperature is instantaneously removed at the end of cure and, as such, results in a single sudden drop in strain. Differences between experimental and FE results like this are particularly apparent on the small-time scales investigated in rapidly curing analyses and require a much more complex model to capture them. However, it is thought that as the time-scales involved are short, the final residual strain is not changed and the modulus is already fully developed, these difference will not have a meaningful impact on the final residual stress values obtained by this model.

Thus, it has been found that this model shows good agreement with experimentally determined strain results for the “Cool” samples tested as they remain below T_g^{cool} . However, this model does not account for curing above T_g^{cured} and it can be seen that this has a large effect on the residual strain output of the model. Consequently, it is thought that residual stress values obtained from the “Cool” analysis will provide a useful insight the development of residual stress in those samples. However, more work would be required to implement a CHILE or viscoelastic model to account for the glass-rubbery transition experienced by the “Hot” samples. Additionally, it is suggested that a more robust simulation package like ABAQUS is used to adequately implement chemical shrinkage strain as a function of DOC.

7.4.3. Residual stress analysis

Cool_thick example

Now that the validity of the thermo-chemical model and structural model has been determined, an analysis of the build-up of transverse residual stress in rapidly cured laminates can be undertaken. The residual stress history of the Cool_thick laminate is shown in Figure 89 to allow for an analysis of how residual stress develops in a typical rapidly cured

laminate. As with the strain analysis in sections 6.4 and 7.4.2, residual stress values are zeroed at gelation as stress is dissipated viscously before then. In the Cool_thick example, time is shown for 1500 seconds after gelation as this allows for a more detailed view and the residual stress profile does not appreciably change after this point.

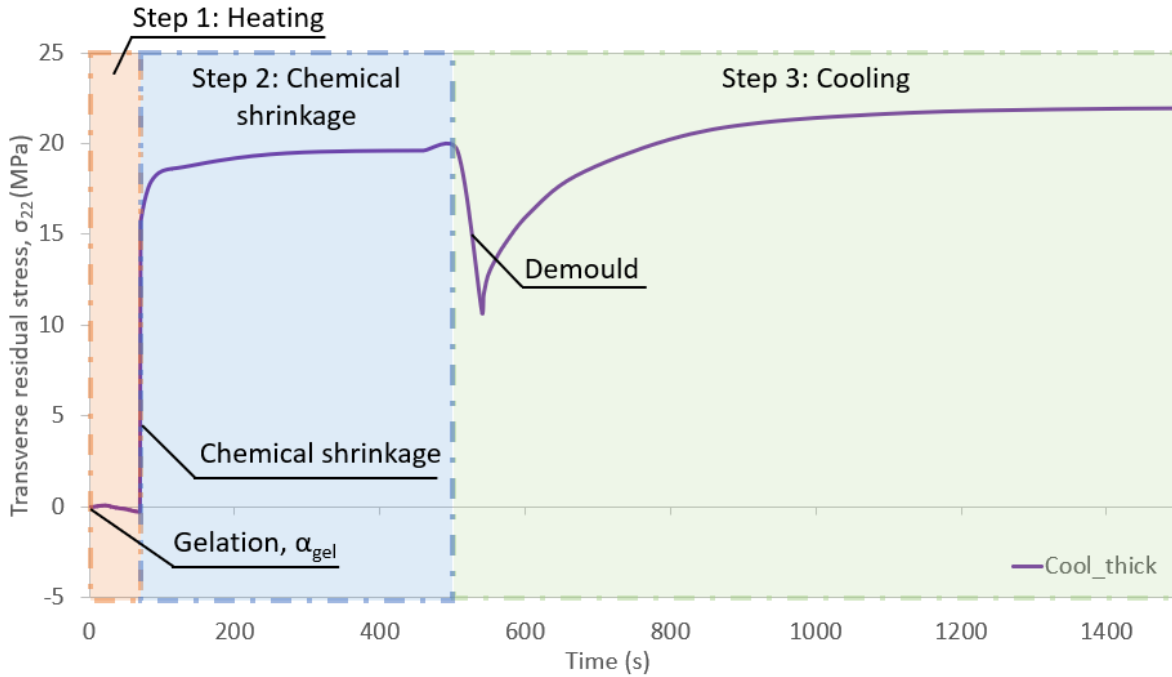


Figure 89: Development of residual stress in Cool_thick laminate with study steps and key events indicated

The first thing to be noted from this residual stress analysis is that stress developed is tensile. This is because the compressive chemical shrinkage and thermal contraction strain development, seen in both the model and FBG analysis shown in section 7.4.2, are stress-free events. It is only when the chemical and thermal contractions are fixed by a boundary does stress begin to develop. Without this boundary no stress would occur. Thus, the chemical and thermal contractions are resisted by the fixed boundary and a tensile stress is developed.

In step 1, very little stress is developed as the laminate has just gelled and the elastic modulus of the resin matrix is low. Therefore, the thermal expansion strain developing from an increase in temperature results in a small compressive stress. Additionally, in the Cool_thick sample the laminate is within 5 °C of its final cure temperature at α_{gel} . This compressive

thermal stress is more pronounced in the Hot_thick laminate, as is shown in the following section, where α_{gel} occurs approximately 15 °C below its cure temperature.

In step 2, a sharp and sudden increase in tensile residual stress is seen when the instantaneous chemical shrinkage is applied to the laminate. As already discussed, this is an approximate average of the real development of residual stress due to chemical shrinkage. If chemical shrinkage was modelled as a function of DOC and progressed linearly with it, a more gradual increase in stress would be seen. Initially, the development of stress would be small as the resin modulus is also small. Then, as cure progressed the amount of tensile stress developed with DOC would increase as the resins elastic modulus also increased. It is thought that the single instantaneous application of chemical shrinkage used in this model will underestimate the total amount of residual stress developed from chemical shrinkage as the modulus of the resin at $\alpha = 0.6$ (when the chemical shrinkage step is applied) is approximately 40% of its maximum. After this, a small amount of tensile residual stress continues to develop as the modulus of the resin continues to increase up to its maximum at α_{vit} .

In step 3, a sudden drop in tensile residual stress is seen as the laminate is removed from the mould and the fixed boundary at the base of the laminate is removed. This allows for approximately 10 MPa of residual stress to be relieved. After this, a tensile stress begins to develop again as the laminate begins to rapidly cool, having been removed from the hot press while still at cure temperature. This continues to develop until the laminate temperature equilibrates with room temperature and the final residual stress state is reached.

Combined results

Now, the development of transverse residual stress for 1500 seconds after α_{gel} is plotted in Figure 90 for all laminates tested for comparison. Little change in residual stress is seen after 1500 seconds and so this region is plotted for easier analysis.

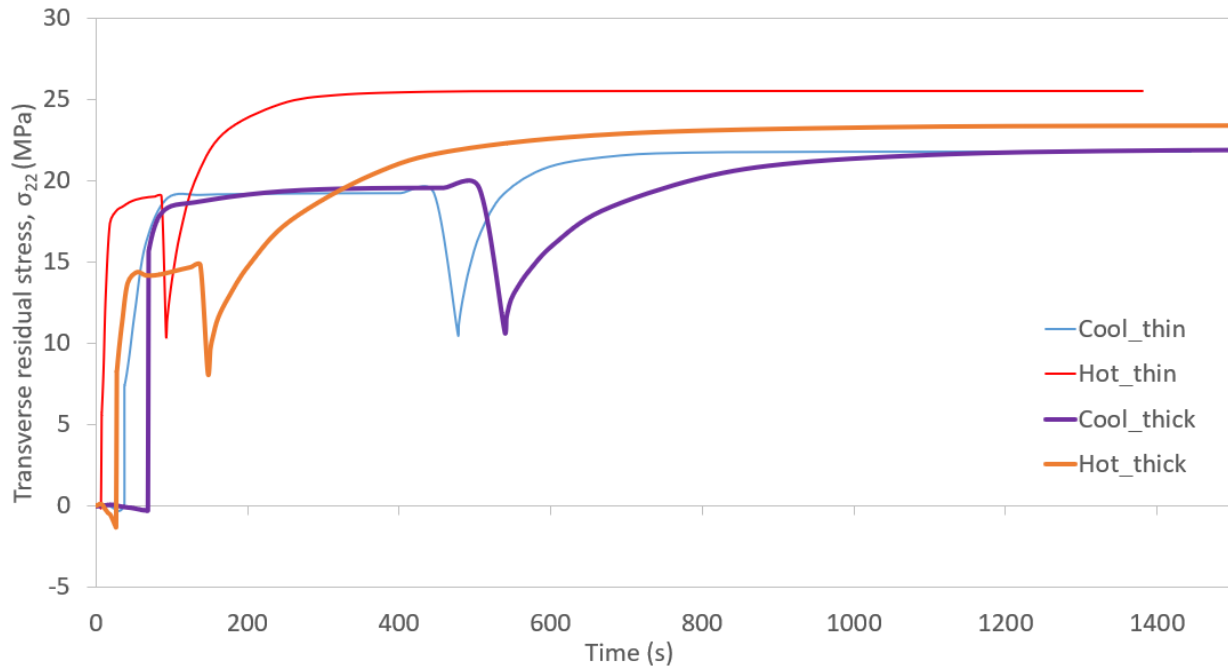


Figure 90: Transverse residual stress developed on the outer ply for all laminates modelled, for 1500 seconds after α_{gel} .

Here, it can be seen that both the “Cool” samples have a similar final residual stress value regardless of thickness. This is not in agreement with the current hypothesis that an increase in laminate thickness will lead to a distributed residual stress profile through the thickness of the laminate. This is thought to be caused by two main factors. First, the application of chemical shrinkage was constant through the thickness of this model, this assumption excludes any thickness effects on residual stress caused by chemical shrinkage. Second, in the “Cool” laminates, the through thickness distribution of temperature at α_{gel} was approximately ± 2 °C and ± 0.5 °C for the “thick” and “thin” cases, respectively. Thus, no through-thickness variation in residual stress developed in the “Cool” laminate models and the same final residual stress value was reached. It is expected that if future work can apply chemical shrinkage as a function of DOC, an increase in residual stress with laminate thickness would be seen in the modelled results.

It is also thought that this inability of the model to account for the through-thickness variation in chemical shrinkage contributes to the model showing no variation in residual stress through the thickness of the laminates modelled. Additionally, in both the modelled thermal history and experimentally determined thermal history, the thermal distribution

through the thickness of the laminate is small after α_{gel} . Therefore, for the laminates tested, there is no through-thickness variation in residual stress.

Next, it can be seen that the residual stress developed due to chemical shrinkage is less for the Hot_thick laminate than the Hot_thin laminate. This is because of the large thermal distribution seen in the Hot_thick sample results in the outer ply of the laminate reaching $\alpha = 0.6$ before the middle of the laminate has reached α_{gel} . As chemical shrinkage must be applied to the whole laminate in this model, chemical shrinkage is applied to the centre of the laminate while the modulus is still quite low. This results in less tensile residual stress being developed in the Hot_thick sample.

The results of this analysis suggest that the “Hot” samples will have a higher tensile residual stress. However, as seen in the strain validation analysis, the “Hot” samples modelled strain does not agree well with the experimental data. This is because the “Hot” samples cure temperature has exceeded the laminate T_g^{hot} by a significant amount during cure, the resin matrix remains rubbery, and stress/strain can be relaxed. As discussed, this is not accounted for by the ILE model used in this work. Thus, the residual stress values predicted by this analysis will be an overestimate of the actual residual stress state of the manufactured laminates. The addition of a more complex CHILE model would predict that less residual stress is developed in the “Hot” samples as the instantaneous resin modulus would remain low until after the cure temperature had dropped below T_g^{hot} . However, from the lack of compressive chemical shrinkage strain developed in the “Hot” samples, as seen in Figure 88, it is likely that an appreciable amount of stress relaxation occurs in these samples. Therefore, a viscoelastic model, with the addition of more variable parameters, will be the most appropriate approach for determine residual stress in the “Hot” samples.

However, one way to approximate what the residual stress might be in the “Hot” laminates is to assume that while the cure temperature is above T_g^{hot} , the residual stress in the samples is zero as it is all dissipated viscously. This is a reasonable approximation as the “Hot” samples did not gel until after T_g^{hot} had been surpassed. Then, by assuming that the resin matrix instantaneously regains its stiffness when the laminate temperature drops below T_g^{hot} of the laminate, an approximation of the residual stress state of the “Hot” laminates can be made. While this is an oversimplification of the viscoelastic behaviour of the “Hot” laminate, it at

least suggests the differences that are present between the “Hot” and “Cool” laminates. The results of the newly calculated residual stress development in “Hot” samples is shown in Figure 91.

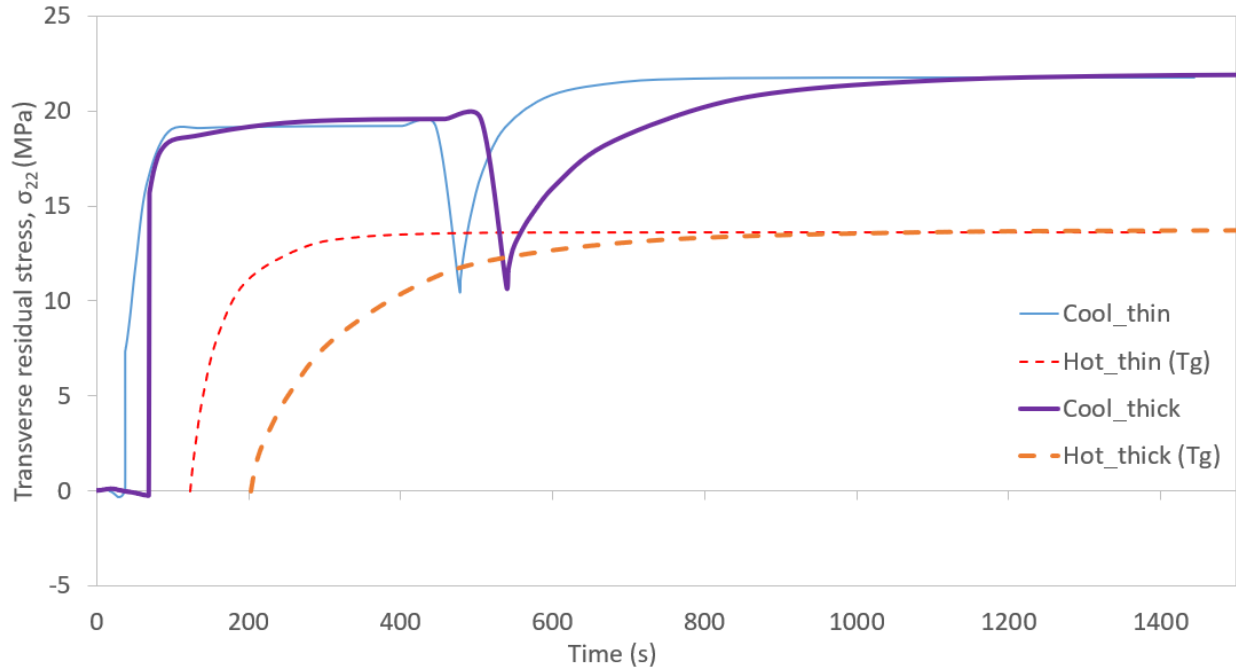


Figure 91: Transverse residual stress developed on the outer ply for all laminates modelled, for 1500 seconds after α_{gel} . With “Hot” samples residual stress modified to account for T_g

Now, it can be seen that the final residual stress state of both of the “Hot” and “Cool” samples is 13.8 MPa and 21.9 MPa, respectively. This gives a difference of approximately 8 MPa less tensile stress in the “Hot” samples than the “Cool” samples. As discussed, this approach of accounting for the glass transition is an over-simplification and the true residual stress value of the “Hot” laminates is likely to lie somewhere between this result and the originally calculated residual stress value for the “Hot” samples. This assumption corroborates well with the data gathered in chapter 5 where it was found that the residual stress in the neat resin sample cured at 140 °C (top and bottom mould temperature) was around 4 MPa more tensile than the sample cured at 180 °C. These results are not directly comparable as the photoelastic analysis omits reinforcing fibre effects and is 3 mm thick resin and the FE model oversimplifies the viscoelastic behaviour during cure. However, a useful parallel between the two can be drawn as the same general trend is exhibited. This will be explored in more detail alongside mechanical performance analysis conducted in section 8.4.

In the literature

To the author's knowledge, there is no work in the literature to directly compare with these results, as no work has investigated rapidly curing laminates. However, a number of authors have investigated residual stress in UD laminates, and some have also embedded FBGs in the laminate to experimentally validate strain. The most relevant work found in the literature is detailed in Table 14.

Table 14: A summary of recent work in the literature using embedded FBGs to measure strain and modelled stress values

Source	Sample (mm)	Cure	Strain ($\mu\epsilon$)	Stress (MPa)
Minakuchi et al [233]	100x100x7.5 FBG transverse	90 °C for 5 h (2 °C/min)	≈ -4000	+0.5
Hu et al [154]	110x110x10 FBG transverse	7.5 h total – 3.5 h @ 180 °C	≈ -9000	+/-0.2
Qi et al [240]	200x200x2.5 FBG transverse	80 °C for 10 min then 100 °C for 20 min	-5183	N/A
Chen et al [263]	80x250x5.4 Axial direction	110 °C for 1 h & 180 °C for 2 h	$\approx +150$	N/A
Patham and Huang [264]	127x127x25 UD glass polyester	5.5 h total 1 h @ 130 °C	N/A	0 resultant. Range: -25+25 during cure
Bogetti and Gillespie [20]	25.4, 18.5 & 13.8 Glass polyester	5.5 h total 1 h @ 130 °C	N/A	Outer: +14, +5, +2 Inner: -8, -3, -2
Wenani [18] 1D FE	25.4, 18.5 & 13.8 Glass polyester	5.5 h total 1 h @ 130 °C	N/A	Outer: +14, +5, +2 Inner: -8, -3, -2
Wenani [18] experiment	400x600x46 Glass epoxy	Resin infusion, 35 °C hot plate – 20 h	≈ -2400	N/A
Yuksel et al [78] with hole drilling	20x20x30 mm UD glass polyester	Pultrusion	-	+6

Magnier et al [62] hole drilling	250x13x2 mm UD CFRP	-	-	+ 10
Baran et al [265] FE	25.4x25.4 mm UD glass polyester	Pultrusion	≈ -3000	+3.7
This work	150x150x (2/6.35) mm FBG transverse	140 °C for 8 min & 180 °C for 1 min	≈ -13,000	+13.8, +21.9

The work by Yuksel et al [78] is of particular interest as it utilises hole drilling with DIC to measure strain fields and calculate stress. This is in contrast to the other work presented which uses cure modelling to determine residual stress. In this work, a UD 20x20x30 mm pultruded bar has a tensile residual stress of 6 MPa, which more closely resembles the results found in this current work. This is also seen in the work by Magnier et al [62], where hole drilling experiments, using a traditional strain gauge rosette, finds a tensile residual stress value of 10 MPa. However, no detail is given on sample manufacture or cure in this study. These results suggest that the models predicting very low levels of residual stress are underestimating residual stress due to under-defined boundary conditions as this is not an issue in the hole drilling analysis. This is corroborated by the analysis conducted by Baran et al [265] which modelled a similar pultruded bar and found a tensile residual stress of 3.7 MPa in the centre of the bar, with a residual strain of -3,000 $\mu\epsilon$. This analysis completely fixed two of the four side during the curing analysis and a reasonably large residual stress value was found.

A wide range of final residual stress values are seen in the literature, with the current work having a larger tensile residual stress value than other comparable work. This is thought to be due to a number of factors. Firstly, this analysis investigates curing which occurs an order of magnitude faster than anything else found in the literature. As discussed throughout this thesis, this will lead to higher levels of residual stress and so a higher stress values are to be expected. Secondly, the boundary conditions used in this residual stress analysis have been found to make a large difference to the final residual stress state of the laminate as this tool-part interaction is a key driver of residual stress development. This is especially true in

the case of UD laminates, where classically it would be assumed that residual stress is zero if heated and cured evenly. Many of the studies found in the literature use less rigid structural boundary conditions than have been used in this current work. Structural boundary conditions are often modelled as a plate with a fixed or frictionless contact and then a completely free top edge. This is applicable for the case of resin infusion or autoclave curing but is not applicable for hot press curing where the laminate is completely enclosed in a ridged mould. Third, many of the values for variables used in this work have been assumed or derived from other sources. Thus, the final residual stress value found here must be viewed with some caution and is more useful as a comparison tool between similarly modelled laminates. Therefore, it is still thought that while the results presented here are high compared to work found in the literature, they are still reasonable and to expected with the faster curing times and more fixed boundary conditions

7.5. Conclusions

The main aim of this chapter was to build a simple multi-physics model to explore the development of residual stress in rapidly curing composites and use it to evaluate the relative differences in residual stress between the curing cases used in the experimental work in this thesis. This has been a challenge. Due to the complex and multi-physics nature of curing composites, especially rapidly curing ones, many assumptions, simplified boundaries and assumed material values are required to begin analysing the development of residual stress. Inevitably, this results in a certain degree of uncertainty when trying to quantify an exact value for residual stress in the simulated laminates. However, while caution must be applied in an over confidence in values, this work has been able to show relative and insightful differences between the variously cured laminates. Good corroboration between experimentally measured, and numerically determined thermal histories for all laminates was seen. Additionally, good corroboration in experimentally measured and modelled strain histories for “Cool” laminates was seen. However, due to “Hot” laminates exceeding T_g^{hot} before reaching α_{gel} , as discussed in chapter 6, good corroboration was not seen for this case. This led to an overestimation of tensile residual stress for the “Hot” cases. However, a simple zero stress above T_g^{hot} assumption was applied to estimate the lower bound of the residual tensile stress in the “Hot” laminates. It is expected that the true residual stress value is somewhere between these two predictions.

In summary:

- Good corroboration between experimental and numerical for thermal histories was found
- Good corroboration between experimental and numerical for strain histories of “Cool” laminates was found
- Unable to accurately model the strain development in the “Hot” laminates as the current model does not account for the glass transition and subsequent relaxation present in these samples
- The model was unable to capture through-thickness variations in residual strain and stress due to the simplified chemical shrinkage assumptions used
- A simple zero stress above T_g^{hot} assumption in the “Hot” laminates resulted in a final tensile residual stress of 13.8 MPa. A final tensile residual stress of 21.9 MPa was found for the “Cool” laminates.

Future work:

- Transition the model to a more customizable software package like ABAQUS to be able to implement the following changes more easily:
 - Develop the model further to include a DOC dependent chemical shrinkage function to better account for through thickness effects.
 - Implement a CHILE or viscoelastic model for curing that occurs above the T_g^{cured} of the modelled laminate to accurately capture phase transition and relaxation of laminates.
 - More work is required to experimentally determine rapidly curing laminate material parameters such as the development of modulus with DOC and cure kinetics parameters.

8. The effect of residual stress on mechanical performance

8.1. Introduction

To gain an insight into the effect of various residual stress and strain states on the mechanical performance of composites laminates, a series of mechanical tests were conducted. The primary property of interest in this work is the transverse matrix strength within the laminate as the majority of thermal and chemical volumetric changes, and therefore stresses, occur in the transverse matrix direction. Here, Transverse Three-Point Bending (T3PB) tests were used to reduce the effective gauge length that experiences the maximum bending stress, σ_{max} , for the transverse strength analysis. This reduces the effect of flaws on the flexural strength of the laminate which can often lead to an underreporting of transverse strength values. T3PB has been found to be an effective way of comparing the generation of transverse residual stress in UD laminates [175]. A μ CT void analysis of samples tested was conducted to investigate the influence of void content on transverse bending strength so that this could be decoupled from thickness and curing temperature effects being analysed. Finally, a discussion incorporating work from throughout this thesis is had to analyse the effect of rapid curing on laminate mechanical properties.

Therefore, the aim of this chapter can be summarised as:

- Determine the effect of curing temperature and laminate thickness on the transverse bending strength of rapidly cured UD laminates

with the objectives being to:

- Manufacture and test samples for T3PB tests from laminates made during chapter 6 so that a range of cure conditions can be analysed
- Use μ CT scans of each laminate tested to determine void content and analyse the influence of voids on T3PB results with respect to residual stress
- Compare and contrast strain data gathered in chapter 6 with T3PB data to determine the effect of residual strain on transverse residual stress in UD laminates

- Incorporate work from throughout this thesis to examine the effect of rapidly curing composites on residual stress

8.2. Materials and method

Transverse tensile tests with a $[90]_n$ layup with all the fibres being transverse to the loading direction, as suggested by ASTM standard D3039 [266], can be used to measure the transverse matrix strength of UD laminates. However, in any successful transverse fibre reinforced composite testing the matrix will be the primary area of failure. As the resin matrix is brittle, this process is usually governed by flaw dominated failure mechanisms with cracks propagating from various defects in the laminate. In transverse tensile tests, this can cause premature failure as the gauge length, and therefore highly stressed area, is large. This makes it very difficult to accurately and repeatedly measure the true transverse matrix strength as flaws often lead to premature failure [175]. Therefore, to reduce the likelihood of there being a flaw which causes premature failure in the gauge length of the sample, an alternative test setup can be used which reduces the effective gauge length of the sample.

In more homogeneous materials, four-point bending tests are generally preferred for material characterization as they allow for a large region of evenly distributed σ_{max} , thereby allowing for a more realistic measurement to be taken. However, in this case, reducing the gauge area that is stressed prevents premature failure of the laminate by focusing the maximum flexural stress on a smaller area of the laminate. Therefore, in the case of transverse UD laminates, the transverse matrix strength values attained from a three-point bending test are more representative of the transverse matrix strength than transverse tensile or four-point bending tests. The maximum flexural and shear stresses in three- and four-point bending is shown diagrammatically in Figure 92.

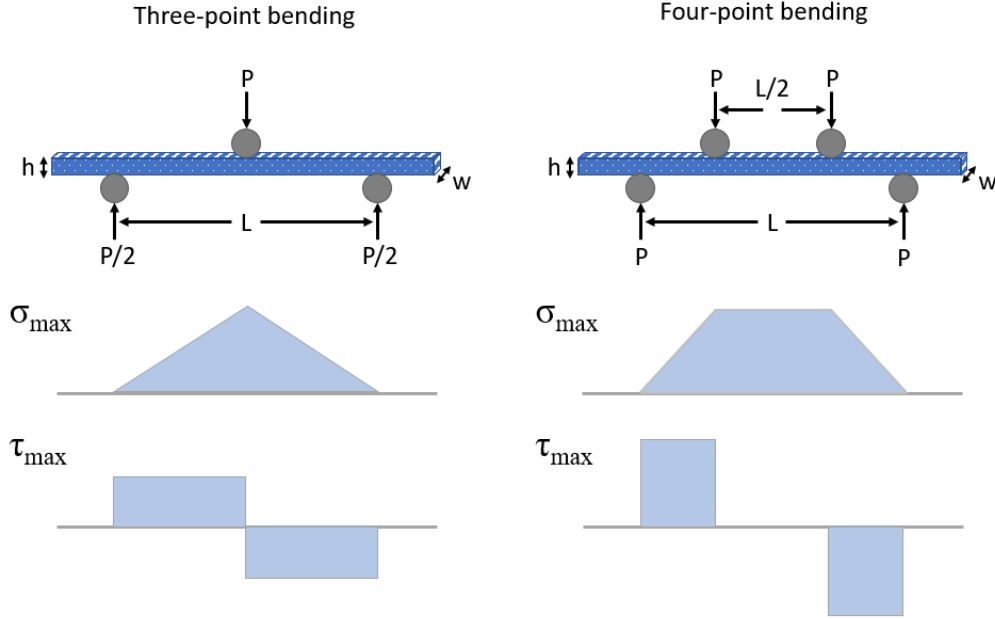


Figure 92: Three and four-point bending diagrams

To ensure failure is caused by bending instead of shear, classical beam theory can be used to determine the maximum flexural stress, σ_{22}^{max} and the maximum through-thickness shear stress, τ_{13} in a square cross-section beam in three-point bending. Thereby determining the minimum theoretical span-to-thickness ratio required for failure to occur due to flexure, σ_{22} and not interlaminar shear, τ_{13} . This relation for a $[90]_n$ laminate is given by Equation (42) and Equation (43) respectively

$$\sigma_{22} = \frac{3PL}{2wh^2} \quad (42)$$

$$\tau_{13} = \frac{3P}{4wh} \quad (43)$$

where P is the applied failure load, L is the span between the support pins, w is the sample width and h is the sample thickness. In transverse flexure specimens the maximum through-thickness shear stress τ_{13} is equal to the maximum interlaminar shear stress τ_{23} . Therefore, the ratio of maximum bending stress to maximum interlaminar shear stress can be written in Equation (44).

$$\frac{\sigma_{22}}{\tau_{23}} = \frac{2L}{h} \quad (44)$$

Thus, only a span-to-thickness ratio of two is required to promote failure due to bending. Adams et al [175] showed this experimentally, finding that span-to-thickness ratios as low as 4:1 still led to failure due to bending and that there was no difference found in flexural

strength with varying span-to-thickness ratios. Thus, in this work span-to-thickness ratios of 8:1 will be used as a compromise between reducing material usage and ease of manufacture whilst still ensuring failure occurs on the bottom surface of the laminate due to a transverse matrix strength failure on the bottom surface of the samples.

Specimen manufacture

Laminates manufactured for the embedded sensor testing series were subsequently used for T3PB and μ CT testing and are shown in Table 11 in section 6.3. Thus, the specimen preparation methodology outlined in section 6.3 was followed for all laminate preparation. For three-point bending and μ CT tests, samples were subsequently cut to length from the larger laminate using a ProtoMax waterjet cutter. All three-point bending and μ CT samples were cut to a width, w of 13 mm as this complies with the guidelines outlines in ASTM D7264 [267] for three-point bending and offers a reasonable thickness for μ CT tests. Standard D7264 also stipulates a span-to-thickness ratio of 32:1 for three-point bending specimens to ensure failure occurs at the outer edge of the specimen due to bending and not to interlaminar shear. However, in the case of $[90]_n$ specimens with the fibre-oriented transverse to the axis of the beam, a much smaller span-to-thickness ratio is required to achieve this as interlaminar shear stress is very low in this case. Therefore, T3PB specimens were cut out of the embedded sensor laminates, away from the embedded FBG itself, with a span-to-thickness ratio of 8:1 and the details of the quantities and dimensions of the various T3PB samples can be seen in Table 15. Additionally, three samples were cut from the Cool_thick laminate which had the embedded FBG running longitudinally along the length of the specimen (transverse to the fibre direction). This was done to determine the effect of embedded FBGs on laminate transverse bending strength. It was only possible to cut three samples from one laminate due to geometric constraints.

Samples were also cut, from the section of the laminate with embedded FBGs, for all cure conditions tested for μ CT test samples. Samples were 13x30 mm in width and length and varied with thickness with respect to laminate thickness. Unfortunately, due to budget constraints, only one sample per curing condition could be scanned in the μ CT machine. Therefore, it was not possible to perform repeat tests for the μ CT void analysis. The sample specifications for the μ CT void analysis are also shown in Table 15.

Table 15: T3PB and μ CT specimen information

Experiment	Sample	With an embedded FBG	No. of specimens	Thickness (mm)	Span length (mm)
T3PB	Hot_thick	No	16	6.65	53.2
	Cool_thick	No	16	6.55	52.4
	Hot_thin	No	13	2.19	17.5
	Cool_thin	No	15	2.19	17.5
	Cool_thick	Yes	3	6.55	52.4
μ CT	Hot_thick	Yes	1	6.65	-
	Cool_thick	Yes	1	6.55	-
	Hot_thin	Yes	1	2.19	-
	Cool_thin	Yes	1	2.19	-

Transverse 3-point bending testing methodology

A 5 kN Tinius Olsen universal testing machine was used for T3PB testing, with a 3-point bending rig mounted to it with 10 mm diameter loading and support pins. The pins were then separated and secured to the relevant span length for each sample, using Vernier callipers to ensure accurate positioning. Load was applied with a crosshead speed of 0.2 mm/min until sample failure. This was repeated for all specimens and the failure load recorded so that the maximum flexural stress, σ_{22}^{max} could be determined using Equation (42).

Void analysis methodology

As discussed in section 2.5, transverse matrix strength testing is dominated by a flaw-based failure mechanism [176][176]. While T3PB reduces the effect of these flaws it is also useful to determine the extent to which there are large flaws, like voids, in each of the samples being tested so that any anomalous results can be assessed. Void identification with μ CT scans has been found to be a reliable and accurate with one comparative study finding a standard deviation of 0.23% in void measurements using μ CT for UD laminates [268]. Thus, μ CT scans of samples with embedded optical fibres were used to determine a representative void content for each laminate configuration tested. For the “thin” samples the same μ CT scans used in the interface analysis in chapter 4 were used to determine void content. For the “thick” samples additional scans were made with a larger field of view to get a more representative

sample area that did not include the large voids in the resin eyes formed around the embedded optical fibres as these would not be present in the T3PB samples tested (with the exception of “Cool_thick FBG”). For these samples the scans used an x-ray tube voltage of 60 kV, a tube current of 108 μ A, and an exposure time of 2 seconds. A total of 1601 projections were collected. A filter (LE3) was used to filter out lower energy x-rays, and an objective lens giving an optical magnification of 4x was selected with binning set to 2, producing an isotropic voxel size of 4.07 μ m. The area around the resin eye was then removed so that representative void content calculations could be made. To determine the void content of each sample the 3D volume information was segmented and analysed in the tomographic software Dragonfly. Voids were segmented from the rest of the laminate by performing a thresholding analysis on the data. The percentage volume of these voids relative to the rest of the sample could then be determined. This involves manually determining intensity limits for what constitutes as a void and removing the remaining data. This is quite a subjective step and as such, not too much importance should be given to the exact numbers extracted from this analysis but rather the relative difference between the outputs should be considered to be valid as any error will be systematic in this case. Additionally, due to the relatively similar densities of the resin matrix and reinforcing carbon fibres, there is a small contrast difference between the two in the μ CT images. Thus, a morphological smoothing step was also needed to remove as much background noise as possible and to fill in internal areas of voids which are not well accounted for.

8.3. Results and discussion

To investigate the effect of various residual stress conditions on the matrix dominated transverse bending response, T3PB tests were conducted on samples with a variety of cure states and laminate thicknesses using the methodology previously outlined. Additionally, a number of Cool_thick samples with an FBG embedded in the gauge length were also tested to determine the impact of the FBG on transverse bending strength relative to a sample without an embedded FBG in a UD laminate. The average results of the T3PB tests are tabulated in Table 16 along with void content values calculated with the μ CT analysis previously outlined and shown individually in Figure 93. The average σ_{22}^{max} omits the Cool_thick with an embedded FBG sample.

Table 16: T3PB results for various residual stress conditions and μ CT void content calculations

Experiment	Average σ_{22}^{\max} (MPa)	Standard deviation	No. of specimens	Void content (%) (excl. around FBG)	DOC from DSC (%)
Cool_thick w. FBG	47.29	5.77	3	1.92	95
Hot_thick	79.72	7.15	16	0.74	98
Cool_thick	74.12	6.87	16	1.68	95
Hot_thin	82.82	10.01	13	0.29	98
Cool_thin	70.24	7.54	15	0.15	97
Average (excl. FBG)	76.72	7.89			

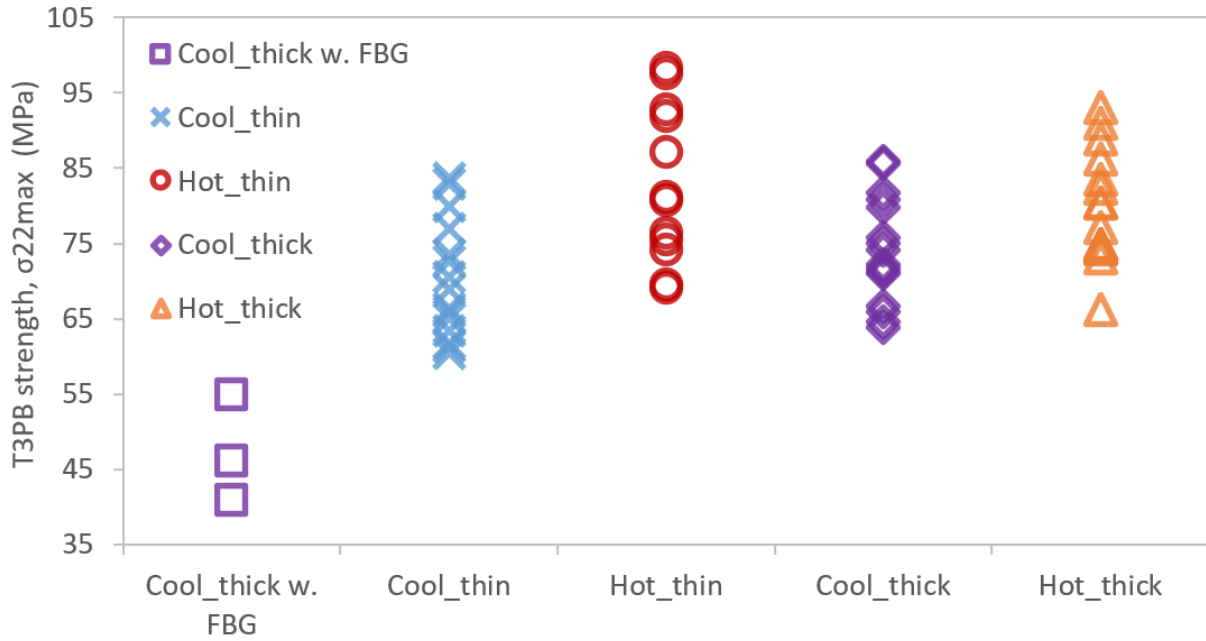


Figure 93: T3PB strength, σ_{22}^{\max} results for all samples tested

Additionally, the DOC of each sample was determined by completing a non-isothermal DSC sweep at 10 °C/min and measuring the residual heat of reaction, $\Delta H_t^{\text{residual}}$ and dividing it by the total heat of reaction, ΔH_t of an uncured sample as determined in chapter 3. All samples were seen to be almost fully cured and have similar DOC values, and as such it is assumed that all their cure dependent mechanical properties are the same and the influence of cure state on the transverse bending response can be neglected.

Statistical analysis

To further this analysis, an unpaired two-tailed t-test was conducted to test the null hypothesis that the difference between two given curing conditions is not statistically significant. A 95% confidence interval is used to determine whether the null hypothesis has been met and there is a statistical difference between the two tests being compared. Therefore, a comparison between two data sets producing a p-value of less than 0.05 is defined to be statistically different. The results of this statistical analysis are shown in Table 17.

Table 17: P-test results for T3PB

Test	Comparison	P-value	Null hypothesis
Cool_thick vs Cool_thick FBG	FBG	0.00001400	Rejected
Cool_thin vs Hot_thin	Cure temperature	0.00143683	Rejected
Cool_thick vs Hot_thick	Cure temperature	0.03666432	Rejected
Cool_thin vs Cool_thick	Thickness	0.15793965	Accepted
Hot_thin vs Hot_thick	Thickness	0.36576771	Accepted

With the aid of the statistical analysis in Table 17, we can confidently identify three trends. First, samples with an embedded FBG along their gauge length fail much earlier than an equivalent sample without. This is shown by the FBG comparison giving a very low p-value, indicating a high degree of statistical confidence that these two data sets are different even though only three samples with an embedded FBG were tested. Second, there is no difference in the reported transverse matrix strength values for samples cured at the same temperature but with varying thickness in these tests. Here, the high p-value (above 0.05 for a 95% confidence interval) indicating that there is not sufficient statistical certainty to define the thickness comparisons between similarly cured samples as different. Third, higher curing temperatures lead to higher transverse matrix strength values being observed for both “thick” and “thin” samples. This is indicated by p-values of below 0.05. However, it should be noted that the difference between the Cool_thick and Hot_thick sample sets is less pronounced than for the “thin” data sets. This is likely due to the higher variability seen in thicker samples which will now be discussed.

Transverse bending strength of samples with embedded FBGs

From Table 16 and Table 17 it is clear that the addition of an embedded FBG dramatically reduces the average transverse flexural strength of the laminate by approximately 35%. Fewer specimens were tested with embedded FBGs, due to the manufacturing methodology used, reducing the statistical significance of this measurement. It is still clear however, that the addition of an FBG has a large impact on the transverse flexural strength of the laminate. This is due to the embedded optical fibre on the outer (tensile) edge of the specimen in T3PB acting as a crack initiation site, thereby causing premature failure. This hypothesis is corroborated by the results previously discussed in section 4.5 (is also evident in Figure 94) where voids were seen to be forming around the resin rich area around the embedded sensor. Whilst this is thought to not impact the effectiveness of the FBG in measuring strain this does still allow for a stress concentration and subsequent crack initiation [150]. It should be noted however that this does not mean that embedding optical fibres in any laminate will reduce the transverse bending strength to this extent. More conventional woven or cross-ply laminates are not as sensitive to the presence of voids as the various fibre angles help to retard the crack growth [174].

The effect of laminate thickness on transverse bending strength and void content

The effect of thickness on the transverse bending strength of the samples is more difficult to identify. This is because as well as the residual strain contributions changing with laminate thickness, so does the void content to an appreciable extent. Thus, it is difficult to determine which factor is the key driving force behind the sample's failure. As shown through the μ CT analysis results in Table 16, there is an abnormally high void content in the Cool_thick sample (1.68%) and a relatively high void content in the Hot_thick sample (0.74%) when compared to the "thin" samples. In the aerospace industry a typical acceptable void content level in composite structures is considered to be below 1% [33]. As the Cool_thick sample is the only sample to exceed this, with the Hot_thick sample having less than half of its void content but still more than double than the Hot_thin sample, this suggests that the Cool_thick samples, and to some extent the Hot_thick samples, failed prematurely due to crack initiations at a void/matrix boundary. To better visualise this a 3D μ CT image of the Hot_thick sample is shown in Figure 94 with voids highlighted in blue and the embedded optical fibre highlighted in red. The large void around the resin eye is clearly visible and was removed for the void

content analysis as this was not present in the samples tested in T3PB which did not have an embedded optical fibre.

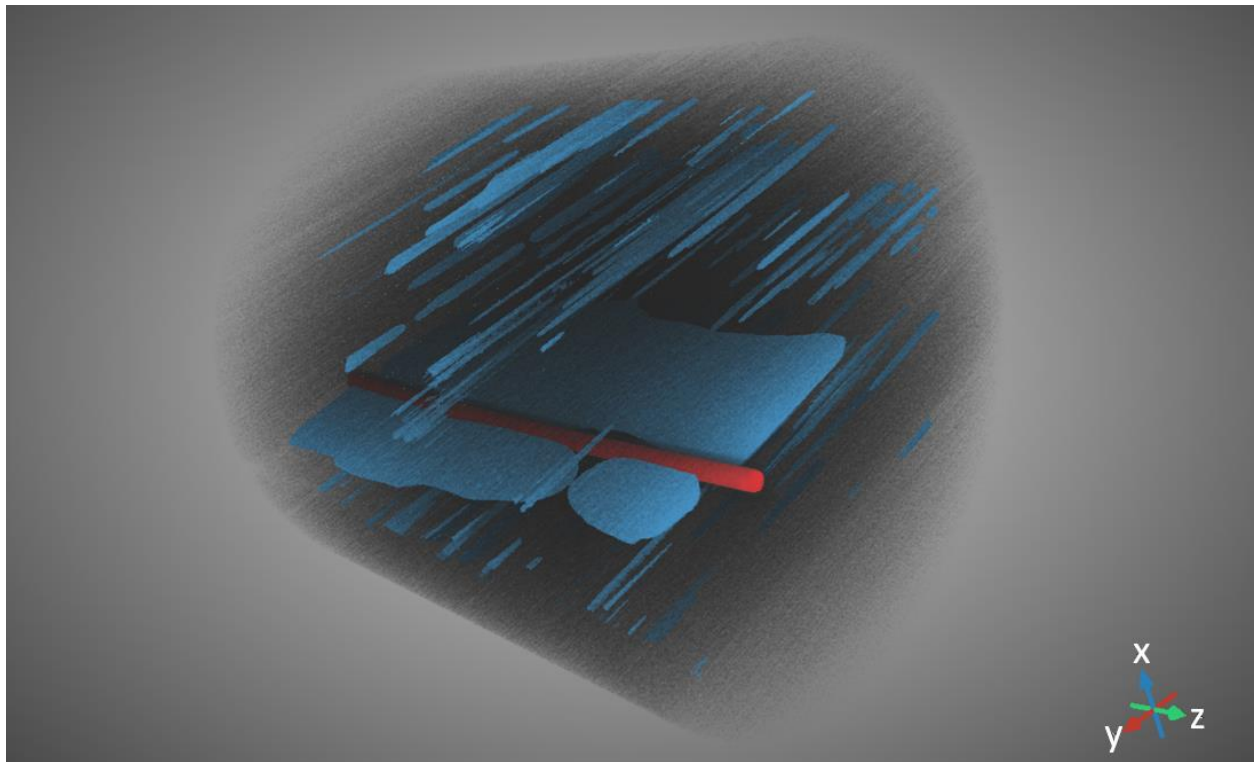


Figure 94: A 3D μ CT image of the Hot_thick sample ($4.07\ \mu\text{m}$ voxel size) with embedded optical fibre (red) and voids (blue) highlighted to visualise void location and size. Voids around resin eye are included.

Here, the voids can be seen to form mainly along the fibre direction (y-axis) which is indicative of poor laminate compaction or inadequate resin flow during cure. As can be seen there are many crack initiation sites present in the “thick” samples, therefore the failure load of the “thick” samples is likely lower than should be expected due to the area of high stress concentration. This is of particular importance when testing the transverse matrix response of UD laminates, as this is very sensitive to flaws and crack growth. Thus, with the data presented here it is difficult to make any inferences on the role of laminate thickness in residual stress in rapidly cured composites with any certainty. There is potential for thickness to still be a contributing factor in the average transverse flexural strength values and therefore in the formation of residual stress. In the future, more work, with an emphasis on controlling void content in thicker laminates, is required to investigate the effect of laminate thickness on transverse bending strength so inferences as to the residual stress state can be made with more certainty.

The effect of curing temperature on transverse bending strength

From the statistical analysis, we can see that both the Hot_thick and Hot_thin samples have higher average transverse matrix strength values than their equivalent “Cool” samples. The Hot_thin laminate in particular, was seen to have the highest average transverse bending strength but also the largest standard deviation when compared to all the other laminates under investigation. In the case of the Hot_thin samples, the high standard deviation is caused by samples either breaking quite early or late, relative to the average, with the lowest and highest reported transverse flexural strength values being 69.0 MPa and 98.4 MPa, respectively. This can be seen in Figure 93 with samples mostly failing in the outer quartiles of the data set. This suggests that the T3PB strength of the Hot_thin sample might be higher than reported in the average value but is failing early in some cases due to either poor loading during testing, voids causing premature failure, other sample flaws or some combination of these factors. Again, the difference between the Hot_thick and Cool_thick samples is more difficult to unpack for the reasons outlined in the previous thickness effects comparison. However, it can still be seen that the Hot_thick samples tend to have a higher transverse matrix values than the Cool_thick samples.

Higher curing temperatures leading to higher transverse matrix strength values is most likely explained by a decrease in tensile residual stress on the outer edge of the laminate. This result is somewhat contrary to the current hypothesis that higher curing temperatures will lead to higher level of compressive strain and tensile residual stress. To better relate the residual strain condition, first shown in Figure 78 in chapter 6, and the T3PB results (excluding Cool_thick FBG) with error bars representing the 95% confidence interval from the mean, these results are plotted together in Figure 95.

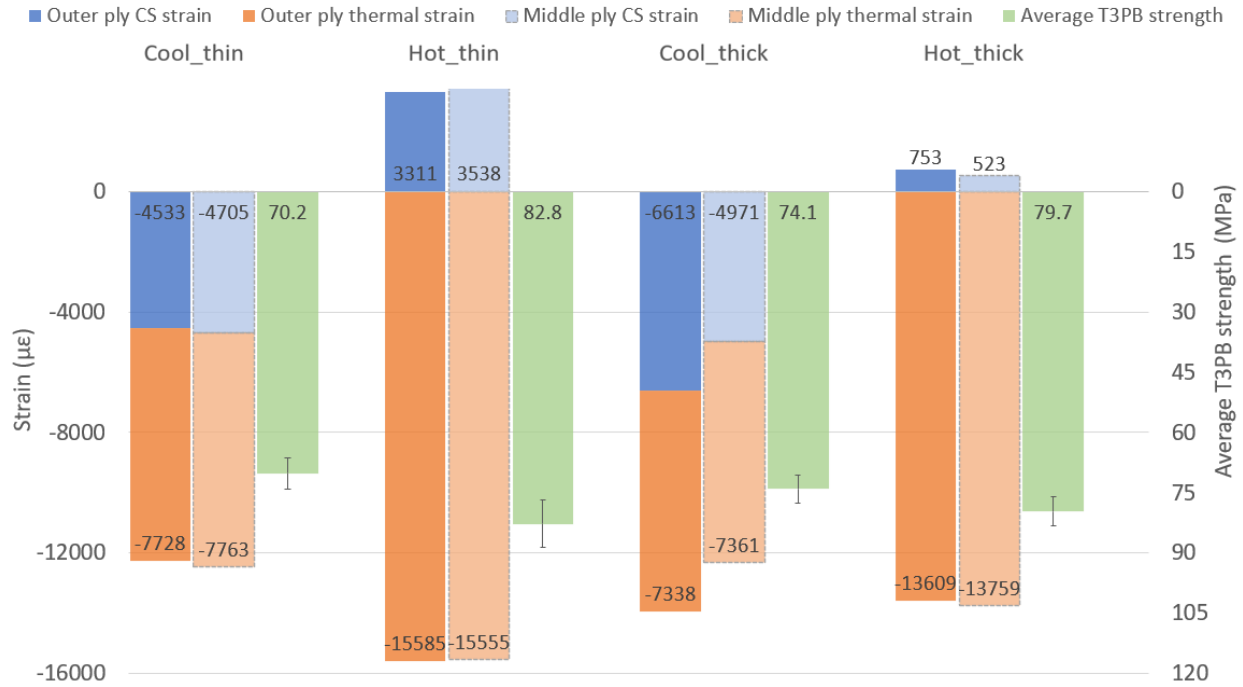


Figure 95: T3PB results for various residual stress conditions with their respective curing strain histories. Error bars are the 95% confidence from the mean and are included for the average transverse bending strength results.

Here, it can be more easily seen that higher levels of compressive thermal residual strain led to higher transverse bending strengths results. Again, this contrary to the current hypothesis that these strains, which occur in the latter half of the cure cycle when the modulus is high, should lead to higher tensile residual stress. Additionally, an increase in chemical shrinkage strain is seen to decrease the transverse bending strength, indicating higher levels of residual stress. Equally, this is contrary to the current hypothesis that more chemical shrinkage strain, which occurs during the period when the matrix is less stiff, should result in less residual stress. Therefore, it is evident that there are other mechanisms at play which are currently not being captured by the embedded FBGs. This will be explored further when a holistic analysis of work done in this thesis so far is used to inform the effect of rapid curing on mechanical properties in the following section.

8.4. The effect of rapid curing on mechanical properties

One aspect that has not been considered so far in the analysis of the effect of rapid curing on transverse bending strength is the time spent above the T_g^{cured} during cure. As determined in section 3.6, the T_g^{cured} of EF7017 is 145 °C (T_g^{hot}) and 170 °C (T_g^{cool}) for the “Hot” and “Cool” cured specimens, respectively. Now, by using the residual strain data captured with embedded FBGs to determine α_{gel} , as discussed in chapter 6, and the simultaneously captured thermal data, Figure 96 can be plotted. Time zero is when the laminate is first placed into the hot press and the α_{gel} is determined through the onset of strain detected by the embedded FBG and is marked with a triangle.

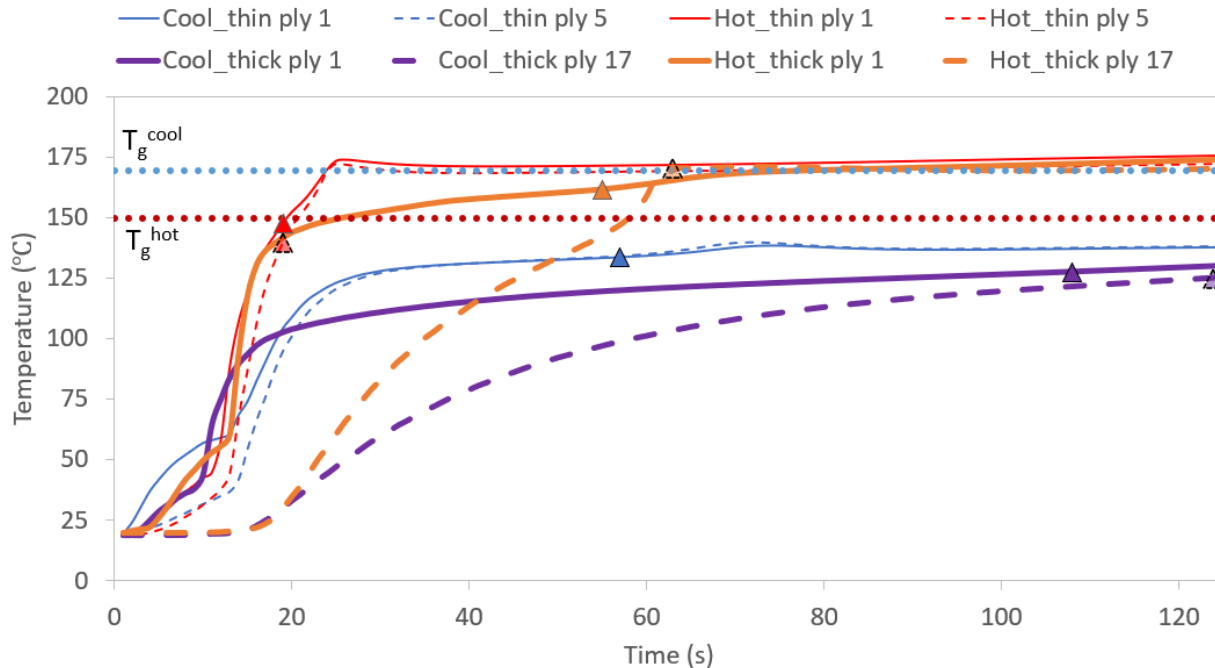


Figure 96: Experimentally measured temperature for all samples tested at outer and inner thicknesses of the laminate from placement within the hot press. Triangle points indicate gelation of the matrix as measured by embedded FBGs. The glass transitions for the “Hot” and “Cool” case are also indicated.

The onset of α_{gel} , through the thickness of the laminate for the “thin” parts is found to occur at the same time, within approximately 1 second, regardless of cure temperature. This is to be expected as the thermal history at the outer and inner thicknesses are very similar throughout the entire cure. However, for the “thick” laminates there is non-uniform gelation

through the thickness of the laminate. This effect is seen more clearly with the “Cool” laminates as the slower heating rate causes there to be a larger thermal gradient through the thickness of the laminate. This will likely cause a small differential residual stress distribution to form through the thickness of the “thick” laminates as the outer edges of the laminate are stiffer and thereby restrain the chemical shrinkage and thermal expansion/contraction of the inner laminate. As discussed in chapter 7, without any further information as to the extent or duration of this stiffness differential in the laminate it is not possible to determine the magnitude of this effect’s contribution to the final residual stress state of the laminate.

Here, it can be seen that both the Hot_thin and Hot_thick samples do not begin to gel until the temperature of the laminate is around T_g^{hot} . This T_g^{hot} value was determined from a mostly cured laminate, and the instantaneous T_g of the “Hot” samples remained below the laminate temperature until after the laminate was removed from the hot press. Therefore, it did not vitrify until after being removed from the hot-press. As the cure temperature was much higher than the instantaneous glass transition temperature there was a significant increase in the loss modulus and the resin was in a rubbery state. This is caused by an increase in molecular mobility of the resin matrix which allows for cross-linking to occur without a large build-up of residual stress and for residual stress already present to be relaxed at a significantly increased rate. To better understand the relationship between DOC and T_g it is proposed that future work use the Di Benedetto equation [220]. This will allow for a more quantified analysis of the extent of E' and E'' development with DOC.

Residual stress begins to develop rapidly again after the laminate temperature drops below T_g^{hot} , and the resin matrix vitrifies, T_{vit} , and becomes glassy again. Additionally, it can also be seen in Figure 96 that the Cool_thin and Cool_thick samples do not exceed T_g^{cool} of the “Cool” samples during cure. This indicates that the “Cool” samples vitrify during the heating phase of the cure cycle, allowing for stress to be more readily developed. This also suggests that the instantaneous glass transition temperature was not exceeded by the laminate temperature by as big an extent as seen in the “Hot” laminate. Thus, the instantaneous elastic modulus in the “Cool” samples remains higher and more residual stress can be developed, and less stress is relaxed. The point at which laminate temperature drops below the T_g^{hot} of both of the “Hot” laminates is marked as T_{vit} on the residual strain data shown in Figure 97.

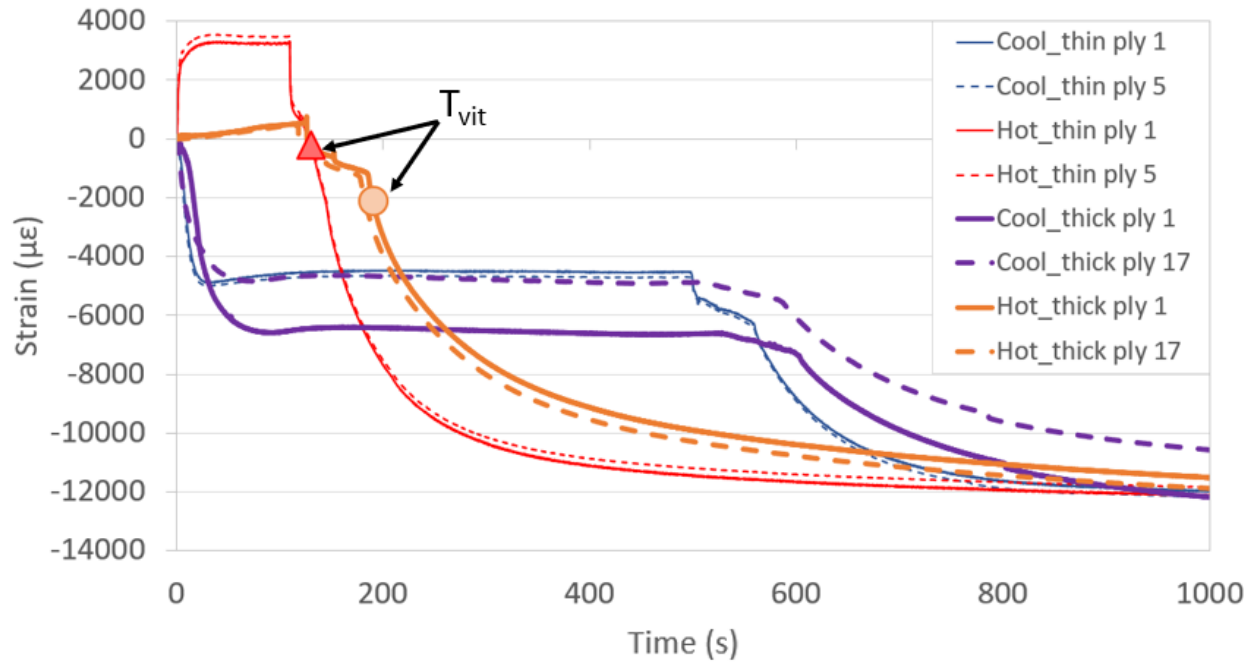


Figure 97: Embedded FBG strain histories between 0-1000 seconds. The point in the strain history when the temperature drops below the T_g^{hot} of the “Hot” laminates is marked as T_{vit} .

As discussed in chapter 6, a large proportion of the strain developed in the “Cool” samples occurs shortly after gelation when the resin modulus is still being developed during the polymerization process, and therefore leads to less residual stress. However, as the resin is still in, or near to being in, its glassy state, a large amount of this strain is stored elastically as residual stress and very little relaxation occurs. Therefore, there is an overall increase in tensile residual stress when compared to the “Hot” samples which are further into their rubbery phase and for longer. This is evident in the T3PB results shown in Table 16. This relaxation behaviour seems to be the major driving factor in the determination of the final residual stress state of the laminates tested in this work. Without this effect it would be inferred from the residual strain data in Figure 95 that the “Hot” samples would have more tensile residual stress as the majority of the strain developed in these laminates occurs when they are mostly cured and their modulus has been fully developed. This is also seen in the results of the FE analysis (Figure 90), where the “Hot” samples were found to have a higher tensile residual stress if the T_g effects were not accounted for.

This explanation is also corroborated by the fact that the through-thickness variation in residual strain in the Hot_thick sample is much lower than the Cool_thick sample. Without considering the effect of the glass transition temperature, this result does not make sense as it would be expected that the sample cured at a higher temperature would experience a larger temperature, and therefore strain gradient after cure. However, as the Hot_thick sample spends a prolonged period in its rubbery phase, this allows for strains and stress to be relaxed and equilibrated through the thickness of the Hot_thick laminate. Therefore, the final residual strain values for the Hot_thick samples are similar on the outer and inner surface of the laminate. However, in the Cool_thick samples these strains are not allowed to relax to the same extent, as the resin matrix vitrifies before it is fully cured. Thus, a resultant through-thickness strain gradient is formed.

The FE analysis in chapter 7 showed a difference between the “Cool” and “Hot” cure condition of approximately 8 MPa after the effect of surpassing the T_g^{hot} had been accounted for. This was thought to be an overestimation of the difference between the curing conditions due to the simplistic glass transition assumption used. As discussed, it was not possible to account for through-thickness variations of residual stress in the model so no inferences can be made to the extent of the through-thickness effect. It is thought that with the future work outlined at the end of chapter 7, it will be possible to determine through-thickness variations within the model. Then, modelling much thicker laminates, which would be unsafe to manufacture due to laminate exotherm, would be possible and insightful as these effects should be enhanced with increasing laminate thickness, making comparison easier.

The “Hot” samples having less tensile residual stress than the “Cool” samples is also seen in the photoelastic analysis carried out in chapter 5. In that analysis it was found that the 3 mm thick neat resin samples cured with an even upper and lower mould temperature of 140 °C (RC10) and 180 °C (RC12) had a tensile residual stress of 29.2 MPa and 25.5 MPa respectively. This difference of 3.7 MPa compares favourably to the difference of T3PB strength in thick samples, 5.6 MPa and thin samples, 12.6 MPa. The photoelastic analysis does not account for the anisotropy inherent in fibre reinforced composites but it can be seen to still allow for an analysis of the through-thickness build-up of transverse residual stress, through large thermal and DOC gradients in the sample during cure. It is thought that the photoelastic analysis under-reports the through-thickness variation in residual stress when compared to the T3PB

results. This is because the addition of a reinforcing phase adds additional constraints to the resin matrix as it thermally expands and chemically shrinks, leading to a higher residual stress. However, it still offers a useful insight into the development of residual stress in UD laminates and corroborates the trend seen in the FBG, FE and T3PB analyses.

This work shows the usefulness of embedding sensors to monitor residual strain during cure. Without this in-situ view of the build-up of residual strain during cure it would not be possible to make any informed inferences about the residual state of the laminates cured in this study. Clearly, the path the build-up of residual strain takes is equally, if not more important than the magnitude of that final strain in the development of residual stress. This is particularly true of rapidly cured composites where even temperature and DOC distribution assumptions cannot be adequately applied.

8.5. Conclusion

The main aim of this chapter was to determine the effect of curing temperature and laminate thickness on the transverse bending strength of rapidly cured UD laminates. It has been shown that samples cured at 180 °C have a higher transverse bending strength than samples cured at 140 °C for the UD EF7017 laminate tested. This indicates a lower level of transverse residual stress present in the “Hot” sample. This was confirmed with a 95% confidence interval using a two-tailed t-test for both the “thick” and “thin” case. However, this effect was due to the “Hot” samples resin matrix spending a prolonged period in their rubbery phase which caused residual stress to be dissipated viscously during the initial phase of the cure. Residual stress was then stored elastically when the curing temperature had dropped below the T_g^{hot} of the resin matrix again, after being removed from the hot press. This result has shown that a higher curing temperature and faster curing time does not necessarily lead to higher levels of residual stress. However, curing above T_g^{cured} could be problematic in an industrial setting as laminates taken out of a hot press, above T_g^{cured} would be very soft and likely lose dimensional stability.

The effect of thickness on the T3PB strength of rapidly cured laminates was more difficult to determine. It was not possible to determine the effect of thickness for either the “Hot” or “Cool” case with a 95% confidence interval using a two-tailed t-test. A μ CT analysis showed the

“thick” samples had a higher void content than the “thin” samples making direct comparison to “thin” samples difficult. This was because transverse matrix strength testing has an inherently flaw-based failure mechanisms and as such a higher void content in the “thick” samples promoted premature failure. Future work is required to control compaction pressure during cure to produce laminates with a lower void content. It was also found that samples tested with an embedded optical fibre, transverse to the fibre direction, failed much earlier than an equivalent sample without, due to suspected crack growth around the resin eye. This suggests that embedded optical fibres are not suitable for in-situ structural health monitoring applications in UD laminates, although their use in cross-ply or woven laminates is still thought to be advisable.

Future work in this area should include investigating variation in T3PB strength with cure temperature using a pressure controlled hot-press and a resin formulation with a high T_g^{cured} . This is so that the effect of cure temperature can be more easily determined without the need to account for excessive relaxation while the resin matrix is in its rubbery phase. It is hypothesised, that if the T_g^{cured} is not exceeded during cure, the samples cured at a higher temperature will have a lower T3PB strength due to higher levels of tensile residual stress.

9. Conclusions and future work

This thesis has focused on the experimental determination of the development of residual strain during the rapid curing of thermosetting fibre reinforced composites. A novel insight into the development of residual strain during this process has been given and the associated residual stresses have begun to be quantified. As with more traditionally cured composites, it was found that there are three main mechanisms that contribute to the development of residual stress: chemical shrinkage, thermal expansion and the mechanical boundary imposed by the mould. It was also found that some laminates cured rapidly in a hot press remain in their rubbery phase for the majority of the cure cycle and only vitrify upon cooling. This significantly impedes the development of residual stress during the initial stages of cure and results in less total transverse tensile residual stress than laminates cured at a lower temperature and for longer. This result was corroborated by results gathered using a photoelastic analysis, embedded Fibre Bragg Gratings (FBG), Finite Element (FE) modelling and Transverse Three-Point Bending (T3PB) mechanical testing.

A review of the various methods for experimentally determining residual stress in fibre reinforced composites was conducted and it was determined that a holistic approach was required for the initial characterization of residual stress in rapidly curing composites as little is known about these resins systems. It was determined that embedding optical fibres with FBGs into the rapidly cured laminates to monitor the development of residual strain during cure would allow for an insightful investigation of the key mechanisms that generate residual stress during cure.

Two rapidly curing resin formulations were proposed by the sponsor of this work, Solvay. Little was known about these resin systems so an initial material characterization was conducted to determine key material properties and which resin system would be most suitable for further analysis. DSC testing was used to determine cure kinetic parameters required for later modelling and to qualitatively assess the resin curing characteristics. A through-thickness thermal analysis during cure at multiple cure temperatures was then conducted to determine the thermal distribution through the thickness of the laminate. It was found that large thermal variations of around 100 °C are present during cure. Asymmetric bending tests were attempted to approximate the contribution of chemical shrinkage and

thermal expansion to residual stress. However, it was not possible to apply a representative heating cycle to the laminate with a free-cantilever setup. DMA tests were conducted to determine the T_g^{cured} of laminates cured at both 140 °C and 180 °C and was found to be 170 °C and 145 °C respectively.

An investigation into the integrity of the optical fibre/resin interface was carried out. SFFT were successfully conducted on a slow curing resin system. A novel Image J fragmentation length measuring system was developed to allow for instantaneous data capture and subsequent fragmentation length analysis. A novel mould design was also developed to allow for preparation of rapidly cured SFFT specimens. However, it was not possible to determine the IFSS values for rapidly cured samples as residual stress caused premature failure in the samples. However, a qualitative assessment of the optical fibre/resin interface was conducted using a SEM and μ CT analysis. It was concluded that poor compaction in thicker samples caused voids around the optical fibre to form but sufficient bonding still remained.

A photoelastic analysis of the through-thickness distribution of residual stress in variably cured neat resin samples was then conducted to determine the build-up of residual stress in non-fibre reinforced samples. This allowed for an insight into the development of residual stress in the transverse and out of plane directions of a UD laminate as these are primarily matrix dependent. It was found that samples cured unevenly would have a higher tensile residual stress on the side cured at the higher temperature. This was because it cured more rapidly and led to an uneven resin modulus through the thickness of the sample. It was also found that samples cured with an even top and bottom mould temperature had more tensile residual stress when cured at a lower temperature. This is thought to be because the samples cured at a higher temperature spent more time their rubbery phase and so dissipated residual stress viscously due to the relaxation of the resin. This same phenomenon was seen in the subsequent chapters.

Optical fibres with FBGs were embedded into rapidly curing laminates to monitor the development of the transverse residual strain during cure. This allowed for a unique insight into the development of residual strain in laminates using these resin systems. The contribution of chemical shrinkage and thermal effects to residual strain could be quantified

and compared between variously cured laminates. It was found that the final residual strain for all samples tested was largely similar, but significantly higher than published values for more conventionally cured laminates. However, the route taken to arrive at the final residual strain varied significantly between the “Hot” and “Cool” samples. The “Cool” samples had a roughly even strain development between chemical shrinkage and thermal shrinkage, while the “Hot” samples had the majority of strain developed from thermal effects. This suggests that while the residual strain values are similar, the final residual stress is not. The variation of strain through the thickness of the laminate was also captured by FBGs placed at the outer and inner thickness of the samples. It was found that the “thick” samples had a significant difference in strain through-thickness while the “thin” samples did not. It was not possible to use tailed FBG sets to perform in-situ measurements of the development of the resin modulus with DOC due to the extended rubbery phase of the resin during cure.

A simple multi-physics numerical analysis of rapidly curing laminates was conducted using COSMOL. An ILE model was used to model the development of residual stress/strain during cure. The model found good agreement with the thermal experimental analysis conducted. The model also corroborated well with strain data captured with FBGs for the “Cool” laminates. However, the “Hot” laminate was not well modelled by the ILE model as it was cured above T_g^{hot} and the rubbery transition was not accounted for by the current model. Thus, it was found that the “Hot” samples had a higher tensile residual stress than the “Cool” samples as no rubbery transition or subsequent relaxation was modelled.

Transverse three-point bending tests were then conducted to determine the influence of residual stress on the transverse matrix strength of rapidly cured laminates. It was found that a higher curing temperature leads to a higher T3PB strength, indicating less tensile residual stress. This is thought to be caused by the “Hot” sample being cured above T_g^{hot} and being able to relax stress viscously and only vitrifying upon cooling, after being removed from the hot-press. No clear trend in the influence of laminate thickness on T3PB, and thus residual stress, was found. This is not thought to be because thickness does not have an effect upon residual stress but rather that this test was unable to detect it. This was concluded after a μ CT void analysis found the “thick” samples had a higher void content compared to the “thin” samples which lead to premature sample failure.

The original hypothesis of this work predicts that an increase in laminate thickness and cure temperature will lead to an increase in residual stress. It was predicted that a distributed tensile residual stress profile would be formed from the uneven curing, chemical shrinkage and thermal volumetric changes. However, it was found that by applying fixed boundaries to all moulding surfaces, in the case of a hot-press, a tensile residual stress was generated through the thickness of the laminate. It is thought that this tensile stress varies through-thickness and that variation will be magnified with laminate thickness, but it has not been possible to show this in the present work. It is suggested that a technique like incremental hole-drilling would be able to better define this variation of residual stress through-thickness. Additionally, it was found that completely curing a laminate above T_g^{cured} will allow for a large amount of stress relaxation to occur and lower the resultant tensile residual stress. Therefore, no simple relationship between laminate cure temperature and residual stress exists.

Future work

More work is needed to develop techniques specifically for rapid curing composites as many of the current techniques are unable to accurately capture the required data. Specifically, developing a method for determining the development of the elastic modulus with the DOC would be valuable for accurate residual stress predictions. Additionally, a more complex cure kinetics relationship is required to capture the multiple cure kinetics present in some of the rapid resin formulations tested.

The fibre pull-out test is suggested as an alternative to SFFT for investigating the interfacial strength of optical fibres and resin to determine the effect of rapid curing on that interface. Additionally, a more extensive μ CT testing regime is suggested so that more than one data point can be analysed to add certainty to the sufficient bonding determination.

For the photoelastic analysis, it is suggested that phase stepping be implemented to disentangle compacted fringes to allow for a more accurate quantification of residual stress in neat resins. Additionally, it is thought that a photoelastic analysis of thin cross-sections of

rapidly cured UD laminates would be insightful for investigating the micromechanical residual stress present.

The testing methodology outlined for embedded FBGs in rapidly curing laminates has been proven effective. However, a larger number and variety of tests are required to be able to begin to predict the residual strain history of new untested laminates with any certainty. It is suggested that a rapidly curing resin formulation with a higher T_g^{cured} is tested so that the effect of cure temperature on residual strain can be decoupled from the influence of the glass transition. It is also suggested that tailed FBG sets be implemented in future work to perform in-situ monitoring of the resin modulus during cure. This is thought to be especially valuable for rapidly curing resins because of the associated difficulty with gathering this data using standard testing methodologies.

To better account for the effect of curing above T_g^{cured} in the analysis of residual stress a more complex model is required than a simple ILE approach. It is thought that a CHILE model may be able to accurately account for the glass transition modulus change. However, the accelerated relaxation that occurs at elevated temperature above T_g^{cured} likely needs a viscoelastic model to accurately describe. One challenge with this will be an accurate determination of various viscoelastic parameters for the analysis of rapidly curing resins. It is also suggested that a different simulation package like ABAQUS is used to more easily implement these more complex models and to allow for chemical shrinkage to be applied as a function of DOC. The proposed model should again, be validated with experimentally determining residual strain data as outlined in this thesis. Thicker laminates at higher curing temperatures could then be modelled to examine the effect of thickness and cure temperature on residual stress. Additionally, more complicated cross-ply laminates should be analysed for better applicability to real world laminates.

Finally, more extensive mechanical tests are required to better understand the influence of residual stress on mechanical performance of composites. It is thought that controlling pressure during the hot-pressing of rapidly curing laminates will reduce void content and allow for a better comparison of T3PB strength between variably cured samples. It is suggested that fatigue tests are pursued as residual stress has been found to play an important role in

the fatigue performance of composites and having an in depth understanding of this is vital for wider adoption in the aerospace industry. Expanding mechanical tests to include more commonly used cross-ply laminates is also thought to be a very valuable line of research. While T3PB of UD laminates controls the failure mechanisms well, it does not tell us much about how residual stress affects the other various failure mechanisms in composites with large amounts of residual stress.

The present work has used a wide range of techniques to develop a holistic initial understanding of how residual stress and strain develops in rapidly curing composites. This new area of study has found multiple challenges specific to rapidly curing resin formulations which must be addressed in future work to improve the prediction of residual stress. This exciting area of study will be crucial for the wider adoption of rapidly curing composites for structural applications.

10. References

- [1] G. V. Research, “Composites Market Size, Share & Trends Analysis Report By Product (Carbon, Glass), By Resin (Thermosetting, Thermoplastic), By Manufacturing Process, By Application, By End Use, And Segment Forecasts, 2018 - 2024,” 2018.
- [2] Airbus, “A350 XWB Family.” [Online]. Available: <https://www.airbus.com/aircraft/passenger-aircraft/a350xwb-family.html>. [Accessed: 25-Mar-2019].
- [3] A. van Grootel, J. Chang, B. L. Wardle, and E. Olivetti, “Manufacturing variability drives significant environmental and economic impact: The case of carbon fiber reinforced polymer composites in the aerospace industry,” *J. Clean. Prod.*, vol. 261, p. 121087, Jul. 2020.
- [4] E. Burgueno Salas, “Aircraft fleet - number of airplanes in service 2021,” *Statista*, 2022. [Online]. Available: <https://www.statista.com/statistics/282237/aircraft-fleet-size/>. [Accessed: 18-Aug-2022].
- [5] Boeing, “Boeing Sets New Airplane Delivery Records, Expands Order Backlog.” [Online]. Available: <https://boeing.mediaroom.com/2019-01-08-Boeing-Sets-New-Airplane-Delivery-Records-Expands-Order-Backlog>. [Accessed: 25-Mar-2019].
- [6] Airbus, “Airbus achieves new commercial aircraft delivery record in 2018.” [Online]. Available: <https://www.airbus.com/newsroom/press-releases/en/2019/01/airbus-achieves-new-commercial-aircraft-delivery-record-in-2018.html>. [Accessed: 25-Mar-2019].
- [7] A. Dong, Y. Zhao, X. Zhao, and Q. Yu, “Cure Cycle Optimization of Rapidly Cured Out-Of-Autoclave Composites,” *Materials (Basel)*, vol. 11, no. 421, pp. 1–15, 2018.
- [8] K. Zhang, Y. Gu, M. li, and Z. Zhang, “Effect of rapid curing process on the properties of carbon fiber/epoxy composite fabricated using vacuum assisted resin infusion molding,” *Mater. Des.*, vol. 54, pp. 624–631, 2014.
- [9] S. L. Agius, K. J. C. Magniez, and B. L. Fox, “Cure behaviour and void development within rapidly cured out-of-autoclave composites,” *Compos. Part B Eng.*, vol. 47, pp. 230–237, 2013.
- [10] K. Rouf, A. Suratkar, J. Imbert-Boyd, J. Wood, M. Worswick, and J. Montesano, “Effect of Strain Rate on the Transverse Tension and Compression Behavior of a Unidirectional Non-Crimp Fabric Carbon Fiber/Snap-Cure Epoxy Composite,” *Mater. (Basel, Switzerland)*, vol. 14, no. 23, Dec. 2021.
- [11] Y. Zeng, “Mechanical Characterization and Computational Modeling of Snap-cure Epoxy,” University of Waterloo, 2020.

- [12] C. R. Wang, Y. Z. Gu, K. M. Zhang, M. Li, and Z. G. Zhang, "Rapid Curing Epoxy Resin and its Application in Carbon Fibre Composite Fabricated Using VARTM Moulding," *Polym. Polym. Compos.*, vol. 21, no. 5, pp. 315–324, 2013.
- [13] A. Reichanadter, D. Bank, and J. A. E. Mansson, "A novel rapid cure epoxy resin with internal mold release," *Polym. Eng. Sci.*, vol. 61, pp. 1819–1828, 2021.
- [14] B. Seers, R. Tomlinson, and P. Fairclough, "Residual stress in fiber reinforced thermosetting composites: A review of measurement techniques," *Polym. Compos.*, pp. 1–17, 2021.
- [15] K. Cinar and N. Ersoy, "3D finite element model for predicting manufacturing distortions of composite parts," *J. Compos. Mater.*, vol. 50, no. 27, pp. 3791–3807, 2016.
- [16] I. M. Daniel and O. Ishai, *Engineering mechanics of composite materials*, 2nd ed. Oxford University press, 2006.
- [17] R. M. Jones, *Mechanics of composite materials*, 2nd ed. Philadelphia: Taylor & Francis Group, 1999.
- [18] M. Wenani, "Prediction of process induced shape distortions and residual stresses in large fibre reinforced composite laminates: With application to Wind Turbine Blades," Technical University of Denmark (DTU), Lyngby, 2013.
- [19] T. M. Junisbekov, V. N. Kestel'man, and N. I. Malinin, *Stress relaxation in viscoelastic materials*. Science Publishers, 2003.
- [20] T. A. Bogetti and J. W. Gillespie, "Process-Induced Stress and Deformation in Thick-Section Thermoset Composite Laminates," *Compos. Mater.*, vol. 26, no. 5, pp. 626–660, 1992.
- [21] Y. K. Kim and S. R. White, "Stress relaxation behavior of 3501-6 epoxy resin during cure," *Polym. Eng. Sci.*, vol. 36, no. 23, pp. 2852–2862, Dec. 1996.
- [22] Y. K. Kim and S. R. White, "Process-Induced Stress Relaxation Analysis of AS4/3501-6 Laminate," *J. Reinf. Plast. Compos.*, vol. 16, no. 1, pp. 2–16, Jan. 1997.
- [23] G. W. Scherer, "Volume Relaxation Far from Equilibrium," *J. Am. Ceram. Soc.*, vol. 69, no. 5, pp. 374–381, May 1986.
- [24] Y. Weitsman, "Optimal Cool-Down in Linear Viscoelasticity," *J. Appl. Mech.*, vol. 47, no. 1, pp. 35–39, Mar. 1980.
- [25] A. R. Maligno, N. A. Warrior, and A. C. Long, "Effects of interphase material properties in unidirectional fibre reinforced composites," *Compos. Sci. Technol.*, vol. 70, no. 1, pp. 36–44, Jan. 2010.

- [26] A. Sjögren, “Matrix and Interface Effects on Microcracking in Polymer Composites,” Lulea Univeristy of Technology, 1997.
- [27] A. Patel, O. G. Kravchenko, I. Manas-Zloczower, and A. Patel, “Effect of Curing Rate on the Microstructure and Macroscopic Properties of Epoxy Fiberglass Composites,” *Polymers (Basel)*, vol. 10, no. 125, pp. 1–11, Jan. 2018.
- [28] C. Li, K. Potter, M. R. Wisnom, and G. Stringer, “In-situ measurement of chemical shrinkage of MY750 epoxy resin by a novel gravimetric method,” *Compos. Sci. Technol.*, vol. 64, no. 1, pp. 55–64, Jan. 2004.
- [29] M. R. Wisnom, M. Gigliotti, N. Ersoy, M. Campbell, and K. D. Potter, “Mechanisms generating residual stresses and distortion during manufacture of polymer–matrix composite structures,” *Compos. Part A Appl. Sci. Manuf.*, vol. 37, no. 4, pp. 522–529, Apr. 2006.
- [30] O. G. Kravchenko, S. G. Kravchenko, A. Casares, and R. B. Pipes, “Digital image correlation measurement of resin chemical and thermal shrinkage after gelation,” *J. Mater. Sci.*, vol. 50, no. 15, pp. 5244–5252, Aug. 2015.
- [31] A. S. Crasto, R. Y. Kim, and J. D. Russell, “In situ monitoring of residual strain development during composite cure,” *Polym. Compos.*, vol. 23, no. 3, pp. 454–463, Jun. 2002.
- [32] R. J. Morgan and J. E. O’Neal, “The microscopic failure processes and their relation to the structure of amine-cured bisphenol-A-diglycidyl ether epoxies,” *J. Mater. Sci.*, vol. 12, no. 10, pp. 1966–1980, Oct. 1977.
- [33] L. Liu, B.-M. Zhang, D.-F. Wang, and Z.-J. Wu, “Effects of cure cycles on void content and mechanical properties of composite laminates,” *Compos. Struct.*, vol. 73, pp. 303–309, 2005.
- [34] S. Teplinsky and E. M. Gutman, “Computer simulation of process induced stress and strain development during cure of thick-section thermosetting composites,” *Comput. Mater. Sci.*, vol. 6, pp. 71–76, 1996.
- [35] A. Dharia, B. Hays, and J. Seferis, “Evaluation of Microcracking in Aerospace Composites Exposed to Thermal Cycling: Effect of Composite Lay-up, Laminate Thickness and Thermal Ramp Rate,” in *International SAMPE Technical Conference*, 2001.
- [36] F. Campbell, *Manufacturing Processes For Advanced Composites*. Oxford: Elsevier Ltd, 2004.
- [37] K. S. Kim and H. T. Hahn, “Residual stress development during processing of graphite/epoxy composites,” *Compos. Sci. Technol.*, vol. 36, no. 2, pp. 121–132, Jan. 1989.

- [38] Y. K. Kim and S. R. White, “Viscoelastic Analysis Of Processing-Induced Residual Stresses In Thick Composite Laminates,” *Mech. Adv. Mater. Struct.*, vol. 4, pp. 361–387, Oct. 1997.
- [39] T. Tsukada, S. Minakuchi, and N. Takeda, “Identification of process-induced residual stress/strain distribution in thick thermoplastic composites based on in situ strain monitoring using optical fiber sensors,” *Compos. Mater.*, vol. 53, no. 24, pp. 3445–3458, 2019.
- [40] P. P. Parlevliet, H. E. N. Bersee, and A. Beukers, “Residual stresses in thermoplastic composites—A study of the literature—Part I: Formation of residual stresses,” *Compos. Part A Appl. Sci. Manuf.*, vol. 37, no. 11, pp. 1847–1857, Nov. 2006.
- [41] L. A. Carlsson, D. F. Adams, and R. B. Pipes, *Experimental Characterization of Advanced Composite Materials*, 4th ed. Boca Raton: Taylor & Francis Group, 2014.
- [42] “Coefficients of Linear Thermal Expansion,” *Engineering Toolbox*. [Online]. Available: https://www.engineeringtoolbox.com/linear-expansion-coefficients-d_95.html. [Accessed: 28-Feb-2019].
- [43] G. Twigg, A. Poursartip, and G. Fernlund, “Tool–part interaction in composites processing. Part I: experimental investigation and analytical model,” *Compos. Part A Appl. Sci. Manuf.*, vol. 35, no. 1, pp. 121–133, Jan. 2004.
- [44] J. M. Svanberg and J. A. Holmberg, “An experimental investigation on mechanisms for manufacturing induced shape distortions in homogeneous and balanced laminates,” *Compos. Part A*, vol. 32, pp. 827–838, 2000.
- [45] F. Groh, E. Kappel, C. Hühne, and W. Brymerski, “Investigation of fast curing epoxy resins regarding process induced distortions of fibre reinforced composites,” *Compos. Struct.*, vol. 207, pp. 923–934, 2019.
- [46] Q. I. Zhu, P. H. Geubelle, M. Li, and C. L. T. Iii, “Dimensional Accuracy of Thermoset Composites: Simulation of Process-Induced Residual Stresses,” *J. Compos. Mater.*, vol. 35, no. 24, pp. 2171–2205, 2001.
- [47] S. R. White and H. T. Hahn, “Cure Cycle Optimization for the Reduction of Processing-Induced Residual Stresses in Composite Materials,” *Compos. Mater.*, vol. 27, pp. 1352–1378, 1993.
- [48] S. Wijskamp, “Shape distortions in composites forming,” University of Twente, 2005.
- [49] P. Sunderland, W. Yu, and J.-A. Manson, “A thermoviscoelastic analysis of process-induced internal stresses in thermoplastic matrix composites,” *Polym. Compos.*, vol. 22, no. 5, pp. 579–592, Oct. 2001.
- [50] D. Kugler and T. J. Moon, “Identification of the Most Significant Processing Parameters

- on the Development of Fiber Waviness in Thin Laminates,” *J. Compos. Mater.*, vol. 36, no. 12, pp. 1451–1479, 2002.
- [51] I. Baran, K. Cinar, N. Ersoy, R. Akkerman, and J. H. Hattel, “A Review on the Mechanical Modeling of Composite Manufacturing Processes,” *Arch. Comput. Methods Eng.*, vol. 24, pp. 365–395, 2017.
- [52] M. M. Shokrieh, *Residual stresses in composite materials*. Philadelphia: Woodhead Publishing Ltd, 2014.
- [53] P. P. Parlevliet, H. E. N. Bersee, and A. Beukers, “Residual stresses in thermoplastic composites—A study of the literature—Part II: Experimental techniques,” *Compos. Part A Appl. Sci. Manuf.*, vol. 38, no. 3, pp. 651–665, Mar. 2007.
- [54] R. G. Treuting and W. T. Read, “A Mechanical Determination of Biaxial Residual Stress in Sheet Materials,” *J. Appl. Phys.*, vol. 22, no. 2, pp. 130–134, Feb. 1951.
- [55] M. P. I. M. Eijpe and P. C. Powell, “Residual stress evaluation in composites using a modified layer removal method,” *Compos. Struct.*, vol. 37, no. 3–4, pp. 335–342, Mar. 1997.
- [56] M. R. L. Gower *et al.*, “Determination of ply level residual stresses in a laminated carbon fibre-reinforced epoxy composite using constant, linear and quadratic variations of the incremental slitting method,” *Compos. Part A*, vol. 90, pp. 441–450, 2016.
- [57] N. Ersoy and O. Vardar, “Measurement of Residual Stresses in Layered Composites by Compliance Method,” *J. Compos. Mater.*, vol. 34, no. 7, pp. 575–598, Apr. 2000.
- [58] T. J. Chapman, J. W. Gillespie, R. B. Pipes, J.-A. E. Manson, and J. C. Seferis, “Prediction of Process-Induced Residual Stresses in Thermoplastic Composites,” *Compos. Mater.*, vol. 24, pp. 616–643, 1990.
- [59] R. G. Reid, “The Measurement of Longitudinal Residual Stresses in Unidirectional Glass Fibre Reinforced Plastic,” University of the Witwatersrand, Johannesburg, Johannesburg, 2009.
- [60] N. J. Rendler and I. Vigness, “Hole-drilling strain-gage method of measuring residual stresses,” *Exp. Mech.*, vol. 6, pp. 577–586, 1966.
- [61] C. B. Prasad, R. Prabhakaran, and S. Tompkins, “Determination of Calibration Constants for the Hole-Drilling Residual Stress Measurement Technique Applied to Orthotropic Composites Part I: Theoretical Considerations,” *Compos. Struct.*, vol. 8, pp. 105–118, 1987.
- [62] A. Magnier, T. Wu, S. R. Tinkloh, T. Tröster, B. Scholtes, and T. Niendorf, “On the reliability of residual stress measurements in unidirectional carbon fibre reinforced epoxy composites,” *Polym. Test.*, vol. 97, p. 107146, May 2021.

- [63] O. Sicot, X. L. Gong, A. Cherouat, and J. Lu, "Determination of Residual Stress in Composite Laminates Using the Incremental Hole-drilling Method," *Compos. Mater.*, vol. 37, no. 9, pp. 831–844, 2003.
- [64] P. Pagliaro and B. Zuccarello, "Residual Stress Analysis of Orthotropic Materials by the Through-hole Drilling Method," *Exp. Mech.*, vol. 47, no. 2, pp. 217–236, Feb. 2007.
- [65] A. Baldi, "Residual Stress Analysis of Orthotropic Materials Using Integrated Digital Image Correlation," *Exp. Mech.*, vol. 54, no. 7, pp. 1279–1292, Sep. 2014.
- [66] A. Baldi, "Residual Stress Measurement Using Hole Drilling and Integrated Digital Image Correlation Techniques," *Exp. Mech.*, vol. 54, pp. 379–391, 2014.
- [67] D. V. Nelson and J. T. McCrickerd, "Residual-stress determination through combined use of holographic interferometry and blind-hole drilling," *Exp. Mech.*, vol. 26, no. 4, pp. 371–378, Dec. 1986.
- [68] Z. Wu, J. Lu, and B. Han, "Study of Residual Stress Distribution by a Combined Method of Moire Interferometry and Incremental Hole Drilling, Part I: Theory," *Appl. Mech.*, vol. 65, pp. 837–843, 1998.
- [69] F. V. Dmh Az, G. H. Kaufmann, and G. E. Galizzi, "Determination of residual stresses using hole drilling and digital speckle pattern interferometry with automated data analysis," *Opt. Lasers Eng.*, vol. 33, pp. 39–48, 2000.
- [70] M. Hagara, F. Trebuň, M. Pástor, R. Huň, and P. L. Lengvarský, "Analysis of the aspects of residual stresses quantification performed by 3D DIC combined with standardized hole-drilling method," *Measurement*, vol. 137, pp. 238–256, 2019.
- [71] T. C. Smit and R. G. Reid, "Residual Stress Measurement in Composite Laminates Using Incremental Hole-Drilling with Power Series," *Exp. Mech.*, vol. 58, no. 8, pp. 1221–1235, Oct. 2018.
- [72] C. Garza, R. Das, A. Shterenlikht, and M. Pavier, "Measurement of assembly stress in composite structures using the deep-hole drilling technique," *Compos. Struct.*, vol. 202, pp. 119–126, 2018.
- [73] H. Hu, S. Li, D. Cao, L. Liu, and M. Pavier, "Measurement of manufacture assembly stresses in thick composite components using a modified DHD method," *Compos. Part A*, vol. 135, p. 105922, 2020.
- [74] J. T. Tsai, J. S. Dustin, and J. A. Mansson, "Distributed optical sensing for monitoring strain evolution during mechanical testing of composite laminates," *Polym. Test.*, vol. 96, p. 107076, Apr. 2021.
- [75] P. Davim, *Machining of Composite Materials*. Hoboken: Wiley, 2010.

- [76] R. Vinayagamoorthy, "A review on the machining of fiber-reinforced polymeric laminates," *J. Reinf. Plast. Compos.*, vol. 37, no. 1, pp. 49–59, Jan. 2018.
- [77] D. F. Liu, Y. J. Tang, and W. L. Cong, "A review of mechanical drilling for composite laminates," *Composite Structures*, vol. 94, pp. 1265–1279, 01-Mar-2012.
- [78] O. Yuksel, I. Baran, N. Ersoy, and R. Akkerman, "Investigation of transverse residual stresses in a thick pultruded composite using digital image correlation with hole drilling," *Compos. Struct.*, vol. 223, p. 110954, 2019.
- [79] L. Mao and F.-P. Chiang, "Interior strain analysis of a woven composite beam using X-ray computed tomography and digital volumetric speckle photography," *Compos. Struct.*, vol. 134, pp. 782–788, 2015.
- [80] R. Gunnert, *Residual Welding Stresses, Method for Measuring Residual Stress and its Application to a Study of Residual Welding Stresses*. Stockholm: Wicksell, Almqvist E., 1955.
- [81] W. Ren and K. Li, "Incremental ring-core cutting around an interferometric strain/slope rosette for residual stress measurement," in *Third International Conference on Experimental Mechanics*, 2002, pp. 139–142.
- [82] R. Ghaedamini, A. Ghassemi, and A. Atrian, "Ring-core method in determining the amount of non-uniform residual stress in laminated composites: experimental, finite element and theoretical evaluation," *Arch Appl Mech*, vol. 88, pp. 755–767, 2018.
- [83] Z. Hu, H. Xie, J. Lu, J. Zhu, and H. Wang, "Residual stresses measurement by using ring-core method and 3D digital image correlation technique," *Meas. Sci. Technol.*, vol. 24, no. 8, pp. 1–8, Aug. 2013.
- [84] A. Baldi, "Using Optical Interferometry to Restart the Ring-Core Method," *Exp. Mech.*, vol. 56, pp. 1191–1202, 2016.
- [85] A. M. Korsunsky, M. Sebastiani, and E. Bemporad, "Focused ion beam ring drilling for residual stress evaluation," *Mater. Lett.*, vol. 63, no. 22, pp. 1961–1963, Sep. 2009.
- [86] A. J. Lunt *et al.*, "A state-of-the-art review of micron-scale spatially resolved residual stress analysis by FIB-DIC ring-core milling and other techniques," *JSA Golden Issue J Strain Anal.*, vol. 50, no. 7, pp. 426–444, 2015.
- [87] N. Sabaté *et al.*, "Measurement of residual stress by slot milling with focused ion-beam equipment," *J. Micromechanics Microengineering*, vol. 16, no. 2, pp. 254–259, Feb. 2006.
- [88] R. Ghaedamini, A. Ghassemi, and A. Atrian, "A comparative experimental study for determination of residual stress in laminated composites using ring core, incremental hole drilling, and slitting methods," *Mater. Res. Express*, vol. 6, p. 025205, 2019.

- [89] A. R. Ghasemi and A. Tabatabaeian, “A unified comparative study on the classical lamination theory, hole drilling, slitting, and curvature measurement methods for assessment of residual stress in laminated polymeric composites,” *Mech. Mater.*, vol. 167, p. 104267, Apr. 2022.
- [90] W. Cheng and I. Finnie, “Measurement of Residual Hoop Stresses in Cylinders Using the Compliance Method,” *Eng. Mater. Technol.*, vol. 108, pp. 87–92, 1985.
- [91] S. Güngör, “Residual stress measurements in fibre reinforced titanium alloy composites,” *Acta Mater.*, vol. 50, pp. 2053–2073, 2002.
- [92] N. Sabaté *et al.*, “Digital image correlation of nanoscale deformation fields for local stress measurement in thin films,” *Nanotechnology*, vol. 17, no. 20, pp. 5264–5270, Oct. 2006.
- [93] S. D. Salehi, M. A. Rastak, M. Shokrieh, & L. Barrallier, and & R. Kubler, “Full-Field Measurement of Residual Stresses in Composite Materials Using the Incremental Slitting and Digital Image Correlation Techniques,” *Exp. Mech.*, 2020.
- [94] M. M. Shokrieh, S. Akbari, and A. Daneshvar, “A comparison between the slitting method and the classical lamination theory in determination of macro-residual stresses in laminated composites,” *Compos. Struct.*, vol. 96, pp. 708–715, 2013.
- [95] S. Akbari, F. Taheri-Behrooz, and M. M. Shokrieh, “Slitting Measurement of Residual Hoop Stresses Through the Wall-Thickness of a Filament Wound Composite Ring,” *Exp. Mech.*, vol. 53, pp. 1509–1518, 2013.
- [96] K. Kechout, A. Amirat, and N. Zeghib, “Residual stress analyses in multilayer PP/GFP/PP composite tube,” *Adv. Manuf. Technol.*, vol. 103, pp. 4221–4231, 2019.
- [97] M. A. Umarfarooq, P. S. Shivakumar Gouda, A. Nandibewoor, N. R. Banapurmath, and G. B. Veeresh Kumar, “Determination of residual stresses in GFRP composite using incremental slitting method by the aid of strain gauge,” in *Advances in Polymer Composites: Mechanics, Characterization and Applications*, 2019.
- [98] A. R. Ghasemi, A. Tabatabaeian, and B. Asghari, “Application of slitting method to characterize the effects of thermal fatigue, lay-up arrangement and MWCNTs on the residual stresses of laminated composites,” *Mech. Mater. J.*, vol. 134, pp. 185–192, 2019.
- [99] R. Zhu, H. Xie, X. Dai, Z. Jianguo, and A. Jin, “Residual stress measurement in thin films using a slitting method with geometric phase analysis under a dual beam (FIB/SEM) system,” *Meas. Sci. Technol.*, vol. 25, p. 095003, 2014.
- [100] D. Hosson, C. Mansilla, D. Martínez-Martínez, V. Ocelík, and J. M. Th De Hosson, “On the determination of local residual stress gradients by the slit milling method,” *Mater. Sci.*, vol. 50, pp. 3646–3655, 2015.

- [101] M. B. Prime and M. R. Hill, "Residual stress, stress relief, and inhomogeneity in aluminum plate," *Scr. Mater.*, vol. 46, pp. 77–82, 2002.
- [102] M. B. Prime, "Residual stress measurement by successive extension of a slot: The crack compliance method," *Appl. Mech. Rev.*, vol. 52, no. 2, pp. 75–96, 1999.
- [103] M. Arhant, N. Meek, D. Penumadu, P. Davies, and N. Garg, "Residual Strains using Integrated Continuous Fiber Optic Sensing in Thermoplastic Composites and Structural Health Monitoring," *Exp. Mech.*, vol. 58, pp. 167–176, 2018.
- [104] S. D. Salehi and M. M. Shokrieh, "Repeated slitting safe distance in the measurement of residual stresses," *Int. J. Mech. Sci.*, vol. 157–158, pp. 599–608, 2019.
- [105] M. B. Prime, "Cross-Sectional Mapping of Residual Stresses by Measuring the Surface Contour After a Cut," *Eng. Fract. Mech.*, vol. 123, pp. 162–168, 2001.
- [106] P. J. Withers, M. Turski, L. Edwards, P. J. Bouchard, and D. J. Buttle, "Recent advances in residual stress measurement," *Int. J. Press. Vessel. Pip.*, vol. 85, pp. 118–127, 2008.
- [107] M. D. Olson, A. T. Dewald, M. B. Prime, and M. R. Hill, "Estimation of Uncertainty for Contour Method Residual Stress Measurements," *Exp. Mech.*, vol. 55, pp. 577–585, 2015.
- [108] R. Y. Kim and H. T. Hahn, "Effect of Curing Stresses on the First Ply-failure in Composite Laminates," *Compos. Mater.*, vol. 13, pp. 2–16, 1979.
- [109] K. D. Cowley and P. W. R. Beaumont, "The measurement and prediction of residual stresses in carbon-fibre/polymer composites," *Compos. Sci. Technol.*, vol. 57, no. 11, pp. 1445–1455, Jan. 1997.
- [110] D. L. Flagg and M. H. Kural, "Experimental Determination of the In Situ Transverse Lamina Strength in Graphite/Epoxy Laminates," *Compos. Mater.*, vol. 16, p. 103, 1982.
- [111] M. A. Sutton, J. Walters, W. H. Peters, W. F. Ranson, and S. R. McNeill, "Determination of displacements using an improved digital correlation method," *Image Vis. Comput.*, vol. 1, pp. 133–139, 1983.
- [112] G. Horne, "Micro-scale residual stress relaxation measurements using focused ion beam slotting and digital image correlation," University of Bristol, Bristol, 2009.
- [113] B. Leblanc, C. Niezrecki, P. Avitabile, J. Chen, and J. Sherwood, "Damage detection and full surface characterization of a wind turbine blade using three-dimensional digital image correlation," *Struct. Heal. Monit.*, vol. 12, no. 6, pp. 430–439, 2013.
- [114] L. P. Canal, C. Gonzalez A ' B, J. M. Molina-Aldareguia, J. Segurado, and J. Llorca A ' B ', "Application of digital image correlation at the microscale in fiber-reinforced composites," *Compos. Part A Appl. Sci. Manuf.*, vol. 43, no. 10, pp. 1630–1638, 2012.

- [115] J. W. Dally and W. F. Riley, *Experimental Stress Analysis*, Fourth. Knoxville: College House Enterprises, LLC, 2005.
- [116] X.-Y. Liu *et al.*, “Quality assessment of speckle patterns for digital image correlation by Shannon entropy,” *Opt. - Int. J. Light Electron Opt.*, vol. 126, pp. 4206–4211, 2015.
- [117] I. De Wolf, “Micro-Raman spectroscopy to study local mechanical stress in silicon integrated circuits,” *Semicond. Sci. Technol.*, vol. 11, pp. 139–154, 1996.
- [118] S. Ganesan, A. A. Maradudin, and J. Oitmaa, “A Lattice Theory of Morphic Effects in Crystals of the Diamond Structure,” *Ann. Phys. (N. Y.)*, vol. 56, pp. 556–594, 1970.
- [119] D. J. Bannister, M. C. Andrews, A. J. Cervenka, and R. J. Young, “Analysis of the single-fibre pull-out test by means of Raman spectroscopy: part ii. micromechanics of deformation for an aramid/epoxy system,” *Compos. Sci. Technol.*, vol. 53, pp. 411–421, 1995.
- [120] J. S. Thomsen and R. Pyrz, “Creep of carbon/polypropylene model composites - a Raman spectroscopic investigation,” *Compos. Sci. Technol.*, vol. 59, pp. 1375–1385, 1999.
- [121] A. S. Nielsen and R. Pyrz, “A novel approach to measure local strains in polymer matrix systems using polarised Raman microscopy,” *Compos. Sci. Technol.*, vol. 62, pp. 2219–2227, 2002.
- [122] Y. Ward, R. J. Young, and R. A. Shatwell, “Application of Raman microscopy to the analysis of silicon carbide monofilaments,” *J. Mater. Sci.*, vol. 39, pp. 6781–6790, 2004.
- [123] R. J. Young and S. J. Eichhorn, “Raman Applications in Synthetic and Natural Polymer Fibres and Their Composites,” in *Raman Spectroscopy for Soft Matter Applications*, M. S. Amer, Ed. John Wiley and Sons, 2008, pp. 63–94.
- [124] J. A. Nairn and P. Zoller, “The Development of Residual Thermal Stresses in Amorphous and Semicrystalline Thermoplastic Matrix Composites,” in *Symposium on Toughened Composites*, 1987, pp. 328–341.
- [125] M. Gigliottia, J. Molimard, F. Jacquemin, and A. Vautrin, “On the nonlinear deformations of thin unsymmetric 0/90 composite plates under hygrothermal loads,” *Compos. Part A*, vol. 37, pp. 624–629, 2006.
- [126] O. G. Kravchenko, S. G. Kravchenko, and R. B. Pipes, “Chemical and thermal shrinkage in thermosetting prepreg,” *Compos. Part A*, vol. 80, pp. 72–81, 2016.
- [127] O. G. Kravchenko, S. G. Kravchenko, and R. B. Pipes, “Cure history dependence of residual deformation in a thermosetting laminate,” *Compos. Part A Appl. Sci. Manuf.*, vol. 99, pp. 186–197, 2017.
- [128] A. S. Crasto and R. Y. Kim, “On the Determination of Residual Stresses in Fiber-

- Reinforced Thermoset Composites,” *Reinf. Plast. Compos.*, vol. 12, pp. 545–558, 1993.
- [129] S. Nelson, A. Hanson, T. Briggs, and B. Werner, “Verification and validation of residual stresses in composite structures,” *Compos. Struct.*, vol. 194, pp. 662–673, 2018.
- [130] M. Gigliotti, M. R. Wisnom, and K. D. Potter, “Development of curvature during the cure of AS4/8552 [0/90] unsymmetric composite plates,” *Compos. Sci. Technol.*, vol. 63, pp. 187–197, 2003.
- [131] O. G. Kravchenko, C. Li, A. Strachan, S. G. Kravchenko, and R. B. Pipes, “Prediction of the chemical and thermal shrinkage in a thermoset polymer,” *Compos. Part A*, vol. 66, pp. 35–43, 2014.
- [132] M. Abouhamzeh, J. Sinke, and R. Benedictus, “Investigation of curing effects on distortion of fibre metal laminates,” *Compos. Struct.*, vol. 122, pp. 546–552, 2015.
- [133] B. W. Kim and J. A. Nairn, “Experimental verification of the effects of friction and residual stress on the analysis of interfacial debonding and toughness in single fiber composites,” *J. Mater. Sci.*, vol. 37, no. 18, pp. 3965–3972, 2002.
- [134] F. Zhao, S. A. Hayes, E. A. Patterson, R. J. Young, and F. R. Jones, “Measurement of micro stress fields in epoxy matrix around a fibre using phase-stepping automated photoelasticity,” *Compos. Sci. Technol.*, vol. 63, no. 12, pp. 1783–1787, Sep. 2003.
- [135] J. A. Nairn and P. Zoller, “Matrix solidification and the resulting residual thermal stresses in composites,” *J. Mater. Sci.*, vol. 20, no. 1, pp. 355–367, Jan. 1985.
- [136] B. Andersson, A. Sjögren, and L. Berglund, “Micro- and meso-level residual stresses in glass-fiber/vinyl-ester composites,” *Compos. Sci. Technol.*, vol. 60, no. 10, pp. 2011–2028, Aug. 2000.
- [137] P. G. Ifju, B. C. Kilday, X. Niu, and S.-C. Liu, “A Novel Method to Measure Residual Stresses in Laminated Composites,” *Compos. Mater.*, vol. 33, no. 16, pp. 1511–1524, 1999.
- [138] W. A. Schulz, D. G. Myers, T. N. Singer, P. G. Ifju, and R. T. Haftka, “Determination of residual stress and thermal history for IM7/977-2 composite laminates,” *Compos. Sci. Technol.*, vol. 65, pp. 2014–2024, 2005.
- [139] P. Ifju, D. Myers, and W. Schulz, “Residual stress and thermal expansion of graphite epoxy laminates subjected to cryogenic temperatures,” *Compos. Sci. Technol.*, vol. 66, no. 14, pp. 2449–2455, Nov. 2006.
- [140] Y. K. Kim, G. W. Woodruff, and I. M. Daniel, “Cure Cycle Effect on Composite Structures Manufactured by Resin Transfer Molding,” *Compos. Mater.*, vol. 36, no. 14, pp. 1725–1743, 2002.
- [141] J. A. Guemes and J. M. Menendez, “Response of Bragg grating fiber-optic sensors when

- embedded in composite laminates,” *Compos. Sci. Technol.*, vol. 62, pp. 959–966, 2002.
- [142] Q. Wang, X. Yang, H. Zhao, X. Zhang, G. Cao, and M. Ren, “Microscopic residual stresses analysis and multi-objective optimization for 3D woven composites,” *Compos. Part A Appl. Sci. Manuf.*, vol. 144, p. 106310, May 2021.
- [143] I. M. Daniel, J. L. Mullineaux, F. J. Ahimaz, and T. Liber, “The Embedded Strain Gage Technique for Testing Boron/Epoxy Composites,” in *Composite Materials: Testing and Design (2nd Conference)*, 1972, pp. 257–272.
- [144] P. P. Parlevliet, “Residual Strains in Thick Thermoplastic Composites,” Technische Universiteit Delft, Delft, 2010.
- [145] H. K. Kang, D. H. Kang, C. S. Hong, and C. G. Kim, “Simultaneous monitoring of strain and temperature during and after cure of unsymmetric composite laminate using fibre-optic sensors,” *Smart Mater. Struct.*, vol. 12, pp. 29–35, 2003.
- [146] A. L. Kalamkarov, S. B. Fitzgerald, and D. O. MacDonald, “The use of Fabry Perot fiber optic sensors to monitor residual strains during pultrusion of FRP composites,” *Compos. Part B Eng.*, vol. 30, no. 2, pp. 167–175, 1999.
- [147] A. Allue *et al.*, “Smart composites with embedded magnetic microwire inclusions allowing non-contact stresses and temperature monitoring,” *Compos. Part A*, vol. 120, pp. 12–20, 2019.
- [148] E. Voet, G. Luyckx, and J. Degrieck, “Response of embedded fibre Bragg gratings: strain transfer effects,” in *20th International Conference on Optical Fibre Sensors*, 2009, vol. 7503, pp. 1–4.
- [149] M. J. O’dwyer, G. M. Maistros, S. W. James, R. P. Tatam, and I. K. Partridge, “Relating the state of cure to the real-time internal strain development in a curing composite using in-fibre Bragg gratings and dielectric sensors,” *Meas. Sci. Technol.*, vol. 9, pp. 1153–1158, 1998.
- [150] K. Shivakumar and A. Bhargava, “Failure Mechanics of a Composite Laminate Embedded with a Fiber Optic Sensor,” *Compos. Mater.*, vol. 39, no. 9, pp. 777–798, 2005.
- [151] Y. Okabe, S. Yashiro, R. Tsuji, T. Mizutani, and N. Takeda, “Effect of thermal residual stress on the reflection spectrum from fiber Bragg grating sensors embedded in CFRP laminates,” *Compos. - Part A Appl. Sci. Manuf.*, vol. 33, pp. 991–999, 2002.
- [152] L. Sorensen, T. Gmür, and J. Botsis, “Residual strain development in an AS4/PPS thermoplastic composite measured using fibre Bragg grating sensors,” *Compos. - Part A Appl. Sci. Manuf.*, vol. 37, pp. 270–281, 2006.
- [153] D. Martínez, M. Gresil, and C. Soutis, “Distributed internal strain measurement during composite manufacturing using optical fibre sensors,” *Compos. Sci. Technol.*, vol. 120,

pp. 49–57, 2015.

- [154] H. Hu *et al.*, “Investigation of non-uniform gelation effects on residual stresses of thick laminates based on tailed FBG sensor,” *Compos. Struct.*, vol. 202, pp. 1361–1372, 2018.
- [155] M. Lai, K. Friedrich, J. Botsis, and T. Burkhart, “Evaluation of residual strains in epoxy with different nano/micro-fillers using embedded fiber Bragg grating sensor,” *Compos. Sci. Technol.*, vol. 70, pp. 2468–2475, 2010.
- [156] J. Jakobsen, A. Skordos, S. James, R. G. Correia, and M. Jensen, “In-situ Curing Strain Monitoring of a Flat Plate Residual Stress Specimen Using a Chopped Stand Mat Glass/Epoxy Composite as Test Material,” *Appl. Compos. Mater.*, vol. 22, pp. 805–822, 2015.
- [157] B. Mahto, S. Kubher, and S. Gururaja, “Characterization of cure residual strain development and associated structural distortion in carbon fiber polymer matrix composites,” *J. Compos. Mater.*, vol. 56, no. 20, pp. 3127–3141, Aug. 2022.
- [158] M. Mülle *et al.*, “Process monitoring of glass reinforced polypropylene laminates using fiber Bragg gratings,” *Compos. Sci. Technol.*, vol. 123, pp. 143–150, 2016.
- [159] H. Hu, S. Li, J. Wang, L. Zu, D. Cao, and Y. Zhong, “Monitoring the gelation and effective chemical shrinkage of composite curing process with a novel FBG approach,” *Compos. Struct.*, vol. 176, pp. 187–194, Sep. 2017.
- [160] S. Minakuchi, “In situ characterization of direction-dependent cure-induced shrinkage in thermoset composite laminates with fiber-optic sensors embedded in through-thickness and in-plane directions,” *Compos. Mater.*, vol. 49, pp. 1021–1034, 2015.
- [161] J.-T. Tsai, J. S. Dustin, and J.-A. Mansson, “Cure strain monitoring in composite laminates with distributed optical sensor,” *Compos. Part A*, vol. 125, p. 105503, 2019.
- [162] H. T. Hahn and N. J. Pagano, “Curing Stresses in Composite Laminates,” *Compos. Mater.*, vol. 9, pp. 91–106, 1975.
- [163] Y. Xu and R. Bao, “Residual stress determination in friction stir butt welded joints using a digital image correlation-aided slitting technique,” *Chinese J. Aeronaut.*, vol. 30, no. 3, pp. 1258–1269, Jun. 2017.
- [164] L. G. Zhao, N. A. Warrior, and A. C. Long, “A micromechanical study of residual stress and its effect on transverse failure in polymer-matrix composites,” *Int. J. Solids Struct.*, vol. 43, pp. 5449–5467, 2005.
- [165] S. L. Agius, M. Joosten, B. Trippit, C. H. Wang, and T. Hilditch, “Rapidly cured epoxy/anhydride composites: Effect of residual stress on laminate shear strength,” *Compos. Part A Appl. Sci. Manuf.*, vol. 90, pp. 125–136, Nov. 2016.

- [166] ASTM, “ASTM 2344 - Standard Test Method for Short-Beam Strength of Polymer Matrix Composite Materials and Their Laminates,” West Conshohocken, 2016.
- [167] D. E. Adams, E. Q. Lewis, and E. Study, “Experimental Study of Three- and Four-Point Shear Test Specimens,” *J. Compos. Technol. Res.*, vol. 17, no. 4, pp. 341–349, 1995.
- [168] R. Talreja and C. Singh, *Damage and Failure of Composite Materials*. Cambridge: Cambridge University Press, 2012.
- [169] S. Nojavan, D. Schesser, and Q. D. Yang, “An in situ fatigue-CZM for unified crack initiation and propagation in composites under cyclic loading,” *Compos. Struct.*, vol. 146, pp. 34–49, 2016.
- [170] M. May and S. R. Hallett, “Damage initiation in polymer matrix composites under high-cycle fatigue loading - A question of definition or a material property?,” *Int. J. Fatigue*, vol. 87, pp. 59–62, 2016.
- [171] M. W. Joosten, S. L. Agius, T. Hilditch, and C. Wang, “Effect of residual stress on the matrix fatigue cracking of rapidly cured epoxy/anhydride composites,” *Compos. Part A Appl. Sci. Manuf.*, vol. 101, pp. 521–528, Oct. 2017.
- [172] G. Fernlund *et al.*, “Experimental and numerical study of the effect of cure cycle, tool surface, geometry, and lay-up on the dimensional fidelity of autoclave-processed composite parts,” *Compos. Part A Appl. Sci. Manuf.*, vol. 33, no. 3, pp. 341–351, Mar. 2002.
- [173] M. A. Stone, I. F. Schwartz, and H. D. Chandler, “Residual stresses associated with post-cure shrinkage in GRP tubes,” *Compos. Sci. Technol.*, vol. 57, pp. 47–54, 1997.
- [174] D. Hull and T. W. Clyne, *An introduction to composite materials*, Second. Cambridge: Cambridge University Press, 1996.
- [175] D. F. Adams, T. R. King, and D. M. Blackketter, “Evaluation of the Transverse Flexure Test Method for Composite Materials,” *Compos. Sci. Technol.*, vol. 39, pp. 341–353, 1990.
- [176] E. Correa, V. Mantič, and F. París, “Effect of thermal residual stresses on matrix failure under transverse tension at micromechanical level: A numerical and experimental analysis,” *Compos. Sci. Technol.*, vol. 71, pp. 622–629, 2011.
- [177] L. E. Asp, L. A. Berglund, and R. Talreja, “Prediction of matrix-initiated transverse failure in polymer composites,” *Compos. Sci. Technol.*, vol. 56, pp. 1089–1097, 1996.
- [178] B. Fiedler, M. Hojo, S. Ochiai, K. Schulte, and M. Ochi, “Finite-element modeling of initial matrix failure in CFRP under static transverse tensile load,” *Compos. Sci. Technol.*, vol. 61, pp. 95–105, 2001.
- [179] L. G. Zhao, N. A. Warrior, and A. C. Long, “A thermo-viscoelastic analysis of process-induced residual stress in fibre-reinforced polymer-matrix composites,” *Mater. Sci. Eng.*

- A, pp. 483–498, 2007.
- [180] M. Hojo, M. Mizuno, T. Hobbiebrunken, T. Adachi, M. Tanaka, and S. K. Ha, “Effect of fiber array irregularities on microscopic interfacial normal stress states of transversely loaded UD-CFRP from viewpoint of failure initiation,” *Compos. Sci. Technol.*, vol. 69, pp. 1726–1734, 2008.
- [181] S. R. White and H. T. Hahn, “Process Modeling of Composite Materials: Residual Stress Development during Cure. Part I. Model Formulation,” *J. Compos. Mater.*, vol. 26, no. 16, pp. 2402–2422, 1992.
- [182] T. Tsukada, S. Minakuchi, and N. Takeda, “Assessing residual stress redistribution during annealing in thick thermoplastic composites using optical fiber sensors,” *J. Thermoplast. Compos. Mater.*, vol. 2020, no. 1, pp. 53–68, 2020.
- [183] S. Jones, “Personal communication.” Apr-2019.
- [184] Solvay, “CYCOM 5320-1 Technical Data Sheet,” Aplpharettta, 2017.
- [185] J. Foreman, S. R. Sauerbrunn, and C. L. Marcozzi, “Exploring the Sensitivity of Thermal Analysis Techniques to the Glass Transition Thermal Analysis & Rheology,” New Castle.
- [186] A. X. H Yong, G. D. Sims, S. J. P Gnaniah, S. L. Ogin, and P. A. Smith, “Heating rate effects on thermal analysis measurement of Tg in composite materials,” *Adv. Manuf. Polym. Compos. Sci.*, vol. 3, no. 2, pp. 43–51, 2017.
- [187] A. Ding, S. Li, J. Wang, and L. Zu, “A three-dimensional thermo-viscoelastic analysis of process-induced residual stress in composite laminates,” *Compos. Struct.*, vol. 129, pp. 60–69, Oct. 2015.
- [188] J. Zhang, B. Fox, and Q. Guo, “Consistent model predictions for isothermal cure kinetics investigation of high performance epoxy prepregs,” *J. Appl. Polym. Sci.*, vol. 107, no. 4, pp. 2231–2237, Feb. 2008.
- [189] J. M. G. Cowie and V. Arrighi, *Polymers: Chemistry and Physics of Modern Materials*, Third. Boca Raton: CRC Press, 2007.
- [190] S. Mutlur, “Thermal Analysis of Composites Using DSC,” in *Advanced Topics in Characterization of Composites*, Trafford Publishing, 2004, pp. 11–33.
- [191] P. Atkins and J. de Paula, *Elements of Physical Chemistry*, Fifth. Oxofrd: Oxofrd University Press, 2009.
- [192] B. Bilyeu, W. Brostow, and K. P. Menard, “Characterization Of Epoxy Curing Using High Heating Rate DSC,” *ASTM Int.*, vol. 2, no. 10, pp. 83–91, 2005.
- [193] C. Evolution, “Cured ply thickness calculator,” *Composite World*. [Online]. Available:

- <https://netcomposites.com/calculator/cured-ply-thickness-calculator/>. [Accessed: 11-May-2021].
- [194] FBGS, “FBGS - Draw Tower Gratings in low bend loss fiber.” [Online]. Available: <https://fbgs.com/components/draw-tower-gratings-dtgs/>. [Accessed: 20-May-2020].
- [195] R. Das, “Stress Relaxation Behavior of Carbon Fiber-Epoxy Prepreg Composites During and After Cure,” Bangladesh University of Engineering and Technology, Wichita, 2012.
- [196] R. de A. A. Lima *et al.*, “Interfacial adhesion between embedded fibre optic sensors and epoxy matrix in composites,” *J. Adhes. Sci. Technol.*, vol. 33, no. 3, pp. 253–272, Feb. 2019.
- [197] J. Li, X. Liu, X. Yao, and Y. Yuan, “A micromechanical debonding analysis of fiber-reinforced composites due to curing residual stress,” *Reinf. Plast.*, vol. 34, no. 12, pp. 962–971, 2015.
- [198] S. Feih, K. Wonsyld, D. Minzari, P. Westermann, and H. Lilholt, “Establishing a Testing Procedure for the Single Fiber Fragmentation Test,” DTU, Roskilde, 2004.
- [199] C. DiFrancia, T. C. Ward, and R. O. Claus, “The single-fibre pull-out test. 1: Review and interpretation,” *Compos. Part A Appl. Sci. Manuf.*, vol. 27, pp. 597–612, 1996.
- [200] S. Zhandarov and E. Mäder, “Characterization of fiber/matrix interface strength: applicability of different tests, approaches and parameters,” *Compos. Sci. Technol.*, vol. 65, pp. 149–160, 2005.
- [201] S. Jj, J. X. Dai, J. Li, Z. Q. Wei, J.-M. Hausherr, and W. Krenkel, “Measurement and analysis of fiber-matrix interface strength of carbon fiber-reinforced phenolic resin matrix composites,” *J. Compos. Mater.*, vol. 48, no. 11, pp. 1303–1311, 2014.
- [202] M. Hardiman, T. J. Vaughan, and C. T. McCarthy, “A review of key developments and pertinent issues in nanoindentation testing of fibre reinforced plastic microstructures,” *Compos. Struct.*, vol. 180, pp. 782–798, 2017.
- [203] A. Kelly and W. R. Tyson, “Tensile Properties of Fibre-Reinforced Metals: Copper/Tungsten and Copper/Molybdenum,” *Mech. Phys. Solids*, vol. 13, pp. 329–350, 1965.
- [204] B. W. Kim and J. A. Nairn, “Observations of Fiber Fracture and Interfacial Debonding Phenomena Using the Fragmentation Test in Single Fiber Composites,” *J. Compos. Mater.*, vol. 36, no. 15, 2002.
- [205] R. C. DeVekey and A. J. Majumdar, “Determining bond strength in fibre-reinforced composites,” *Mag. Concr. Res.*, vol. 20, no. 65, pp. 229–234, Dec. 1968.
- [206] M. R. Piggott, “Debonding and friction at fibre-polymer interfaces. I: Criteria for failure and sliding,” *Compos. Sci. Technol.*, vol. 30, no. 4, pp. 295–306, Jan. 1987.

- [207] Toray, “T800H Intermediate modulus carbon fiber,” 2018.
- [208] Easy Composites, “3K Carbon Fibre Tow,” Stoke-on-Trent, 2021.
- [209] Easy Composites, “E12 Epoxy laminating resin-Technical Datasheet,” Stoke-on-Trent, 2021.
- [210] A. Abidi, S. Ben Salem, A. Bezazi, and H. Boumediri, “A comparative study on the effect of milling and abrasive water jet cutting technologies on the tensile behavior of composite carbon/ epoxy laminates,” *Mech. Compos. Mater.*, vol. 57, no. 4, pp. 539–550, 2021.
- [211] F. A. Ramirez, A. L. A. Carlsson, and A. B. A. Acha, “Evaluation of water degradation of vinylester and epoxy matrix composites by single fiber and composite tests,” *J. Mater. Sci.*, vol. 43, pp. 5230–5242, 2008.
- [212] K. L. Pickering and T. L. Murray, “Weak link scaling analysis of high-strength carbon fibre,” *Compos. Part A Appl. Sci. Manuf.*, vol. 30, no. 8, pp. 1017–1021, Aug. 1999.
- [213] J. Zhang, “Different surface treatments of carbon fibers and their influence on the interfacial properties of carbon fiber/epoxy composites,” Ecole Centrale Paris, 2012.
- [214] Z. Zhao *et al.*, “Mechanical, thermal and interfacial performances of carbon fiber reinforced composites flavored by carbon nanotube in matrix/interface,” *Compos. Struct.*, vol. 159, pp. 761–772, 2017.
- [215] R. J. Sager *et al.*, “Effect of carbon nanotubes on the interfacial shear strength of T650 carbon fiber in an epoxy matrix,” *Compos. Sci. Technol.*, vol. 69, pp. 898–904, 2009.
- [216] I. J. Beyerlein and S. L. Phoenix, “Statistics for the strength and size effects of microcomposites with four carbon fibers in epoxy resin,” *Compos. Sci. Technol.*, vol. 56, pp. 75–92, Jan. 1996.
- [217] H.-B. Wang, Y.-G. Yang, H.-H. Yu, W.-M. Sun, Y.-H. Zhang, and H.-W. Zhou, “Assessment of residual stresses during cure and cooling of epoxy resins,” *Polym. Eng. Sci.*, vol. 35, no. 23, pp. 1895–1899, Dec. 1995.
- [218] P. Prasatya, G. B. McKenna, and S. L. Simon, “A Viscoelastic Model for Predicting Isotropic Residual Stresses in Thermosetting Materials: Effects of Processing Parameters;,” *J. Compos. Mater.*, vol. 35, no. 10, pp. 826–848, Dec. 2001.
- [219] J. Holmberg, “Influence of chemical shrinkage on shape distortions of RTM composites,” in *19th Int. SAMPE European Conference of the Society for the Advancement of Material and Process Engineering*, 1998, pp. 13–34.
- [220] L. Khoun, T. Centea, and P. Hubert, “Characterization Methodology of Thermoset Resins for the Processing of Composite Materials — Case Study: CYCOM 890RTM Epoxy

- Resin;” *J. Compos. Mater.*, vol. 44, no. 11, pp. 1397–1415, Dec. 2010.
- [221] S. L. Simon, G. B. Mckenna, and O. Sindt, “Modeling the Evolution of the Dynamic Mechanical Properties of a Commercial Epoxy During Cure after Gelation,” *J. Appl. Polym. Sci.*, vol. 76, pp. 495–508, 2000.
- [222] Z. Zhu, X. Sun, H. Yuan, C. Song, Y. Cao, and X. Li, “Determination of gel time and gel point of epoxy-amine thermosets by in-situ near infrared spectroscopy,” *Polym. Test.*, vol. 72, pp. 416–422, Dec. 2018.
- [223] Buehler, *Buehler SumMet - The Sum of Our Experience, A Guide to Materials Preparation & Analysis*, Fourth. Lake Bluff, 2018.
- [224] D. Bradford, K. Lease, and P. M. A. Sherwood, “Evaluation of the Effect of a Custom Fiber Surface Treatment on the Adhesion Level in a Polymer-Based Composite Using the Single Fiber Fragmentation Test,” 2000.
- [225] G. Cloud, *Optical Methods of Engineering Analysis*, First. New York: Cambridge University Press, 1995.
- [226] F. W. Hecker and B. Morche, “Computer-Aided Measurement of Relative Retardations in Plane Photoelasticity,” in *Experimental Stress Analysis*, Springer, Dordrecht, 1986, pp. 535–542.
- [227] K. Ramesh, T. Kasimayan, and N. Simon, “Digital photoelasticity - A comprehensive review,” *J. Strain Anal.*, vol. 46, pp. 245–266, 2011.
- [228] Z. F. Wang and E. A. Patterson, “Use of Phase-Stepping with Demodulation and Fuzzy Sets for Birefringence Measurement,” *Opt. Lasers Eng.*, vol. 22, pp. 91–104, 1995.
- [229] E. A. Patterson and Z. F. Wang, “Simultaneous observation of phase-stepped images for automated photoelasticity,” *J. Strain Anal.*, vol. 33, no. 1, pp. 1–15, 1998.
- [230] S. E. Falconer, “Modelling, Materials and Methods for Needle Insertion Investigation in Biomechanics,” University of Sheffield, 2020.
- [231] FBGS, “DTG coating Ormocer ®-T for Temperature Sensing Applications,” 2015.
- [232] SmartFibres, “SmartScope FBG Interrogator,” Bracknell, 2022.
- [233] S. Minakuchi, S. Niwa, K. Takagaki, and N. Takeda, “Composite cure simulation scheme fully integrating internal strain measurement,” *Compos. Part A*, vol. 84, pp. 53–63, 2016.
- [234] R. Prussak, D. Stefaniak, E. Kappel, C. Hühne, and M. Sinapius, “Smart cure cycles for fiber metal laminates using embedded fiber Bragg grating sensors,” *Compos. Struct.*, vol. 213, pp. 252–260, 2019.

- [235] S. Khadka, J. Hoffman, and M. Kumosa, “FBG monitoring of curing in single fiber polymer composites,” *Compos. Sci. Technol.*, vol. 198, p. 108308, 2020.
- [236] R. Montanini and L. D. ’ Acquisto, “Simultaneous measurement of temperature and strain in glass fiber/epoxy composites by embedded fiber optic sensors: I. Cure monitoring,” *Smart Mater. Struct.*, vol. 16, pp. 1718–1726, 2007.
- [237] S. Hisada, S. Minakuchi, and N. Takeda, “Cure-induced strain and failure in deltoid of composite T-joints,” *Compos. Part A Appl. Sci. Manuf.*, vol. 141, p. 106210, Feb. 2021.
- [238] K. Takagaki, S. Minakuchi, and N. Takeda, “Process-induced strain and distortion in curved composites. Part I: Development of fiber-optic strain monitoring technique and analytical methods,” *Compos. Part A Appl. Sci. Manuf.*, vol. 103, pp. 236–251, 2017.
- [239] K. Takagaki, S. Minakuchi, and N. Takeda, “Process-induced strain and distortion in curved composites. Part II: Parametric study and application,” *Compos. Part A Appl. Sci. Manuf.*, vol. 103, pp. 219–229, 2017.
- [240] Y. Qi, D. Jiang, S. Ju, and J. Zhang, “Investigation of strain history in fast and conventional curing epoxy matrix composites by FBGs,” *Compos. Sci. Technol.*, vol. 159, pp. 18–24, May 2018.
- [241] G. Zhang, J. Wang, A. Ni, H. Hu, A. Ding, and S. Li, “Process-induced deformation of L-shaped variable-stiffness composite structures during cure,” *Compos. Struct.*, vol. 230, p. 111461, Dec. 2019.
- [242] N.-K. Jha, J. Reinoso, H. Dehghani, and J. Merodio, “Computational model for fiber-reinforced composites: hyperelastic constitutive formulation including residual stresses and damage,” *Comput. Mech.*, vol. 63, pp. 931–948, 2019.
- [243] B. Patham, “COMSOL® Implementation of a viscoelastic model with cure-temperature-time superposition for predicting cure stresses and springback in a thermoset resin,” in *COMSOL Conference*, 2009.
- [244] S. Nakouzi, J. Pancrace, F. M. Schmidt, Y. Le Maout, and F. Berthet, “Curing simulation of composites coupled with infrared heating,” *Int. J. Mater. Form.*, vol. 3, pp. 587–590, 2010.
- [245] S. Anandan, G. S. Dhaliwal, Z. Huo, K. Chandrashekhara, N. Apetre, and N. Iyyer, “Curing of Thick Thermoset Composite Laminates: Multiphysics Modeling and Experiments,” *Appl. Compos. Mater.*, vol. 25, no. 5, pp. 1155–1168, Oct. 2018.
- [246] H. J. Borchardt and F. Daniels, “The Application of Differential Thermal Analysis to the Study of Reaction Kinetics,” *Am. Chem. Society*, vol. 70, p. 41, Apr. 1957.
- [247] R. Sfar Zbed, S. Le Corre, and V. Sobotka, “Process-induced strains measurements through a multi-axial characterization during the entire curing cycle of an interlayer

- toughened Carbon/Epoxy prepreg,” *Compos. Part A Appl. Sci. Manuf.*, vol. 153, p. 106689, Feb. 2022.
- [248] A. Ding, S. Li, J. Sun, J. Wang, and L. Zu, “A thermo-viscoelastic model of process-induced residual stresses in composite structures with considering thermal dependence,” *Compos. Struct.*, vol. 136, pp. 34–43, Feb. 2016.
- [249] A. Johnston, R. Vaziri, and A. Poursartip, “A Plane Strain Model for Process-Induced Deformation of Laminated Composite Structures,” *J. Compos. Mater.*, vol. 35, no. 16, pp. 1435–1469, 2001.
- [250] A. Plepys, M. S. Vratsanos, and R. J. Farris, “Determination of residual stresses using incremental linear elasticity,” *Compos. Struct.*, vol. 27, no. 1–2, pp. 51–56, 1994.
- [251] X. Hui, Y. Xu, J. Wang, and W. Zhang, “Microscale viscoplastic analysis of unidirectional CFRP composites under the influence of curing process,” *Compos. Struct.*, vol. 266, p. 113786, Jun. 2021.
- [252] J. Dai, S. Xi, and D. Li, “Numerical Analysis of Curing Residual Stress and Deformation in Thermosetting Composite Laminates with Comparison between Different Constitutive Models,” *Materials (Basel)*, vol. 12, no. 4, pp. 572–589, Feb. 2019.
- [253] A. Keller, K. Masania, A. C. Taylor, and C. Dransfeld, “Fast-curing epoxy polymers with silica nanoparticles: properties and rheo-kinetic modelling,” *J. Mater. Sci.*, vol. 51, pp. 236–251, 2016.
- [254] M. Srinivasan *et al.*, “Out of Plane Thermal Conductivity of Carbon Fiber Reinforced Composite Filled with Diamond Powder,” *Open J. Compos. Mater.*, vol. 6, pp. 41–57, 2016.
- [255] Y. Nawab, P. Casari, N. Boyard, and F. Jacquemin, “Characterization of the cure shrinkage, reaction kinetics, bulk modulus and thermal conductivity of thermoset resin from a single experiment,” *J. Mater. Sci.*, vol. 48, no. 6, pp. 2394–2403, Mar. 2013.
- [256] D. A. Belov *et al.*, “Curing Processes Simulation of Complex Shape Carbon Fiber Reinforced Composite Components Produced by Vacuum Infusion,” *Polym. Compos.*, pp. 2252–2259, 2016.
- [257] A. S. Patil, R. Moheimani, and H. Dalir, “Thermomechanical analysis of composite plates curing process using ANSYS composite cure simulation,” *Therm. Sci. Eng. Prog.*, vol. 14, p. 100419, Dec. 2019.
- [258] M. R. Kamal and S. Sourour, “Kinetics and thermal characterization of thermoset cure,” *Polym. Eng. Sci.*, vol. 13, no. 1, pp. 59–64, Jan. 1973.
- [259] L. Moretti, B. Castanié, G. Rard Bernhart, and P. Olivier, “Characterization and modelling of cure-dependent properties and strains during composites manufacturing,” *J. Compos. Mater.*, vol. 0, no. 0, pp. 1–16, 2020.

- [260] J. M. Svanberg and J. A. Holmberg, "Prediction of shape distortions. Part II. Experimental validation and analysis of boundary conditions," *Compos. Part A Appl. Sci. Manuf.*, vol. 35, pp. 723–734, 2004.
- [261] N. Ersoy, K. Potter, M. R. Wisnom, and M. J. Clegg, "An experimental method to study the frictional processes during composites manufacturing," *Compos. Part A Appl. Sci. Manuf.*, vol. 36, pp. 1536–1544, 2005.
- [262] L. Khoun, R. De Oliveira, V. Michaud, and P. Hubert, "Investigation of process-induced strains development by fibre Bragg grating sensors in resin transfer moulded composites," *Compos. Part A*, vol. 42, pp. 274–282, 2011.
- [263] J. Chen, J. Wang, X. Li, L. Sun, S. Li, and A. Ding, "Monitoring of temperature and cure-induced strain gradient in laminated composite plate with FBG sensors," *Compos. Struct.*, vol. 242, p. 112168, 2020.
- [264] B. Patham and X. Huang, "Multiscale Modeling of Residual Stress Development in Continuous Fiber-Reinforced Unidirectional Thick Thermoset Composites," *J. Compos.*, pp. 1–17, 2014.
- [265] I. Baran, C. C. Tutum, M. W. Nielsen, and J. H. Hattel, "Process induced residual stresses and distortions in pultrusion," *Compos. Part B*, vol. 51, pp. 148–161, 2013.
- [266] ASTM, "ASTM - D3039 Tensile properties of polymer matrix composite materials," West Conshocken, 2017.
- [267] ASTM, "ASTM7264 - Standard Test Method for Flexural Properties of Polymer Matrix Composite Materials," West Conshohocken, 2021.
- [268] J. E. Little, X. Yuan, and M. I. Jones, "Characterisation of voids in fibre reinforced composite materials," *NDT E Int.*, vol. 46, no. 1, pp. 122–127, Mar. 2012.

11. Appendices

Appendix A

Composite mechanical properties are calculated using a self-consistent field model using the equations below [20].

Longitudinal Young's modulus:

$$E_{11} = E_{11f}V_f + E_m(1 - V_f) + \frac{4(v_m - v_{12f}^2)k_f k_m G_m (1 - V_f)V_f}{(k_f + G_m)k_m + (k_f - k_m)G_m V_f} \quad (\text{A1})$$

Transverse Young's modulus:

$$E_{22} = E_{33} = \frac{1}{\left(\frac{1}{4k_T}\right) + \left(\frac{1}{4G_{23}}\right) + \left(\frac{v_{12}^2}{E_{11}}\right)} \quad (\text{A2})$$

In-plane shear modulus:

$$G_{12} = G_{13} = G_m \frac{(G_{12f} + G_m) + (G_{12f} - G_m)V_f}{(G_{12f} + G_m) - (G_{12f} - G_m)V_f} \quad (\text{A3})$$

Out-of-plane shear modulus:

$$G_{23} = \frac{G_m [k_m(G_m + G_{23f}) + 2G_{23f}G_m + k_m(G_{23f} - G_m)V_f]}{k_m(G_{23f} + G_m) + 2G_{23f}G_m - (k_m + 2G_m)(G_{23f} - G_m)V_f} \quad (\text{A4})$$

Poisson's ratio:

$$v_{12} = v_{13} = v_{12f}V_f + v_m(1 - V_f) + \frac{(v_m - v_{12f})(k_m - k_f)G_m(1 - V_f)V_f}{(k_f + G_m)k_m + (k_f - k_m)G_m V_f} \quad (\text{A5})$$

$$v_{23} = \frac{2E_{11}k_T - E_{11}E_{22} - 4v_{12}^2 k_T E_{22}}{2E_{11}k_T} \quad (\text{A6})$$

Factors:

$$G_m = \frac{E_m}{2(1 + v_m)} \quad (\text{A7})$$

$$G_{23f} = \frac{E_{33f}}{2(1 + v_{23f})} \quad (\text{A8})$$

$$k_T = \frac{(k_f + G_m)k_m + (k_f - k_m)G_m V_f}{(k_f + G_m) - (k_f - k_m)V_f} \quad (\text{A9})$$

$$k_m = \frac{E_m}{2(1 - v_m - 2v_m^2)} \quad (\text{A10})$$

$$k_f = \frac{E_{33f}}{2(1 - v_{23f} - 2v_{23f}^2)} \quad (\text{A11})$$

Appendix B

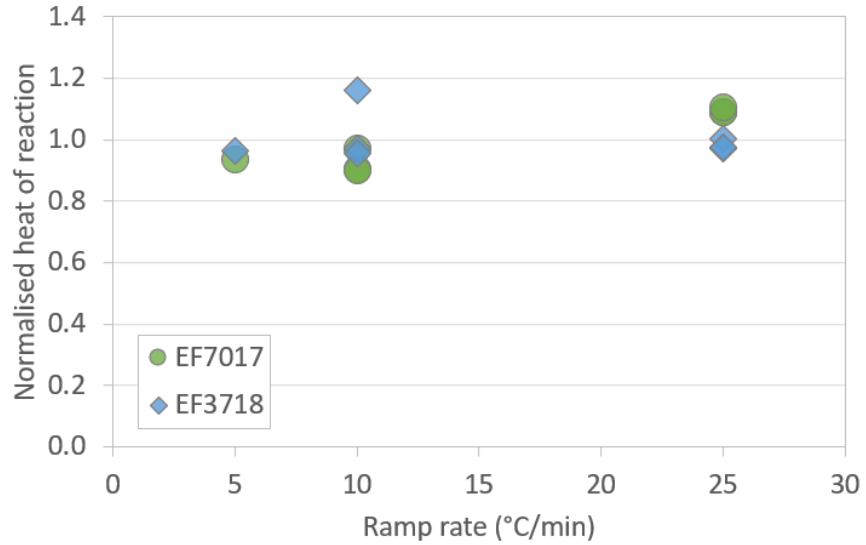


Figure 98: Heat of reaction values for EF7017 and EF3718, normalised around their respective averages. Ramp rates of 5, 10 and 25 °C/min are tested

Appendix C

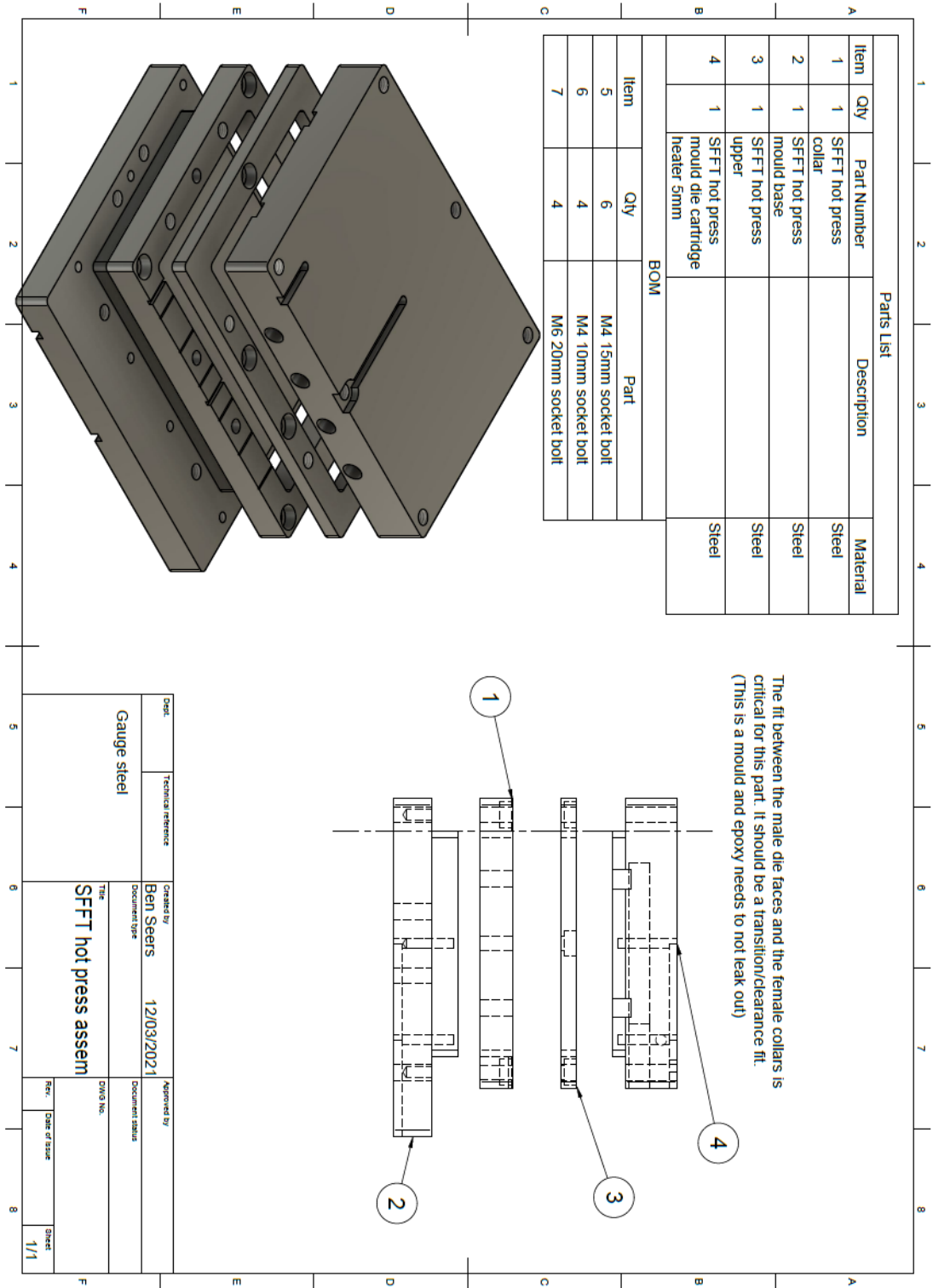


Figure 99: Rapid curing SFFT hot press drawing - assembly

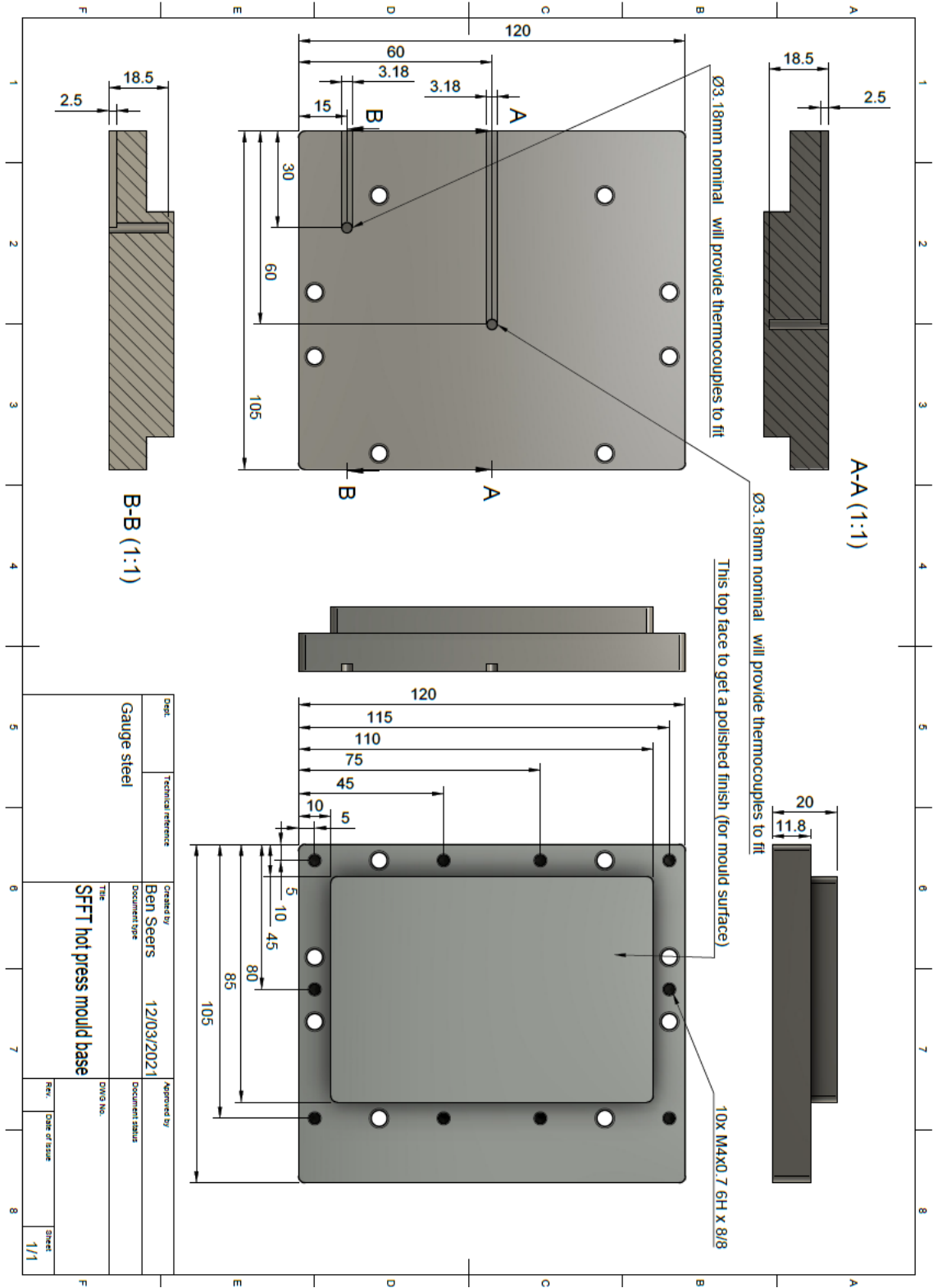


Figure 100: Rapid curing SFFT hot press drawing – mould base

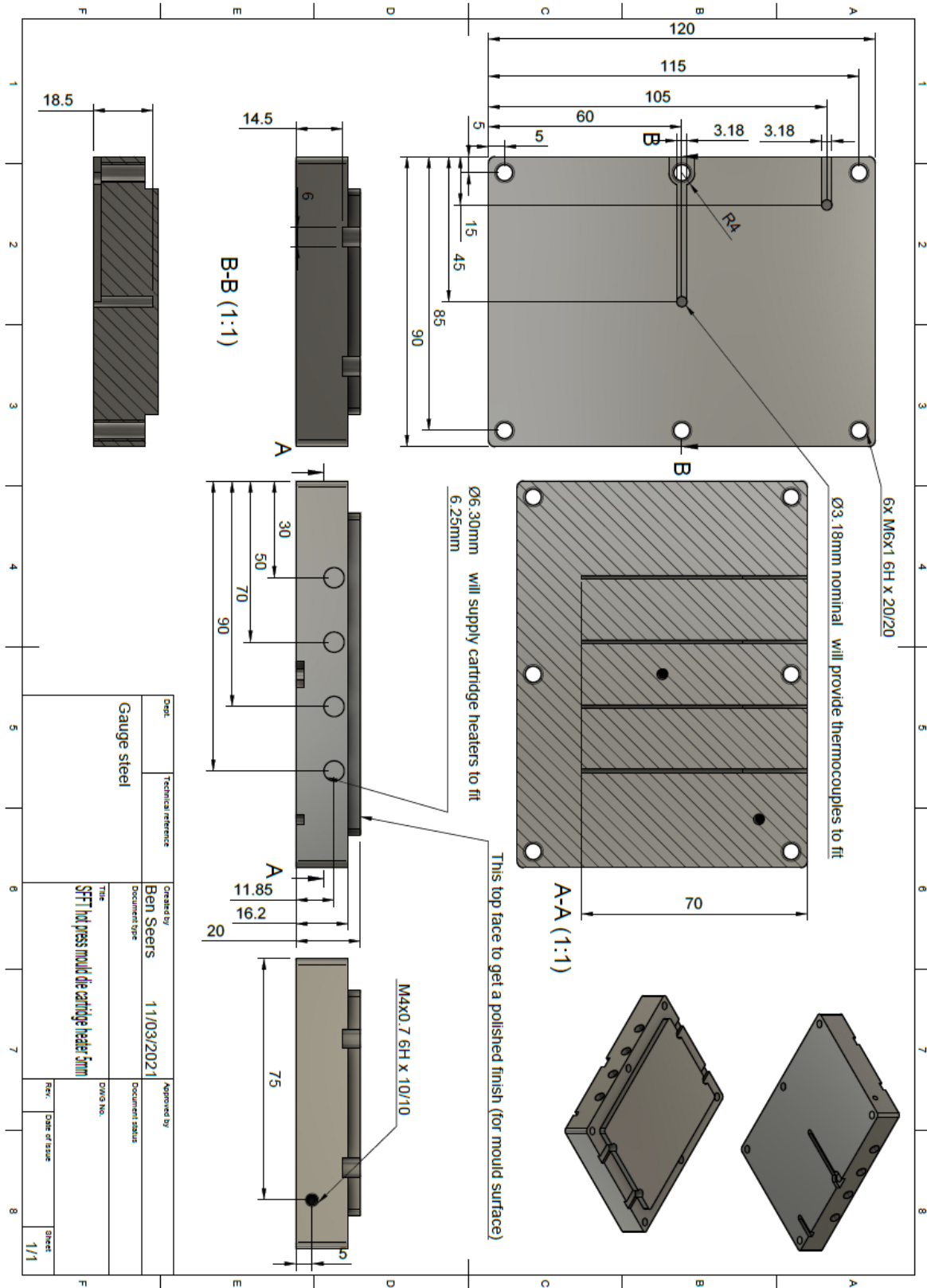


Figure 101: Rapid curing SFFT hot press drawing - mould top

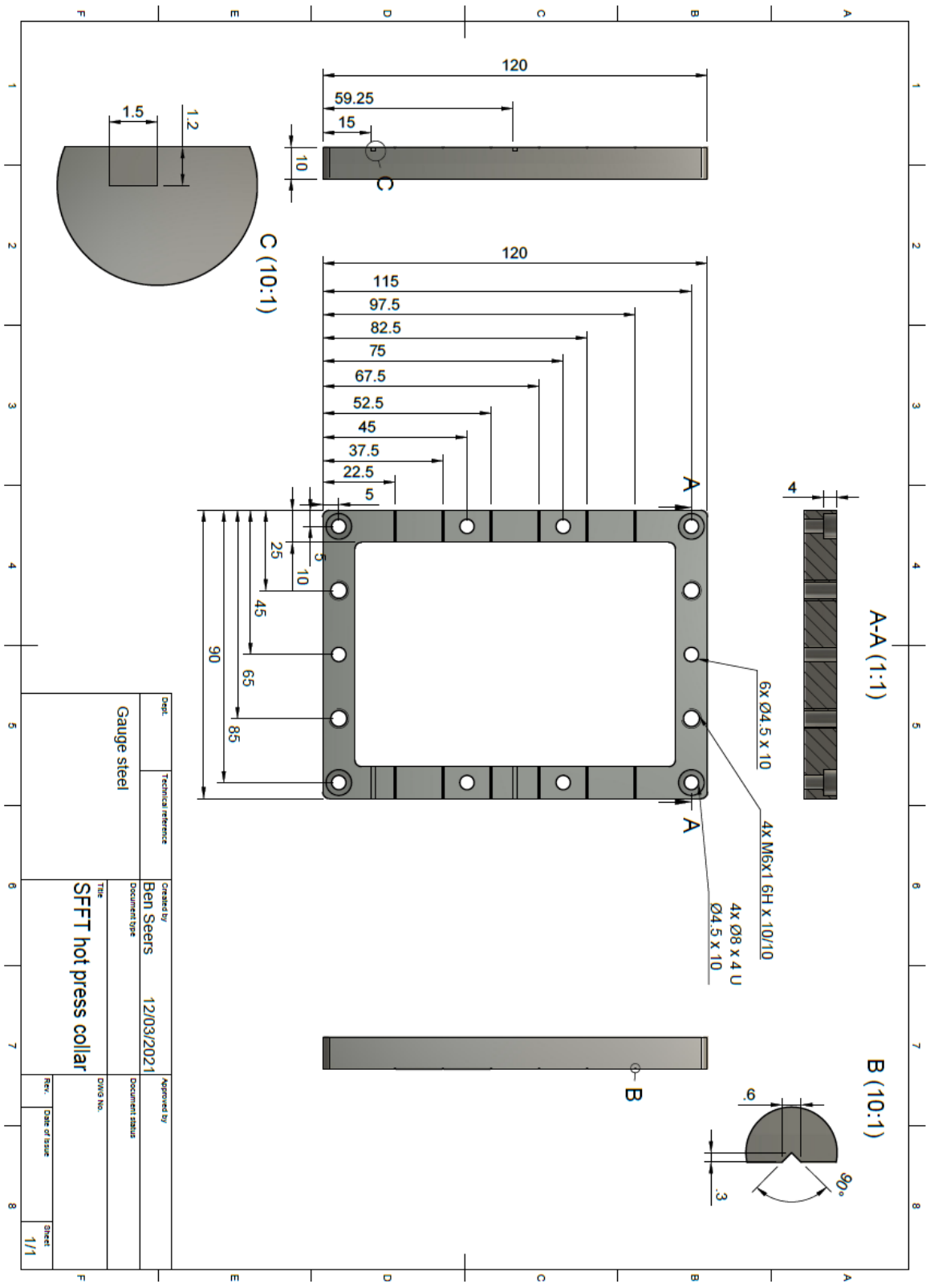


Figure 102: Rapid curing SFFT hot press drawing – fibre collar

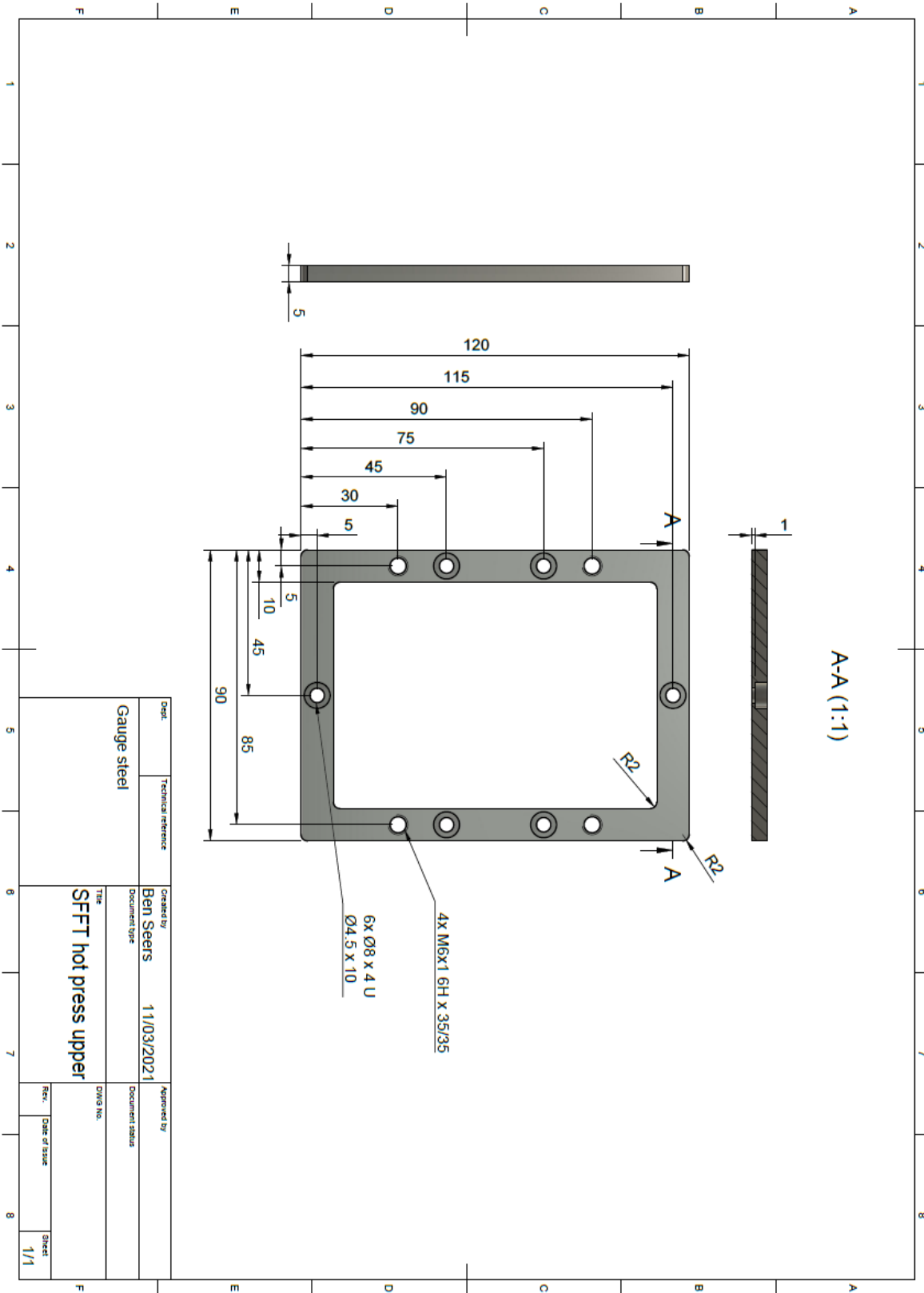


Figure 103: Rapid curing SFFT hot press drawing – retaining collar

Appendix D

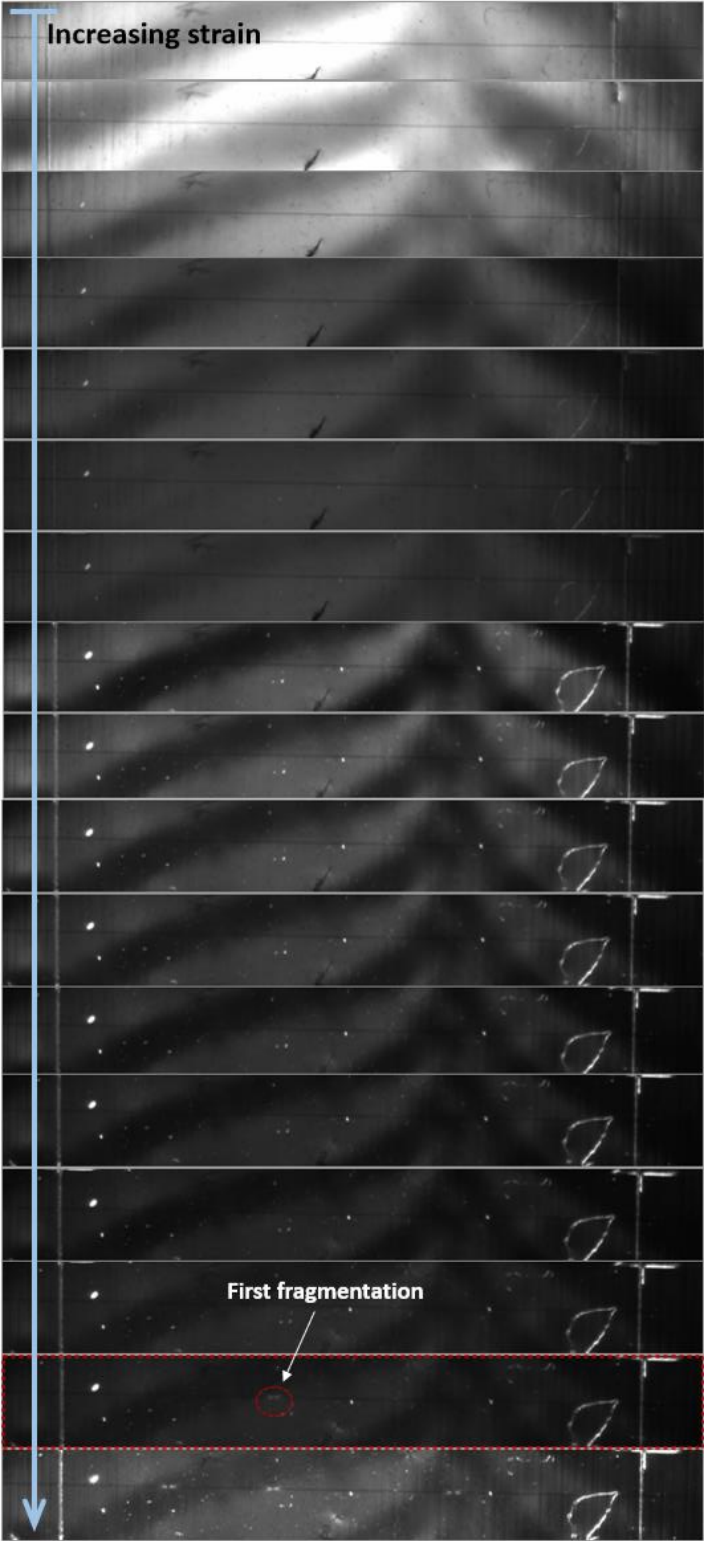


Figure 104: Rapid SFFT results for RC4_A

Appendix E

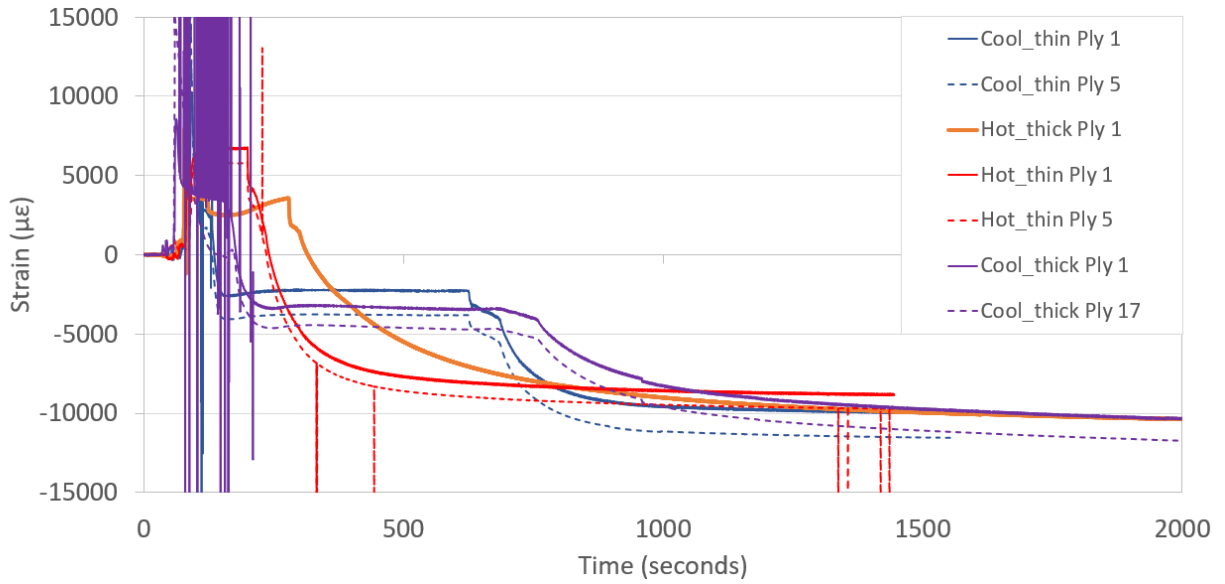


Figure 105: Embedded FBG raw data for time 0-2000 seconds

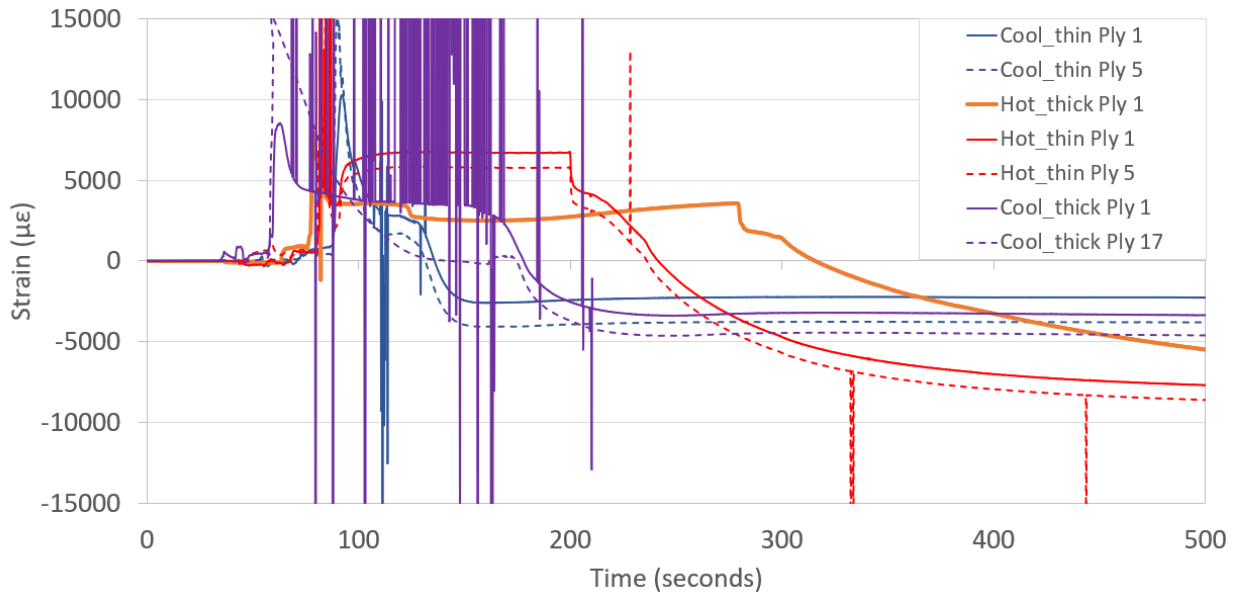


Figure 106: Embedded FBG raw data for time 0-500 seconds